A

Presented to
the faculty of the School of Engineering and Applied Science
University of Virginia

in partial fulfillment
of the requirements for the degree

by

APPROVAL SHEET

This

is submitted in partial fulfillment of the requirements
for the degree of

Author:

Advisor:

Advisor:

Committee Member:

Committee Member:

Committee Member:

Committee Member:

Committee Member:

Committee Member:

Accepted for the School of Engineering and Applied Science:

Craig H. Benson, School of Engineering and Applied Science

Abstract

Mechanisms of thermal transport vary drastically from the nanoscale to the macroscale. At the nanoscale, the characteristic length and time scales over which heat transfer occurs can be on the order of nanometers and picoseconds, respectively. For example, in nanoelectronics, thin adhesion layers (< 10 nm) will often be implemented to better increase adherence of Au contacts. The interfacial conductances of these regions, however, can pose as limiting resistors of the system, potentially limiting the maximum allowable heat to be transferred into the heat-sinking substrate. Macroscale analogies for these nanoscale structures can additionally be found throughout the aerospace industry. Specifically, coatings for gas turbine engine blades consist of thick, steam-resistive materials bonded to a high thermal conductivity, heat-sinking blade via a thin, insulating amorphous layer. The time and length scales over which heat transfer typically considered in these components are orders of magnitude larger than their nanoscopic counterparts, occurring on the order of seconds to hours and microns to millimeters. Engine efficiencies are dictated by the maximum allowable operating temperatures, thus necessitating a robust understanding of the thermal profiles found in each layer of the multilayer turbine blade coating.

In this dissertation, these nano- to macroscale phenomena are addressed through a series of experimental works using an advancement in pump/probe metrology that will provide insight into heat transfer mechanisms in composite coatings at these differing time and length scales. At the nanoscale, an emphasis is placed on the Au/TiO_x system, which offers a plethora of information relevant to the nanoelectronics industry while providing an ideal test system to study how chemistry at heterogeneous material boundaries impacts thermal transport processes across orders of magnitude time and length scales. Specifically, this dissertation elucidates mechanisms of thermal transport in Ti adhesion layers that are oxygen defected. This includes the influence of said defects on the electron-phonon coupling factor in these layers via examining the picosecond pump/probe dynamics of time-domain thermoreflectance and implementing a two-temperature model analysis to understand mechanisms of heat flow between the two fundamental carriers of heat in substoichiometric TiO_x. To study heat transport mechanisms across meso-to-macroscopic length scales, environmental barrier coating materials will provide this focus. This will include analysis of the thermal conductivity anisotropy of β-$Y_2Si_2O_7$, a rare earth disilicate that is commonly implemented as a barrier coating material. Additionally, the spatio-temporal evolution of a steam-cycled β-$Yb_2Si_2O_7$ coating and its ultimate influence on the thermal profile experienced in the hot-section of a gas-turbine engine is presented, exemplifying the need for an understanding of the thermal properties of these evolving systems.

In examining each of these systems, significant advancements in pump/probe metrology are made. By further developing these techniques to examine the spatially-varying thermal characteristics of macroscale systems on the order of just a few micrometers, and by using advanced modeling to understand the excited carrier dynamics of thin films in regimes of non-equilibrium, this dissertation provides an advancement in the understanding of heat transport mechanisms in multilayer systems at mesoscopic length and time scales.

Acknowledgements

I owe a great deal of thanks to many individuals that have contributed, directly or indirectly, to this dissertation. Without their help, writing and performing experiments for this document would have been a gargantuan feat that I would have otherwise thought unfathomable.

First, I am extremely grateful to my advisor, Patrick Hopkins. Patrick has been with me every step of the way in working towards this dissertation, providing crucial experimental and theoretical insight. His breadth of knowledge on all subject matters inspires me to be a better experimentalist, researcher, and person. I am especially grateful for Patrick's trust in me, as he has afforded me several opportunities to explore experimental avenues on the heat transfer front, perform niche characterization techniques that have expanded my scientific knowledge, and ultimately allowed me to study what was of most interest to me.

I would also like to extend thanks to the members of my committee, Dr. Chloe Dedic, Dr. Elizabeth Opila, Dr. Stephen McDonnell, and Dr. Adam Chamberlain, many of whom have contributed to this dissertation in some manner or another, and all of whom may be the only individuals to ever read it. In particular, Dr. Opila and Dr. Chamberlain have provided insight into the dynamic processes of thermal/environmental barrier coatings, and Dr. McDonnell helped me to understand the importance of minute chemical differences in materials and their influence on heat transfer.

In addition to the members of my committee, the work performed throughout my graduate school career would not have been possible without the help from individuals from other lab groups, universities, and institutions. In particular, I would like to thank Dr. Haydn Wadley and Dr. Jeroen Deijkers of the Wadley Research Group, Tianhui Zhu, Md Rosul, and Dr. Zebarjadi of E-Snail, Dr. Keren Freedy and Maria Sales from the SMCD Group, Dr. Cory Parker and Dr. Valentina-Angelici Avincola from the Opila Research Group, Dr. Teng-Fei Lu and Dr. Oleg Prezhdo from the Laboratory for Quantum Dynamics, and Dr. Robert Golden and Dr. Gregory Harrington from Rolls-Royce Inc.

I am extremely privileged to have worked in the ExSiTE lab throughout graduate school. The collaborative, helping environment is ultimately what enabled me to further my experimental and scientific understanding of heat transfer, physics, materials science, chemistry, and beyond. In my first years at the ExSiTE lab, many of the senior members were extremely patient when I was first acclimating to an optical table. It was this patience that allowed me to create a foundation of optics that has carried me through the years. I am grateful to Dr. John Gaskins, Dr. Leonard Braun, Dr. Albert Tomko, Ethan Scott, and Dr. Mallory Rykal, who have been extremely critical of my work for its betterment. It is safe to say that without all members of the ExSiTE lab, I would not be the researcher that I am today.

Without the continued support and understanding of my family, this dissertation would not have been possible. My mom has always been supportive of my endeavors, and while she may not always understand what my research entails, I know that she is immensely proud of me. Likewise, my dad has always been interested in and supportive of my dissertation research, although he knows enough materials science to question it. I am especially grateful to both of them for dragging me on family vacations when Patrick would have preferred me in the lab. To my siblings, thank you for bringing a sense of normalcy to my life when it was otherwise engulfed in science.

Most importantly, I am grateful to my loving girlfriend, Theresa, who has helped me grow as a person these last four years. At the end of a long day or week, it's always nice to take a break from the lab, and Theresa was always there for me.

Finally, I am grateful for funding from the Virginia Commonwealth Fellowship through UVa, the Virginia Space Grant Consortium (VSGC) Fellowship, and National Defense Science and Engineering Graduate (NDSEG) Fellowship.

I always choose a lazy person to do a hard job, because a lazy person will find an easy way to do it.

–Bill Gates

Contents

List of Figures

List of Tables

Chapter 1

Introduction

Thermal management is critical to a wide array of modern technologies. In the continuum, macroscopic limit, temperature gradients experienced by materials follow the phenomenological Fourier's Law [1],

$$q = -\kappa \nabla T. \tag{1.1}$$

In this equation, the heat flux, q, is proportional to the temperature gradient, ∇T, via the thermal conductivity κ, where the negative sign arises due to the fact that heat must flow from hot to cold. Inspection of Fourier's Law indicates that the temperature gradient experienced in a material is inversely proportional to its thermal conductivity, whereby increasing the thermal conductivity mitigates ∇T, and reducing the thermal conductivity increases ∇T. In this continuum limit, carriers within a material traverse diffusively, scattering only with one another as they transfer heat.

As the characteristic dimension of the material approaches that of its heat carriers, Fourier's Law fails to adequately describe heat conduction at this scale. In addition to scattering with one another, heat carriers are now subject to scattering with additional, extrinsic factors. These include thin film boundaries [2], material interfaces [3], grain boundaries [4], and defects [5, 6], to name a few. In this micro- nanoscopic limit, mechanisms of heat transfer become non-diffusive, and the thermal conductivity must be defined under a different light. Under the kinetic theory of gasses [7], in which carriers are treated as particles, the thermal conductivity is

$$\kappa = \frac{1}{3}Cv\lambda = \frac{1}{3}Cv^2\tau, \tag{1.2}$$

where C is the volumetric heat capacity, v is the carrier velocity, λ is the mean-free-path, or distance between scattering events, and τ is the scattering time, or time between scattering events. Thus, the thermal conductivity is dictated by the energy of the carrier, C, traversing through the material at velocity v, before scattering at a distance λ. The aforementioned extrinsic influences can significantly affect λ, reducing this value and ultimately reducing the thermal conductivity.

As one might expect, mechanisms of thermal transport vary drastically in these macroscopic and nanoscopic limits. At the nanoscale, the characteristic length and time scales over which heat transfer occurs can be on the order of nanometers and picoseconds, respectively. For example, in nanoelectronics, thin adhesion layers ($<$ 10 nm) will often be implemented to better increase adherence of Au contacts. In these heterogeneous systems, the conductances at material/material interfaces can pose as limiting resistors of such systems, potentially limiting the maximum allowable heat to be transferred into a heat-sinking substrate. Additional considerations must be made when accounting for the contribution of and interaction between diverse carriers to the transport processes. Macroscale analogies for these nanoscale structures can additionally be found throughout the aerospace industry. Specifically, coatings for gas turbine engine blades consist of thick, steam-resistive materials bonded to a high thermal conductivity, heat-sinking blade via a thin, insulating amorphous layer. The time and length scales over which heat transfer occurs in these components are orders of magnitude larger than their nanoscopic counterparts, occurring on the order of seconds to hours and microns to millimeters.

Recent advancements in thermal characterization have afforded the opportunity for the thermal characterization of these thin, nanoscopic, and bulk, macroscopic systems. As nanoelectronic device length scales approach the characteristic length scales of fundamental heat carriers, namely electrons and phonons, novel metrologies that can probe all pertinent length, as well as time, scales are necessary. This has resulted in the implementation of laser-based techniques to access the characteristic dimensions of devices, as diffraction-limited beams can readily achieve length scales on the order of just a few micrometers or less. Specifically, ultrafast pump/probe techniques provide the temporal and spatial resolution necessary for understanding excited carrier dynamics on ultrafast timescales while performing measurements of nanoscopic thermal resistances. In addition to probing these nanoscopic processes, such techniques retain the added benefit of the ability to monitor carrier diffusion in the macroscopic limit.

1.1 Applications

Unsurprisingly, understanding mechanisms of heat transfer has far-reaching applications. In general, we can break up applications in which we want to enhance or impede the flow of heat. Those necessitating enhanced heat transfer will require a larger net thermal conductance so that the temperature gradients of a device or system are minimized. Such applications include those in central processing units (CPUs), in which heat generated during high-frequency operation must be removed as efficiently as possible so as not to compromise functionality. Additional applications are found in energy-generation, as in solar cells where photovoltaic efficiency is thwarted by an increase in temperature [8], or in nuclear fuel particles for high temperature nuclear reactors [9, 10]. Thermoelectric devices, which generate an electric field based on an induced temperature gradient [11, 12], on the other hand, require materials that impede the flow of heat so that charge separation is maintained. In hot environments, where operating temperatures can exceed the melting temperatures of many materials, insulating materials that create a large temperature differential are preferred. In the following two subsections, I go into more detail surrounding the applications associated with heat transfer, specifically applied to environmental/thermal barrier coating systems as well as in nanoelectronic devices.

Environmental and Thermal Barrier Coatings

Gas turbine engines are used for generating thrust on aerospace vehicles as well as for generating electricity on land [13]. In a gas turbine engine, air is ingested through the inlet and is subsequently compressed to elevated pressures using a gas compressor. This compressed air is mixed with fuel at a certain ratio, and subsequently ignited in the combustion chamber. Ignition of this fuel/air mixture results in an increase in temperature and rapid expansion of the gasses in the chamber. These hot, high velocity gasses force the rotation of blades of the turbine, which in turn drives the compressor and increases the air intake at the engine inlet. The turbine also generates electricity by driving the shaft of a generator, and the high velocity gasses produce thrust upon exiting the exhaust section of the engine.

A critical component of the gas-turbine engine is its operating temperature. Fundamentally, the efficiency of a gas-turbine engine is dependent on the temperature of its hot-section. In the hot-section of a gas-turbine engine, temperatures will easily reach 1300 °C,

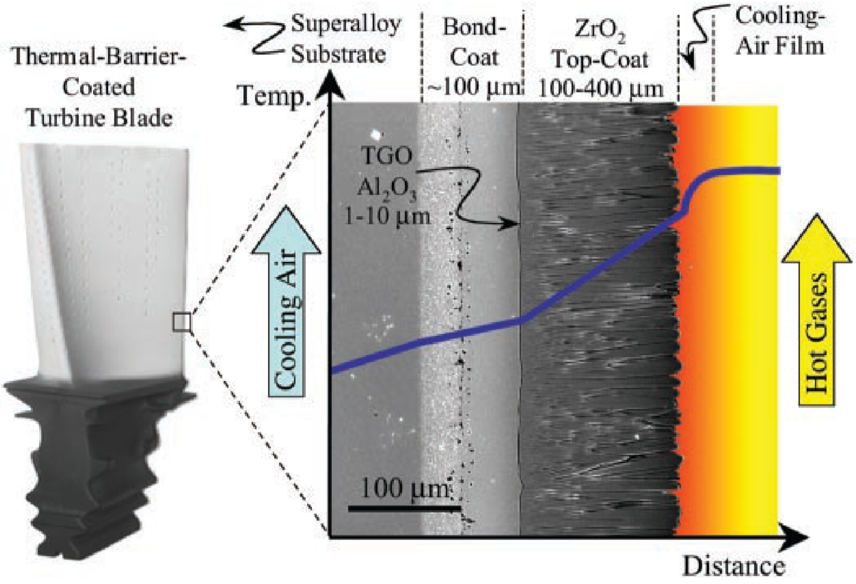

Figure 1.1. Functionality of thermal barrier coating on a turbine blade. A superalloy turbine blade is coated with a ZrO_2 thermal barrier coating to induce a temperature disparity between the turbine blade and hot gasses in the engine environment. From Padture *et al.*, *Science* 12, 2002. Reprinted with permission from AAAS.

and thus a foundational understanding of the thermal characteristics of each component required in the implementation of turbine blades is required. The use of a low thermal conductivity thermal barrier coating (TBC) has allowed for an increase in insulation for metallic turbine blades, allowing for the hot section to surpass the turbine blade melting temperature and ultimately increase engine efficiencies [14, 15]. An example of a TBC is shown in Fig. 1.1, in which a ZrO_2 top-coat is bonded to the superalloy turbine blade by a bond coat. The TBC creates a large temperature disparity between the superalloy substrate and hot gasses in the engine environment, allowing for an increase in operating temperatures to be achieved beyond the melting temperature of the superalloy.

Turbine blades were initially composed of Ni-based superalloys, operating in the range of 900-1000 °C, see Fig. 1.2(a). In absence of the implementation of a TBC, operating temperatures of Ni-based superalloys alone have remained stagnant for the past several decades, limited by their relatively low melting temperatures. While TBCs have drastically improved operating temperatures, and therefore efficiencies, their maximum attainable operating temperatures are limited by phase stability [16] and infiltration of silicates in the engine atmosphere [17, 18].

Recently, efforts have been made to transition from turbine blades composed of superalloy substrates to silicon carbide ceramic matrix composites (SiC CMCs) due to their high specific strength and increased mechanical stability at elevated temperatures [19–21]. However, unlike the conventional TBC implemented for Ni-based superalloy turbine blades, in which porosity and microstructural defects are plentiful, SiC CMC turbine blades require a dense coating that is more environmentally protective. Hence, SiC CMC turbine blades have sought the use of environmental barrier coatings (EBCs), which consist of a rare-earth silicate top coat bonded to the turbine blade via a Si bond coat. At the surface of the Si bond coat, a thermally grown oxide will form a result of the interaction with oxidizing species that have permeated the rare-earth silicate top coat. The primary purpose of an EBC is to prevent the formation of gaseous CO, CO_2, and/or $Si(OH)_4$ and recession of the turbine component [16, 22, 23]. This does not exclude the thermally insulating characteristics of

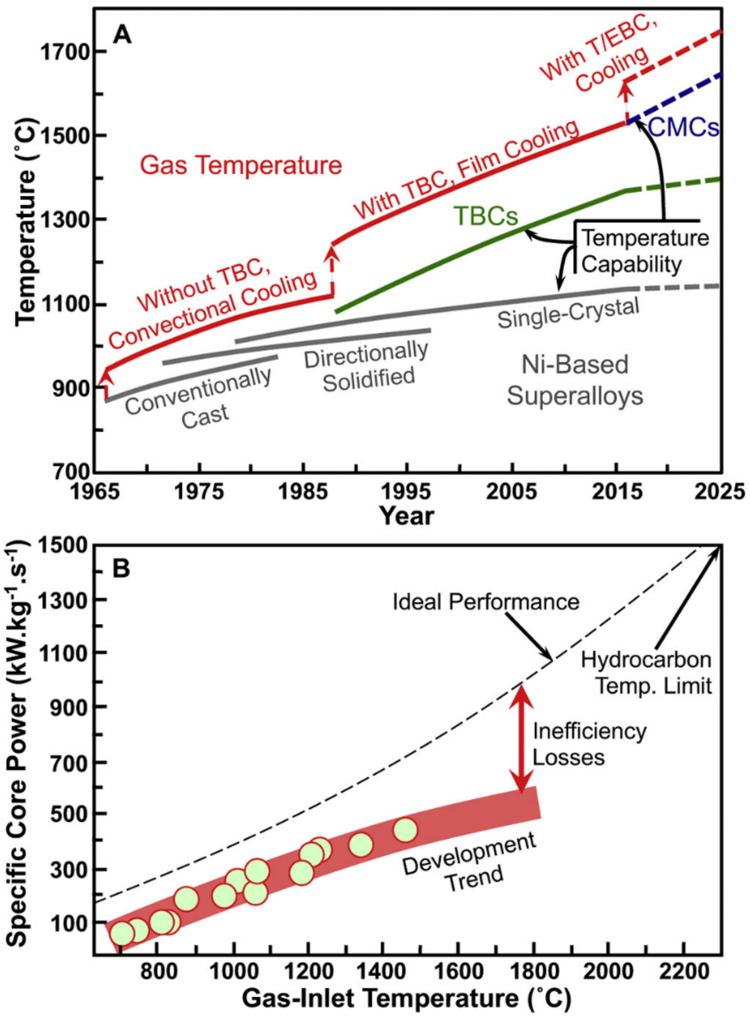

Figure 1.2. (a) Progression of relevant gas-turbine engine temperatures with respect to the gas, Ni-based superalloys, thermal barrier coatings (TBCs) and ceramic matrix composites (CMCs). (b) Specific core power versus gas-inlet temperature, exemplifying the disparity between development trends and ideal performance. Reprinted from Turcer *et al.*, *Scripta Materialia* 154, 2018. Copyright 2018 with permission from Elsevier.

the EBC, as a large temperature gradient between the hot gasses in the engine environment and the CMC substrate is desired. The use of CMC turbine blades will enable a large increase in the gas inlet temperature, reaching nearly 1700 °C [22, 24, 25]. Correspondingly, this will result in an increase in efficiency, see Fig. 1.2(b). As the gas-inlet temperature has evolved from 750 °C to 1500 °C over the past several decades, a nearly 5-fold increase in the specific core power has been achieved. With an improved understanding and tuning of the insulating characteristics of T/EBC used on the turbine blades of modern engines, in addition to the plethora of other modalities used to increase the engine operating temperature [17], realizing engines with improved efficiencies due to their operating temperatures is something that can be readily addressed.

Nanoelectronic Devices

In addition to the more macro-scale requirements of thermal management in the hot-section of a gas-turbine engine, the management of heat and mitigation of temperature rises is fundamental for electronic devices at the micro/nanoscale. Recent progress in the synthesis and processing of nanometer-sized structures in the electronics industry have necessitated the need to account for differences in thermal transport at this sub-continuum length scale. In particular, interfaces between adjacent media have the potential to significantly impede heat flow into a heat sinking substrate by the inclusion of an interfacial resistance [26]. Several applications contingent on the implementation of these interfaces are presented in Fig. 1.3. These applications range from light emitting diodes, which implement

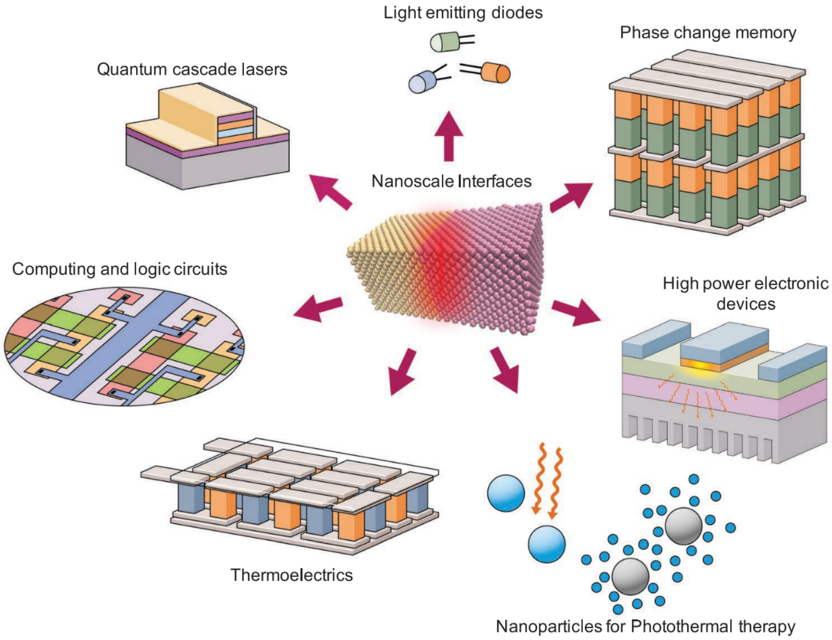

Figure 1.3. Various technologies contingent on the implementation of heterogeneous interfaces in nanoscale devices. Reproduced with permissions from Giri *et al.*, *Adv. Fun. Mat.* 20, 8 (2020). Copyright 2010 WILEY-VCH Verlag GmbH & Co. KGaA, Weinheim.

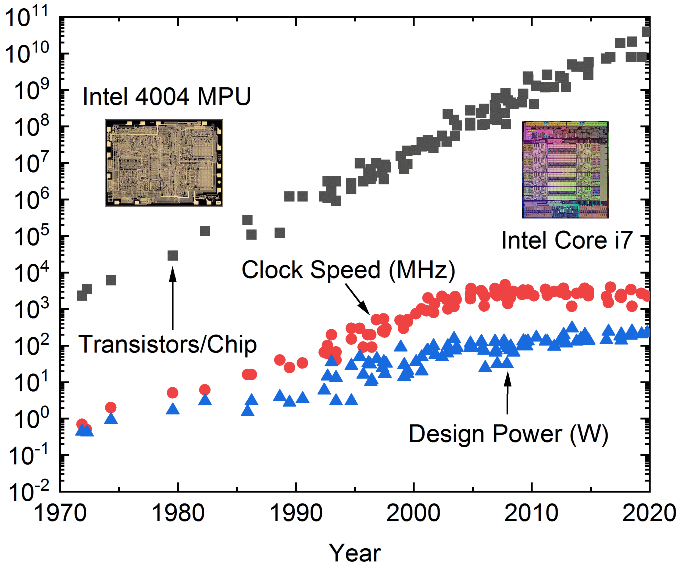

Figure 1.4. Evolution of number of transistors per chip, CPU clock speed, and CPU design power for the past 50 years. The Intel 4004 microprocessor unit (MPU) and Core i7 central processing unit (CPU) are shown to exemplify the differences in transistor densities. The data are from Ref. 27, while the images are from Refs. 28, 29.

p-n junctions to induce stimulated emission, to integrated circuits necessary for performing complex computational algorithms, to nanoparticles utilized for photothermal therapy. In all of these applications, energy transfer from one material to another must occur through material interfaces, and thus an understanding of these processes is foundational for their continued optimization.

One such device at this subcontinuum length scale that features heterogenous material interfaces is the transistor, which functions as a nanoscopic electrical switch and is the foundation for modern computing. Integrated onto a single chip, permutations of transistor design result in the logic necessary for performing complex calculations that would be otherwise unfathomable. Such a progression of the number of transistors implemented on these chips through the years is shown in Fig. 1.4, where the first microprocessor unit (MPU) developed by Intel in 1970 contained a mere 2000 transistors to perform the necessary calculations, and at just a clock speed of $\sim$1 MHz [30]. Fundamentally, the clock speed determines the rate at which calculations can be made by the processor. By the early 2000s, 10 million transistors had been integrated onto a single chip, with clock speeds now operating in the GHz range [31]. Improvements in the clock speed have been stagnant since this time period, due to the fact that the temperature rise associated with the building block of the processors–the transistor–were becoming too large at higher operating frequencies. Indeed, the typical length scale in a modern transistor is < 100 nm, with chip power densities on the order of a rocket nozzle [32]. Mitigating this temperature rise has primarily been addressed from the macroscopic scale–using large grid fins or cooling fans to remove heat from these devices. However, as the majority of this heat is produced at nanometer length scales, optimizing transport processes at these length scales will help to drive the design of processors, allowing them to operate at higher clock speeds.

1.2 Dissertation Structure

The overarching goal of this dissertation is to address thermal transport processes in both the continuum and subcontinuum limits using the laser-based thermoreflectance technique time-domain thermoreflectance (TDTR). This includes significant strides in expanding the experimental capabilities of TDTR, and by using the complex modeling to analyze the carrier dynamics during conditions of non-equilibrium following ultrafast laser excitation. On the experimental front, the dissertation seeks to develop a thermal conductivity microscope that is able to spatially monitor the thermal conductivity of a material system on the order of just a few micrometers. The emphasis of this application will be placed in the coatings of a gas-turbine engine blade. Additionally, the dissertation will examine thin Au contacts with a TiO_x wetting layer and its influence on the interfacial resistance. This will involve analysis of electron and phonon temperatures in the system to understand the underlying energy transfer mechanisms with the presence of a defected wetting layer.

To address each of the aforementioned goals, the dissertation will be structured as follows:

- **Chapter 2:** The theory of thermal transport will be presented. At first, I will discuss the tensorial representation of thermal conductivity, which is applicable in the continuum limit. Following, I will delve into its definition in the subcontinuum limit, where the descriptions of the thermal conductivity from the perspective of electrons or phonons will be presented. Finally, I will consider interfacial transport at dielectric/dielectric, metal/metal, and metal/dielectric interfaces.

- **Chapter 3:** The necessary metrology and modeling required for addressing thermal transport processes in the continuum and subconitinuum limits will be discussed in this chapter. Because thermoreflectance and lock-in amplification are foundational for the implementation of time-domain thermoreflectance, I provide a brief background on the concepts in this chapter. Following, I discuss the two-tint implementation of time-domain thermoreflectance that I implemented during my first year as a PhD candidate. The mathematical formalisms for analyzing the data garnered by this technique will be discussed from the perspective of carrier equilibrium and carrier non-equilibrium. Finally, the requirements for the extension of TDTR to spatially probe thermal properties will be presented.

- **Chapter 4:** The thermal conductivity characteristics of an EBC and its constituents will be assessed. Specifically, the anisotropic thermal conductivity of β-$Y_2Si_2O_7$ is measured using the thermal conductivity mapping technique outlined in the previous chapter. This enables for the extraction of the tensorial representation of the thermal conductivity of β-$Y_2Si_2O_7$. In the latter half of the chapter, I assess the spatio-temporal evolution of the thermal conductivity in a β-$Yb_2Si_2O_7$ EBC. Specifically, thermal conductivity measurements are performed over the topcoat of the EBC and correlated to scanning electron and electron backscatter micrographs, with insight into the reactions driving the dynamic stability of the coating as it is cycled to several thousand hours.

- **Chapter 5:** Continuing on with the theme of EBCs, this chapter examines a critical component of a multilayer EBC system: the thermally grown oxide. The crystallization and subsequent phase transformations of this oxide layer can result in premature failure of the EBC via spallation, and thus understanding the crystallization processes are necessary for longterm thermomechanical stability of an EBC. In this chapter, I utilize the thermal conductivity as a gauge for understanding devitrification effects in a TGO layer. This is done by first performing a case study on a fused silica ($aSiO_2$) glass slide that has been steam cycled to induce devitrification and observing the local variations in thermal conductivity. Subsequently, the same characterization is performed on a relevant EBC system. It is shown that gauging the crystalline characteristics of the TGO layer can be performed by localized thermal conductivity measurements with greater contrast than conventional optical techniques.

- **Chapter 6:** This chapter elucidates thermal transport processes at metal/dielectric interfaces. Specifically, candidate Au/TiO_x material systems are examined for the influence of TiO_x stoichiometry on interfacial transport. In the first half of this chapter, these processes are examined from a purely interfacial conductance perspective. The results indicate that both stoichiometry and thickness of adhesion layers play a critical role in interfacial transport processes. Following, electron-phonon coupling characteristics of these systems are examined using a two-temperature formalism. The results indicate that defects in the adhesion layers significantly influence carrier interactions, fundamentally driving interfacial transport into the substrate.

- **Chapter 7:** A summary of the dissertation is provided, and each of the chapters are related such that they are in congruence with the aims of the dissertation. Several possibilities in regards to future avenues of research are presented.

It is important to note that while the sections of each chapter follow a similar theme in terms of material system and/or characterization, the introductions of each are motivated in such a way that they may be overlapped and reiterated. This is done so that each section may be read in a standalone fashion, without the need to refer to the Introduction of the dissertation.

1.3 Impact

Several advancements in the field of thermal transport have been achieved as a result of the works compiled in this dissertation. Primarily, the dissertation sought the expansion of the experimental capabilities in the optical pump/probe TDTR. Specifically, the work resulted in the development of a thermal property microscope, enabling micrometer-scale measurements of a thermal property over an aerial region of interest. Additionally, by further examining the picosecond pump/probe dynamics as garnered by TDTR, novel two-temperature model analyses were developed to characterize carrier interactions at these time scales.

In surveying the literature for measurements of thermal conductivity, a large fraction of the literature has devoted their thermal characterization to macroscopic techniques. These include the guarded hot plate [33], transient hot-wire [34], transient plane source [35], and laser flash [36] techniques. In all of these techniques, measurements are typically performed on macroscopic specimens, with lateral dimensions on the order of millimeters. As such, the acquired thermal conductivity is representative of an average of the constituents present in the system of interest, and does not delineate between variations at the microstructural level. By implementing TDTR, and achieving probing scales at this microstructural level ($<10\ \mu$m), these delineations are more easily made. In this dissertation, I was able to expand these capabilities by the development of a thermal property microscope, in which the thermal property of interest can be determined at the micrometer level over aerial regions extending to several hundred micrometers in dimension. Effectively, the microscope aided in bridging the gap between TDTR and conventional, macroscopic methods for determining thermal conductivity.

Further developments were made in TDTR and its application in the characterization of nanoscale systems. At these length scales, additional considerations for the interfaces between adjacent media must be made for understanding the thermal transport processes. As metal contacts to dielectric substrates are ubiquitous in the nanoelectronics industry, they also provided focus in this dissertation. Specifically, these processes were examined under regimes both of carrier equilibrium and carrier non-equilibrium for contacts with idealized and non-idealized metal adhesion layers. The results help to emphasize the importance of impurities and how they are able to enhance transport from the metal contact to the substrate. Additionally, by modeling these dynamic systems under regimes of non-equilibrium at picosecond timescales using a two-temperature formalism, the extraction of electron-phonon energy transport mechanisms in defected material systems is enabled. In considering the dynamics of these systems in regimes of equilibrium and non-equilibrium, a greater understanding of transport processes at non-idealized contacts is achieved.

By further developing TDTR in each of these capacities, robust characterizations of a material's thermal conductivity in a macroscopic setting as well as the carrier dynamics in nanoscopic systems are able to be made. The thermal property microscope is just one of a few present in academia and industry, and is a significant advancement in characterizing the thermal property of a system with local variations on the order of just a few micrometers. Likewise, the characterization of metal/metal oxide systems via two-temperature modeling offers exciting new opportunities for understanding carrier-carrier dynamics at picosecond timescales in a variety of device-relevant nanotechnologies. In all, the advancements in thermal characterization brought forth by this dissertation will help to paint a better picture of the transport processes pertaining to macro- and nanoscopic phenomena.

Chapter 2

Thermal Transport: Continuum and Subcontinuum

In this chapter, I will provide the reader with a basic understanding of heat transfer mechanisms in continuum and subcontinuum limits. In the continuum limit, an emphasis will be placed on the tensorial representation of the thermal conductivity. In the subcontinuum limit, the interpretation of the thermal conductivity will be made from the perspective of kinetic theory. As such, it will include the discussion of the volumetric heat capacities, propagation speeds, and scattering rates of carriers pertinent to this dissertation–phonons and electrons. Finally, I will address the mechanisms of heat transfer at heterogeneous material interfaces from the perspective of these carriers.

2.1 Thermal Conductivity

Conduction of heat through a medium is phenomenologically defined via Fourier's Law [1], which relates the heat flux, q_z to the temperature gradient, $\frac{dT}{dz}$, via the thermal conductivity, κ. In one dimension, the equation is

$$q_z = -\kappa \frac{dT}{dz}. \tag{2.1}$$

Inspection of Eq. 2.1 indicates that the temperature gradient formed in a material is fundamentally defined via κ, and that, for bulk media, the heat flux q_z will result in a temperature gradient that is inversely proportional to κ. Thus, if κ is very large, the temperature differential across a medium will be very small, and if κ is very small, the temperature differential will be much larger. This has vast implications for a variety of fields, such as in gas turbine engines, where coatings require a low κ to increase the temperature differential to prevent the turbine blade from melting. On the other end, a high thermal conductivity is required when the temperature rise must be mitigated, such as in nanoelectronic devices.

These two examples are characteristic of two very separate length scales. On one hand, coatings on a turbine blade will operate moreso in the continuum limit, as these coatings will typically be on the order of $\sim$100 μm in thickness. On the other hand, as implied by its name, nanoelectronic devices rely on nanometer-scale components, and thus operate in a subcontinuum limit. The differences in thermal transport at these two scales will be elucidated in the following two subsections, with focus on the thermal conductivity tensor of a material in the continuum limit, and then a discussion of the fundamental carriers that drive thermal transport in the subcontinuum limit.

2.1.1 Continuum

In the continuum limit, we begin with Fourier's law, Eq. 2.1. In order to generalize Eq. 2.1 to all dimensions, we must first make a few adjustments to the equation. The heat flux along the z-direction, q_z, now becomes the heat flux vector, **q** with components q_x, q_y, and q_z:

$$\mathbf{q} = \begin{bmatrix} q_x \\ q_y \\ q_z \end{bmatrix}. \tag{2.2}$$

Similarly, the one-dimensional temperature gradient $\frac{dT}{dz}$ becomes the temperature field, $\nabla\mathbf{T}$, with components $\frac{\partial T}{\partial x}$, $\frac{\partial T}{\partial y}$, and $\frac{\partial T}{\partial z}$:

$$\nabla\mathbf{T} = \begin{bmatrix} \frac{\partial T}{\partial x} \\ \frac{\partial T}{\partial y} \\ \frac{\partial T}{\partial z} \end{bmatrix}. \tag{2.3}$$

In order to relate the heat flux vector, $\mathbf{q}$, to the temperature field, $\nabla\mathbf{T}$, the thermal conductivity must enter into its tensorial formalism. For now, we will assume that the thermal conductivity tensor, $\widetilde{\mathbf{K}}$ contains 9 independent components, κ_{ij} for $i, j = x, y, z$:

$$\widetilde{\mathbf{K}} = \begin{bmatrix} \kappa_{xx} & \kappa_{xy} & \kappa_{xz} \\ \kappa_{yx} & \kappa_{yy} & \kappa_{yz} \\ \kappa_{zx} & \kappa_{zy} & \kappa_{zz} \end{bmatrix}. \tag{2.4}$$

Each of the components of the thermal conductivity tensor relate a component of the heat flux vector to another component of the temperature field, which may not be in the same direction (i.e., κ_{xz} relates the heat flux in the x-direction, q_x, to the temperature gradient in the z-direction, $\frac{\partial T}{\partial z}$). In the case of Eq. 2.4, $\widetilde{\mathbf{K}}$ relates the heat flux to the temperature field for a *triclinic* crystal system. The formalism for $\widetilde{\mathbf{K}}$ in crystal systems of differing symmetries will be discussed later.

In its full form, Fourier's law now becomes

$$\begin{bmatrix} q_x \\ q_y \\ q_z \end{bmatrix} = -\begin{bmatrix} \kappa_{xx} & \kappa_{xy} & \kappa_{xz} \\ \kappa_{yx} & \kappa_{yy} & \kappa_{yz} \\ \kappa_{zx} & \kappa_{zy} & \kappa_{zz} \end{bmatrix} \begin{bmatrix} \frac{\partial T}{\partial x} \\ \frac{\partial T}{\partial y} \\ \frac{\partial T}{\partial z} \end{bmatrix}. \tag{2.5}$$

There are several simplifications that can be made to Eq. 2.5, each of which reside in $\widetilde{\mathbf{K}}$. Using Onsager's Principle Theorem [37, 38], the theoretical basis of which is deeply rooted in statistical mechanics and is beyond the scope of this dissertation, symmetry of $\widetilde{\mathbf{K}}$ can be invoked, resulting in $\kappa_{ij} = \kappa_{ji}$. If this relation were not true, not only would it invalidate the second law of thermodynamics, it would also result in a spiral heat flow in crystals. While several experiments attempted to validate this spiral heat flow, it was determined that heat flow from an isolated point can be drawn via a straight line, confirming Onsager's Theorem [39, 40].

At this point, the thermal conductivity tensor takes the form

$$\widetilde{\mathbf{K}} = \begin{bmatrix} \kappa_{xx} & \kappa_{xy} & \kappa_{xz} \\ \kappa_{xy} & \kappa_{yy} & \kappa_{yz} \\ \kappa_{xz} & \kappa_{yz} & \kappa_{zz} \end{bmatrix}. \tag{2.6}$$

It is important to note that, in order to be in congruence with Fourier's law, the determinant of $\widetilde{\mathbf{K}}$ must be positive so that heat may flow from a hot to cold bath. As such, it is possible for the off-diagonal components of $\widetilde{\mathbf{K}}$ to be negative in value.

The tensorial representation of $\widetilde{\mathbf{K}}$ is primarily implemented to relate crystallographic to cartesian systems, where the principle axes of the crystal are, in general, not aligned with the cartesian coordinate system. Thus far, we have used the thermal conductivity tensor to describe a *triclinic* system, where the x-direction in the cartesian coordinate system is aligned with the [100] direction of the crystal, but the y- and z-directions are not aligned with the [010] and [001] directions of the crystal, see Fig. 2.1(a). The crystal system is based off a labradorite specimen with lattice parameters $a = 8.1736$ $\AA$, $b = 12.8736$ $\AA$, $c = 7.1022$ $\AA$, $\alpha = 93.462^\circ, \beta = 116.054^\circ$, and $\gamma = 90.475^\circ$ [41]. Figure 2.1(a) shows the large disparity, especially between the $\hat{\mathbf{z}}$ and [001] directions, between the cartesian and crystal systems. It is because of this disparity that the off-diagonal terms appear in the thermal conductivity tensor. When viewing down the -$\hat{\mathbf{y}}$ direction, as in Fig. 2.1(b), this is made more apparent. If we want to relate the heat flux in the x-direction, q_x to the temperature gradient imposed in the z-direction, $\frac{\partial T}{\partial z}$, then the tensor component relating the two will be κ_{xz}. However, because the [001] vector has components in the -$\hat{x}$ direction, this results in a κ_{xz} that will be negative.

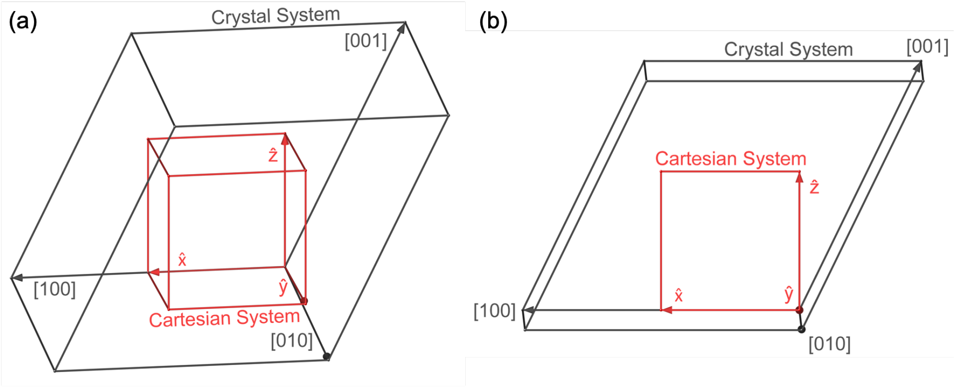

Figure 2.1. (a) Representation of cartesian and crystallographic coordinate systems, where the crystallographic coordinate system is triclinic. (b) Same as (a), but viewed down the -**ŷ** direction.

As most materials are not triclinic in nature, further simplifications to $\widetilde{\mathbf{K}}$ can be made based on the symmetry of the crystal. The associated $\widetilde{\mathbf{K}}$ for various systems is summarized in Table 2.1. For all of these systems, the κ_{xx} component, which relates the heat flux and temperature gradient in the x-direction, is aligned to be along the [100] direction of the crystal system.

Now suppose one wishes to perform a measurement of thermal conductivity on a triclinic system of arbitrary orientation. This occurs via the use of elementary tensor rotations, where $\widetilde{\mathbf{K}}$ in the new coordinate system is

$$\widetilde{\mathbf{K}}' = \mathbf{R}^T \widetilde{\mathbf{K}} \mathbf{R}. \tag{2.7}$$

In this equation, $\mathbf{R}$ is the rotation matrix and $\mathbf{R}^T$ is its transpose, where the component a_{ij} is the cosine of the angle between the two coordinate systems:

$$\mathbf{R} = \begin{bmatrix} a_{11} & a_{12} & a_{13} \\ a_{21} & a_{22} & a_{23} \\ a_{31} & a_{32} & a_{33} \end{bmatrix}. \tag{2.8}$$

Successive rotations of θ and ϕ about the z- and y-axes, respectively, using the rotation

System	# of Tensor Components	$\widetilde{\mathbf{K}}$
Cubic	1	$\begin{bmatrix} \kappa_{xx} & 0 & 0 \\ 0 & \kappa_{xx} & 0 \\ 0 & 0 & \kappa_{xx} \end{bmatrix}$
Tetragonal Hexagonal Trigonal	2	$\begin{bmatrix} \kappa_{xx} & 0 & 0 \\ 0 & \kappa_{xx} & 0 \\ 0 & 0 & \kappa_{zz} \end{bmatrix}$
Orthorhombic	3	$\begin{bmatrix} \kappa_{xx} & 0 & 0 \\ 0 & \kappa_{yy} & 0 \\ 0 & 0 & \kappa_{zz} \end{bmatrix}$
Monoclinic	4	$\begin{bmatrix} \kappa_{xx} & 0 & \kappa_{xz} \\ 0 & \kappa_{yy} & 0 \\ \kappa_{xz} & 0 & \kappa_{zz} \end{bmatrix}$
Triclinic	6	$\begin{bmatrix} \kappa_{xx} & \kappa_{xy} & \kappa_{xz} \\ \kappa_{xy} & \kappa_{yy} & \kappa_{yz} \\ \kappa_{xz} & \kappa_{yz} & \kappa_{zz} \end{bmatrix}$

Table 2.1. Summary of thermal conductivity tensors, $\widetilde{\mathbf{K}}$, for systems of various symmetries.

matrices $\mathbf{R}_z$ and $\mathbf{R}_y$, results in a representation of $\widetilde{\mathbf{K}}$ in the final coordinate system:

$$\widetilde{\mathbf{K}}'' = \mathbf{R}_y{}^T(\phi)\mathbf{R}_z{}^T(\theta)\widetilde{\mathbf{K}}\mathbf{R}_z(\theta)\mathbf{R}_y(\phi). \tag{2.9}$$

At this point, one now knows the thermal conductivity tensor of the crystal relative to the measurement orientation. If the measurement can be performed such that the component along any direction can be independently extracted, the components of Eq. 2.9 describes the magnitude of that component. However, as this is generally not feasible for most measurement configurations, let us assume that the measurement is primarily sensitive to the component orthogonal to the surface of the crystal, κ''_{zz}, or just $\kappa(\theta,\phi)$. While it is generally rigorous to perform elementary tensor rotations to arrive to $\kappa(\theta,\phi)$, its extraction is also possible via the equation

$$\kappa(\theta,\phi) = \kappa_{ij}l_il_j, \tag{2.10}$$

where κ_{ij} are components of the thermal conductivity tensor and l_i and l_j are the direction cosines,

$$\begin{aligned} l_1 &= \sin\phi\cos\theta \\ l_2 &= \sin\phi\sin\theta \\ l_3 &= \cos\phi. \end{aligned} \tag{2.11}$$

The full equation for the directional-dependent thermal conductivity is thus

$$\begin{aligned} \kappa(\theta,\phi) &= \kappa_{xx}\sin^2\phi\cos^2\theta + \kappa_{yy}\sin^2\phi\sin^2\theta + \kappa_{zz}\cos^2\phi \\ +2\kappa_{xy}\sin^2\phi\cos\theta\sin\theta &+ 2\kappa_{xz}\sin\phi\cos\theta\cos\phi + 2\kappa_{yz}\sin\phi\sin\theta\cos\phi, \end{aligned} \tag{2.12}$$

where simplifications based on crystal symmetry can be made in accordance with Table 2.1. Equation 2.12 is used to extract all components of $\widetilde{\mathbf{K}}$ in a monoclinic system using a polycrystalline sample in Chapter 4, and, in systems lacking cubic symmetry, is the thermal conductivity along the orientation probed during TDTR measurements.

A critical component in analyzing the thermal conductivity in this manner is the orientation of the crystal relative to the measurement. X-ray diffraction can be an ideal technique for the characterization of the orientation of single crystal materials, or in materials in which grain sizes are on the order of the beam size, ∼2 × 12 mm. In polycrystalline materials with grain sizes on the order of 50 μm or less, the orientation cannot be resolved due to the size of the X-ray beam, even when using a microdiffractometer. Implementing electron-backscatter diffraction (EBSD) overcomes this limitation, as the resolution is on the order of nanometers. Sample preparation is, however, difficult, but so long as the surface is sufficiently specular for a standard thermoreflectance experiment, EBSD can be readily implemented.

The information garnered by EBSD relates successive rotations about the X-Z-X directions in the commonly used Bunge convention [42]. The Eulerian angles associated with these rotations are ϕ_1, Φ, ϕ_2, where the relations

$$\begin{aligned}\phi &= \Phi \\ \theta &= \frac{\pi}{2} - \phi_2\end{aligned} \tag{2.13}$$

can be utilized to extract ϕ and θ. As such, with knowledge of the associated Eulerian angles for a given crystallite, one can extract the direction cosines to the direction of interest. For polycrystalline systems with multiple grains in which EBSD can be performed, the information garnered allows for the understanding of the orientation-dependent thermal conductivity.

2.1.2 Subcontinuum

Thus far, I have discussed the thermal conductivity from a continuum perspective, neglecting micro- and nanoscopic phenomena that pose to influence temperature gradients at these length scales. The primary two carriers that we will consider in this dissertation, mostly pertaining to Chapter 6, are phonons and electrons. A basic depiction of the interaction of and between these carriers in a medium is shown in Fig. 2.2, where carriers of different wavelengths and temperatures interact with inclusions, grain boundaries, and defects, all of which are able to influence the thermal conductivity of a material.

Before considering the thermal conductivity of electrons and phonons individually, consider one-dimensional heat flow of particles in the z-direction, orthogonal to a particular surface. At the surface, the heat flux of the particles, q_z, is defined by the difference of the heat flux in positive and negative directions, q_z = q_z^+ - q_z^-, where q_z^+ and q_z^- are the heat fluxes in the positive and negative directions, respectively. Now, consider n particles traversing through the surface with a velocity v, each of which have an energy ε, and scatter with other particles at a mean free path, λ. It is also possible to define a scattering time, or time between scattering events, based on the velocity of the particles and mean free path, $v = \lambda\tau^{-1}$, where τ is the scattering time. If the heat flux in a given direction is the product

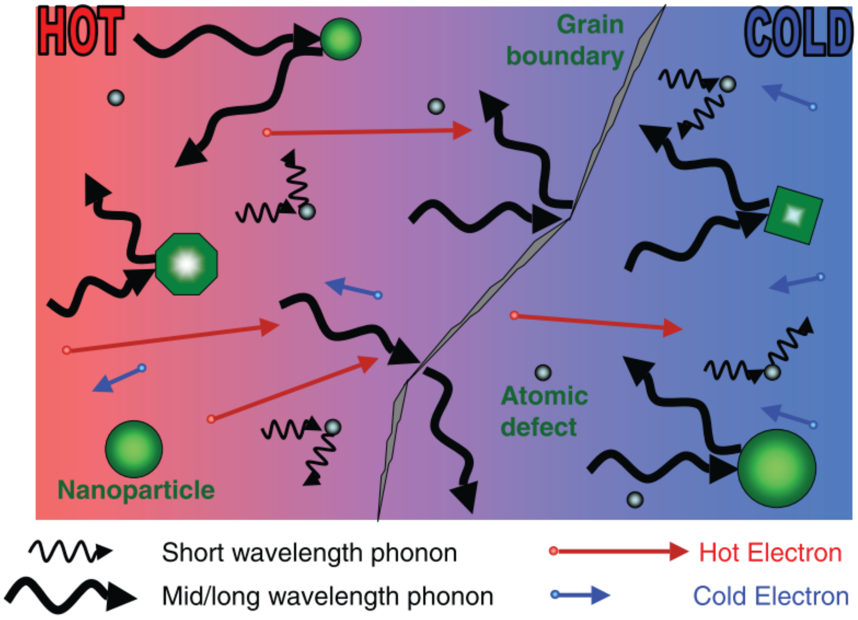

Figure 2.2. Diagram depicting electrons and phonons in a material as well as the means by which they scatter. Reproduced with permissions from Vineis *et al.*, *Adv. Mat.* 22, 36 (2010). Copyright 2010 WILEY-VCH Verlag GmbH & Co. KGaA, Weinheim.

of the velocity, energy per particle, and number of particles within a mean free path of the surface, then the net heat flux at the surface will be

$$q_z = q_z^+ - q_z^- = \frac{1}{2}\left((n\varepsilon v_z)|_{-\lambda} - (n\varepsilon v_z)|_{+\lambda}\right). \tag{2.14}$$

Using a Taylor expansion, q_z is further simplified:

$$q_z = -\lambda\frac{d}{dz}(\varepsilon n v_z) = v_z\tau\frac{d}{dz}(\varepsilon n v_z). \tag{2.15}$$

If v_z is independent of z, then the isotropic assumption can be made such that $v_z^2 = v^2/3$, where v is the average random velocity of the particles in all directions. Additionally, the total energy can be defined, $U = n\varepsilon$, where the heat capacity, C, is the temperature derivative of U, dU/dT. The equation for q_z then becomes

$$q_z = -\frac{v^2}{3}\frac{dU}{dT}\frac{dT}{dz}\tau = -\frac{1}{3}Cv^2\tau\frac{dT}{dz}. \tag{2.16}$$

Recall that Fourier's law in one dimension was defined as $q_z = -\kappa \frac{dT}{dz}$. Inspection of Eqs. 2.1 and 2.16 reveals the equation for κ in a microscopic setting:

$$\kappa = \frac{1}{3} C v^2 \tau. \tag{2.17}$$

Now that κ has been addressed in this subcontinuum limit, I will now break down each component of the equation – the heat capacity, C, velocity v, and scattering rate, τ – each for phonons and electrons.

Phonons

In crystals, heat transport is dominated by quantized lattice vibrations, or phonons. In insulators and semiconductors, phonons are the dominant heat carriers and carry heat through propagating elastic waves. To introduce this concept, consider a one-dimensional atomic chain of atoms, connected via a spring with stiffness K at an equilibrium distance a. This merits the use of Hooke's law, $F = m\ddot{x} = -Kx$, where m is the mass of the atom, x is its position, and $\ddot{x}$ is the second derivative with respect to time of the position of the atom, or its acceleration.

Using a wave-like solution, $e^{kax-\omega t}$, where k is the wavevector and ω is the angular frequency, one can arrive at the phonon dispersion, relating ω and k:

$$\omega(k) = (\frac{4K}{m})^{1/2} \sin(\frac{kx}{a}). \tag{2.18}$$

The group velocity v_g is further defined as the derivative of $\omega(k)$ with respect to k,

$$v_g = \frac{d\omega}{dk} = (\frac{4K}{m})^{1/2} \frac{x}{a} \cos(\frac{kx}{a}). \tag{2.19}$$

When the assumption is made that the system lacks dispersion (i.e., in the Debye formalism), v_g is approximated as ω/k. Recall, the thermal conductivity, κ, was directly proportional to v^2, which can be assumed is v_g^2. Thus, κ is directly proportional to the "stiffness" of the spring connecting the atoms, and inversely proportional to the mass of the atom as well as its interatomic spacing according to Eq. 2.19. This is one of the many reasons diamond has the highest thermal conductivity of any material – its ultralight carbon atoms, coupled with hybridized sp^3 bonding, and a small interatomic spacing result in an ultrahigh thermal conductivity of >1500 W m^{-1} K^{-1} at room temperature [5].

To define the phonon volumetric heat capacity, C_l, we must first consider the available phonon states in a given system, or the density of states (DOS, D). In three dimesions, it can be shown that the DOS of a carrier is

$$D(k) = \frac{4\pi k^2}{(2\pi)^3}. \tag{2.20}$$

Invoking the Debye formalism and performing a change of variables, the phonon DOS becomes

$$D(\omega) = \frac{\omega^2}{2\pi^2 v_g^3}. \tag{2.21}$$

It is now possible to calculate the volumetric heat capacity, C_l, of phonons. When first deriving κ in the subcontinuum limit, the assumption was made $C = dU/dT$, where U was total energy of the system and was the product of the number of carriers, n, and their energy, ε. Because phonons are quantized, $\varepsilon = \hbar\omega$, where $\hbar$ is the reduced Planck's constant. To determine n, or the number of available phonons that contribute to U, the product of the phonon DOS from Eq. 2.21 and the Bose-Einstein distribution, $f_{BE}(\omega, T)$, is taken. $f_{BE}(\omega, T)$ describes the number of equilibrium states for bosons at a given frequency and temperature:

$$f_{BE}(\omega, T) = \frac{1}{\exp[\frac{\hbar\omega}{k_B T}] - 1}. \tag{2.22}$$

Thus, U becomes

$$U = \int_0^{\omega_D} \hbar\omega D(\omega) f_{BE}(\omega, T) d\omega, \tag{2.23}$$

where $\omega_D = \theta_D/T$ is the Debye cutoff frequency, where θ_D is the Debye temperature. Taking the partial derivative with respect to T, and as the temperature dependence is only present in $f_{BE}(\omega, T)$, we find

$$C_l = \frac{\partial U}{\partial T} = \int_0^{\omega_D} \hbar\omega D(\omega) \frac{\partial f_{BE}(\omega, T)}{\partial T} d\omega. \tag{2.24}$$

Using an exchange of variables, $x = \hbar\omega / k_B T$, it can be shown that

$$C_l = 9k_B(\frac{N}{V})(\frac{T}{\theta_D})^3 \int_0^{\theta_D/T} \frac{x^4 e^x}{(e^x - 1)^2} dx. \tag{2.25}$$

Inspection of Eq. 2.25 yields various insight into the temperature dependence of C_l. In particular, as $T \to 0$, where an infinite number of phonon states at a particular frequency are able to exist, $C_l \propto T^3$. On the other hand, when $T \gg 0$, C_l is approximately constant up to the melting temperature of the material. Throughout this dissertation, I primarily use C_l from the literature in analyzing TDTR data to extract κ.

From Fig. 2.2, it is evident that a variety of factors contribute to the scattering of phonons, including nanoparticles, atomic defects, inclusions, and grain boundaries, to name a few. All of these affect the τ of phonons, and ultimately help to define the thermal conductivity of a material. As a fundamental understanding of these scattering rates is not the focus of this dissertation, τ is defined by Matthiessen's rule, which states that the scattering rate (τ^{-1}) is the sum of various scattering events a phonon will undergo (τ_j^{-1}), i.e.,

$$\frac{1}{\tau} = \sum_j \frac{1}{\tau_j}. \tag{2.26}$$

As mentioned previously, τ is material dependent, and depends on temperature, geometry of the material, and the defect concentration. In Chapter 4, I attribute the anisotropic thermal conductivity in yttrium disilicate to the varying τ along differing crystallographic directions.

Now that I have addressed each of the components that comprise κ for phonons in this subcontinuum limit, I will now address each of these for electrons.

Electrons

Unlike phonons, whose energy is dependent on the frequency of oscillation, $\varepsilon = \hbar\omega$, the allowable energy states of electrons in crystalline materials is dependent on the electron wavevector, k, as well as its effective mass, m^*:

$$\varepsilon - \varepsilon_C = \frac{\hbar^2 k^2}{2m^*}. \tag{2.27}$$

In this equation, the electron energy ε is referenced to its conduction band energy, ε_C. Because the formalism for the DOS in Eq. 2.20 is generalized for all carriers in k-space, Eq. 2.20 can be adjusted to yield the electron DOS in energy space. Doing so results in

$$D(\varepsilon) = \frac{1}{2\pi^2}(\frac{2m^*}{\hbar^2})^{3/2}(\varepsilon - \varepsilon_C)^{1/2}. \tag{2.28}$$

Thus, the electronic DOS is primarily proportional to $\sqrt{\varepsilon}$.

In crystals, the number of electrons per unit volume is

$$n_e = \int_0^\infty f_{FD}(\varepsilon, T, \mu) D(\varepsilon) d\varepsilon, \tag{2.29}$$

where $f_{FD}(\varepsilon, T, \mu)$ is the Fermi-Dirac distribution,

$$f_{FD}(\varepsilon, T, \mu) = \frac{1}{\exp[\frac{\varepsilon - \mu}{k_B T}] + 1}, \tag{2.30}$$

where μ is the chemical potential. In the low temperature limit, $T \rightarrow 0\text{K}$, we can neglect $f_{FD}(\varepsilon, T, \mu)$ in the integral, integrating from the conduction band to the Fermi level,

$$n_e = \int_{\varepsilon_C}^{\varepsilon_F} D(\varepsilon) d\varepsilon = \frac{1}{3\pi^2}(\frac{2m^*}{\hbar^2})^{3/2}(\varepsilon_F - \varepsilon_C)^{3/2}. \tag{2.31}$$

Since $D(\varepsilon)$ have been previously defined, which closely resembles the above equation for

n_e, n_e can be written as

$$n_e = \frac{2}{3}\varepsilon_F D(\varepsilon_F). \tag{2.32}$$

Now that the electronic DOS as well as the number of electrons per unit volume in a crystal has been addressed, C_e, v_e, and τ_e can be determined using the same formalisms as applied to phonons. In the same way that U was determined in phonons, the same can be done so with electrons by starting with the number of electrons, n_e, and taking the integral of the product of the electron energy ε, Fermi-Dirac distribution $f_{FD}(\varepsilon, T, \mu)$, and density of states $D(\varepsilon)$:

$$U = \int_0^\infty \varepsilon f_{FD}(\varepsilon, T, \mu) D(\varepsilon) d\varepsilon. \tag{2.33}$$

This equation can be rearranged such that

$$U = \int_0^\infty (\varepsilon - \varepsilon_F) f_{FD}(\varepsilon, T, \mu) D(\varepsilon) d\varepsilon + \varepsilon_F n_e, \tag{2.34}$$

where ε_F is the Fermi level and the only temperature dependence of the equation lies in $f_{FD}(\varepsilon, T, \mu)$. Taking the derivative of Eq. 2.34 with respect to temperature, and evaluating the integral, the electronic heat capacity becomes

$$C_e = \frac{\pi^2}{3} k_B^2 D(\varepsilon_F) T = \gamma T, \tag{2.35}$$

or

$$C_e = \frac{1}{2} \frac{\pi^2 n_e k_B^2}{\varepsilon_F} T = \gamma T. \tag{2.36}$$

Thus, the electronic heat capacity is directly proportional to the temperature of the electronic system by a proportionality constant, γ, which is dependent on the number of electrons per unit volume, n_e, and the Fermi energy, ε_F. The relation $\gamma = \frac{\pi^2}{3} k_B^2 D(\varepsilon_F)$ is critical for the derivation of the electron-electron interfacial conductance, discussed later. At low electron temperatures, < 1000 K, Eq. 2.36 is in excellent agreement with first-principles calculations in the literature [43]. I account for the temperature dependence of the electronic heat capacity using two-temperature model calculations in Chapter 6. Because typical values for C_e are orders of magnitude lower than C_l, the electronic contribution to heat capacity is ignored when extracting the thermal conductivity of a material using TDTR.

Unlike phonons, because electron mean-free-paths are short for pure metals [44], electrons are less likely to be influenced by extrinsic factors. Instead, the scattering time in metals is considered to originate from electron-electron and electron-phonon interactions, whose relaxation times are τ_{ee} and τ_{ep}, respectively. From low temperature resistivity measurements, it was determined that $\tau_{ee}^{-1} = AT_e^2$ and $\tau_{ep}^{-1} = BT_l$, where A and B are constant pertaining to the metal [45]. Note that electron-electron scattering is dependent on the electronic temperature, while electron-phonon scattering is dependent on the lattice temperature. In an identical fashion to phonons, the net scattering rate in electrons is

$$\frac{1}{\tau} = \frac{1}{AT_e^2} + \frac{1}{BT_l}. \tag{2.37}$$

In metals, the assumption is made that electrons propagate at the Fermi velocity, v_F. Combining the acquired electronic heat capacity, velocity, and scattering rate, the electronic thermal conductivity becomes

$$\kappa_e = \frac{1}{3}C_e v_F^2 \tau = \frac{1}{3}\gamma T_e v_F^2 \left(\frac{1}{AT_e^2} + \frac{1}{BT_l}\right)^{-1}. \tag{2.38}$$

While this provides sufficient insight into the temperature dependent thermal conductivity of electrons, it is not something that is readily implemented into a simulation like the two-temperature model. Instead, consider the equilibrium electron thermal conductivity, in which the electron temperature is equivalent to the lattice temperature:

$$\kappa_{e,\text{Eq.}} = \frac{1}{3}C_e v_F^2 \tau = \frac{1}{3}\gamma T_l v_F^2 \tau. \tag{2.39}$$

Taking the ratio of Eqs. 2.38 and 2.39, we find that

$$\frac{\kappa_e}{\kappa_{e,\text{Eq.}}} = \frac{T_e}{T_l}, \tag{2.40}$$

which can be rearranged so that

$$\kappa_e(T_e, T_l) = \frac{T_e}{T_l}\kappa_{e,\text{Eq.}}. \tag{2.41}$$

This is the expression for the electronic thermal conductivity that will be implemented in the two-temperature model, as discussed in Chapter 3.

As discussed earlier, the electronic scattering rate τ was determined to exhibit electronic and lattice contributions based on low-temperature resistivity measurements. In fact, the ratio of the thermal conductivity of a metal to its electrical conductivity (κ_e/σ, where σ is the electrical conductivity) was found to be approximately constant across most metals by Gustav Wiedmann and Rudolph Franz in 1853 [46]. Later, Ludvig Lorenz extended the work of Wiedemann and Franz to establish the relation between the thermal and electrical conductivities of a metal as a function of temperature [47]. It is easy to show that the ratio of electron thermal conductivity, κ_e, to the electrical conductivity, σ, is proportional to temperature via a constant L_0:

$$L_0 T = \frac{\kappa_e}{\sigma} = \frac{mC_e v_F^2}{3ne^2}T = 2.44 \times 10^{-8} W\Omega K^{-2} T. \tag{2.42}$$

In this equation, the relation $\sigma = \frac{ne^2}{m}\tau_F$ can be derived according to Ref. 48. With a little bit of rearranging, the electron thermal conductivity can be determined via the well-known Wiedemann-Franz Law so long as its electrical conductivity is known:

$$\kappa_e = \sigma L_0 T. \tag{2.43}$$

I use the Wiedemann-Franz law throughout this dissertation to determine the electronic thermal conductivity of the Al transducer film utilized in TDTR, where the electrical conductivity is determined via a four-point probe measurement. While the relation only provides the electronic contribution to the total thermal conductivity of a metal, typical phononic thermal conductivities in metals are usually 1–2 orders of magnitude lower than its electronic counterpart [49] and can thus be neglected.

From the Wiedemann-Franz law, the electronic thermal conductivity is inherently tied to its electrical conductivity. Recall, the scattering rate for electrons was dependent on both electron-electron and electron-phonon mechanisms, see Eq. 2.37. In the limit of high electron temperatures, $T_e \gg T_l$, the net electron scattering rate is primarily proportional to the lattice temperature via the constant B, which is related to electron-phonon scattering.

There is a rich history regarding the interactions between electrons and phonons, much of it residing in Soviet literature [50–52]. In 1957, Kaganov *et al.* [50] presented the formalism for electron-phonon coupling in which the energy transfer from electrons to the phonons is proportional to their temperature difference by the electron-phonon coupling factor, i.e.,

$$\frac{\partial E_e}{\partial t} = g(T_l - T_e), \tag{2.44}$$

where E_e is the electron energy, g is the electron-phonon coupling factor, and T_l and T_e are the lattice and electronic temperatures. This transmission of energy is not only vital for energy transfer within a given material between the two subsystems, but also at material/material interfaces. Since I have addressed the primary mechanisms of energy transfer within a given material, I will now delve into the associated energy transfer processes at the interfaces between materials.

2.2 Interfacial Transport

In an equivalent manner to Fourier's law, whereby the heat flux in a material is proportional to the temperature gradient by its thermal conductivity, the heat flux at the interface between two materials will be proportional to the temperature difference at the interface via the inverse of the interfacial resistance, R_K:

$$q = \frac{1}{R_K}\Delta T. \tag{2.45}$$

In this equation, R_K is the inverse of the interfacial thermal conductance, h_K or G, and is referred to as the Kaptiza resistance after P. L. Kapitza observed a discontinuity in temperature at the interface between Cu and liquid He II [26].

This interfacial resistance is not exclusive to the Cu/He II system, but is also presented at the interfaces between metals and nonmetals, liquids, solids, and gasses, and anything in between [53]. In the following three subsections, I will give a brief background on the mathematical formalisms associated with energy transfer at dielectric/dielectric, metal/metal, and metal/non-metal interfaces, as all are pertinent to Chapter 6 of my dissertation.

2.2.1 Dielectric/Dielectric Interfaces

Recall, in dielectric materials, heat transfer is dominated by quantized lattice vibrations or phonons. Thus, the heat transfer process at an interface in which the adjacent materials are dielectrics will be dominated by phonons. Following the formalism of Swartz and Pohl [54], the probability of transmission for phonons traversing from material 1 to material 2 will be $\alpha_{1\rightarrow 2}$, where the probability of reflection is $1-\alpha_{1\rightarrow 2}$. If we generalize $\alpha_{1\rightarrow 2}$ such that it is dependent on the incident phonon angle θ, mode j, frequency ω, and wavevector $\mathbf{k}$, the net transmission at the interface will then be

$$\zeta_{1,j} = \int_0^{\pi/2} \alpha_{1\rightarrow 2}(\theta, j, \omega, \mathbf{k})\cos(\theta)\sin(\theta)d\theta. \tag{2.46}$$

The interfacial conductance, accounting for this net transmission will be

$$h_K = \frac{1}{2}\sum_j c_{1,j}\zeta_{1,j}\int_0^{\omega_1^{\text{Debye}}} \hbar\omega \frac{dN_{1,f}(\omega,T)}{dT}d\omega, \tag{2.47}$$

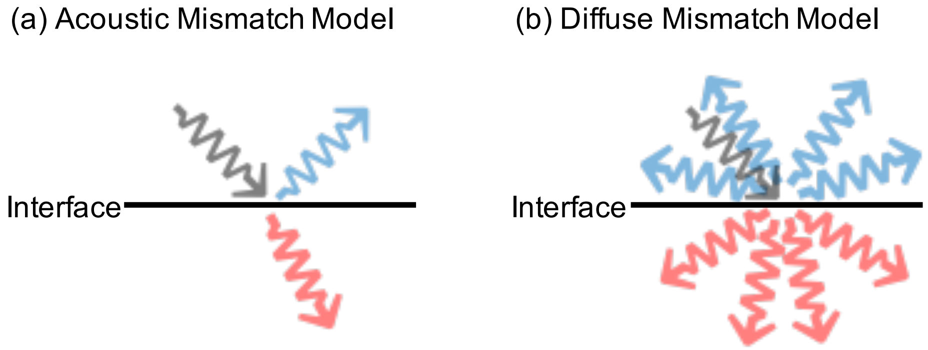

Figure 2.3. Representative formalisms for (a) acoustic and (b) diffusive energy transport at an interface. Black, blue, and red arrows reflect the incident, reflected, and transmitted carriers, respectively.

where $c_{1,j}$ is the phonon velocity of material 1 for branch j, ω_1^{Debye} is the Debye cuttoff frequency of material 1, and $N_{1,f}(\omega,T)$ is the product of the phonon density of states and Bose-Einstein distribution, or the number of equilibrium states for a given frequency and temperature.

Equations 2.46 and 2.47 form the basis of determining the interfacial conductance at material interfaces, and can be readily calculated if the system parameters are known. However, the formalism regarding the transmission probability, $\alpha_{1\to 2}$, is subjected to acoustic and diffusive interpretations.

The acoustic mismatch model (AMM) is graphically depicted in Fig. 2.3(a), and makes the continuum assumption that phonons propagate as plane waves whereby they are only able to reflect or transmit at an interface. Under this assumption, the transmission probability can be approximated via that provided by Lord Baron Rayleigh [55], and is dependent on the acoustic impedances, $Z_i = \rho_i c_i$, where ρ_i is the density of the material and c_i is its sound velocity, of the constituent materials:

$$\alpha_{1\to 2} = \alpha_{2\to 1} = \frac{4Z_1Z_2}{Z_1+Z_2}. \tag{2.48}$$

With this definition of $\alpha_{1\to 2}$, Eq. 2.47 can be evaluated if the other material parameters are known. The assumptions made in the AMM, however, neglect the contribution of diffusive scattering events that occur at a material interface. In stark contrast to the AMM, it is assumed that all phonons scatter diffusely in the diffusive mismatch model (DMM).

Under the DMM, graphically depicted in Fig. 2.3(b), the probability of transmission is dependent solely on the mismatch in the phonon density of states. Because all phonons diffusely scatter at the interface under this formalism, the transmission probability will be independent of the phonon wavevector $\mathbf{k}$ and mode j, and is only dependent on the phonon frequency ω. Additionally, the probability of transmission from one material to another will be such that

$$\alpha_{1\to2}(\omega) = 1 - \alpha_{2\to1}(\omega). \tag{2.49}$$

As the transmission/reflection probabilities from one material to another have been addressed, the phonon flux from material 1 to material 2 over all incident angles can be calculated via

$$q_{\text{phonon}} = \frac{1}{4\pi}\sum_j \int_0^{2\pi} d\phi \int_0^{\pi/2} \cos(\theta) d\theta c_{1,j} N_{1,j}(\omega,T)\alpha_{1\to2}(\omega), \tag{2.50}$$

which results in

$$q_{\text{phonon}} = \frac{1}{4}\sum_j c_{i,j} N_{i,j}(\omega,T)\alpha_{1\to2}(\omega). \tag{2.51}$$

By making the assumption of detailed balanced, which states that the sum of the fractions of phonons traversing from materials 1 to 2 and 2 to 1 must be unity, one is able to determine the transmission coefficient:

$$\alpha_{1\to2}(\omega) = \frac{\sum\limits_j c_{2,j} N_{2,j}(\omega,T)}{\sum\limits_j c_{1,j} N_{1,j}(\omega,T) + \sum\limits_j c_{2,j} N_{2,j}(\omega,T)}. \tag{2.52}$$

When used in conjunction with Eqs. 2.46 and 2.47, along with the density of states and sound velocities of each material, one is able to determine the thermal conductance at material/material interfaces when heat conduction in both those materials is dominated by phonons.

2.2.2 Metal/Metal Interfaces

As one might expect, as the interfacial conductance at dielectric/dielectric interfaces is dictated by phonons, electrons dictate this parameter at metal/metal interfaces. If similar assumptions are made as to phonons in the DMM, the transmission coefficient from material 1 to material 2 in electron-dominated systems is

$$\alpha_{1\to2}(\varepsilon)=\frac{c_2(\varepsilon)N_2(\varepsilon)}{c_1(\varepsilon)N_1(\varepsilon)+c_2(\varepsilon)N_2(\varepsilon)}, \tag{2.53}$$

where c_i is now the electron velocity and N_i is the occupied electron density of states. The net transmission at the interface is then

$$\zeta_1(\varepsilon)=\int_0^{\pi/2}\frac{c_2(\varepsilon)N_2(\varepsilon)}{c_1(\varepsilon)N_1(\varepsilon)+c_2(\varepsilon)N_2(\varepsilon)}\cos(\theta)\sin(\theta)d\theta \tag{2.54}$$

If only electrons at the Fermi level, ε_F, participate in the energy exchange process, and the Fermi surface is isotropic, then Eq. 2.54 can be simplified to

$$\zeta_1(\varepsilon_F)=\frac{1}{2}\frac{c_2(\varepsilon_F)N_2(\varepsilon_F)}{c_1(\varepsilon_F)N_1(\varepsilon_F)+c_2(\varepsilon_F)N_2(\varepsilon_F)}. \tag{2.55}$$

Finally, in an analogous manner to phonons, the electron-electron interfacial conductance will be

$$G_{ee}=\frac{1}{2}c_1(\varepsilon_F)\zeta_1(\varepsilon_F)\int_0^{\infty}\varepsilon\frac{dN_1(\varepsilon,T)}{dT}d\varepsilon \tag{2.56}$$

To further simplify this expression, recall that the electronic heat capacity is the temperature derivative of the total internal energy of the system. Recognizing that the integral is identical to this expression, G_{ee} can be rewritten such that

$$G_{ee}=\frac{Z_1Z_2}{4(Z_1+Z_2)}. \tag{2.57}$$

In this equation, $Z_i = \gamma_i v_{F,i} T$. More generally, Eq. 2.57 is

$$G_{ee} = \frac{\gamma_1 v_{F,1} \gamma_2 v_{F,2}}{4(\gamma_1 v_{F,1} + \gamma_2 v_{F,2})} T = \Gamma T, \tag{2.58}$$

where Γ is often referred to as the proportionality constant to the electron-electron thermal conductance. Typical values of Γ will be on the order of several hundred MW m^{-2} K^{-2}, yielding interfacial conductances on the order of several GW m^{-2} K^{-1} for electron temperatures near room temperature [56]. The expression described in Eq. 2.58 for the electron-electron conductance is included in two-temperature model calculations, outlined in Chapter 3 and performed in Chapter 6.

2.2.3 Metal/Dielectric Interfaces

Thus far, I have derived the thermal conductance at interfaces when the dominant carrier is the same on both sides of the interface. However, in many nanoelectronic applications in which a metal is in direct contact with a dielectric material, charge carriers must interact with one another prior to transmitting energy across an interface.

To exemplify this energy exchange process, I will use the characteristic metal/dielectric system visualized in Fig. 2.4. Due to the fact that phonons are present in both the metal and dielectric systems, energy transmission at the interface will be phonon dominated. The interfacial conductance, G, will describe the energy exchange process of phonons at the interface. However, as the dominant carrier in metals is the electron, electrons in the metal must first couple their energy to phonons in the metal so that they may transmit their energy across the interface. This energy exchange process is dictated by the electron-phonon coupling factor, g. The net resistance at the interface will then be the series resistance of the electron-phonon resistance, R_{ep}, and the interfacial phonon-phonon resistance, $R_{pp} = G_{pp}^{-1}$:

$$G_{\text{net}}^{-1} = R = R_{ep} + R_{pp}. \tag{2.59}$$

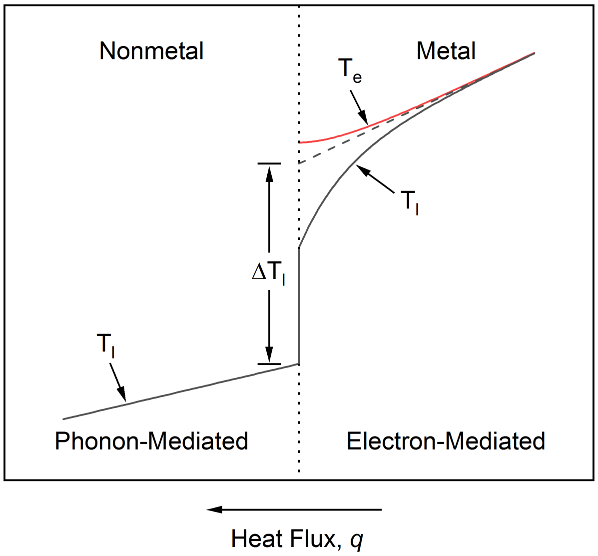

Figure 2.4. Schematic representation of interfacial transport at a metal/dielectric interface. In the metal, heat transfer is mediated by electrons, while in the dielectric, heat transfer is mediated by phonons. Electrons in the metal must couple their energy to phonons in the metal before energy can be transferred to the dielectric.

To better understand this equation as it specifically relates to g, consider the electron and phonon thermal conductivities in the metal, κ_e and κ_p, respectively. The associated electron-phonon length scale associated with the electron conductivity will be $\lambda_e = \sqrt{\kappa_e/g}$, while that of the phonon thermal conductivity will be $\lambda_p = \sqrt{\kappa_p/g}$. Recall, the electron thermal conductivity in metals is typically 1–2 orders of magnitude larger than its phonon counterpart, and thus the electron-phonon coupling length scale will be dictated by the phonon thermal conductivity. The resistance associated with electron-phonon coupling will then be $R_{ep} = \kappa_p/\lambda_p = (g\kappa_p)^{-1/2}$.

As such, the net conductance at the interface of a metal/dielectric system, G_{net}, will be:

$$G_{\text{net}} = \frac{\sqrt{g\kappa_p}}{1+\frac{\sqrt{g\kappa_p}}{G_{pp}}}. \tag{2.60}$$

Inspection of Eq. 2.60 provides insight into the net conductance of materials depending on the strength of g. For the same G_{pp}, a poor electron-phonon coupling factor will result in a lower G_{net}, while a higher electron-phonon coupling factor will result in the opposite. Thus, to maximize energy transmission at a metal/dielectric interface, it is preferable for the metal to have a high electron-phonon coupling factor. However, metals with high electron-phonon coupling factors typically exhibit low electronic contributions to their thermal conductivity [43, 49], reducing λ_e such that it is comparable to λ_p.

To maximize the electrical conductivity of a contact and to maintain a high interfacial conductance, an intermediate metallic wetting layer between the top electrode and dielectric substrate is typically implemented. This wetting layer should exhibit a high g and a large G_{pp} with the dielectric substrate. This wetting layer adds an additional resistance in series, associated with the electron-electron resistance at the interface between the top metal contact and wetting layer. However, the electron-electron interfacial resistance is very low for metal/metal interfaces based on the earlier discussion, Eq. 2.60 is still valid for the system with a wetting layer, where g, κ_p, and G_{pp} now pertain to that of the wetting layer. An investigation of the net conductance at Au/Al_2O_3 contacts with TiO_x wetting layers is presented in Chapter 6, where the electron-phonon coupling characteristics of the wetting layer are further elucidated in the latter half of the chapter.

2.3 Summary

In this chapter, I provided the basic theory surrounding heat transfer and the pertinent descriptors to this dissertation. I started by providing the definition of thermal conductivity in the continuum limit, specifically describing the associated tensorial representation of systems with varying crystal symmetries. The microscopic definition of thermal conductivity was then explored, relating it specifically to the associated heat capacities, velocities, and mean free paths of carriers pertinent to a material system. Finally, I addressed the interfacial transfer processes associated with dielectric/dielectric, metal/metal, and metal/dielectric interfaces. In the following chapter, I will present the metrology used in this dissertation that allows for the extraction of each of the thermophysical properties presented thus far.

Chapter 3

Metrology

In this chapter, I will outline the metrology used throughout my dissertation. This includes time-domain thermoreflectance (TDTR), which utilizes pulsed lasers to heat and monitor the temperature at the surface of a sample. The techniques steady-state and frequency-domain thermoreflectance (SSTR and FDTR, respectively), which utilize continuous wave (cw) lasers, operate in a similar fashion. The extension of the analysis to SSTR and FDTR from TDTR is provided, although the experimental configurations of the former two are not provided as they do not contribute significantly to this dissertation. A summary of the characteristic excitations and responses for each of these techniques is shown in Fig. 3.1. The mathematical formalism with which I analyze the data garnered by TDTR will be provided under carrier equilibrium. Because a portion of my dissertation involves conditions in which carrier non-equilibrium is present, I outline the analysis performed via implementation of the two-temperature model (TTM). For conditions of carrier equilibrium, discussion regarding the thermal penetration depth, or probing volume, is provided, alongside an extension of TDTR to a two-dimensional setting, enabling the imaging of thermal properties.

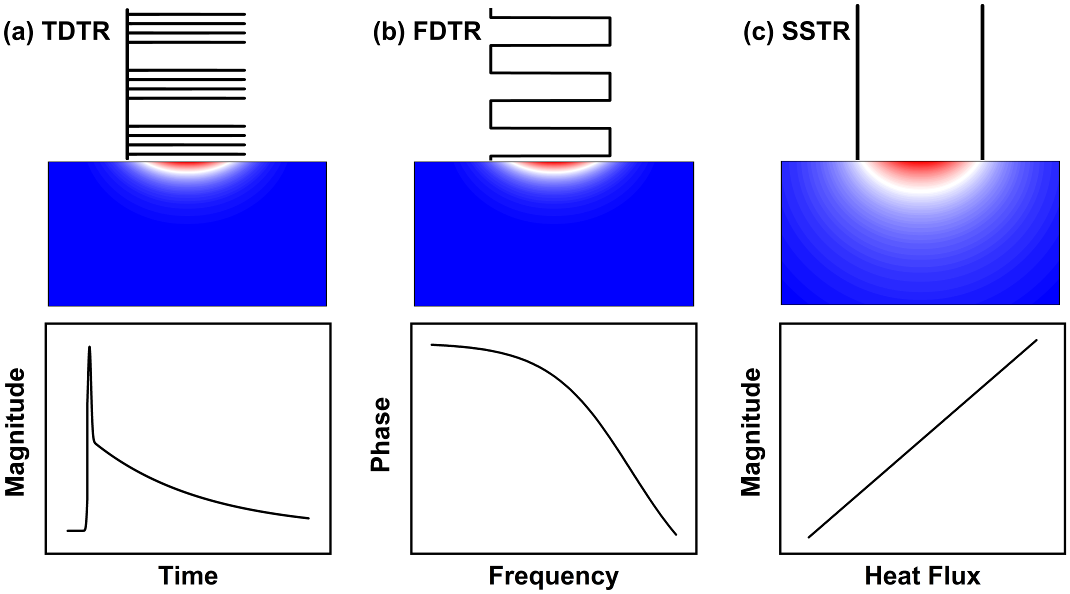

Figure 3.1. Characteristic excitations and corresponding responses for (a) TDTR, (b) FDTR, and (c) SSTR techniques. In TDTR, the magnitude of the thermoreflectance is monitored as a function of pump-probe delay time, while in FDTR the thermally-induced phase lag between the pump and probe is monitored as a function of frequency. In SSTR, the steady-state induced magnitude of the thermoreflectance is monitored for given changes in heat flux. Notice the increase in thermal penetration depth, δ_{thermal}, which is proportional to the spot size in a SSTR experiment, resulting from the lower modulation frequencies employed in SSTR.

3.1 Background

3.1.1 Thermoreflectance

In order for each of the following techniques to be adequate in measuring the temperature at a samples surface, it is necessary for them to capitalize on the temperature dependent reflectivity (i.e., thermoreflectance) of a material. The thermoreflectance, β, is defined through the relation

$$\frac{\Delta R}{R} = \frac{1}{R}\frac{\delta R}{\delta T}\Delta T = \beta T, \tag{3.1}$$

where R and T are the material reflectivity and temperature, respectively. As such, the normalized reflectivity of a material is directly proportional to its temperature via the thermoreflectance coefficient. Knowing this, a slew of laser-based optical pump-probe techniques have been developed in the last several decades [57–60], all of which utilize a thin, metal transducer. The transducer serves two purposes (1) to transduce optical to thermal energy via absorption at the pump wavelength and (2) to provide high reflectivity and thermoreflectance at the probe wavelength. Without these two conditions met, the signal to noise of optical pump-probe techniques diminishes very quickly. Indeed, β for many metals is just on the order of 10^{-5}–10^{-4} K^{-1} [61, 62]. As a result, lock-in amplification is typically utilized to monitor the reflected probe intensity ΔV as a function of delay time, heating power, and heating frequency for time-domain, steady-state, and frequency-domain thermoreflectance techniques, respectively.

3.1.2 Lock-In Amplification

As a result of the low magnitude of thermoreflectance associated with many materials, lock-in amplification is typically implemented to capture the reflected intensity of a probe beam. In order to demodulate a voltage oscillating at a frequency of ω, a reference signal with real and imaginary components must first be generated, which follows the form

$$V_{\mathrm{ref}}(t) = V_{\mathrm{ref}} e^{i\omega t} = V_{\mathrm{ref}} \cos(\omega t) - V_{\mathrm{ref}} i \sin(\omega t), \tag{3.2}$$

where V_{ref} is the amplitude of the signal, ω is the frequency, t is time, and i is the imaginary unit. This reference wave is mixed with the input signal, which takes a similar form as the reference wave, but with an amplitude of V_{sig} and a phase of ϕ:

$$V_{\mathrm{sig}}(t) = V_{\mathrm{sig}} \cos(\omega t + \phi). \tag{3.3}$$

It can be shown that the time-independent portion of the mixed signal can be reduced to

$$V_{\mathrm{mix}}(t) = V_{\mathrm{ref}}(t) \dot{V}_{\mathrm{sig}}(t) = \frac{V_{\mathrm{ref}} V_{\mathrm{sig}}}{2} \dot{(} \cos(\phi) - i \sin(\phi)), \tag{3.4}$$

which is directly proportional to V_{sig}, the voltage of interest. The mixed signal contains

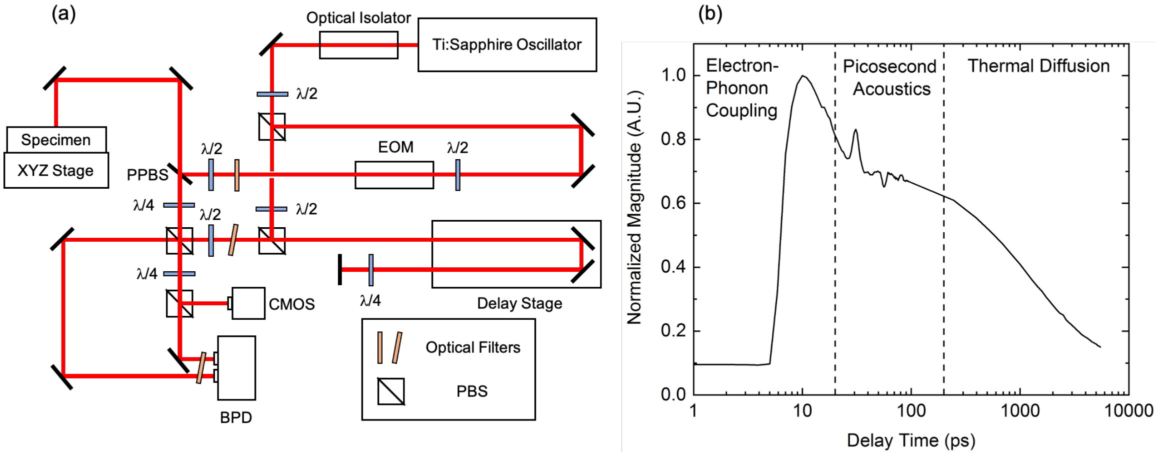

Figure 3.2. (a) Two-tint time-domain thermoreflectance (TDTR) system. $\lambda/2$ = half wave-plate, $\lambda/4$ = quarter wave-plate, PBS = polarizing beamsplitter, PPBS = polarizing plate beamsplitter, EOM = electro-optic modulator, CMOS = complimentary metal-oxide-semiconductor camera, BPD = balanced photodetector. (b) Characteristic TDTR data, offset by 10 ps, showing electron-phonon coupling, picosecond acoustic, and thermal diffusion regimes.

real and imaginary components, pertaining to the in-phase and out-of-phase voltages, V_{in} and V_{out}, respectively. These voltages, as well as their magnitude ($V = \sqrt{V_{\text{in}}^2 + V_{\text{out}}^2}$), are necessary for the analysis of all thermoreflectance techniques.

3.2 Time-Domain Thermoreflectance

Time-domain thermoreflectance (TDTR) is one of the many techniques that utilizes lock-in amplification to monitor the surface temperature of a system via its thermoreflectance. A schematic of the TDTR system that I built during my first year at the ExSiTE lab can be seen in Fig. 3.2. This is a “two-tint” implementation of TDTR, meaning that the pump and probe beams are spectrally separated by just a few nanometers. In this implementation, pulses emanate from a Ti:Sapphire oscillator at a repetition rate of 80 MHz and duration of ∼100 fs, with a center wavelength of 808.5 and FWHM of ∼15 nm. The output of the oscillator is energetically split into a high energy pump and low energy probe paths via a polarizing beamsplitter (PBS). The pump is electro-optically modulated via a Conoptics electro-optic modulator (EOM) in the frequency range of 10 kHz – 20 MHz, and creates a frequency-dependent heating event at the sample surface after being focused through an objective lens.

The unmodulated probe beam is mechanically delayed in time, up to ~5.5 ns, and is combined with the pump just prior to the sample via a polarizing plate beamsplitter (PPBS). The probe then monitors the reflectivity at the sample surface, which is temperature dependent, and is directed to a balanced photodetector (BPD) where the reflected signal is subtracted from the probe reference signal to increase signal-to-noise. The differential signal is demodulated using lock-in amplification to acquire the temperature evolution at the sample surface, which is compared to the radially symmetric heat diffusion equation to extract parameters of interest. As mentioned initially, sharp-edge optical filters are used to spectrally separate the pump and probe. This ensures that artifacts of the modulated pump beam do not erroneously impact the acquired data.

In addition to the two-tint TDTR system that I built, I also utilized a two-color system for numerous projects during my period at the ExSiTE lab. The system is virtually identical to that shown in Fig. 3.2, although the center wavelength of the beam exiting the oscillator is 800 nm. Instead of using sharp-edge optical filters to spectrally separate the pump and probe, the pump is focused through a nonlinear $BiBO_3$ crystal following the electro-optic modulator. The $BiBO_3$ crystal frequency doubles the pump to 400 nm, hence making the system "two-color". By making the pump laser 400 nm, increased absorption in specimens coated with Au can be achieved, which helps to remediate the low thermoreflectance of Au at 800 nm [62].

In both systems, the voltage acquired by demodulating the probe contains in-phase (V_{in}) and out-of-phase (V_{out}) components, where the magnitude of these components ($\sqrt{V_{\text{in}}^2 + V_{\text{out}}^2}$) is directly proportional to the change in reflectivity at the sample surface as a result of the pump heating event. Typically, I will interpret the ratio of the in- to out-of-phase voltages ($-V_{\text{in}}/V_{\text{out}}$) or the phase of the signal ($\tan^{-1}\frac{V_{\text{out}}}{V_{\text{in}}}$). However, there is an additional phase present in the system when demodulating the acquired reflectivity. This additional phase is dependent on a variety of factors, including the path length from the sample to the detector and driving electronics, and does not allow for a comparison of the acquired data to the model of interest. In order to address this additional phase, it is necessary to recognize the fact that at the 0 time delay, when the pump and probe are temporally overlapped, the change in the demodulated out-of-phase component (ΔV_{out}) should be 0. Thus, a rotation of the acquired complex vector about the complex plane can be made such that $\Delta V_{\mathrm{out}} = 0$ across the 0 time delay. Performing this phase correction allows for the direct comparison of the acquired data to the heat diffusion equation.

The temporal evolution of the magnitude of an Al-coated Al_2O_3 reference specimen can be seen in Fig. 3.2(b), which has been demarcated with several regimes pertinent to this dissertation: (i) electron-phonon coupling, (ii) picosecond acoustics, and (iii) thermal diffusion.

Excitation of the sample surface by the pump pulse results in the deposition of energy into the electronic system, increasing the temperature of electrons to several hundred Kelvin above the lattice temperature and inducing non-equilbrium between the two carriers. In order for these carriers to reequilibrate, electrons must scatter with phonons so that their temperatures are nominally in equilibrium. This usually occurs within several picoseconds following laser excitation. In heterogeneous material systems, where the electron-phonon coupling factor in adjacent layers differs significantly, this non-equilibrium electron-phonon coupling regime can be extended to several hundred picoseconds.

Excitation of the sample surface also induces a significant amount of strain at the surface of the sample. This strain propagates through the material system via the longitudinal sound speeds of the constituent media, and, depending on the piezo-optic coefficient of the transducer utilized, as well as the mismatch in acoustic impedances ($Z = \rho c$, where ρ is the density and c is the longitudinal sound speed) between adjacent layers, results in acoustic signatures in the 10–200 ps temporal regime. These acoustic signatures are indicative of the bonding environment at material interfaces [63, 64], and can give insight into acoustic phonon transmission between materials [65]. In this dissertation, these acoustic signatures are primarily used for the extraction of the Al transducer thickness based on the speed of sound in Al from the literature [66], as successive peaks/troughs are indicative of round-trip propagation times in this top film.

Following electron-phonon coupling and picosecond acoustics is the thermal diffusion regime. It is in this regime that I compare the radially symmetric heat diffusion equation to extract thermal parameters of interest. These parameters include the thermal effusivity, thickness, and interfacial conductances of a material system, provided that sufficient sensitivity to these parameters is available.

3.3 Mathematical Formalism

It is now necessary to understand the analyses associated with TDTR. To start, I will begin with deriving the equilibrium heat transfer analysis associated with each of the aforementioned thermoreflectance techniques. Following, I will discuss the heat transfer analysis associated with carrier nonequilibrium, which is primarily applicable to the short time response of TDTR under particular experimental configurations.

3.3.1 Carrier Equilibrium: Heat Transfer Analysis

I have already discussed the performance of the lock-in amplifier, and how it is able to extract the signal magnitude and the in- and out-of-phase voltages. In general, output of the lock-in amplifier contains both real and imaginary components, and for a pulsed pump/probe experiment, takes the form

$$V = Z(\omega_0)e^{i\omega_0 t}, \tag{3.5}$$

where $Z(\omega_0)$ is the complex output of the lock-in demodulated at a frequency ω_0:

$$Z(\omega_0) = A_0 \sum_{k=-\infty}^{k=\infty} H(\omega_0 + k\omega_s)e^{ik\omega_s \tau}. \tag{3.6}$$

In this equation, $H(\omega)$ is the sample frequency response, evaluated at $\omega_0 + k\omega_s$ where ω_s is the frequency of pulses, k is an integer, and τ is the delay time between pump and probe pulses [67]. A_0 is a constant that encompasses characteristics of the repetition rate of the laser, the thermoreflectance at the sample surface, the absorbed pump fluence, as well as the gain of the electronics in the system. The summation over k is made to account for frequency contributions above and below the modulation frequency as a result of the pulsed nature in TDTR.

In the case of steady-state thermoreflectance (SSTR) and frequency-domain thermoreflectance (FDTR), the sample frequency response only needs to be evaluated at the modulation frequency, ω_0, and there is no associated temporal evolution. Thus, the output of the lock-in amplifier is greatly simplified:

$$Z(\omega_0) = A_0 H(\omega_0). \tag{3.7}$$

Now that output of the lock-in has been addressed, I will now focus on $H(\omega)$, the sample frequency response. This is done for a two-dimensional, transversely isotropic system. While several works in the literature have expanded this derivation for the full thermal conductivity tensor of a material system [68, 69], the transverse isotropy assumption is pertinent to most material systems. Indeed, while I extract the thermal conductivity tensor of a material system in Chapter 4, this is done so by limiting sensitivity of the experiment solely to κ_{zz}. As such, for the following derivation I will use κ_r and κ_z to represent the in- and cross-plane thermal conductivities.

Figure 3.3 describes the N layer system in which the surface temperature is to be determined. Each layer can be described by its cross- and in-plane thermal conductivities, κ_z and κ_r, respectively, volumetric heat capacity, C, and thickness, d. At the interfaces between layers, an interfacial conductance, G, is prescribed. The heat conduction equation

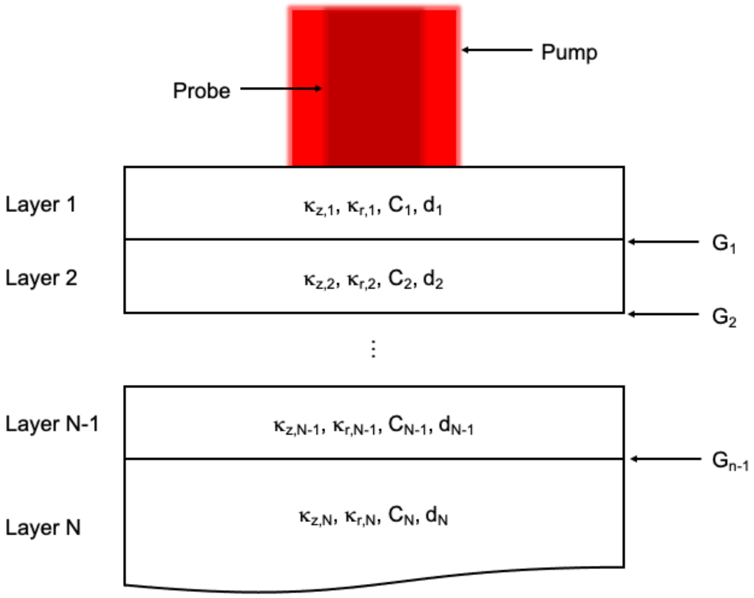

Figure 3.3. N layer system for which the heat diffusion equation is solved assuming a periodic, gaussian heat source. $\kappa_{r,n}$, $\kappa_{z,n}$, C_n, d_n and G_n are the in-plane thermal conductivity, cross-plane thermal conductivity, volumetric heat capacity, and thickness of the n^{th} layer, where G_n is the interfacial conductance between layer n and $n+1$.

in cylindrical coordinates which describes the system is

$$\frac{\kappa_r}{r}\frac{\partial}{\partial r}(r\frac{\partial \mathrm{T}}{\partial r})+\kappa_z\frac{\partial^2 \mathrm{T}}{\partial z^2}=C\frac{\partial T}{\partial t}, \tag{3.8}$$

where T is the temperature. Adiabatic boundary conditions are imposed, which prescribe the top ($z=0$) and bottom ($z=d$) temperatures, T_{top} and T_{bot}, respectively, and top and bottom heat fluxes, $\widetilde{q}_{top}$ and $\widetilde{q}_{bot}$, respectively, of the system:

$$T(0,r,t)=T_{top}; \quad \frac{\partial T(z,r,t)}{\partial z}|_{z=0}=-\frac{1}{\kappa_z}\widetilde{q}_{top} \tag{3.9}$$

$$T(d,r,t)=T_{bot}; \quad \frac{\partial T(z,r,t)}{\partial z}|_{z=d}=-\frac{1}{\kappa_z}\widetilde{q}_{bot}. \tag{3.10}$$

By applying Hankel and Fourier transforms to Eq. 3.8, such that T(z,r,t) $\rightarrow$ θ(z, k, ω), one can arrive at

$$\frac{\partial^2\theta}{\partial z^2}=q^2\theta, \tag{3.11}$$

where

$$q^2 = \frac{\kappa_r k^2 + Ci\omega}{\kappa_z}. \tag{3.12}$$

The solution to Eq. 3.11 takes the form

$$\theta(k,z,\omega) = a\cosh(qz) + b\sinh(qz). \tag{3.13}$$

Imposing adiabatic boundary conditions, the temperature, θ, and heat flux, $\widetilde{q}$, evaluated at $z = d$, become

$$\theta_{bot} = \cosh(qd)\theta_{top} - \frac{1}{\kappa_z q}\sinh(qd)\widetilde{q}_{top} \tag{3.14}$$

and

$$\widetilde{q}_{bot} = -\kappa_z q\sinh(qd)\theta_{top} + \cosh(qd)\widetilde{q}_{top}, \tag{3.15}$$

which can be generalized for an n^{th} layer with thickness d_n, and written as a matrix equation:

$$\begin{bmatrix} \theta_{n,bot} \\ \widetilde{q}_{n,bot} \end{bmatrix} = \begin{bmatrix} \cosh(qL) & -\frac{1}{\kappa_z q}\sinh(qd_n) \\ -\kappa_z q\sinh(qd_n) & \cosh(qd_n) \end{bmatrix} \begin{bmatrix} \theta_{n,top} \\ \widetilde{q}_{n,top} \end{bmatrix} \tag{3.16}$$

For multilayer systems, as with a typical Al-coated substrate system, one can relate the top and bottom temperatures and heat fluxes by multiplying the matrices, M_n, describing each layer:

$$\begin{bmatrix} \theta_{bot} \\ \widetilde{q}_{bot} \end{bmatrix} = \prod_{i=N}^{i=1} M_i \begin{bmatrix} \theta_{top} \\ \widetilde{q}_{top} \end{bmatrix} \tag{3.17}$$

Note that M_N is the bottom-most layer, usually a semi-infinite substrate. For materials adjacent to one another, an interfacial resistance is usually present. In this case, a small heat capacity can be assumed for the layer whose thickness and thermal conductivity provide an equivalent conductance (i.e., $G = \kappa_z/d$, where d is the thickness and G is the conductance).

The matrix equation governing heat transfer at the interface becomes

$$\begin{bmatrix} \theta_{n,bot} \\ \widetilde{q}_{n,bot} \end{bmatrix} = \begin{bmatrix} 1 & -\frac{d}{\kappa_z} \\ 0 & 1 \end{bmatrix} \begin{bmatrix} \theta_{n,top} \\ \widetilde{q}_{n,top} \end{bmatrix}. \tag{3.18}$$

Inspection of Eq. 3.18 allows for the recovery of the equation of G that we presented in Chapter 2, $G(\theta_{n,top} - \theta_{n,bot}) = \widetilde{q}_{n,top}$.

For simplicity, I will generalize the matrix multiplication shown in Eq. 3.17 such that

$$\prod_{i=N}^{i=1} M_i = \begin{bmatrix} A & B \\ C & D \end{bmatrix}. \tag{3.19}$$

By applying an adiabatic boundary condition at the bottom of the substrate layer, $i = N$, it can be shown that the surface temperature becomes

$$\theta_{top} = -\frac{D}{C}\widetilde{q}_{top}. \tag{3.20}$$

Now that the surface temperature of a multilayer system has been addressed, accounting for thickness, volumetric heat capacity, anisotropy in thermal conductivity, as well as interfacial resistances, I will now address the heat flux at the sample surface, $\widetilde{q}_{top}$. For a laser beam propagating as a TEM$_{00}$ mode impinging on the sample surface, the surface heat flux can be modeled as a Gaussian:

$$\widetilde{q}_{top}(r) = \frac{2P_0}{\pi w_0^2}\exp(-\frac{2r^2}{w_0^2}). \tag{3.21}$$

In this equation, P_0 is the absorbed pump power and w_0 is the 1/e^2 radius of the pump at the sample surface. As with the heat conduction equation, performing a Hankel transform, Eq. 3.21 becomes

$$\widetilde{q}_{top}(k) = \frac{P_0}{2\pi}\exp(-\frac{k^2 w_0^2}{8}). \tag{3.22}$$

Inserting this into Eq. 3.20 yields the surface temperature distribution in k space:

$$\theta_{top} = -\frac{D}{C}\frac{P_0}{2\pi}\exp(-\frac{-k^2 w_0^2}{8}). \tag{3.23}$$

Acquiring the surface temperature distribution in real space is performed by taking the inverse Hankel transform, which results in

$$\theta_{top} = -\frac{P_0}{2\pi}\int_0^\infty kJ_0(kr)\frac{D}{C}\exp(-\frac{-k^2 w_0^2}{8})dk \tag{3.24}$$

where $J_0(kr)$ is the zeroeth order Bessel function of the first kind evaluated at kr. In order to acquire $H(\omega)$, a weighted average must be performed between Eq. 3.24 and the coaxial intensity of the probe, which is mathematically identical to Eq. 3.21, but with radius w_1. We also neglect the absorbed probe power, as in this formalism it does not contribute to heating of the sample surface. $H(\omega)$ thus becomes

$$H(\omega) = -\frac{P_0}{2\pi}\int_0^\infty (\frac{2}{\pi w_1^2})\exp(-\frac{2r^2}{w_1^2})2\pi r dr\int_0^\infty kJ_0(kr)\frac{D}{C}\exp(-\frac{-k^2 w_0^2}{8})dk. \tag{3.25}$$

After recognizing that the product of the integrated probe intensity and $J_0(kr)$ is related to the Hankel transform of the probe intensity, the final form of $H(\omega)$ is:

$$H(\omega) = -\frac{P_0}{2\pi}\int_0^\infty k\frac{D}{C}\exp(\frac{-k^2(w_0^2+w_1^2)}{8})dk. \tag{3.26}$$

Substituting $H(\omega)$ evaluated at $\omega = \omega_0 + k\omega_s$ for TDTR in Eq. 3.6 and $\omega = \omega_0$ for SSTR and FDTR in Eq. 3.7, the lock-in response for a particular frequency, $Z(\omega_0)$, can be acquired.

Recall, the output of the lock-in amplifier contains real and imaginary components, pertaining to the in- and out-of-phase voltages, V_{in} and V_{out}, respectively. These voltages can also be utilized in calculating the phase, $\phi = \tan^{-1}(\frac{V_{\text{out}}}{V_{\text{in}}})$, and magnitude, $V = \sqrt{V_{\text{in}}^2 + V_{\text{out}}^2}$. Thus, the expected output of the lock-in amplifier, $Z(\omega)$, can be compared to the actual out-

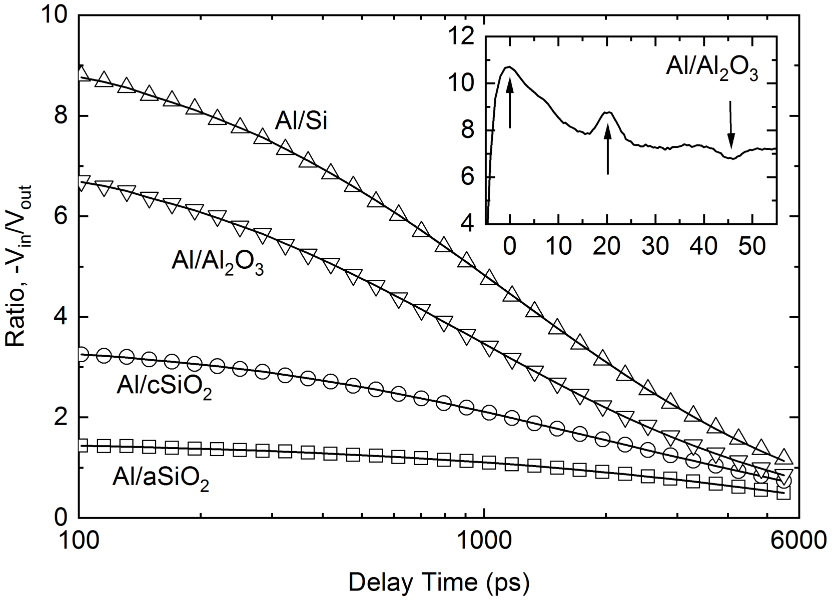

Figure 3.4. Characteristic TDTR data and best fits for $aSiO_2$, $cSiO_2$ (α-quartz), Al_2O_3, and Si. The inset shows the early delay time picosecond acoustics response on Al_2O_3, where the arrows denote locations at which the round-trip times for strain wave propagation are chosen to extract the thickness of the Al transducer.

put over the phase space of interest to extract thermal parameters of interest. It is important to note that V_{in}, V_{out}, and V are all dependent on the absorbed pump fluence, thermoreflectance of the probe, and gain of the electronics on the system. Thus, when analyzing each of these components of the lock-in output, the experimental data is typically normalized to a particular delay time for TDTR. While feasible in practice, V_{in}, V_{out}, and V are prone to changes in the acquired photodetector voltage due to thermal drift, and are thus not typically analyzed. The ratio of in- to out-of-phase voltages, $-V_{\text{in}}/V_{\text{out}}$, of the lock-in amplifier is typically compared to $Z(\omega)$, as variations in V_{in} and V_{out} are effectively cancelled out.

Characteristic TDTR data and best fits can be seen in Fig. 3.4 for Al-coated $aSiO_2$, $cSiO_2$ (α-quartz), Al_2O_3, and Si, which have thermal conductivities of 1.4, 10.5 (c-axis), 35, and 140 W m^{-1} K^{-1}, respectively. These data were acquired on the system I built during my first year in the ExSiTE lab, and are the typical calibration samples we use to ensure the system is performing optimally on a day-to-day basis. Best fits were acquired by performing a least-squares minimization routine between the model and data using a MATLAB program to determine the thermal conductivity of the substrate layer as well as the interfacial conductance at the Al/substrate interface.

Sensitivity and Uncertainty

In order to adequately determine the validity of the model in the extraction of the thermal parameter of interest, it is necessary to determine the associated sensitivity to that parameter. Likewise, the sensitivity to said parameter fundamentally dictates its associated uncertainty. To understand how sensitive our thermal model is to a parameter of interest, I will consider two characteristic systems: Al/aSiO_2 and Al/Al_2O_3. In these systems, material properties are outlined in Table 3.1, where the 1/e^2 diameters of the pump and probe are 22 and 11 μm, respectively, and the modulation frequency is 10 MHz.

Calculated TDTR models are shown in Fig. 3.5(a) as solid lines for the Al/aSiO_2 and Al/Al_2O_3 systems. To initially determine how sensitive the model is to a parameter in the multilayer system, say the thermal conductivity of the substrate κ, the volumetric heat capacity of the substrate C, and the Al/substrate interfacial conductance G, the model is recalculated, adjusting each of these parameters by ± 10%. When perturbing κ by ± 10%, it is clear that the models for both systems are influenced at earlier pump/probe delay times. Further, perturbing C by ± 10%, results in an identical model change in both systems. This indicates that TDTR fundamentally measures the thermal *effusivity*, $\sqrt{\kappa C}$, of an

Layer	Volumetric Heat Capacity (MJ m^{-3} K^{-1})	Thermal Conductivity (W m^{-1} K^{-1})	Thickness (nm)
Al	2.42	180	80
aSiO_2	1.63	1.4	–
Al_2O_3	3.06	35	–
Si	1.65	140	–

Table 3.1. Parameters utilized for calculating sensitivity and δ_{thermal} for Al/aSiO_2, Al/Al_2O_3, and Al/Si systems. For all systems, the interfacial conductance is fixed to 100 MW m^{-2} K^{-1}.

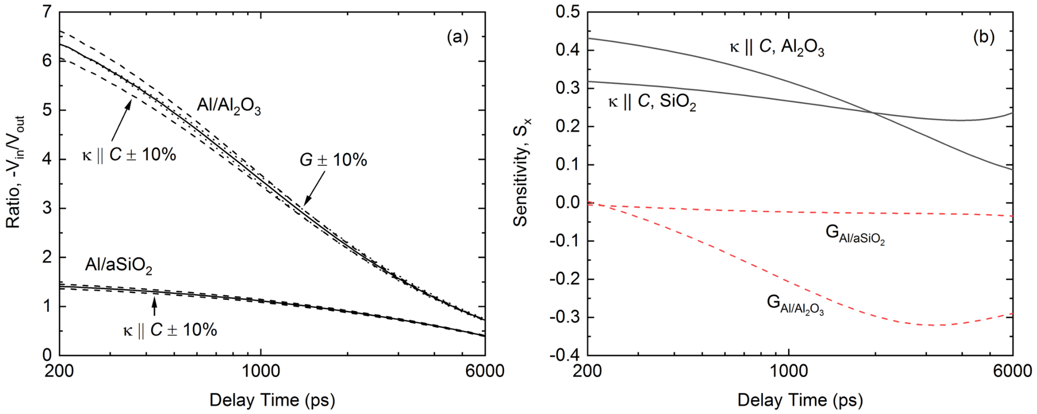

Figure 3.5. (a) Models for Al/aSiO$_2$ and Al/Al$_2$O$_3$ (solid lines) systems, also calculated with 10% pertubations on $\kappa \,||\, C$ (dashed lines) and G (dotted line, Al/Al$_2$O$_3$ only). (b) Sensitivity to κ, C, and G in Al/aSiO$_2$ and Al/Al$_2$O$_3$ systems.

Al/substrate system, at least for experiments performed under similar conditions to those simulated here. When perturbing G by ± 10%, the model for Al/Al$_2$O$_3$ is primarily influenced as the relative resistance of the interface is larger in the Al/Al$_2$O$_3$ system compared to Al/aSiO$_2$.

What I have presented thus far is the fundamental of sensitivity analyses that is performed for TDTR. To normalize out differences in the magnitude of $-V_{\text{in}}/V_{\text{out}}$, Gundrum *et al.* [56] have defined the sensitivity to a particular parameter, S_x, to be the derivative of the logarithm of the signal divided by the derivative of the logarithm of the parameter of interest, x:

$$S_x = \frac{d\ln(-V_{\text{in}}/V_{\text{out}})}{d\ln x}. \tag{3.27}$$

Sensitivity calculations based on Eq. 3.27 to κ, C, and G for Al/aSiO$_2$ and Al/Al$_2$O$_3$ systems are shown in Fig. 3.5(b). As discussed earlier, because sensitivity to κ and C are identical for a given substrate, TDTR fundamentally measures the thermal effusivity of that substrate. Thus, when determining κ alone, it is necessary to extract C from the literature. It is possible to extract κ and C using multiple modulation frequencies in TDTR for high thermal conductivity bulk films and thin films sandwiched between the Al transducer and substrate [70, 71], although this was not performed in this dissertation.

Sensitivity is considered to be "high" to a particular parameter based on its (1) magnitude and/or (2) curvature. Sensitivity to $\kappa \,||\, C$ is high for both Al/aSiO$_2$ and Al/Al$_2$O$_3$ material systems, suggesting that either can be extracted if one of them is considered to be a known parameter. Based on the sensitivity magnitude and curvature, sensitivity to the Al/substrate interfacial conductance is high when the substrate is Al$_2$O$_3$ and low when it is aSiO$_2$. Typically, a fitting routine is performed to determine the thermal conductivity of the substrate and the Al/substrate interfacial conductance. Sensitivity to the interfacial conductance becomes important when expanding TDTR to spatially probe the thermal conductivity of a material system, as discussed later.

The sensitivity to a particular parameter in TDTR is also descriptive of the associated uncertainty in determining that parameter. If the sensitivity is high to a parameter, then it is likely that it can be determined with low uncertainty. On the other hand, if sensitivity is low to a parameter, then the associated uncertainty will be relatively larger. Other parameters in a material system, such as the Al transducer thickness, Al heat capacity, and substrate heat capacity, also influence the uncertainty of the extracted parameter based on their respective sensitivities.

Propagating the absolute uncertainty of a parameter x, δx, based on its sensitivity, S_x, when fitting for parameter y, whose sensitivity is S_y, will be $\delta_x' = \frac{S_x}{S_y}\frac{\delta x}{x}$ [72]. If uncertainty is present in multiple "known" parameters of the system, the then global, absolute uncertainty of parameter y will be addition of δ_x' in quadrature:

$$(\frac{\delta y}{y})^2 = \sum_x (\frac{S_x}{S_y}\frac{\delta x}{x})^2. \tag{3.28}$$

Depending on the material system of interest, a number of parameters may contribute to the uncertainty of the acquired parameters. As an example, calculated sensitivities for all material parameters in an Al/aSiO$_2$ system, based on Table 3.1, can be found in Fig. 3.6. Note the large sensitivity to the Al thickness and volumetric heat capacity. At these spot sizes, sensitivity to the spot size and Al thermal conductivity is relatively low, and

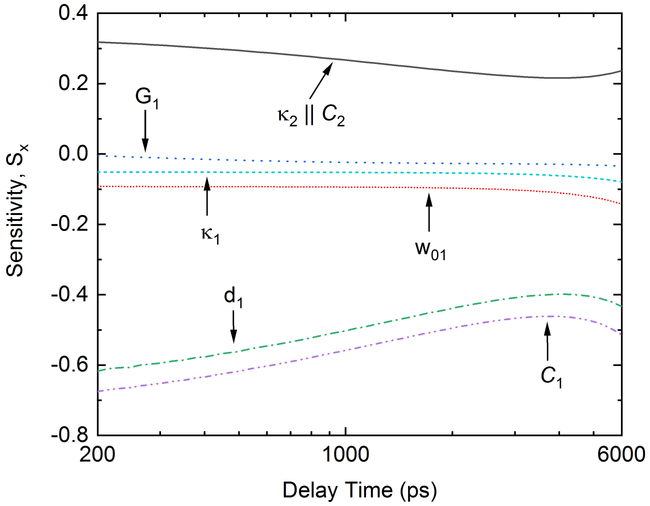

Figure 3.6. Sensitivity calculations for all parameters in an Al/aSiO$_2$ system, according to Table 3.1.

do not propagate significantly into the uncertainty of the extracted parameters. For an Al/substrate system, I will typically include uncertainties of 2.5% in the Al heat capacity, Al thermal conductivity, and thickness, and 5% for the pump/probe spot sizes and substrate heat capacity. When accounting for spot-to-spot variations on a sample, this usually results in an uncertainty of ∼10–15% for the substrate thermal conductivity.

Thermal Penetration

An often overlooked and oversimplified factor in pump/probe experiments is the associated thermal penetration depth, δ_{thermal}, which fundamentally describes the probing volume of pump/probe experiments. To understand the thermal penetration depth, we consider the solution to the heat diffusion equation of a semi-infinite, isotropic medium. Following the solution as proposed by Carslaw and Jaeger [73], the subsurface temperature distribution is

$$T(z) \sim e^{-qz}, \tag{3.29}$$

where q is defined earlier, simplified to $\sqrt{k^2 + \frac{i\omega}{D}}$ for an isotropic material with diffusivity D. During the numerical integration process of Eq. 3.26, the upper bound of k is typically set to $(w_0^2 + w_1^2)^{-1/2}$, and thus, for the purpose of this example, one can make $k \approx w_0^{-1}$. In the high frequency limit, $\omega \gg D/w_0^2$,

$$q^{-1} = \delta_{\text{thermal}} = \sqrt{\frac{2D}{\omega}}. \tag{3.30}$$

This is the definition most commonly used for the penetration depth associated with pump/probe thermoreflectance experiments. Various works have relied upon Eq. 3.30 in their analysis of mean-free paths in TDTR and FDTR studies [74–76]. In the low frequency limit, $\omega \ll D/w_0^2$, however,

$$\delta_{\text{thermal}} = w_0, \tag{3.31}$$

which fundamentally limits the penetration depth of pump/probe experiments to the heater radius for the case of a semi-infinite medium. In material systems consisting of two layers or more, however, Eqs. 3.30 and 3.31 fail to adequately describe δ_{thermal}, as both interfacial resistances and heat spreading have the potential to strongly influence this descriptor [77].

As an example, the normalized temperature distributions in Al/aSiO$_2$ and Al/Si are shown in Fig. 3.7 for the same modulated heat flux of 100 mHz. Parameters utilized in these calculations are shown in Table 3.1, where the 1/e^2 pump radius is 10 μm. Evidently, δ_{thermal} significantly varies for both systems, in both the cross- ($\delta_{\text{thermal},\perp}$) and in-plane ($\delta_{\text{thermal},//}$) directions.

In Al/aSiO$_2$, $\delta_{\text{thermal},\perp}$ and $\delta_{\text{thermal},//}$ are approximately 14 and 21 μm, respectively. The large increase in both $\delta_{\text{thermal},\perp}$ and $\delta_{\text{thermal},//}$ can be attributed to the high thermal conductivity of the Al transducer, which helps to radially spread heat at the sample surface, effectively increasing the surface-heated region beyond that of the pump diameter. For Al/Si, $\delta_{\text{thermal},\perp}$ and $\delta_{\text{thermal},//}$ are ~5 and ~10 μm. In this case, because of the high thermal conductivity substrate (~140 W m^{-1} K^{-1}), radial heat spreading in the transducer is less prevalent than in the Al/SiO$_2$ system, which ultimately reduces both $\delta_{\text{thermal},\perp}$ and

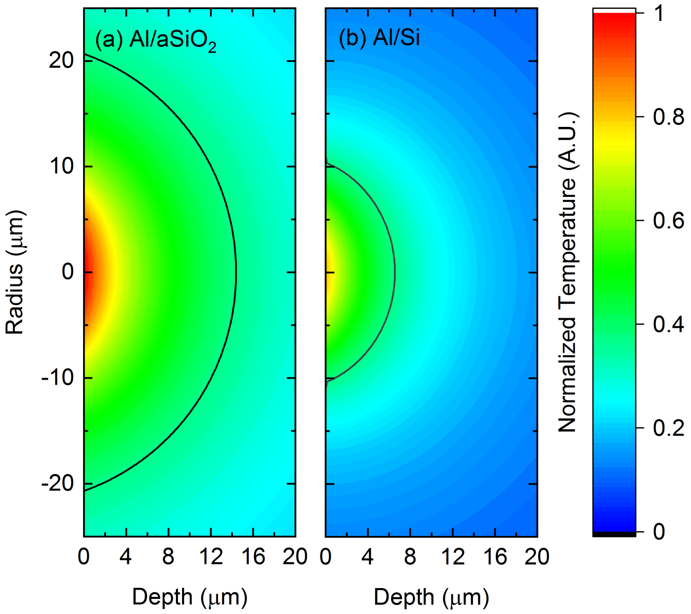

Figure 3.7. Calculated normalized temperature distributions for (a) Al/aSiO$_2$ and (b) Al/Si. The solid line is the distance at which the temperature has decayed to 1/e of its maximum value.

$\delta_{\text{thermal},//}$.

Measurements in TDTR are typically performed at much higher frequencies than 100 mHz. For high-resolution thermal conductivity mapping experiments, the 1/e^2 radii of the pump and probe are much smaller, and can be on the order of ~1 μm. Thus, to exemplify the nature of $\delta_{\text{thermal},\perp}$ and $\delta_{\text{thermal},//}$ and the dependency on frequency and spot size, we repeat the calculations made in Fig. 3.7 for the frequency range of 100 mHz to 100 MHz. The calculations are shown in Fig. 3.8 for (a) w_0 = 10 μm and (b) w_0 = 1 μm. Also shown are calculations from Eq. 3.30 for aSiO$_2$ and Si.

The calculations indicate that $\delta_{\text{thermal},\perp}$ and $\delta_{\text{thermal},//}$ are highly dependent on the frequency and spot size of the measurement, seldom agreeing with Eq. 3.30. At low modulation frequencies for w_0 = 10 μm, Fig. 3.8(a), $\delta_{\text{thermal},\perp}$ and $\delta_{\text{thermal},\perp}$ for Al/aSiO$_2$ are much greater than that of Al/Si, for reasons discussed earlier. As the frequency of the heating event is increased, $\delta_{\text{thermal},//}$ for both systems converges to ~7 μm, suggesting that the heat transfer becomes one dimensional. In the cross-plane direction, $\delta_{\text{thermal},\perp}$ begins to approach that of Eq. 3.30 at moderately high frequencies, although is heavily influenced

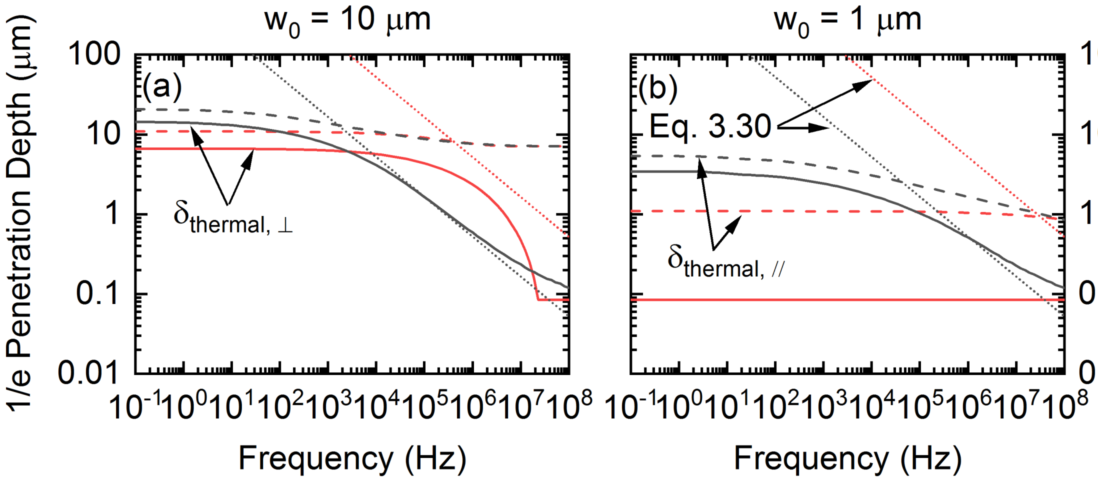

Figure 3.8. 1/e thermal penetration depths in the cross- (solid lines, $\delta_{\text{thermal},\perp}$) and in-plane (dashed lines, $\delta_{\text{thermal},//}$) directions in Al/aSiO$_2$ (black lines)and Al/Si (red lines) systems for pump spot sizes (a) w_0 = 10 μm and (b) w_0 = 1 μm.

by the interfacial conductance, *G*. This is especially true for Al/Si, as $\delta_{\text{thermal},\perp}$ becomes 80 nm, the thickness of the Al transducer layer, at ~20 MHz.

When the spot radius is 1 μm, the influence of the Al thermal conductivity and Al/substrate interfacial conductance are further exaggerated. In the low frequency limit, $\delta_{\text{thermal},//}$ for the two systems is vastly different. In Al/aSiO$_2$, $\delta_{\text{thermal},//}$ approaches 5.5 μm, while that for Al/Si remains at ~1 μm. It is not until much higher modulation frequencies (>10 MHz) that $\delta_{\text{thermal},//}$ becomes ~1 μm for both systems. In the cross-plane direction for Al/aSiO$_2$, $\delta_{\text{thermal},\perp}$ remains at ~3.5 μm, related to radial heat spreading in the Al layer. On the other hand, $\delta_{\text{thermal},\perp}$ in the Al/Si system remains at 80 nm as a result of the moderately low interfacial conductance of 100 MW m^{-2} K^{-1}, which creates a large enough temperature drop at the Al/Si interface to bring the temperature to 1/e of the surface value.

The thermal penetration depth associated with optical pump/probe techniques is an important descriptor that cannot be overlooked or oversimplified. Fundamentally, this parameter determines the probing volume, and therefore sensitivity to different thermal parameters of a material system. Depending on the frequency of the heating event, heat transfer through a multilayer system can be tuned to be primarily spherical or one-dimensional. The heating frequency has a significant impact on the in-plane thermal penetration depth, suggesting that experiments necessitating higher spatial resolution should be performed at higher frequencies to capitalize on the reduced in-plane penetration.

3.3.2 Carrier Nonequilibrium: Two-Temperature Model

When solving the heat diffusion equation, the assumption is made that all carriers present in the simulated system are in thermal equilibrium. When analyzing TDTR data with the heat diffusion equation, however, we typically analyze data from ∼200 ps and onwards. This is due to the fact that the ultrafast pulse will remove electrons from the equilibrium temperatures, bringing them to several hundred Kelvin above the lattice temperature without perturbing the latter. This creates a large non-equilibrium between the two carriers, who must couple with one another via the electron-phonon coupling factor so that their temperatures are able to equilibrate, usually on the order of ∼10 ps. During this time regime of non-equilibrium, the heat diffusion equation fails to capture the characteristic response garnered by TDTR. As a result, it is necessary to implement the phenomenological two-temperature model (TTM) [52] to better understand the carrier interactions associated with an ultrafast laser heating event.

The TTM has long been a prominent descriptor of the transfer of energy between the electronic and phononic subsystems, described by the following coupled differential equations [52]:

$$C_e\frac{\partial T_e}{\partial t} = \nabla\cdot(\kappa_e\nabla T_e) - g(T_e - T_l) + S(x,t) \tag{3.32}$$

$$C_l\frac{\partial T_l}{\partial t} = \nabla\cdot(\kappa_l\nabla T_l) + g(T_e - T_l). \tag{3.33}$$

In these equations, C_e and C_l are the electronic and lattice heat capacities, respectively, T_e and T_l are the electronic and lattice temperatures, respectively, g is the electron-phonon coupling parameter, and $S(x,t)$ is the source term, which deposits energy into the electronic system, defined as such [78]:

$$S(x,t) = -0.94\frac{1-R}{t_p}J\cdot\exp[-2.77(\frac{t}{t_p})^2]\frac{dI}{dx}. \tag{3.34}$$

In this equation, R is the surface reflectivity, J is the incident fluence, t_p is the duration of the pump pulse, and x and t are the space and time variables, respectively. $\frac{dI}{dx}$ is the spatial derivative of the light intensity distribution in the sample, which is calculated using a transfer matrix method with the complex indices of refraction, $\tilde{n}$, at the pump wavelength.

Discretization

Equations 3.32–3.34 are solved numerically via the Crank-Nicolson method [79]. This involves discretization of these equations both temporally and spatially by Δt and Δx, respectively. To perform this discretization, the carrier temperature, T_m, where m is the carrier, is approximated as the average of the carrier temperature at the current time step, n, and next time step, $n+1$, for layer i:

$$T_m = \frac{1}{2}(T^{n+1}_{m,i} + T^{n}_{m,i}). \tag{3.35}$$

The partial derivative of the carrier temperature in time is approximated as the difference in temperature at the next and current time step for layer i, divided by Δt:

$$\frac{\partial T_m}{\partial t} = \frac{T^{n+1}_{m,i} - T^{n}_{m,i}}{\Delta t}. \tag{3.36}$$

Finally, $\nabla \cdot (\kappa_m \nabla T_m)$ is approximated using the combined method, which weights implicit and explicit methods of discretization based on the constant a:

$$\begin{aligned} \nabla \cdot (\kappa_m \nabla T_m) = \frac{a}{\Delta x^2}[\kappa_{m,i} T^{n+1}_{m,i+1} - (\kappa_{m,i} + \kappa_{m,i-1}) T^{n+1}_{m,i} + \kappa_{m,i-1} T^{n+1}_{m,i-1}] \\ + \frac{(1-a)}{\Delta x^2}[\kappa_{m,i} T^{n}_{m,i+1} - (\kappa_{m,i} + \kappa_{m,i-1}) T^{n}_{m,i} + \kappa_{m,i-1} T^{n}_{m,i-1}]. \end{aligned} \tag{3.37}$$

Because we are using the Crank-Nicolson method, $a = 1/2$.

Discretization via Eqs. 3.35–3.37 is performed for both the electronic and lattice subsystems. After some rearranging and collecting of terms, the matrix equation for both systems takes the following form:

$$\tilde{\mathbf{A}}\mathbf{T}_e^{n+1} + \tilde{\mathbf{B}}\mathbf{T}_l^{n+1} = \tilde{\mathbf{C}}\mathbf{T}_e^{n} + \tilde{\mathbf{D}}\mathbf{T}_l^{n} + \mathbf{S} \tag{3.38}$$

$$\tilde{\mathbf{E}}\mathbf{T}_e^{n+1} + \tilde{\mathbf{F}}\mathbf{T}_l^{n+1} = \tilde{\mathbf{G}}\mathbf{T}_e^{n} + \tilde{\mathbf{H}}\mathbf{T}_l^{n}. \tag{3.39}$$

In these equations, $\tilde{\mathbf{A}}$–$\tilde{\mathbf{H}}$ are $N \times N$ matrices and $\mathbf{T}_m^n$, $\mathbf{T}_m^{n+1}$, and $\mathbf{S}$ are $N \times 1$ matrices. The matrices $\tilde{\mathbf{A}}$–$\tilde{\mathbf{H}}$ are tridiagonal, and contain information about the electron-phonon coupling parameter, heat capacities, and thermal conductivities of each layer. The transpose of $\mathbf{T}_m^n$ is $[T_{m,1}^n T_{m,2}^n ... T_{m,N-1}^n T_{m,N}^n]$.

Recognizing that the unknowns in Eqs. 3.38 and 3.39 are the electronic and lattice temperatures at the next time step, $\mathbf{T}_e^{n+1}$ and $\mathbf{T}_l^{n+1}$, respectively, the system of equations can be solved via substitution. This allows for the determination of the electronic temperature at the next time step for the system,

$$\mathbf{T}_e^{n+1} = (\tilde{\mathbf{A}} - \tilde{\mathbf{B}}\tilde{\mathbf{F}}^{-1}\tilde{\mathbf{E}})^{-1}[(\tilde{\mathbf{C}} - \tilde{\mathbf{B}}\tilde{\mathbf{F}}^{-1}\tilde{\mathbf{G}})\mathbf{T}_e^n + (\tilde{\mathbf{D}} - \tilde{\mathbf{B}}\tilde{\mathbf{F}}^{-1}\tilde{\mathbf{H}})\mathbf{T}_l^n + \mathbf{S}], \tag{3.40}$$

as well as the lattice temperatures at the next time step,

$$\mathbf{T}_l^{n+1} = \tilde{\mathbf{F}}^{-1}(\tilde{\mathbf{G}}\mathbf{T}_e^n + \tilde{\mathbf{H}}\mathbf{T}_l^n - \tilde{\mathbf{E}}\mathbf{T}_e^{n+1}). \tag{3.41}$$

A MATLAB program was implemented in order to perform the matrix multiplication and inversion necessary for solving $\mathbf{T}_e^{n+1}$ and $\mathbf{T}_l^{n+1}$.

Typical spatial and temporal discretizations in the MATLAB program of 0.5 nm and 50 fs, respectively, are used in TTM calculations. For systems with substrates, the substrate is modeled to be 100 nm, where the final discretized layer is fixed to have an infinite C_l to emulate a semi-infinite substrate. The electronic heat capacity of each layer is chosen to be proportional to temperature via the electronic heat capacity coefficient γ, $C_e = \gamma T_e$, which is valid for the range of electronic temperatures in this dissertation [43]. The electron-phonon coupling factor g is approximately independent of lattice and electronic temperatures for

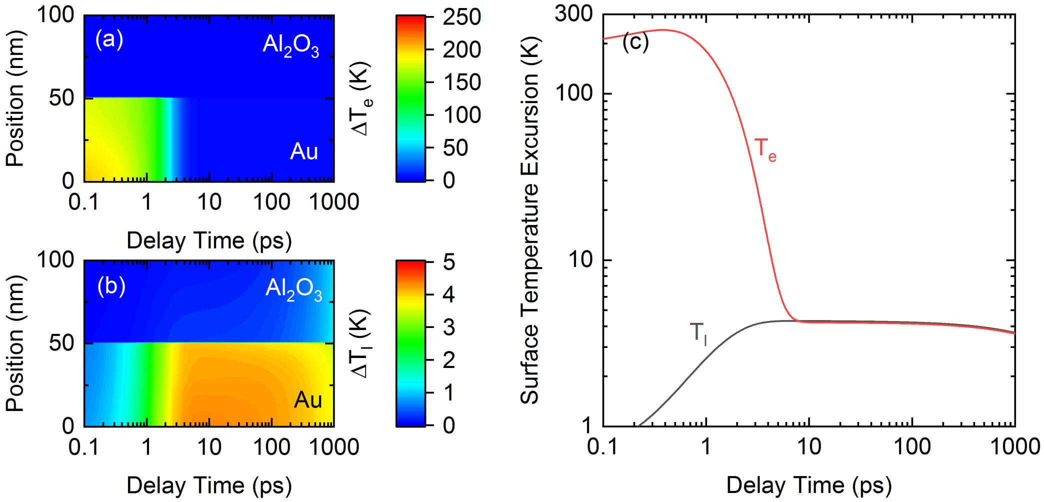

Figure 3.9. Example TTM modeling for a 50 nm Au film on Al_2O_3. Contours show the temporal and spatial evolutions of the (a) electronic and (b) lattice temperature excursions. (c) Surface temperature excursion for electronic and lattice systems.

low temperature perturbations [43], and is thus chosen to be constant.

For modeling interfaces, interface thicknesses of 0.5 nm are prescribed. For phonons, the thermal conductivity of the interface is determined such that an equivalent phonon conductance G is achieved, i.e., $\kappa_{\text{interface}} = Gd$, where d is the thickness of the discretized layer, 0.5 nm. For electrons, the electron thermal conductance is determined by the product of the average of the electronic temperatures on either side of the interface and Γ (i.e., $\Gamma T_{\text{e,ave}}$, where $T_{\text{e,ave}}$ is the average electronic temperature on either side of the interface.) to be in accordance with electron diffuse-mismatch model [56].

Example TTM calculations are shown in Fig. 3.9, which shows the (a) electron and (b) lattice temperatures temporally and spatially for a 50 nm Au layer on Al_2O_3. Energy deposition can clearly be observed in the electronic system of Au layer, where the electron temperature reaches nearly 250 K by 1 ps. At this point, electrons couple their energy to the lattice via the electron-phonon coupling factor, resulting in an increase in the lattice temperature. Because the lattice heat capacity is much larger than its electronic counterpart, the lattice temperature rise is only ∼4 K. The surface temperature excursions of the electronic and lattice systems are shown in Fig. 3.9(c), where the convergence of the two temperature can clearly be seen at ∼6 ps.

Energy Deposition

To model energy deposition into the electronic system via the source term **S**, I utilize a transfer matrix method to determine the intensity of the light distribution in the material system of interest. In absence of this transfer matrix method, the light intensity distribution, $I(x)$ is simply

$$I(x) = \exp(-\frac{x}{\delta}), \tag{3.42}$$

where δ is the 1/e optical penetration depth at the pump wavelength. This equation for the light intensity distribution is primarily applicable for homogenous material systems, where material interfaces do not contribute to the electric field intensity in a given layer. Further, in heterogenous material systems where the complex indices of refraction, $\tilde{n}$, are not consistent from one film to another, then the use of δ for the surface film is not merited.

To determine the light intensity distribution in a multi-layer material system, we follow the formalism of Pettersson *et al.* [80] by first determining the net transmissivity and reflectivity of a multilayer system, T_{net} and R_{net}. Fundamentally, I am interested in determining the matrix **M** that relates the electric field components propagating in the positive and negative directions at the top and bottom of the multilayer stack:

$$\begin{bmatrix} E_0^+ \\ E_0^- \end{bmatrix} = \mathbf{M} \begin{bmatrix} E_{N+1}^+ \\ E_{N+1}^- \end{bmatrix} \tag{3.43}$$

In this equation, E_0^+ and E_0^- are the electric field components propagating in the positive and negative directions at the top of the stack, respectively, while E_{N+1}^+ and E_{N+1}^- are those at the bottom of the stack.

Similar to the matrix multiplication method used to solve the heat diffusion equation, matrix multiplication is also utilized here. At the interfaces between materials j and k, the interface matrix describing the propagation of the electric field from one medium into another will be

$$\mathbf{D}_{jk} = \frac{1}{t_{jk}} \begin{bmatrix} 1 & r_{jk} \\ r_{jk} & 1 \end{bmatrix}, \tag{3.44}$$

where r_{jk} and t_{jk} are the complex reflection and transmission coefficients, respectively,

$$r_{jk} = \frac{\tilde{n}_j - \tilde{n}_k}{\tilde{n}_j + \tilde{n}_k} \tag{3.45}$$

$$t_{jk} = \frac{2\tilde{n}_j}{\tilde{n}_j + \tilde{n}_k}. \tag{3.46}$$

The matrix describing propagation of the electric field in the layer will be

$$\mathbf{P}_j = \begin{bmatrix} \exp(-i\xi_j d_j) & 0 \\ 0 & \exp(i\xi_j d_j) \end{bmatrix} \tag{3.47}$$

where $\xi_j = \frac{2\pi}{\lambda}\tilde{n}_j$ and d_j is the thickness of the discretized layer.

The net scattering matrix, **M**, which relates the electric field at the top and bottom of the multilayer system, can be defined as

$$\mathbf{M} = \begin{bmatrix} M_{11} & M_{12} \\ M_{21} & M_{22} \end{bmatrix} = (\prod_{v=1}^{m} \mathbf{D}_{(v-1)v}\mathbf{P}_v) \cdot \mathbf{D}_{N(N+1)}. \tag{3.48}$$

Finally, T_{net} and R_{net} can be determined via

$$T_{\text{net}} = |\frac{M_{21}}{M_{11}}|^2 \tag{3.49}$$

and

$$R_{\text{net}} = |\frac{1}{M_{11}}|^2. \tag{3.50}$$

These equations are useful for determining the net reflectivity and transmissivity of a material system, but do not provide the light intensity distribution within each layer. The net scattering matrix, **M**, can separated into partial system transfer matrices, $\mathbf{M}'_j$ and $\mathbf{M}''_j$,

$$\mathbf{M} = \mathbf{M}'_j \mathbf{P}_j \mathbf{M}''_j, \tag{3.51}$$

where $\mathbf{P}_j$ is defined as before. $\mathbf{M}'_j$ and $\mathbf{M}''_j$ are both defined similarly to **M**,

$$\mathbf{M}'_j = \begin{bmatrix} M'_{j11} & M'_{j12} \\ M'_{j21} & M'_{j22} \end{bmatrix} = (\prod_{\nu=1}^{j-1} \mathbf{D}_{(\nu-1)\nu} \mathbf{P}_\nu) \cdot \mathbf{D}_{(j-1)j}, \tag{3.52}$$

$$\mathbf{M}''_j = \begin{bmatrix} M''_{j11} & M''_{j12} \\ M''_{j21} & M''_{j22} \end{bmatrix} = (\prod_{\nu=j+1}^{m} \mathbf{D}_{(\nu-1)\nu} \mathbf{P}_\nu) \cdot \mathbf{D}_{N(N+1)}. \tag{3.53}$$

Finally, the electric field intensity, $E_j(x)$, can be determined using

$$E_j(x) = \frac{M''_{j11} \cdot e^{-i\xi(d_j - x)} + M''_{j21} \cdot e^{i\xi(d_j - x)}}{M'_{j11} M''_{j11} \cdot e^{-i\xi d_j} + M'_{j21} M''_{j21} \cdot e^{i\xi d_j}} E_0^+, \tag{3.54}$$

where E_0^+ is the electric field intensity incident at the surface of the system. The electric field intensity, however, does not correlate to the number of excited states in a given material. Since we are trying to determine the light intensity distribution $I(x)$ in our multilayer system, which deposits energy into the electronic system, we calculate the time-averaged energy dissipation per second, $Q_j(x)$, via

$$Q_j(x) = \frac{1}{2} c \varepsilon_0 \alpha_j \mathrm{Re}(\tilde{n}) |E_j(x)|^2, \tag{3.55}$$

where c is the speed of light, ε_0 is the permittivity of free space, and $\alpha_j = \frac{4\pi \mathrm{Im}(\tilde{n})}{\lambda}$ is the absorption coefficient at the position x. The light intensity distribution is calculated using the product of absorbed fluence, F, and $Q_j(x)$ normalized by its surface intensity, i.e.,

$$I(x) = F \frac{Q_j(x)}{Q_j(x=0)}. \tag{3.56}$$

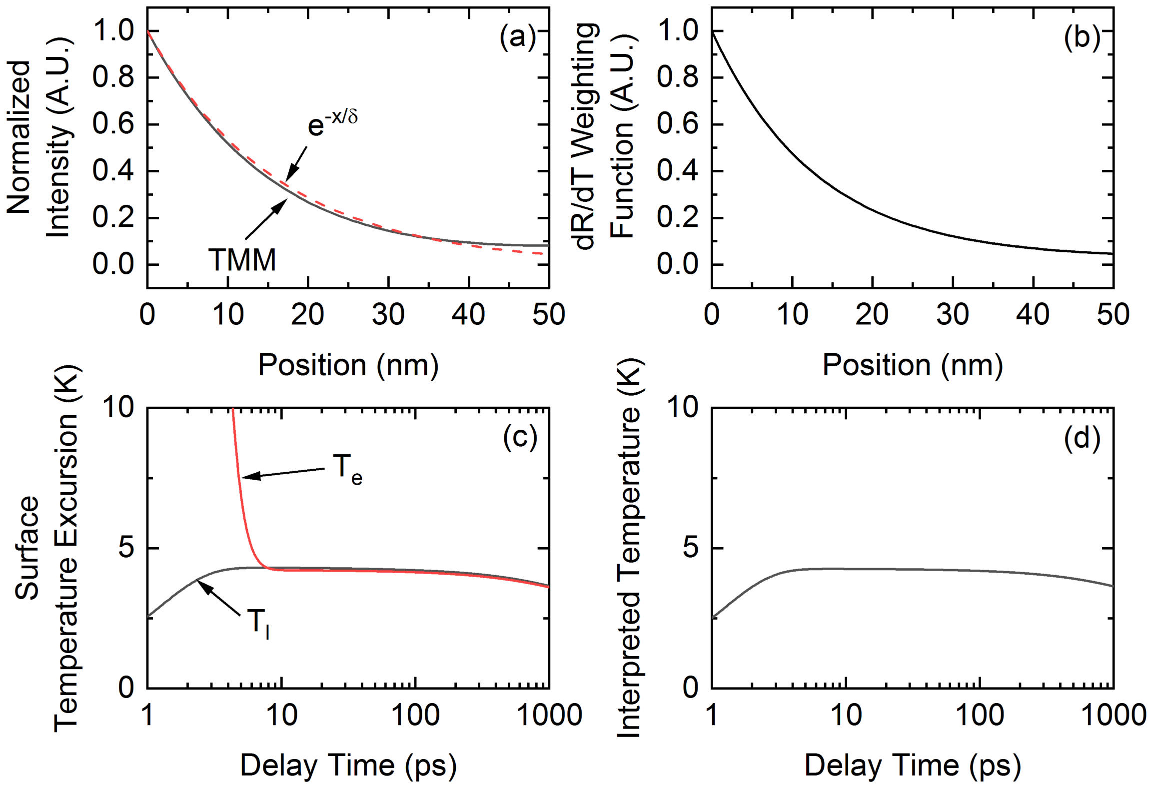

Figure 3.10. (a) Light intensity distribution in a 50 nm Au film on Al_2O_3, calculated using Eqs. 3.42 and 3.56. (b) dR/dT weighting function, used to calculate the temperature excursion as interpreted in a pump/probe experiment. (c) Surface electronic and lattice temperature excursions for a 50 nm Au film on Al_2O_3. (d) Interpreted temperature excursion using the dR/dT weighting function for comparison to experimental data.

Example calculations of $I(x)$ based on Eq. 3.42 and Eq. 3.56 are shown in Fig. 3.10(a). The calculations are made for a 50 nm Au film on Al_2O_3 using an incident wavelength of 400 nm. When using Eq. 3.42, δ is calculated via the equation $\delta = \frac{\lambda}{4\pi k}$, where k is the imaginary portion of $\tilde{n}$. On the other hand, using Eq. 3.56 requires the use of both the real and imaginary components of $\tilde{n}$ for both the Au film as well as the Al_2O_3 substrate. While the differences are not exceptionally large for this film on substrate system, when a multilayer system is present on the substrate the transfer matrix method is the most rigorous way in determining the light intensity distribution.

Signal Interpretation

Part of the analysis relies on the interpretation of the electronic and phononic temperanttures acquired by solving the TTM. In general, the reflectivity acquired in a pump/probe experiment exhibits contributions from the electronic and lattice subsystems [81]:

$$\Delta R = a\Delta T_e + b\Delta T_l. \tag{3.57}$$

In this equation, ΔR is the change in reflectivity resulting in perturbations in the electronic and lattice temperatures, ΔT_e and ΔT_l, respectively. The factors a and b are scaling constants that determine the contributions of each of these systems to ΔR.

Because the signal acquired in TDTR encompasses both electronic and lattice contributions to the thermoreflectivity, and that the electronic contribution to thermoreflectivity becomes negligible ~5 ps after excitation by the laser pulse near 800 nm for fluences used in this dissertation [82, 83], we choose to interpret the lattice temperature acquired by the TTM and compare it to our measured data 3 ps after excitation. This interpretation accounts for the subsurface temperature profile and its influence on the thermoreflectivity [84], where the temperature at each discrete point beneath the surface contributes to the reflectivity and approximately follows the optical attenuation depth. The weighting function with which we use to interpret this subsurface temperature utilizes the indices of refraction, $\tilde{n}$, of the material system and includes temperature dependence, $d\tilde{n}/dT$, at our probing wavelength, 800 nm, using previously reported data [62].

To determine this weighting function, the net reflectivity of the multilayer system, R_{net}, is calculated as described by Eq. 3.50. Following, the index of refraction of the top sublayer is perturbed by $d\tilde{n}/dT \times \Delta T$ and recalculate the net reflectivity of the multilayer system under this perturbed condition, $R_{\text{pert.}}$. The index of refraction of this top sublayer is returned to its original value, and the process is repeated for all sublayers.

Now that the reflectivity has been determined for each sublayer perturbation, the weighting function can be determined by

$$\frac{dR}{dT} = \frac{R_{\text{net}} - R_{\text{pert.}}}{\Delta T}. \tag{3.58}$$

Similar to determining $I(x)$, $\frac{dR}{dT}$ is normalized to its intensity at the surface of the system. These calculations are performed for a 50 nm Au on Al_2O_3, shown in Fig. 3.10(b) using indices of refraction and their temperature dependent values from the literature [62].

Finally, the weighting function defined in Eq. 3.58 is used to acquire the signal at each time-step. This is performed by summing the lattice temperatures of each sublayer in the system by the weighting function calculated using Eq. 3.58. The weighted lattice temperature according to $\frac{dR}{dT}$ is normalized to the data to allow for a comparison between the two, usually at ∼100 ps. As a comparison between the surface lattice temperature excursion and the interpreted lattice temperature excursion, see Figs. 3.10(c) and (d) for 50 nm Au on Al_2O_3. The surface lattice and electronic temperature excursions are shown in Fig. 3.10(c)– by applying the weighting function at each time step, the interpreted temperature can be acquired, shown in Fig. 3.10(d). Note, the surface lattice temperature closely follows that of the weighting function, suggesting that, in systems comprising just one material, the surface lattice temperature offers a good approximation to the interpreted temperature. In multilayer systems, however, where there is a large contribution of $d\tilde{n}/dT$ from subsurface materials, the surface lattice temperature will not appropriately capture the data.

Now that I have addressed the heat transfer analyses associated with conditions of carrier equilibrium and carrier non-equilibrium, I will now present the basis of thermal property imaging. This imaging is primarily applicable to conditions of carrier equilibrium, i.e., in the heat diffusion regime, although could in practice be extended to conditions of carrier non-equilibrium.

3.4 Imaging Thermal Properties

TDTR has exemplified its efficacy in determining the thermal conductivity, volumetric heat capacity, and interfacial conductances in a variety of material systems. Conventionally, these measurements are indicative of properties at a single position on a sample, and may not be representative in the case of spatially inhomogenous specimens. Indeed, typical measurements performed via TDTR are done so with large pump/probe diameters (>10 μm) in order to reduce sensitivity to the Al transducer thermal conductivity and in-plane thermal transport, as well to the pump/probe diameters. This enables high-throughput measurements with little uncertainty, but at the expense of aerial resolution.

As such, a significant portion of my early dissertation career was devoted to performing measurements with higher objective lenses, usually $20\times$ and $50\times$, in an effort to increase aerial resolution. This required precise knowledge of the Al thermal conductivity, as sensitivity to in-plane transport in the Al transducer becomes more significant as the pump/probe diameters are reduced. Additionally, increased sensitivity to the pump/probe diameters necessitated a new paradigm in their determination, as well as a methodology by which one could repetitively acquire consistent diameters. As discussed in the following subsections, this was accomplished by the integration of a stepper motor that swept through the focal plane, resulting in precise acquisition of the focus well within the Rayleigh lengths of the focused beams and in congruence with the stringent uncertainties necessitated for TDTR.

Once I was able to perform TDTR measurements with higher lateral resolution using these objective lenses, the focus was then shifted towards the aerial acquisition of thermal parameters. By integrating two stepper motors orthogonal to the incident pump and probe beams, I developed rastering algorithms that moved the sample in a predetermined manner, synchronized with the stepper motor controlling the focal plane. This was accomplished by developing a novel MATLAB program, allowing for the acquisition of thermal parameters over an aerial region of interest with relative ease and minimal uncertainty. In essence, a thermal property microscope was developed.

Inspection of the TDTR data in Fig. 3.4 presents the basis of expanding conventional TDTR, which probes a single spot on the sample surface, to extract thermal properties of interest over an area of interest. In particular, at a given pump/probe delay time it is observed that as the thermal conductivity of the underlying material increases, a correlation can be made with an increasing ratio signal, $-V_{\text{in}}/V_{\text{out}}$. Fundamentally, this is the premise of thermal property imaging via TDTR: correlating the ratio to the thermal parameter of interest at a given pump/probe delay time over an aerial region of interest.

3.4.1 Thermal Conductivity Correlation Function

In order to appropriately determine the pump/probe delay time to acquire an aerial map of the thermal conductivity, it is necessary to first perform several single-point TDTR measurements to determine the approximate thermal conductivities and interfacial conductances to be probed. Recall, I will typically fit for these two parameters in a single-point TDTR scan, whose delay times cover 100–5500 ps. At a single pump/probe delay time, however, it is impossible to determine both the interfacial conductance and substrate thermal conductivity simultaneously. It is thus necessary to determine the interfacial conductance prior to performing an aerial map of the thermal conductivity, and choose a pump/probe delay time such that sensitivity to G is minimized.

As an example, consider two material systems: (1) Al/aSiO_2, where the substrate thermal conductivity ($\sim$1.4 W m^{-1} K^{-1}) is low, and (2) Al/Al_2O_3, where the substrate thermal conductivity ($\sim$35 W m^{-1} K^{-1}) is relatively high. Characteristic TDTR data and best fits are shown for the two systems in Fig. 3.11(a), where a conductance of $\sim$150 MW m^{-2} K^{-1}is determined for G of both systems. Sensitivities to κ and G are shown in Fig. 3.11(b), where sensitivity to the Al/aSiO_2 interfacial conductance is small due to the large resistance in the substrate. In the Al/Al_2O_3 system, however, sensitivity to the Al/Al_2O_3 interface conductance is large, as the resistance of the interface is comparable to that of the substrate for the volume probed. For Al/aSiO_2, because sensitivity to the interface is small in the 100 to 1000 ps range, any delay time within this regime can be chosen, as it is

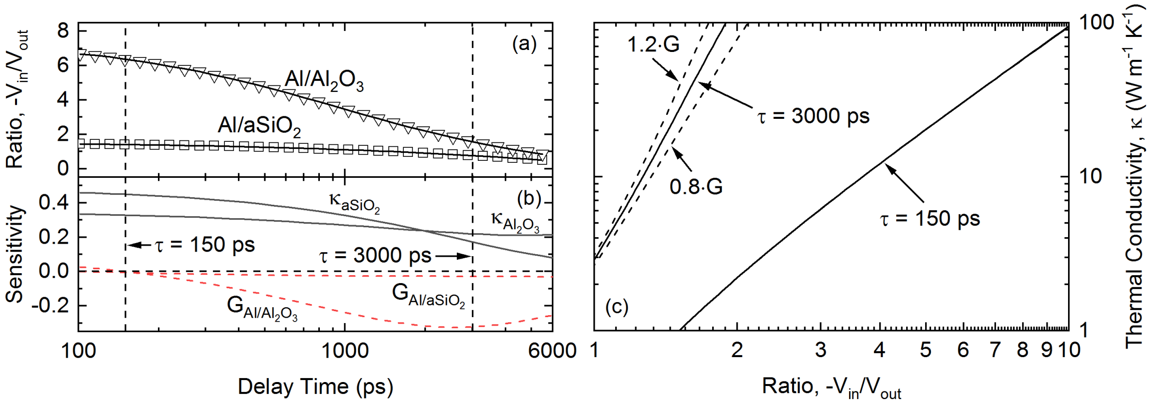

Figure 3.11. (a) Characteristic TDTR scans for Al/Al_2O_3 and $Al/aSiO_2$, as well as (b) sensitivity to κ of the substrate and G of the Al/substrate interface. (c) Thermal conductivity correlation functions at 150 and 3000 ps. When present, the dashed lines are for a ±20% perturbation on G.

well past the relaxation time electrons in the Al transducer and offers high sensitivity to κ while minimizing sensitivity to G. For Al/Al_2O_3, the delay time at which the sensitivity to G crosses zero is chosen such that changes in the acquired signal are reflective of changes in κ, and not G.

To determine the spatially varying thermal conductivity, the simulated ratio, $-V_{\mathrm{in}}/V_{\mathrm{out}}$, is correlated to the thermal conductivity of the substrate. This is done by evaluating the response function, $Z(\omega)$, at a given delay time for a range of thermal conductivities. The acquired correlation function is shown in Fig. 3.11(c) for two delay times, 150 and 3000 ps, for an Al/substrate system where $G = 150$ MW m^{-2} K^{-1}. When present, dashed lines are presented for a ±20% change in G. At short pump/probe delay times, sensitivity to G is minimal for low and high thermal conductivity systems–perturbations of G by 20% result in a negligible change in the acquired κ. At longer pump/probe delay times, however, one must accurately determine G in order to correctly correlate the acquired ratio to thermal conductivity, even for low thermal conductivity materials. Thus, measurements performed at short delay times, or when sensitivity to G is close to zero, is preferable. Performing measurements at short delay times also provides added precision to the acquired thermal conductivity, as for an equivalent signal-to-noise ratio at 150 and 3000 ps, the slope of the thermal conductivity correlation function is lower when evaluated at 150 ps.

3.4.2 Hardware and Algorithms

Now that I have addressed the correlation function used to derive κ from the measured ratio, I will now address the hardware and algorithms associated with spatially determining the thermal conductivity. In order to expand conventional, single-point TDTR to a mapping configuration, two systems were implemented.

Hardware

The first of these systems utilizes a home-built XYZ system, comprising of stepper motor actuators (Thorlabs ZST225B), each with 25 mm of travel (<5 μm bidirectional repeatability). Each stepper motor actuator interfaces with its own individual controller (Thorlabs KST101), which can be controlled manually or programmatically. This system is typically utilized for lower magnification objectives, i.e., 10× and 20× objectives, and is aligned in such a way that lateral movements of the sample over several hundred micrometers do not result in deviations in the pump/probe focal point. This is considered the “coarse” system.

The second system is a 3-axis NanoMax stage (Thorlabs MAX311D). The system utilizes stepper motors with 4 mm travel (<5 μm bidirectional repeatability) for each axis as well as a closed-loop piezo motor with 20 μm travel (5 nm bidirectional repeatability). Stepper motors in the X and Y directions are used to raster the sample over the region of interest, while the Z position of the sample is ensured via the closed-loop piezo for that direction. Because of the finer resolution and higher bidirectional repeatability of the z-axis, the system utilizing the NanoMax is utilized for high-resolution measurements (20×, 50×, and 100× objectives).

Beam Diameter Consideration

In both systems, the laser spot size must remain in focus at each pixel so as to not introduce additional errors into the analysis. The Rayleigh length of an ideal Gaussian

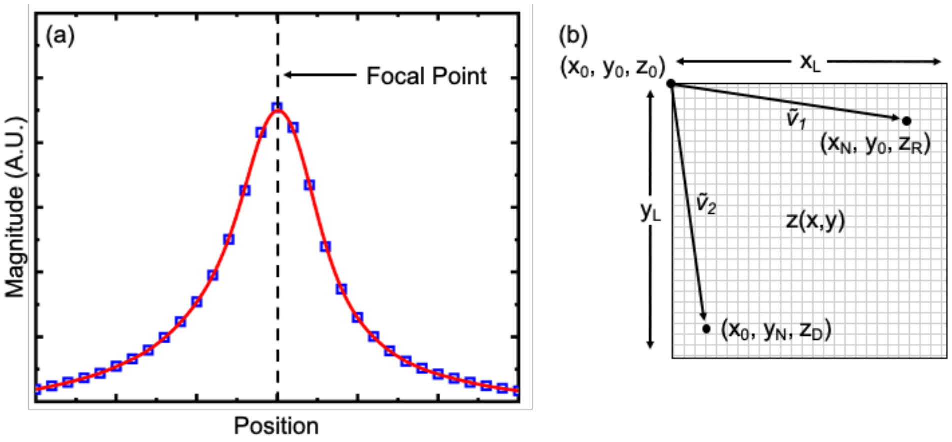

Figure 3.12. (a) Example autofocusing algorithm used to determine the focal point in the experiment. (b) Schematic illustration of parameters utilized to determine the focal position of the beam as the position of the sample is adjusted.

beam is defined as [85]

$$z_R = \frac{\pi w_0^2}{\lambda}, \tag{3.59}$$

where w_0 is the focused beam spot diameter and λ is the wavelength. For the probe beam using 50×, 20×, and 10 × objectives, where w_0 are ~2, ~7, ~11 μm, respectively, z_R is can be calculated to be 16, 190, and 470 μm for each objective lens. At a distance z from the focal point, the diameter will be

$$w(z) = w_0\sqrt{1+(\frac{z}{z_r})}. \tag{3.60}$$

At $z = z_R$, the focused beam diameter will increase by a factor of $\sqrt{2} \approx 1.41$, and thus the beam must remain well within the Rayleigh range for the measurement duration to minimize uncertainty in spot size. For the "coarse" system, which is used primarily for 10× and 20× objectives, this is achieved by aligning the stepper motors with the machined holes in the optical table, and monitoring the DC reflectivity of the beam as well as its shape in the camera as it traverses over the area of interest. If the DC reflectivity drops significantly, or the camera image defocuses, manual adjustments are made until neither of the two occur.

For the high-resolution system, I capitalize on the use of the piezo motor integrated into the z-direction of the stage. For many of the samples measured in this dissertation, the assumption can be made that the region probed is planar. At the home position (x_0, y_0, z_0), the beam will be in focus as determined by maximizing the signal through the focal plane, see Fig. 3.12(a). Moving to the positions near the corners of the intended map, (x_N, y_0) and (x_0, y_N), the required focal points, z_R and z_D, respectively, can be acquired. Because only three points are required to determine a plane, the equation for $z(x,y)$ can then be determined:

$$z(x,y) = z_0 + \frac{a}{c}(x_0 - x) + \frac{b}{c}(y_0 - y), \tag{3.61}$$

where (x,y) is the current position of the stage, and a, b, and c are constants pertaining to the equation of the plane. A schematic illustration of this calculation is shown in Fig. 3.12(b), where vectors $\tilde{v}_1$ and $\tilde{v}_2$ are shown in order to determine the equation of the plane.

Rastering Algorithms

The premise of rastering in both aformentioned systems is graphically depicted in Fig. 3.13. Initially, rastering was performed in a discrete manner, whereby a coordinate (x_n, y_n, z_n) is sent to the controller and waits for the stepper motor to reach its new position. Following, an additional wait time is included, relating to the settling time of the filter and the time constant of the lock-in amplifier. Finally, V_{in} and V_{out} are recorded for the coordinate set, and the next coordinates are sent to the controller, repeating the process. This is the rastering algorithm implemented for the NanoMax. While intuitive, the procedure is involved and generally inefficient, as loops utilized for determining whether or not a motor is at its required position adds additional, although necessary, wait times.

Image acquisition time was improved upon by implementing an algorithm that continuously scans the sample surface, rather than discretely at each coordinate. In this continuous scanning approach, the sample is moved to the starting x- and y-positions (x_0, y_0). Following, the stepper motor controlling the x-axis of the sample is given a new position to move to, x_N, which is at the end of the raster line. The stepper motor controller is configured

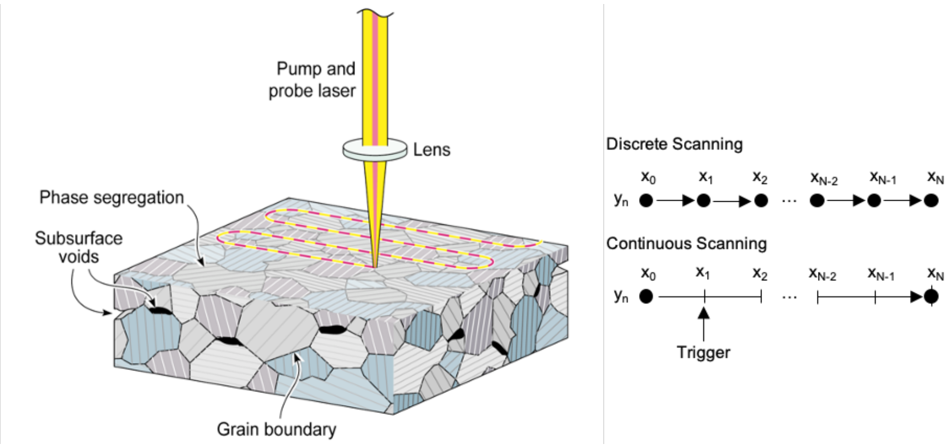

Figure 3.13. Schematic representation for rastering algorithms implemented for the determination of thermal properties.

such that while moving to this new position, a trigger pulse is sent to the lock-in amplifier after each step, x_s, until it reaches x_N. This procedure is continued for all y-positions until an aerial map is produced.

In this continuous scanning approach, the velocity with which this axis moves is of the utmost importance, as it determines the rate of averaging over a given pixel. If the velocity is too slow, then the acquired pixel will be an average of the adjacent pixels. If too fast, then the pixel will not be representative of an average over the area of interest. To calculate the velocity, we begin with the step size, x_s. For an impulse response, the lock-in will settle to the new signal over a period of τ_{settle}. The main parameters that influence τ_{settle} are the filter order of the lock-in, m, as well as the lock-in time constant, TC, as well as the desired accuracy of each pixel, which I take as 99%. For a filter order m, the settling time to 99% will be $\tau_{\text{settle}} = f(m) \cdot \text{TC}$, where $f(m)$ is a function describing multiplier constant required to achieve a settling time to 99%. For a settling time to 99%, $f(m)$ ranges from 4.6 to 16.0 for filter orders 1 through 8, while TC is typically 2–20 ms. The velocity of the motor can be calculated by dividing the step size by the settling time:

$$v = \frac{x_s}{\tau_{\text{settle}}} = \frac{x_s}{f(m) \cdot \text{TC}}. \tag{3.62}$$

Implementing this continuous scanning algorithm reduces image acquisition time by over an order of magnitude compared to the discrete scanning algorithm, and has enabled the characterization of sub-micron crystallization features in thermally grown oxides, as discussed in Chapter 5.

3.5 Summary

In this chapter, I outlined the experimental techniques used in this dissertation and the analyses pertinent to them. In order to grasp the essence of a pump/probe experiment, it is necessary to understand the concepts of thermoreflectance and lock-in amplification. Without these two key factors, pump/probe experiments would be virtually impossible. Following, I outlined the TDTR system I built during my first year in the ExSiTE lab. The associated mathematical formalism used in analyzing this techniques was presented, where we further delved into the two-temperature model when carrier non-equilibrium was included. Finally, I provided the basic premise of spatially understanding thermal properties using TDTR. In the next chapter, I will use this approaching to mapping the thermal properties of materials to extract both the anisotropic thermal conductivity tensor of β-$Y_2Si_2O_7$ as well as the spatially varying thermal conductivity of a steam-cycled β-$Yb_2Si_2O_7$ system.

Chapter 4

Thermal Conductivity of Thermal/Environmental Barrier Coatings

4.1 Anisotropic Thermal Conductivity of Yttrium Disilicate

The work presented in this section has previously been published in *Acta Materialia* [86], and is a culmination of work from individuals in the *ExSiTE Lab* and *Opila Research Group* at UVa. In particular, Valentina-Angelici Avincola and Cory Parker of the *Opila Research Group* were foundational in fabricating the specimen of interest and characterizing it using electron-backscatter diffraction. Leonard Braun, John Gaskins, and Albert Tomko of the *ExSiTE Lab* aided in the development of the thermal conductivity microscope, as well as interpreting the data in a tensorial manner. Experimental guidance was provided by Elizabeth Opila and Patrick Hopkins.

4.1.1 Background

The harsh conditions experienced by coatings in extreme environments intensifies the rate at which materials fail. For example, the localized power densities and associated temperature increases in high temperature chemically reacting atmospheres can give rise to hot spots and large thermal gradients [87–89] and resulting thermal expansion and material deformation [90–92], and promote coating failure via cracking, delamination, oxidation, corrosion and spallation [93–96]. Due to the thermochemical and thermomechanical constraints on materials in these environments, the phase space of materials available for use in these extreme atmospheres is limited. SiC-based turbine components in combination with an environmental barrier coating (EBC) are promising material systems for their implementation as turbine engine components [95, 97]. Due to the intense combustion environments in which these material systems operate in, EBCs possessing high water-vapor resistance, low contrast in thermal expansion coefficient to adjacent and subsurface materials, and chemical and mechanical stability at high temperatures make them attractive for the protection of subsurface materials [98]. Rare earth (RE) silicates exhibit the above qualities [16, 23], with the capacity to withstand temperatures up to and higher than 1316 °C for thousands of hours [99]. These combined characteristics have brought RE silicates to the forefront of technological relevance in the search for EBCs for turbine component protective coatings in extreme environments.

Yttrium-based silicate coatings have been identified as promising candidates for EBCs. Compared to early barium strontium aluminosilicate (BSAS) EBCs, yttrium silicates exhibit improved stability, all while maintaining high temperature thermomechanical stability [100]. The comparable coefficient of thermal expansion (CTE) of γ-$Y_2Si_2O_7$ to those of SiC and mullite make it a suitable EBC in addition to its stability at elevated temperatures [16, 101], offering a further relief from the stresses arising from thermal cycling [100, 102–105]. In all, $Y_2Si_2O_7$ is a promising candidate for EBC applications.

The thermal conductivity associated with these silicates is a critical property that needs to be taken into consideration when designing EBCs, as this ultimately dictates the heat spreading ability of the material, resultant internal energy densities, and local temperature rises. Various works have examined the thermal conductivity of yttria-based silicates in their bulk form with values ranging from 0.161 to 4.91 W m^{-1} K^{-1}, depending on the porosity of the system [101, 105–108]. Thermal conductivity for these reported values generally represent an average thermal conductivity of a polycrystalline, possibly multiphase system. For example, in all of the aforementioned reports of yttria-based silicate thermal conductivity, laser-flash was employed, thus sampling the average thermal diffusivity over the entire volume of the sample. These measurements cannot isolate the microstructural or anisotropic influences that different grains have on thermal transport in the sample, especially when the structure is monoclinic as is for the majority of the rare earth monosilicates and disilicates. Clarke *et al.* [106] have shown that at high temperatures, the thermal conductivity of various disilicates can achieve exceptionally low values, reaching the theoretical minimum limit to thermal conductivity [109]. Additionally, they demonstrate that the thermal conductivity of Y-, Yb-, and Lu-based disilicates can theoretically be anisotropic. For these complicated systems, an anisotropic thermal conductivity tensor dictating the flow of heat is not to be ignored, and has the potential to largely influence EBC applications at the macroscale.

The challenge, however, is in determining the thermal conductivity tensor in this polycrystalline system with an anisotropic crystal structure. At large length scales, much larger than the characteristic grain sizes in a material, non-textured polycrystalline materials with anisotropic crystal structures yield an isotropic thermal conductivity. This thermal conductivity isotropy breaks down at the length scale of the energy carriers, in our case, the mean free paths of the phonons. Thus, while the thermal conductivity may appear isotropic at macroscopic scales, spatially varying temperature rises and local hot spots can occur that defy this isotropic assumption, since the microscopic nature of the crystal structure in the grains, which is anisotropic, will dictate the phonon scattering and local temperature rises. While structural characterization techniques can clearly resolve differences in local crystal orientation and phases (e.g., electron-backscatter diffraction), thermal measurement techniques have not been afforded the luxury of measuring local anisotropy variation from grain to grain over length scales consisting of several grains. This has led to a void in our understanding of not only how the local thermal conductivity of anisotropic polycrystalline samples relates to the more globally-averaged values, but also leaves several theoretical treatments of thermal conductivity anisotropy in crystal systems of lower symmetry unvetted.

In this work, we experimentally measure the thermal conductivity tensor of β-$Y_2Si_2O_7$ by conducting an areal map of the thermal conductivity of polycrystalline β-$Y_2Si_2O_7$ with $\sim$2 micrometer resolution. Locally probing grains and correlating their crystalline orientations to electron-backscatter diffraction (EBSD) data allows us to measure the orientation-dependence of heat conduction as quantified by the thermal conductivity. In doing so, we determine the thermal conductivity tensor of the monoclinic β-$Y_2Si_2O_7$ system. We find that β-$Y_2Si_2O_7$ is reasonably anisotropic, with an $\sim$40% change in thermal conductivity from its most to least-insulating orientations. This strong variation in thermal conductivity of β-$Y_2Si_2O_7$ based on grain orientation, which is driven by the naturally large anisotropy in the crystal, has major implications with regard to predicting mechanisms of failure based on local thermal strains, and suggests the potential to preferentially texture polycrystalline EBCs to enhance, restrict, and/or direct heat flow.

4.1.2 Materials & Methods

An atmospheric plasma spray (APS) process was implemented to fabricate a bulk $Y_2Si_2O_7$ specimen. The APS process is a non-equilibrium line of sight thermal spray process, in which a plasma is created using a high amperage anode with either hydrogen or helium. This plasma has a core temperature of $\sim$20,000 K with a steep temperature gradient. $Y_2Si_2O_7$ powders are fed into the torch and ejected into the plasma using high flow rates of an inert gas on the order of hundreds of cubic feet per hour. The inhomogenous heating of the powders and variation in powder size results in a heterogeneous mixture of non-equilibrium phases in the coating. A post-anneal of 1200 °C for 120 hours in ambi-

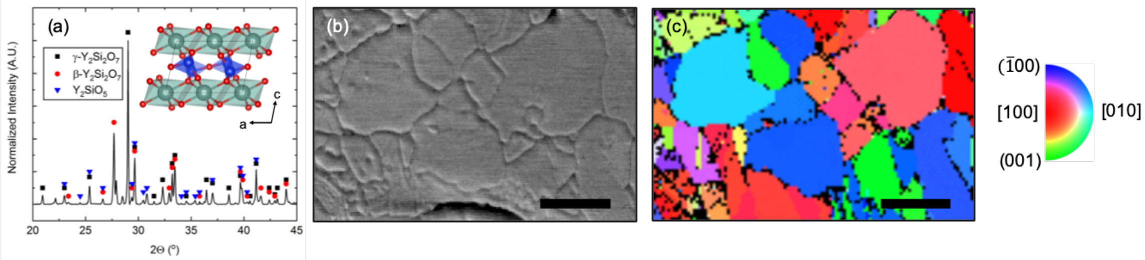

Figure 4.1. (a) X-ray diffractogram of the sample of interest, confirming the presence of Y_2SiO_5 and γ- and β-phases of $Y_2Si_2O_7$. (b) Representative SEM of select grains for reference. (c) Inverse pole figure Z (IPF Z) electron backscatter diffraction orientation micrograph, showing the differing orientations of grains in (b). See Appendix B1 for EBSD phase micrograph of the same region. The scale bar in (b) and (c) is 5 μm.

ent conditions was performed in order to finalize the heterogeneous mixture of the system. The sample is further characterized via scanning electron-microscopy and EBSD for local variations in phase and orientation using a Helios UC G4 Dual Beam FIB-SEM. X-ray diffraction was performed using a Panalytical Empyrean XRD.

The post-annealed bulk $Y_2Si_2O_7$ specimen obtained is polycrystalline with microstructural features on the order of tens of micrometers. Representative X-ray diffraction (XRD) of the sample can be seen in Fig. 4.1(a), which shows that the sample is a multi-phase system consisting of γ and β phases of $Y_2Si_2O_7$ as well as Y_2SiO_5. Representative SEM and EBSD micrographs of select grains are shown in Figs. 4.1(b) and (c). The EBSD orientation image shows the varying orientations of grains present in Fig. 4.1(b). Both γ- and β-$Y_2Si_2O_7$ are present in this region, as shown via EBSD phase micrographs in Appendix B1. Because of the predominantly β phase $Y_2Si_2O_7$ in our EBSD maps, we choose to analyze anisotropic thermal conductivity solely in this phase. EBSD phase micrographs for all regions analyzed in this work can be found in Appendix B1. We further selectively examine areas via ESBD to verify crystalline orientations of various grains in different regions of the sample. Grains of interest can be seen in representative SEM and EBSD micrographs in Fig. 4.2. We note that various orientations of the disilicate are present, with grain sizes on the order of ∼5 μm. The lattice parameters of β-$Y_2Si_2O_7$ are a = 6.8691 Å, b = 8.960 Å, c = 4.7168 Å, and β = 101.73° [110]. In order to facilitate spatial thermal conductivity

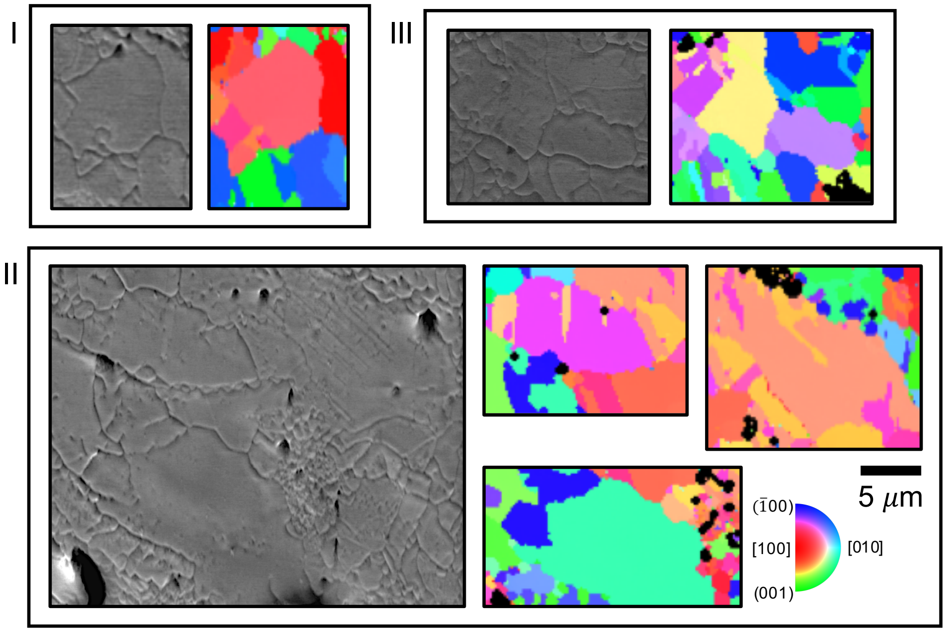

Figure 4.2. SEM and inverse pole figure (IPF) Z EBSD micrographs of the grains of interest. Regions are denoted by Roman numerals in the top left of each box. The IPF Z key demonstrates orientation of the grains in EBSD micrographs. Note that all EBSD micrographs contain grains with those of similar and different orientations.

mapping via time-domain thermoreflectance (TDTR), we deposit an aluminum transducer with a nominal thickness of 80 nm via electron-beam deposition.

TDTR and similar pump-probe metrologies are widely used and vetted in the literature [57, 111, 112], and is the technique that we use to characterize local variations in the thermal conductivity of β-$Y_2Si_2O_7$. In our experimental configuration, we spectrally separate the 808.5 nm output of a 80 MHz Ti:Sapphire oscillator into pump and probe paths. The pump path is electro-optically modulated at 8.4 MHz, and creates a frequency-dependent heating event at the sample surface coated with Al. The probe is mechanically delayed in time, and monitors the thermoreflectance at the sample surface. The cooling curve is compared to the radially symmetric heat diffusion equation to extract the thermal conductivity.

Typically, optical pump-probe techniques utilizing higher modulation frequencies are relatively insensitive to in-plane thermal conductivity compared to cross-plane conductivities [111]. At lower modulation frequencies, TDTR and frequency-domain thermoreflectance (FDTR) can gain increased sensitivities to anisotropy in the thermal conductivity tensor. Various methods have been proposed for measurements of this anisotropy, including beam-offset [68, 113, 114] and elliptic-beam techniques [115, 116]. While versatile, these methods are highly sensitive to the ellipticity of the beam and the repeatability of the measured FWHM of the cross-correlation of the pump and probe in beam-offset approaches [68]. Additionally, these methodologies generally require the use of a low thermal conductivity transducer, such as NbV, to enhance sensitivity to in-plane transport in the underlying material and reduce uncertainties in the extracted parameters. For elliptic-beam techniques, either the beam or specimen must be systematically rotated until the measurement axis is along the axis of interest, which introduces additional uncertainties into the beam size and/or specimen orientation. Further difficulties lie in the interpretation of EBSD in-plane orientations, which are necessary to extract in-plane thermal conductivities for offset and elliptic beam techniques. Precise knowledge of sample orientation relative to the EBSD data is required for accurate determination of in-plane thermal conductivity. Neither the measurement nor the post-processing associated with these measurements are trivial. This further demonstrates the power of extracting the cross-plane thermal conductivity for grains of a variety of orientations to extract the thermal conductivity tensor of a material system.

Using a typical thermal model for a two layer system (i.e., 80 nm Al transducer on a substrate), TDTR is capable of measuring both the thermal boundary conductance between the Al transducer and the underlying media, as well as the thermal conductivity of the media. An example cooling curve used to extract these two parameters for a select grain in Region II can be found in Appendix B1. To perform thermal conductivity mapping, however, the thermal boundary conductance should be adequately known, as the data from a single pump-probe delay time is used to extract the thermal conductivity of the underlying material. Numerous full TDTR scans are acquired across all regions of interest, allowing for the extraction of the thermal conductivity of the disilicate and the thermal boundary conductance between the Al transducer and the underlying material. At a modulation frequency of 8.4 MHz, we maintain one-dimensionality and are sensitive to primarily the cross-plane thermal conductivity and thermal boundary conductance, leaving any influence from in-plane transport to be negligible. We find that the thermal boundary conductance in regions I, II, and III are 43 ± 2, 56 ± 3, and 41 ± 3 MW m^{-2} K^{-1}, which reflect the measured conductance from multiple full TDTR scans in a given region. These values are then used in our sensitivity analysis for the determination of our pump-probe delay time for the mapping procedure, which is further discussed in Appendix B1. In our measurements, the RMS pump/probe radii is $\sim$1.6 μm, and is determined by fitting the spot size using a sapphire reference sample. We calculate uncertainties based on the work of Wei *et al.* [72], with errors of 2.5% in the pump/probe radii, 6% in the thermal conductivity of the Al transducer, 2.5% in the thickness of the Al transducer, 5% in the boundary conductance at the Al/disilicate interface, and 5% in the volumetric heat capacity of the disilicate. At this modulation frequency, we take into account an error in phase of 0.2 mrad. Uncertainty analysis for all grains analyzed in this work can be found in Appendix B1.

To facilitate thermal conductivity mapping of the specimen, we mount it on a 3-axis stage, with motors along the sample orientation having a bidirectional repeatability of $<$0.5 μm and a closed-loop piezo motor controlling the focal plane of the sample. We orient the stage in such a way such that movements along the sample surface result in no appreciable change in focus as indicated by the constant DC intensity of the probe beam. The pump/probe delay time is chosen, as previously discussed, such that we maximize our sensitivity to the thermal conductivity of the disilicate. Following, the sample is rastered over a region of interest to probe the thermal conductivity as a function of microstructural variation across the sample. Unless otherwise specified, the step size in the thermal conductivity micrographs is 0.25 μm.

The spatial resolution of the measurement is affected by a multitude of parameters beyond the 1/e^2 pump/probe radii. These include the modulation frequency of the pump, the thermal conductivity and thickness of the Al transducer, the thermal conductivity of the underlying disilicate, and the thermal conductance at the Al/disilicate interface. At the modulation frequency with which we perform our experiment (8.4 MHz), the in-plane thermal penetration depth, and thus the spatial resolution of the measurement, is greatly

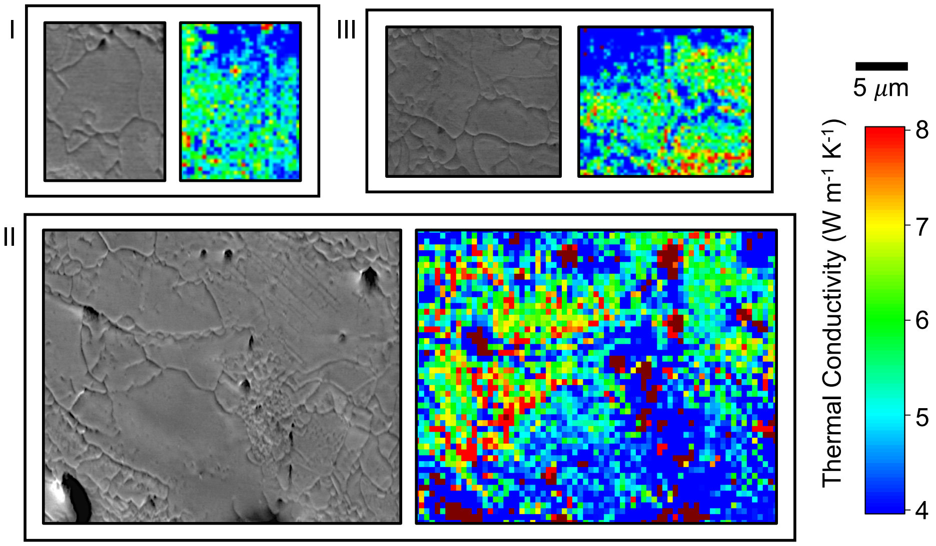

Figure 4.3. Thermal conductivity maps for each of the three regions examined. The step size in regions I and III is 0.25. μm, while that in region II is 0.5 μm. Maps with finer resolution of grains presented in Region II can be found in Appendix B1.

diminished as a result of the predominantly one-dimensional heating event. In general, an increase in transducer thickness and thermal conductivity will result in increased in-plane heat spreading, and extend the spatial resolution for a fixed modulation frequency. While the thermal penetration depth in the high-frequency limit (i.e., $\sqrt{\kappa/\pi C f}$) has often been used to estimate in-plane thermal penetration depths, this parameter must be numerically determined to account for geometrical considerations of the material system [72, 117]. The in- and cross-plane thermal penetration depths as a function of modulation frequency can be found in Appendix B1, where we show that the in-plane thermal penetration depth for a system of this geometry follows $\sim f^{-0.1}$ in the high-frequency limit. Based on the parameters of our system, we find that the in-plane thermal penetration depth, and thus the spatial resolution of our experiment, is $\sim$1.1 μm.

4.1.3 Results

Thermal conductivity micrographs of the three regions of interest are shown in Fig. 4.3. The thermal conductivity ranges from 5 to 7 W m^{-1} K^{-1} in the grains of interest.

Regions in which the probe beam is diffusely scattered create artifacts in our acquired signal, and therefore cannot be analyzed with confidence. To overcome these artifacts, we choose to only analyze regions in which the probe is highly reflective so that they do not erroneously impact our results. The specific details are discussed further in Appendix B1, along with reflectivity micrographs of the surface of each region. At these length scales, we do not expect a reduction in the thermal conductivity near grain boundaries to influence our results, as this is only to be expected in materials with mean free paths greater than our spot sizes, such as diamond [118]. Maps corresponding to the uncertainty in thermal conductivity can be found in Appendix B1, along with higher-resolution micrographs of Regions II.

The stereographic projection of the measured values with respect to the monoclinic system can be found in Fig. 4.4(a), where the dots represent the orientations of the grains analyzed for their thermal conductivity. The error in the measured thermal conductivity values is on the order of ∼20%, as an error of 2.5% in the spot size propagates into an error of ∼15% in thermal conductivity. The exact measured values and uncertainties for each grain are tabulated in Appendix B1. We further examine the thermal conductivity from a continuum approach, extracting the thermal conductivity tensor of the system.

The thermal conductivity tensor of a monoclinic system takes the form [119]

$$\widetilde{\mathbf{K}} = \begin{bmatrix} \kappa_{xx} & 0 & \kappa_{xz} \\ 0 & \kappa_{yy} & 0 \\ \kappa_{xz} & 0 & \kappa_{zz} \end{bmatrix},$$

where κ_{xx} and κ_{yy} are thermal conductivities measured along the [100] and [010] directions, respectively, and κ_{zz} is the thermal conductivity measured orthogonal to [100] and [010], β-90 degrees from the [001] direction, where β is the angle between the [100] and [001] directions. We will refer to the [100] and [010] directions as $\hat{x}$ and $\hat{y}$, respectively, and the orthogonal to the two as $\hat{z}$. One can explicitly derive the angular dependence of thermal conductivity of a monoclinic system on θ and ϕ:

$$\begin{aligned}\kappa(\theta,\phi) = \kappa_{xx}\sin^2\phi\cos^2\theta + \kappa_{yy}\sin^2\phi\sin^2\theta + \kappa_{zz}\cos^2\phi \\ +2\kappa_{xz}\sin\phi\cos\theta\cos\phi.\end{aligned} \tag{4.1}$$

In this equation, ϕ is the angle from the $\hat{z}$ direction, and θ is the angle from the $\hat{x}$ direction to the projection of the grain orientation onto the $\hat{x}$-$\hat{y}$ plane. The full derivation can be found in Appendix B1.

As the orientation of the grains are known from EBSD, a least-squares minimization of Eq. 4.1 allows us to recover the components of the thermal conductivity tensor. The thermal conductivity tensor of β-$Y_2Si_2O_7$ takes the final form

$$\widetilde{\mathbf{K}} = \begin{bmatrix} 7.2\pm1.7 & 0 & -0.2\pm0.1 \\ 0 & 5.3\pm1.4 & 0 \\ -0.2\pm0.1 & 0 & 5.3\pm1.6 \end{bmatrix} \text{W m}^{-1}\text{ K}^{-1},$$

where the uncertainties include the uncertainties in the measured parameters as well as the 95% confidence interval of the best fit to Eq. 4.1. It is important to note that the appearance of κ_{xz} is due to the deflection of the monoclinic from the Cartesian coordinate system, and that the determinant of the thermal conductivity tensor must be positive so as to be in congruence with the second law of thermodynamics. The negative thermal conductivity of κ_{xz} suggests that a temperature gradient imposed in the $\hat{x}$ direction would result in a heat flux in the -$\hat{z}$ direction, and vice versa. A rotation of π about the $\hat{z}$ direction results in a positive κ_{xz} component.

To better visualize the thermal conductivity tensor of this system as it relates to the structure, we plot these thermal conductivities as a stereographic projection of the crystal system, shown in Fig. 4.4(b). We note that the thermal conductivity along the [100] and [$\bar{1}$00] directions are identical in thermal conductivity due to the symmetry of the monoclinic system. We also find that the thermal conductivity along the [001] and [010] directions are both smaller in magnitude than the [100] direction. The minimum attainable thermal con-

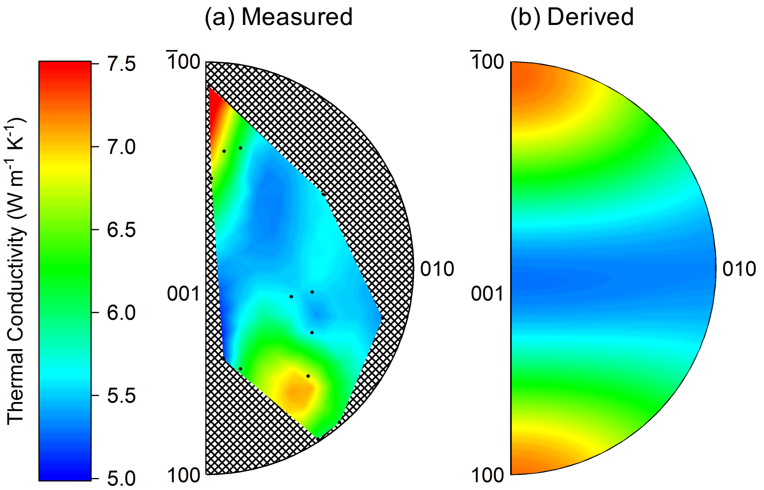

Figure 4.4. (a) The measured thermal conductivity from the three selected regions, plotted as a stereographic projection of the monoclinic crystal. The black data points represent measured data from each of the three regions. Hashed regions indicate orientations of grains that are not present in the three regions analyzed. (b) Thermal conductivity orientation map of β-$Y_2Si_2O_7$ based on the derived thermal conductivity tensor, represented as an inverse pole figure of the monoclinic structure.

ductivity occurs in the [010] direction. Overall, the directional-dependent thermal conductivity as represented in Fig. 4.4(b) is in good agreement with our measured data. Tabulated values from Eq. 4.1 using our extracted thermal conductivity tensor can be found in Table B2 of Appendix B1. In Figs. 4.5, we show the (a) thermal conductivity magnitude from Eq. 4.1 and (b) the representation ellipsoid defined by

$$1 = K_{ij} x_i x_j, \tag{4.2}$$

where x_i and x_j are the coordinates of the system. The radius of the thermal conductivity ellipsoid in Fig. 4.5(b) for a given coordinate pair is the inverse of the root of the thermal conductivity magnitude for that coordinate pair (i.e., $\kappa^{-1/2}$, where κ is the thermal conductivity for some x_i and x_j).

4.1.4 Discussion

From the kinetic theory of gasses, the phonon contribution to thermal conductivity can be approximated as $\kappa = \frac{1}{3}Cv^2\tau$ [120]. In this equation, C is the volumetric heat capacity, v is the group velocity of thermal carriers, and τ is the scattering rate. We take C to be identical for each of the crystalline orientations, which is reasonable because the volumetric heat capacity of a given system takes no directional dependence. If the directional-dependence to the thermal conductivity is dictated by the group velocity of the thermal carriers, then we should see variations in this parameter based on calculated velocities from the elastic constants of the system. Using elastic constants from the literature [121], the Christoffel equation can be solved for an arbitrary orientation in the system to extract the group velocities of longitudinal and transverse modes [122]. The Debye velocity, v_D, can then be calculated as

$$\frac{3}{v_D^2} = \frac{1}{v_l^2} + \frac{1}{v_{t,1}^2} + \frac{1}{v_{t,2}^2} \tag{4.3}$$

where v_l is the speed of the longitudinal mode, and $v_{t,1}$ and $v_{t,2}$ are the speeds of the two transverse modes. We find v_D to be ~5500, ~4400, and ~5300 m/s along the [100], [010], and [001] directions, respectively. Steps to solve the Christoffel equation can be found in Appendix B1. Between the [010] and [100] directions, good agreement is found in trend

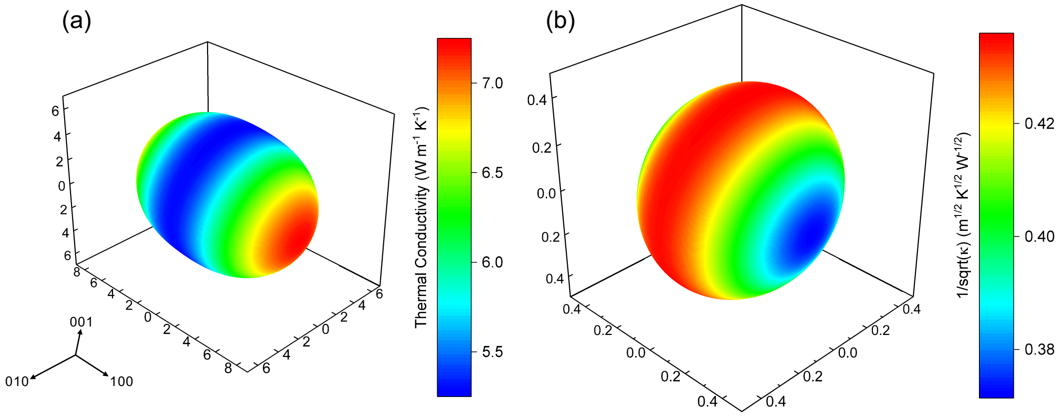

Figure 4.5. Representation quadrics of the (a) thermal conductivity magnitude and (b) thermal conductivity ellipsoid of β-$Y_2Si_2O_7$.

between the calculated Debye velocities and thermal conductivity, whereby an increase in the thermal conductivity is observed for increasing v_D. However, the thermal conductivity along the [010] and [001] directions are identical despite having different carrier velocities along these directions. Thus, we attribute the observed changes in thermal conductivity to the scattering rate, τ, arising from the differing atomic environments along these crystalline directions. We present a visual representation of these differing crystalline orientations in Appendix B1.

Very few works in the literature have experimentally examined the anisotropic thermal conductivity of β-$Y_2Si_2O_7$. Zhou *et al.* [123] and Tian *et al.* [121] both presented experimental measurements of thermal diffusivity via the laser-flash method. In both previous works, heat capacity was confirmed independently, either by differential scanning calorimetry (DSC) or by employing the Neumann-Kopp rule as an approximation based on the constituents of the system. Regardless, both previous works describe the thermal conductivity of a bulk system, where microstructural effects and anisotropy are averaged to determine a single thermal conductivity. Furthermore, Tian *et al.* [121] have determined the anisotropic minimum thermal conductivity based on the Debye approximation in the high-temperature limit, showing a two-fold change in thermal conductivity based on crystalline orientation. The representation quadric of the thermal conductivity determined in our work is inconsistent with that obtained in Ref. 121. They determine the directional dependence of the thermal conductivity from the anisotropic velocity as obtained from the anisotropic Young's modulus. However, this directional dependence is derived from the fourth-rank elasticity tensor, in which four extrema are possible for a given plane and the interpretation of the thermal conductivity in this manner is inconsistent with the second-rank nature of the thermal conductivity tensor, in which just two extrema are possible for a given plane, the values of which reflect the eigenvalues to the in-plane thermal conductivity tensor for that plane.

Our values are higher than those found in the literature for room temperature measurements; however, we can attribute the differences in our results to the measurement technique. For polycrystalline samples measured via laser flash, an average thermal conductivity of all crystalline directions and polymorphs is determined. One can define an effective thermal conductivity related to the determinant of the tensor determined as $\kappa_{\text{eff}} = \sqrt[3]{\det(\widetilde{\mathbf{K}})}$, where the cube root arises due to the dimensionality of the system. For our results, we find that κ_{eff} = 5.9 ± 1.1 W m^{-1} K^{-1}, which one would expect to recover in the event that the measurement technique is sensitive to all components of the thermal conductivity tensor, or in the limit that the measurement spot size in TDTR is much larger than the mean grain size in a non-textured, polycrystalline β-$Y_2Si_2O_7$ sample and the extracted parameter is not influenced via the inclusion of grain boundaries or other extrinsic effects. Our results are the first to report on spatially measuring thermal conductivity via TDTR to reproduce the thermal conductivity tensor of an anisotropic material system, specifically that of β-$Y_2Si_2O_7$.

Based on the similarity of the elastic constants of β-$Y_2Si_2O_7$ to other monoclinic disilicates used in the coatings community (Yb, Lu), we can expect similar trends in thermal conductivity based on these elastic constants. Ultimately, this suggests the need to better understand texturing techniques along directions of low thermal conductivity, which may allow for tailoring heat flow in order to enhance the performance of gas turbine engines. Anisotropic thermal conductivities in these material systems can provide several key advantages in bettering these efficiencies. Beyond creating a larger temperature gradient between hot engine gasses and the underlying turbine blade, improved lateral heat flow along the surface of the coating will allow for more convective cooling near the surface. Indeed, numerical simulations have shown the potential for hot spot generation on gas turbine blades, and these findings offer a mitigation strategy toward solving this problem [88].

In summary, we fabricated polycrystalline $Y_2Si_2O_7$ that contains various polymorphs of the disilicate. Conventional methods of determining the thermal conductivity of these materials rely on bulk sample measurements, which do not yield insight into the microstructurally dependent thermal conductivity of individual grains, instead averaging the thermal conductivity of the entire system. We show that TDTR is capable of spatially separating thermal conductivities in grains on the order of ∼5 μm. This allows us to verify anisotropy in the thermal conductivity of the β-$Y_2Si_2O_7$ based on EBSD-correlated grain orientation, ultimately providing us with the ability to calculate the thermal conductivity tensor of the system. In all, this work demonstrates the power of laser-based transient techniques for the determination of thermal conductivity for samples in which variations in thermal conductivity at the microstructural level are present in the material system.

4.2 Spatiotemporal Thermal Conductivity Evolution of Steam Cycled Ytterbium Silicate/Silicon Environmental Barrier Coatings

The work presented in this section has previously been published in *Materials Today Physics* [124], and is at the intersection of materials science and thermal characterization for multifunctional coating systems. The section sought contributions from the *ExSiTE Lab*, *Opila Research Group*, and *Wadley Research Group*. Jeroen Deijkers and Bradley Richards of the *Wadley Research Group* facilitated in the fabrication and cycling of the coated specimens, as well as characterization via scanning electron microscopy. From the *ExSiTE Lab*, Kathleen Quiambao-Tomko performed the necessary electron-backscatter diffraction characterization, while John Gaskins aided in thermal conductivity measurements as well as their interpretation. Experimental and theoretical guidance were provided by Elizabeth Opila, Patrick Hopkins, and Haydn Wadley.

4.2.1 Background

Silicon carbide based ceramic matrix composites (SiC CMCs) are beginning to be implemented in the hottest section of advanced gas turbine engines where their surface is exposed to hot (∼1500 °C), high pressure combustion gas flow [98]. In these environments, the SiC surface reacts with both residual oxygen and water vapor to simultaneously form a silica thermally grown oxide (TGO) layer which is also volatilized by reactions with the steam to form gaseous silicon hydroxide species such as $Si(OH)_4$ [93, 94]. These reactions lead to loss of the SiC at rates of up to several micrometers per hour, sufficient to greatly reduce the useful life of the component [94, 125]. This problem is presently addressed by the deposition of an environmental barrier coating (EBC) to the surface of the CMC exposed to the gas flow. The primary function of an EBC is to avoid oxidation and volatilization of the SiC component but, if made from materials with low thermal conductivity, can also function as a thermal and environmental barrier coating (T-EBC) that reduces the maximum temperature of the underlying composite. Characterization of the thermal transport behavior of T-EBC systems is therefore an area of considerable current interest.

State-of-the-art EBC systems utilize a silicon bond coat with a low silica activity, rare-earth disilicate top coat [23, 95, 105, 141]. In the absence of a Si bond coat, SiC will form gaseous oxidation products, such as gaseous CO, which will introduce interfacial porosity and ultimately result in coating spallation. Thus, the primary function of the Si bond coat is to prevent oxidation of the SiC by preferentially forming a SiO_2 TGO on its exterior surface [98], as the very low oxygen activity at the interior silicon-SiO_2 interface greatly reduces the oxidizer flux that reaches the SiC surface. The coefficient of thermal expansion (CTE) of the bond coat, 4×10^{-6} °C^{-1}, is similar to that of the SiC composite, 4–5×10^{-6} °C^{-1}, and thus reduces the driving force for delamination arising from mismatch in thermal strain between the CMC and bond coat during thermal cycling. Unfortunately, the TGO layer of the bond coat crystallizes at elevated temperatures to form β-cristobalite. On cooling through $\sim$240–270 °C, it transforms to the α-phase with a 4–7% reduction in volume [90–92, 142]. The large elastic strain created by this transformation then creates a driving force for delamination at the Si-TGO interface that increases with TGO thickness [95].

The rare-earth silicate top coat serves multiple purposes. It reduces the oxidizer flux that permeates to the bond coat, thereby reducing the rate of SiO_2 scale formation and consumption of the bond coat [143]. In addition to a high resistance to the permeation of

Material	Crystal Structure	κ (W m^{-1} K^{-1})	CTE (10^{-6} K^{-1})	Steam Volatility Resistance
β-$Yb_2Si_2O_7$	Monoclinic	4.5–5.0 [121, 126]	3.6–4.5 [127–129]	moderate [16]
Yb_2SiO_5	Monoclinic	2.5–3.0 [105]	2.7–10.5 [18, 105, 127, 130–132]	high [16]
APS Si Powder	Cubic	10–20 [133][a]	2.5-4.5 [16, 134]	low [135]
SiC	Hexagonal	10–73 [136–138]	3–5.5 [16, 127, 139]	low [140]

Table 4.1. Crystal structure, room temperature thermal conductivity (κ), coefficient of thermal expansion (CTE), and steam volatility resistance for β-$Yb_2Si_2O_7$, Yb_2SiO_5, APS Si, and SiC/SiC CMCs from the literature.

[a] Atmospheric plasma spray powders.

oxidizing species, this exterior layer must have a low steam volatility since its outer surface is in contact with the combustion gas flow [144, 145]. To reduce the risk of coating failure by thermomechanical mechanisms, the rare earth silicate CTE needs to be well matched to the Si-SiC composite on which it is attached.

Top coats with a low thermal conductivity are preferred since they are then able to decrease the temperature of the Si bond coat to prevent melting and reduce the rate of thermally-activated TGO thickening. The low thermal conductivity also helps to reduce the temperature of the SiC CMC, whose strength is reduced as the temperature approaches 1500 °C [20, 21, 105]. Ytterbium disilicate (β-phase $Yb_2Si_2O_7$; YbDS) is widely used and such a Si-YbDS system, schematically illustrated in Fig. 4.6, has exhibited good thermomechanical stability and resistance to volatilization for up to 2000 hours of steam cycling between 110 and 1316 °C [95]. The CTE match to SiC and moderately low thermal conductivity of 5–7 W m^{-1} K^{-1} at room temperature make it a strong candidate for top coats in a T-EBC system.

YbDS top coats are applied using atmospheric plasma spray (APS) deposition of nominally pure YbDS powders [95]. However, a second ytterbium monosilicate (Yb_2SiO_5; YbMS) phase is usually present either from contamination of the powder or by loss of SiO_2 during the thermal spray process [146]. As a result, the ytterbium silicate top coat typically consists of a two-phase system with 10–15% YbMS as elongated solidified droplets in a YbDS matrix [97]. This has significant implications on the operating performance of the coating as the thermal conductivity, CTE, and steam volatility resistance of the two phases are very different, shown in Table 4.1. On one hand, a coating consisting entirely of the YbDS phase has been thought to be preferable since its CTE is well matched with the α-SiC substrate. However, the steam volatility resistance of YbMS is much greater than that of YbDS alone [16, 147, 148]. In practice, the presence of some YbMS in YbDS coatings appears unavoidable, the effective thermo-physical properties of the coating are then determined by the volume fractions and dispersion (i.e., microstructure) of the two phases. In addition, as the EBC is thermally cycled in steam, SiO_2 loss from the YbDS transforms the outer surface to more slowly volatilized YbMS [95].

From a CMC thermal protection perspective, low thermal conductivity ($\sim$2.5 W m^{-1} K^{-1} at room temperature) YbMS offers a higher thermal resistance compared to YbDS ($\sim$5–7 W m^{-1} K^{-1}) at room temperature [105, 121, 126, 149]. Considerations, however, have not been made for the anisotropic nature of these materials. We have previously determined the anisotropic thermal conductivity tensor of β-$Y_2Si_2O_7$ [86], and expect YbDS to have similar anisotropy based on its similarity in elastic constants [121]. At the atomic scale, Zhou *et al.* [126] and Xiang *et al.* [149] have argued that the thermal conductivities of YbMS and YbDS can be attributed to the heterogenous bonding environment of the crystal, where weak Yb-O bonding results in low sound velocities and Debye temperatures and, ultimately, low thermal conductivity. Indeed, the sound velocity and Debye temperature are smaller in YbMS compared to YbDS, despite YbMS possessing a higher atomic density [126, 149]. At the microscopic scale, additional scattering of phonons occurs at grain boundaries, a mechanism that has been shown to reduce the thermal conductivity of materials relative to their bulk counterparts [150, 151].

In addition, due to the anisotropic CTE of YbMS [132] and YbDS [126, 128], it is generally thought that the small grain size formed during the thermal spray deposition process is preferable so that large variations in CTE anisotropy at the microscopic scale are averaged out. This results in a reduction of local strain and a reduced chance of coating cracks. However, small YbDS grain size provides a fast transport path for molecular oxygen and hydroxyl group diffusion to the bond coat, and is therefore not desirable for slowing the rate of TGO growth [152]. In practice, during the high temperature use of an EBC, retention of the small grain size is unlikely, and the microstructure of the system dynamically evolves. An understanding of the microstructural evolution of a thermally cycled ytterbium silicate coating and its influence on the associated thermal profile would be helpful during the design of coatings for the hot sections of a gas turbine engine. To design coatings with a reliable use life, an understanding of the dynamic behavior of the EBC phase fractions and microstructure during its use in high temperature, oxygen and steam cyclic conditions, and implications for thermophysical properties, is therefore needed.

Here, we characterize the evolution of the phase fractions and microstructure of a model APS deposited Si-YbDS EBC and measure the thermal conductivity distribution of the EBC system subjected to varying periods of thermal cycling in a flowing oxygen/steam environment. This is accomplished by combining scanning electron microscopy techniques with spatially resolved time-domain thermoreflectance (TDTR) thermal conductivity measurements. We characterize these structural and thermal property variations in the as-deposited material state, after stabilization annealing, and periodically during thermal cycling between 110 and 1316 °C for up to 2000 1-hour cycles in a flowing steam-oxygen environment. In addition to the anticipated phase fraction and microstructure evolutions, we have also observed a disappearance of the YbMS phase near the TGO, consistent with the solid state reaction of silica from the TGO with YbMS to form YbDS.

4.2.2 Materials & Methods

Coating layers were deposited on 25.4 mm x 12.7 mm x 4.8 mm α-SiC substrates (Chand Associates, Inc., Plymouth, MA). The edges of the SiC substrates were chamfered at 45° to allow for over-spraying of the edges, reducing the risk of coating delamination. The SiC surface was conditioned using a light grit blast, followed by an ultrasonic clean in ethanol prior to the deposition procedure. The Si/YbDS EBC system was deposited using an atmospheric plasma spray (APS) system located in a spray cell equipped with exhaust and particle trap systems, described in Ref. 153. This system used Praxair-TAFA Model SG-100 torch with a Model 02083-175 anode configuration and was attached to a six-axis robot whose pattern of translation was preprogrammed and remotely controlled from outside the spray cell. Additional details regarding the APS deposition process can be found in Appendix B2.

We use TDTR to locally probe variations in the thermal conductivity of the YbDS EBC. An 80 MHz Ti:Sapphire oscillator centered at 808.5 nm is energetically split into pump and probe paths. The pump is electro-optically modulated at 8.4 MHz, and creates a frequency-dependent heating event at the sample surface. In a conventional TDTR measurement, the probe is mechanically delayed in time, monitoring the thermoreflectance at the sample surface following the pump heating event. The data are fit to the radially-symmetric heat diffusion equation to extract thermal parameters of interest, namely the thermal conductivity of the underlying EBC. To expedite this process, and spatially monitor the thermal conductivity, we fix the delay time and raster the sample over the region of interest. The delay time is chosen such that changes in the acquired signals are reflective of changes in the thermal conductivity of the underlying EBC, not the resistance associated with the Al/EBC interfacial region. The specific delay times for each of the specimens examined in this work are further discussed in Appendix B2. The effective pump/probe $1/e^2$ radii of 5 μm provides sufficient resolution to delineate between the ytterbium mono- and disilicate phases present in the EBC system. For finer resolution micrographs, the effective pump/probe $1/e^2$ radii is 1.4 μm. In regions where microstructural and phase features are smaller than the effective pump/probe radii, TDTR measures a volume-averaged thermal conductivity, which includes the influence of grain boundaries, nanoporosity, and any residual stresses that may be present in the coating structure. Several works in the literature outline the methodology and analysis associated with TDTR [57, 112], as well as the extension of the technique to spatially understanding variations in thermal properties [154–157].

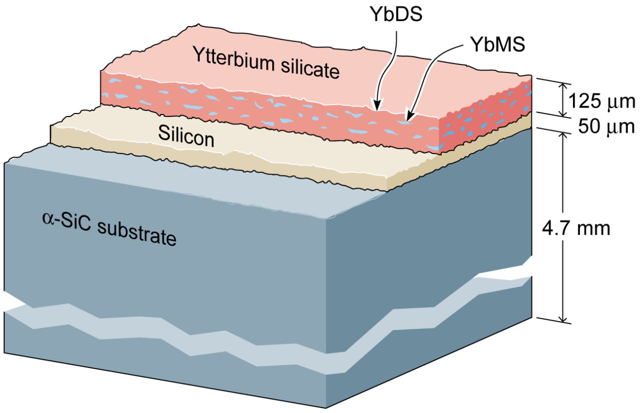

Figure 4.6. Schematic illustration of a Si-ytterbium silicate EBC system applied to an α-SiC substrate. The ytterbium silicate top coat consists of ytterbium disilicate (YbDS) and ytterbium monosilicate (YbMS).

SEM BSE micrographs were acquired using a Helios UC G4 Dual-Beam FIB-SEM at an accelerating voltage of 20 kV. We use the focused ion beam (FIB) to etch trenches approximately 100 μm apart through the coating to be able to better identify those regions when performing TDTR measurements. Electron backscatter diffraction (EBSD) micrographs were procured using a FEI Quanta 650 Field-Emission SEM in high-vacuum using a specimen pre-tilt of 70°. The typical step size for EBSD micrographs was 0.25 μm.

The EBC system consisted of an $\sim$125 μm thick, predominantly YbDS top coat and an $\sim$50 μm Si bond coat deposited by APS on an α-SiC substrate, see Fig. 4.6. Specimens were stabilization annealed at 1250 °C for 24 hours before being subjected to thermal cycling in a 90 vol% H_2O/10 vol% O_2 gas environment at a pressure of one atmosphere for 500 and 2000 cycles. Each cycle consisted of a 60-minute hold at 1316 °C followed by cooling to $\sim$110 °C for 10 minutes. The gas flow rate was 4.4 cm/s. We removed specimens after 500 and 2000 cycles, yielding three total samples including the stabilization annealed specimen. All specimens were cross-sectioned, polished, and coated with a nominal 80 nm Al transducer to facilitate thermal conductivity measurements in the plane of the coating via TDTR, as discussed in the Methods section.

4.2.3 Results

Figure 4.7 shows cross-section SEM images taken in backscattered electron (BSE) imaging mode so that pixels of lighter contrast correspond to regions with a higher concentration of high atomic number elements such as Yb. Thermal conductivity micrographs of the same regions acquired using TDTR are also shown in Fig. 4.7. See Appendix B2 for SEM BSE and thermal conductivity micrographs of the as-deposited specimen. Also shown in Fig. 4.7 are the thermal conductivity and phase profiles for each specimen, where black and red lines represent the YbMS and YbDS volume fractions, respectively, while the blue band is representative of the range of thermal conductivities measured in the same region.

In the following three subsections, we discuss the phase, thermal conductivity, and

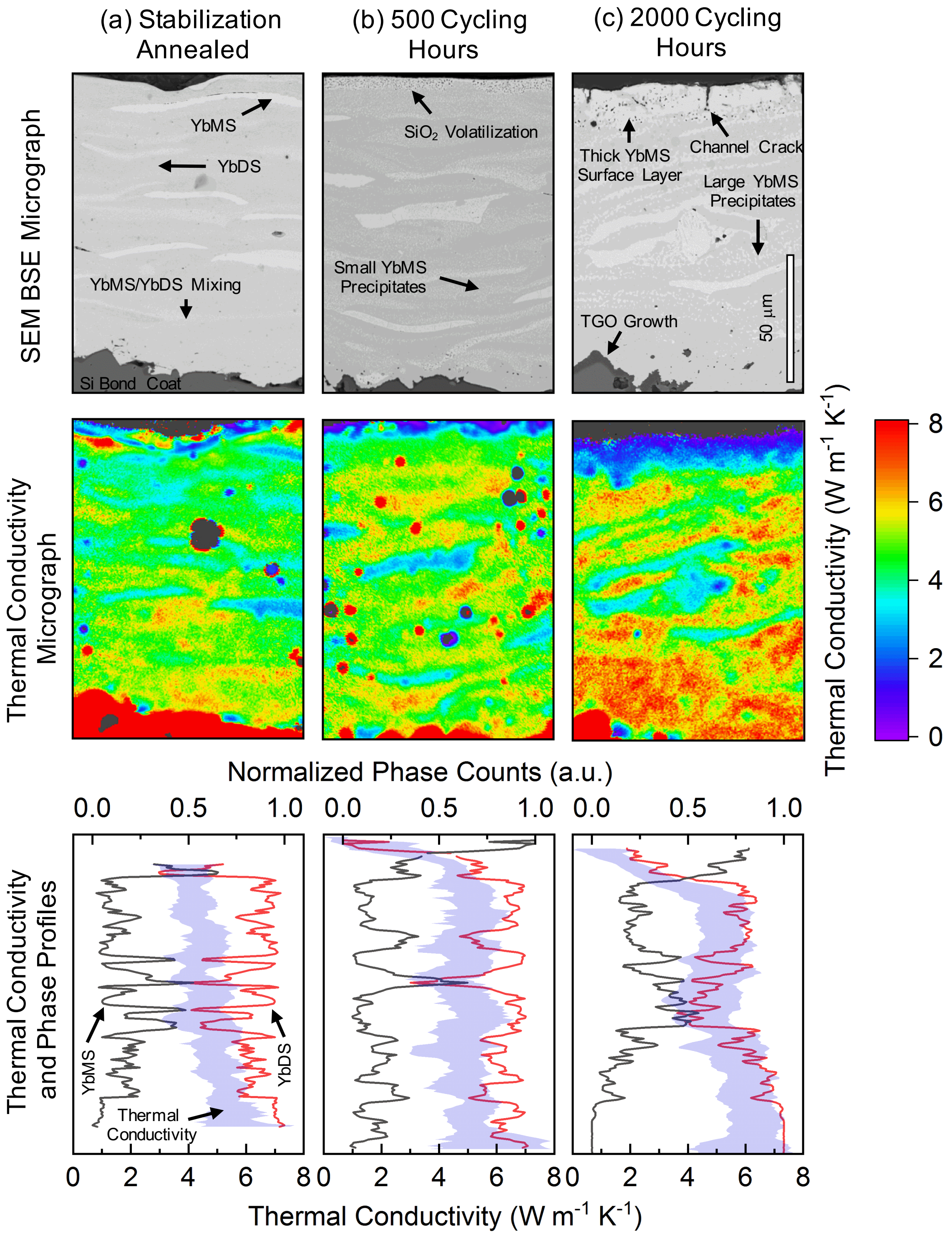

Figure 4.7. Cross-section back-scattered electron (BSE) micrographs, thermal conductivity micrographs, and normalized phase counts and depth-dependent thermal conductivity for the (a) stabilization-annealed specimen and specimens cycled for (b) 500 and (c) 2000 hours in a steam environment. The red and black lines correspond to the darker/lighter area fractions in micrographs corresponding to the YbDS and YbMS phases, respectively, while the blue band corresponds to the range of thermal conductivity measured as a function of depth.

microstructural profiles of the coatings as they evolve in time, where the observed trends in phase and thermal conductivity are summarized in Table 4.2 for reference.

Phase

The presence and spatial distribution of YbMS regions within the predominantly YbDS coating can clearly be observed in the BSE SEM micrographs of Fig. 4.7 as areas with lighter contrast. This phase distribution is also confirmed via EBSD phase micrographs, see Appendix B2. The YbMS/YbDS phase fraction in the stabilization specimen was approximately uniform throughout the coating, see Table 4.2. Splats in this specimen were composed of either YbMS, YbDS, or some fraction of the two. Trace amounts of Yb_2O_3 have also been reported to be present in the coating [153]. Many of the splats have a curved, thin plate morphology–a structure that is consistent with the impact of liquid droplets with the rough coating surface during the APS deposition process.

During steam cycling, the SEM images reveal the development of a surface region with substantially reduced YbDS. This resulted from differential steam volatilization rates for the YbDS and YbMS phases in the coating. Costa and Jacobsen [147] have shown that mixtures of $Yb_2O_3 + Yb_2SiO_5$ have a lower silica activity than $Yb_2Si_2O_7 + Yb_2SiO_5$ mixtures. As a result, during the reaction of water vapor with these silica rich compounds in which $SiO_2 + H_2O \rightleftharpoons Si(OH)_4$, silica loss at 1316 °C is approximately 100-fold higher from the YbDS compared to YbMS under equilibrium conditions. The loss of SiO_2 from the YbDS phase is accompanied by a partially constrained $\sim$26 % volume reduction [95], resulting in a porous silica depleted YbMS reaction product layer. The combination of underlying YbDS constrained lateral shrinkage during the reaction and the higher CTE of the reaction product results in channel cracking and local reaction product delamination upon cooling, reducing its subsequent utility for resisting inward permeation of oxidizers towards the bond coat [95].

After 500 hours of steam cycling, the outer YbDS surface region shows evidence of this volatilization, resulting in the formation of a thin ($\sim$5 μm thick) YbMS layer at the steam-

Cycling Hours		YbDS Fraction	YbMS Fraction	κ (W m^{-1} K^{-1})
0				
	Top	0.74	0.26	4.0 ± 0.7
	Middle	0.80	0.20	4.8 ± 0.9
	Bottom	0.90	0.10	5.3 ± 0.9
500				
	Top	0.33	0.67	2.6 ± 0.8
	Middle	0.81	0.19	4.9 ± 0.9
	Bottom	0.87	0.13	5.4 ± 1.1
2000				
	Top	0.30	0.70	1.8 ± 0.6
	Middle	0.75	0.25	5.2 ± 1.0
	Bottom	0.99	0.01	6.2 ± 1.1

Table 4.2. Summary of dynamic and spatially varying phase and thermal conductivity (κ) distributions of cycled specimens at the top, middle, and bottom of the coating. The top region is considered to be within ~10 μm from the surface of the coating, while the bottom is considered to be within ~15 μm from the Si bond coat. The middle region excludes the top and bottom regions.

exposed surface of the coating. Not only does this result in a porous YbMS layer, the YbMS fraction rose from ~25 to ~67% within 10 μm of the coating surface. The remainder of the coating matrix was predominantly a YbDS matrix containing a fine distribution of YbMS particulates. The average YbMS fraction was ~20% but could vary significantly from 0 to 50% from one splat to another, see Table 4.2.

The specimen cycled for 2000 hours, Fig. 4.7(c), shows the presence of a 10–15 μm thick steam volatilized region near the outer surface of the coating. This layer was both porous and had suffered channel cracking. Its YbMS phase fraction, as indicated by the profile in Fig. 4.7(c), indicated the YbMS volume fraction was on average ~70% within 10 μm of the coating surface. The YbDS volume fraction in the bulk of the coating was similar to the stabilization annealed specimen as well as the specimen cycled for 500 hours, at ~75%. Within 15 μm of the TGO, however, this volume fraction increased to 99%, and a lack of YbMS present is confirmed via Raman spectroscopy (see Appendix B2).

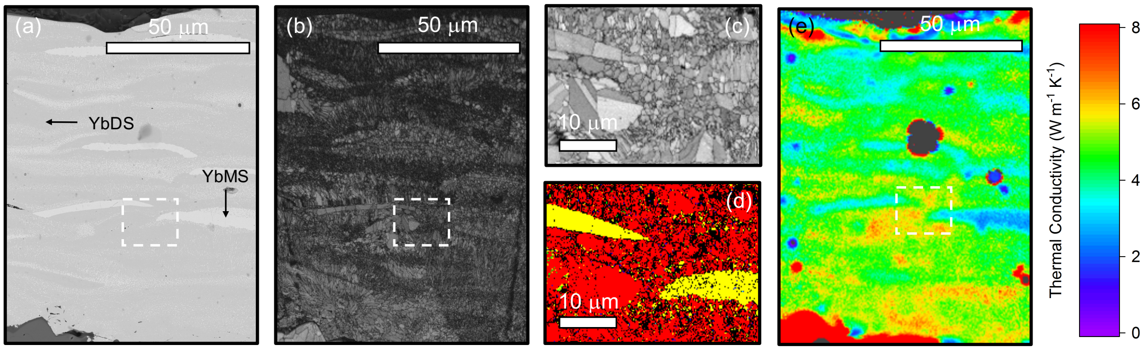

Figure 4.8. (a) SEM BSE and (b) EBSD band contrast micrographs of the stabilization annealed specimen. (c) High-resolution EBSD band and (d) phase contrast micrographs from the region outlined in (a) and (b). In (d), red and yellow regions are representative of YbDS and YbMS, respectively. (e) Thermal conductivity micrograph of the region shown in (a).

Microstructure

EBSD band and phase contrast micrographs of the stabilization annealed specimen are shown in Fig. 4.8. Figure 4.8(a) shows the SEM BSE micrograph together with a thermal conductivity map from Fig. 4.7(a) for reference.This micrograph shows a wide variation in gray scale of the individual splats that had solidified to form the coating. Splats of darker and lighter contrast consisted of almost pure YbDs and YbMS, respectively. This is also confirmed via EBSD phase contrast micrographs, see Appendix B2.

The stabilization annealing process is intended to fully crystallize the as-deposited coating and transform metastable phases which are often present after thermal spray deposition [95]. EBSD micrographs of the as deposited specimen can be found in Appendix B2, and indicate an amorphous/nanocrystalline matrix with the occasional large YbDS crystallite.

Inspection of the EBSD data in Fig. 4.8(b) indicates that the average grain size within the stabilized YbDS rich regions was very small ($< 2\ \mu$m). High resolution band and phase micrographs are shown in Figs. 4.8(c) and (d), respectively, and indicate that in YbDS rich regions the grain size was ~100 nm, conducive to grain boundary transport of oxidizing species to the bond coat [152]. However, in splats composed of almost pure YbMS, such as those entering the upper left of the dotted white box in Fig. 4.8(b), the grains were much larger and of comparable size to the width of the splat (1–5 μm). The grain size that

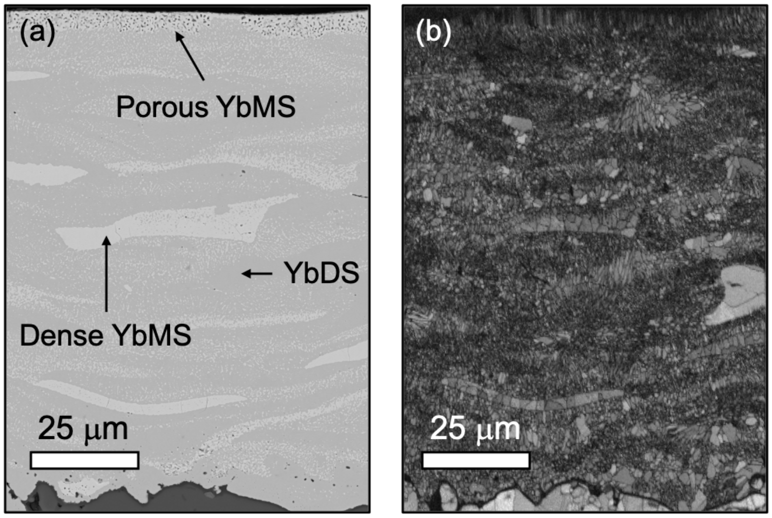

Figure 4.9. (a) BSE and (b) EBSD band contrast micrographs of the specimen after cycling for 500 hours in a steam environment.

results from a directional solidification process like that encountered in APS deposition is influenced by the cooling rate, and by the thermal and compositional gradients in the melt, with the latter dependent on the diffusivity of the silica and ytterbia in the melt. However, a rationalization of these differences must await future assessments of the solidification processes. Grain size distributions for YbMS and YbDS can be found in Appendix B2 for the stabilization annealed specimen.

YbMS and YbDS grain size distributions for the specimen cycled for 500 hours can be found in Appendix B2. Figure 4.9 shows the (a) BSE micrograph and (b) EBSD band contrast micrograph of the system subjected to 500 steam cycles. Near the surface of the coating, where the YbMS phase counts dominated the first $\sim$10 μm, the grain size was relatively small, $<$ 500 nm. This was similar to the grain size within fine YbMS particulates interspersed throughout the YbDS matrix. Regions of pure YbMS had larger grain sizes, approaching $\sim$4–5 μm in some cases. The YbDS matrix had an average grain size of $\sim$1 μm. Near the Si bond coat, grain coarsening of YbDS was observed, resulting in a grain size of $\sim$5 μm in the region depleted of YbMS. The TGO thickness of $\sim$500 nm remained similar to the stabilization annealed sample, consistent with the delayed permeation of oxidizing species to the bond coat surface.

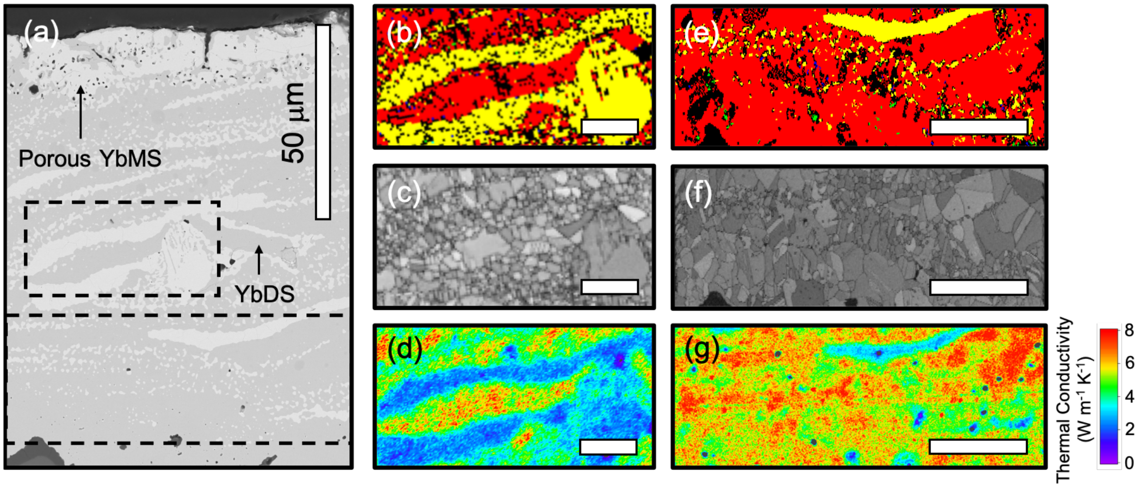

Figure 4.10. (a) SEM BSE micrograph of coating cycled for 2000 hours. High resolution (b) phase contrast, (c) band contrast, and (d) thermal conductivity micrographs of region outlined in the middle of (a). High resolution (e) phase contrast, (f) band contrast, and (g) thermal conductivity micrograph of region outlined at bottom of (a). In the EBSD phase contrast micrographs, red and yellow regions are representative of YbDS and YbMS, respectively, while trace amounts of α-cristobalite can also be observed as green. In (b)-(d) and (e)-(g), the scale bars are 5 and 25 μm, respectively.

EBSD characterization of the specimen cycled for 2000 hours is shown in Fig. 4.10, which shows (a,c,f) EBSD band and (b,e) phase micrographs of the same region as that found in Fig. 4.7(c). See Appendix B2 for band contrast micrograph of Fig. 4.10(a), which shows mean grain sizes increasing from ~500 nm after 500 cycling hours to ~2–3 μm in the volatilized region. In Fig. 4.10(c), near the center of the coating, the mean grain size of the YbMS and YbDS are $\leq$1 μm for the majority of the grains present in the region. Regions in which the YbMS fraction was larger exhibited larger grain sizes, on the order of ~5 μm, consistent with the coarsening mechanisms of two-phase systems [158, 159]. Towards the bottom of the coating, in Fig. 4.10(f), grains of the YbDS phase are much larger in size, on the order of 5–10 μm. While YbMS precipitates are present in this region, they are much smaller than in the rest of the coating and their phase fraction relative to YbDS decreases significantly closer to the bond coat, see Table 4.2.

Thermal Conductivity

Prior to cycling, the stabilization annealed specimen exhibits a spatially varying thermal conductivity dependent on the local YbMS/YbDS phase fraction, see Fig. 4.7(a). In regions consisting of primarily YbMS, the thermal conductivity is $\sim$2 W m^{-1} K^{-1}, whereas in those composed of YbDS, the thermal conductivity is closer to $\sim$6 W m^{-1} K^{-1}. Because TDTR measures a spatially averaged thermal conductivity, regions in which finer YbMS and YbDS features are present tend to result in a composite thermal conductivity of 4-5 W m^{-1} K^{-1}. Interestingly, we see a progressive increase in thermal conductivity from the surface of the coating to the bond coat, as indicated by the profile outlined in Fig. 4.7(a).

The grain sizes for YbDS and YbMS, in general, are larger near the Si bond coat compared to the surface of the stabilization annealed coating. Various previous works have indicated a reduction in thermal conductivity with a decrease in the mean grain size of a material system [71, 150, 151, 160]. This appears to be consistent with our observations between the EBSD band contrast and thermal conductivity micrographs. Indeed, the small grain sizes near the top of the coating are associated with a lower thermal conductivity, while the relatively coarser grains near the Si bond coat are correlated with a higher thermal conductivity. This is graphically represented by the thermal conductivity profile in Fig. 4.7(a), where the thermal conductivity of the coating increases progressively from $\sim$4 W m^{-1} K^{-1} to $\sim$6 W m^{-1} K^{-1} from top to bottom of the coating. However, we cannot solely attribute the observed trends in thermal conductivity to a difference in grain size. Indeed, since the laser spot size used in our TDTR measurements is large compared to the characteristic grain size, and thus inherently samples over the multi-phase system with large grain and phase boundary densities.

The volatilization of silica from YbDS to form a porous YbMS layer at the surface of the coating, Fig. 4.7(b) and 4.7(c), is correlated with a lower thermal conductivity ($\sim$2 W m^{-1} K^{-1}) region near the exterior surface of the coating. We note that the presence of porosity as well as the low thermal conductivity of the YbMS phase (2–3 W m^{-1} K^{-1} evident in the interior of the coating) will have contributed to the measured value [161–

163]. The lower thermal conductivity of this partially volatilized region, in practice, aids in increasing the temperature gradient between hot gasses in the combustion environment and the turbine blade.

The thermal conductivity of the part of the coatings that had not been steam volatilized also evolved during thermal exposure. When cycled for 500 or 2000 hours, the average thermal conductivity of the central region of the coating increased slightly compared to the stabilization annealed specimen to $\sim$5 W m^{-1} K^{-1}. These increases were much greater near the Si bond coat, from $\sim$5 W m^{-1} K^{-1} after the stabilization anneal and cycling for 500 hours to $\sim$6 W m^{-1} K^{-1} after cycling for 2000 hours. The thickness of this higher conductivity region also increased with cycling time, consistent with a loss of the low thermal conductivity YbMS phase.

To further investigate the loss of this phase, we utilize EBSD to monitor phase and microstructural changes as they relate to the thermal conductivity of the coating following cycling. High resolution thermal conductivity micrographs of regions presented in Figs. 4.10(c) and (f) can be found in Figs. 4.10(d) and (g), respectively. In Fig. 4.10(d), the thermal conductivity is approximately equivalent in regions composed entirely of YbMS, even when the grain size approaches 5 μm as on the right of Fig. 4.10(d). This is in contrast to what was observed in the stabilization annealed specimen, where we observed a progressive increase in the thermal conductivity of the coating from the surface to the bond coat, see Fig. 4.7(a). However, we note that the grain sizes in the stabilization annealed specimen near the surface were on the order of $\sim$100 nm, while those in the specimen cycled for 2000 hours are on the order of $\sim$1 μm. The grain boundary density, thus, is much smaller in the cycled specimen, and our measurement will then average over fewer grain boundaries that could potentially reduce our measured thermal conductivity. In Fig. 4.10(g), near the Si bond coat, a relatively high thermal conductivity (5-6 W m^{-1} K^{-1}) was measured in regions devoid of YbMS. We attribute this higher thermal conductivity primarily to the large phase YbDS fraction near the TGO. We do not observe any significant differences between measurements in Fig. 4.10(g) and in Fig. 4.7(c), suggesting that grain boundary density is low enough to not contribute to our measured thermal conductivity.

4.2.4 Discussion

Thermal cycling of a Si-YbDS EBC system between 110 °C and 1316 °C in a steam environment results in a significant change in the coating phase fractions, their spatial distributions and in the associated local thermal conductivity within the coating system. These macrostructural characteristics are summarized in Fig. 4.11(a), which shows the thicknesses of the YbMS surface layer, the YbDS-rich region near the bond coat, and that of the TGO layer. The growth of the YbMS surface layer and YbDS-rich region near the bond coat are both parabolic in nature, while the thickness of the TGO remained at $\sim$500 nm for the stabilization annealed specimen and that cycled for 500 hours, increasing to $\sim$2 μm after 2000 hours of cycling.

From a thermal property perspective, the stabilization annealed specimen as well as the specimen cycled for 500 hours show similar thermal conductivities in the central portion of the coating. As the stabilization annealed specimen has yet to be cycled, it does not exhibit a volatilized surface region primarily composed of YbMS, suggesting that the specimen cycled for 500 hours offers comparably better insulating characteristics. At 2000 hours, we also see a reduction in thermal conductivity at the surface of the coating as a result of YbDS volatilization. Within 15 μm of the Si bond coat, the thermal conductivity is increased, and was correlated with an increase of the YbDS fraction to $>$99%, Table 4.2, which we attribute to a reaction between silica in the TGO and nearby YbMS.

Inspection of the Yb_2O_3-SiO_2 phase diagram at elevated temperatures shows that it is thermodynamically favorable to form YbDS from YbMS and silica [164]. At the YbDS/Si bond coat interface, the reaction between residual YbMS in the YbDS layer and SiO_2 in the TGO is as follows [165]:

$$\mathrm{Yb_2SiO_5}(s) + \mathrm{SiO_2}(s) \rightarrow \mathrm{Yb_2Si_2O_7}(s). \tag{4.4}$$

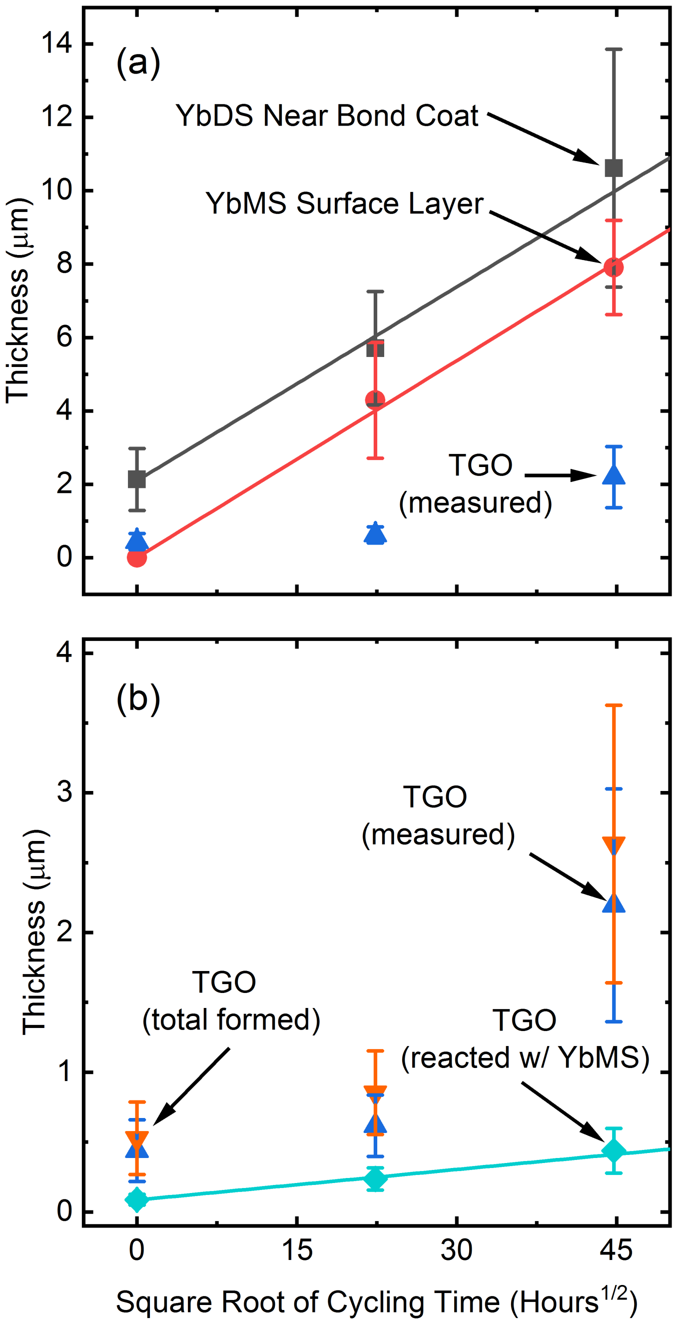

Figure 4.11. (a) Relevant layer thicknesses following thermal cycling for YbMS (circles), YbDS (squares), and the TGO (upward-facing triangles). The thicknesses of YbMS surface layer and YbDS near the Si bond coat grow approximately parabolically, while the growth rate of the TGO is approximately linear. (b) Measured TGO thickness (upward-facing triangles), derived total TGO thickness formed (downward-facing triangles), and derived TGO lost (diamonds) to the reaction given in Eq. 4.4.

The result is consistent with previous reports in an ytterbium-hafnate/ytterbium-silicate TBC/EBC system [166], and possible reactions in a yttrium monosilicate EBC [165].

The reaction between SiO_2 and residual YbMS near the TGO is further exemplified via the SEM BSE micrographs in Fig. 4.12, where we examine the YbMS distribution near the Si bond coat. In the stabilization annealed specimen, shown in Fig. 4.12(a), fine YbMS particulates are present near the TGO, which remains amorphous prior to cycling at elevated temperatures. The observation that YbMS is never in direct contact with the TGO layer is consistent with the reaction described by Eq. 4.4, which occurs with the substrate held at 1200 °C in ambient conditions. The elevated temperature of deposition also increases the rate of Si oxidation, which creates a SiO_2 source for YbMS to react with and form YbDS. Upon cycling to 500 hours the fraction of YbMS near the Si bond coat is greatly diminished, and this layer extends to $\sim$5 μm despite the TGO remaining at a constant thickness, as in Fig. 4.12(b). Small YbMS particulates are still present within this region, although much less so than those in the stabilization annealed specimen. In the specimen that has been cycled for 2000 hours, a region of $\sim$10–15 μm within the TGO is predominantly YbDS, with a very small phase fraction being YbMS. The reaction between cristobalite and residual YbMS near the TGO is also confirmed via EBSD phase micrographs (see Appendix B2), where trace amounts of cristobalite can be found within this region void of YbMS.

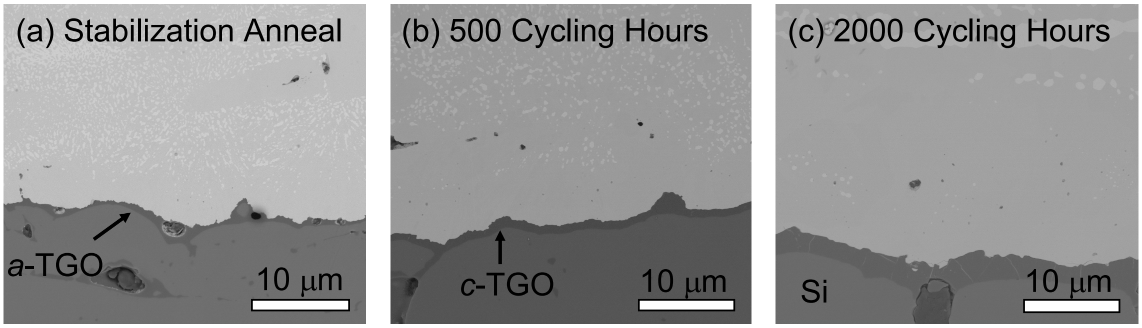

Figure 4.12. SEM micrographs near the Si bond coat for specimens after (a) stabilization annealling and cycling in a steam environment for (b) 500 and (c) 2000 hours. In the stabilization annealed specimen, the TGO remains amorphous, while vertical cracking in the TGO after 500 and 2000 cycles is suggestive of TGO crystallization.

The reaction between the TGO and residual YbMS near the bond coat has significant implications on the performance of EBCs. Previously, it has been shown that the lifetime of YbDS-based EBCs are contingent on the thermomechanical stability of the TGO layer [95, 97]. Recall that crystallization of the as-deposited amorphous TGO layer at elevated temperatures results in the formation of β-cristobalite, which is accompanied by a 4-7% volume change upon cooling to the α phase at lower temperatures [90–92]. Richards *et al.* have shown that this results in additional strains along the Si-SiO_2 interface, increasing the risk of delamination [95]. As growth of the TGO layer via oxidation of the bond coat occurs in parallel with the reaction between the TGO and residual YbMS, the net growth of the TGO layer is mitigated by the competition of the two processes.

The measured thicknesses of the TGO formed due to cycling, shown in Fig. 4.11(a), fundamentally underestimates the total thickness of the TGO that would form as a result of the reaction given by Eq. 4.4. To estimate the total amount of SiO_2 formed, we begin with our measured thicknesses for the YbDS enriched region. First, we assume that this YbDS region initially consisted of an average of 12.5 ± 2.5 mol% YbMS. Following, the number of reacted moles of YbMS can be calculated by using the molar volume of YbDS and YbMS. For each mole of YbMS formed, one mole of SiO_2 is required to form YbDS. By using the molar volume of β-cristobalite, the thickness of the SiO_2 lost to the reaction in Eq. 4.4 can be estimated and the total thickness of SiO_2 that would have been formed can be calculated. Details regarding the calculations can be found in Appendix B2, and the results of these calculations are shown in Fig. 4.11(b). They indicate that the fraction of SiO_2 lost from the TGO as a result of the reaction with YbMS is parabolic in nature.

The increase in TGO thickness from ∼0.5 μm to ∼2 μm after cycling for 500 and 2000 hours, respectively, is consistent with diffusion of oxidizing species through the YbDS/YbMS top coat to reach the TGO/Si interface, whereupon they react with Si to increase the thickness of the TGO layer. At the same time, SiO_2 is taken to diffuse through YbDS to reach regions in which YbMS exists. The trend seen in Fig. 4.11(b) indicates the fraction of SiO_2 lost from the TGO as a result of the reaction with YbMS is parabolic, and therefore consistent with diffusion through a YbMS depleted layer whose thickness increases with time. The presence of porosity may have provided fast diffusion pathways for SiO_2 from the TGO, increasing the extent to which it reacted with YbMS to form YbDS [166]. Poerschke *et al.* [167] have extensively examined SiO_2 diffusion in YbMS/Yb_6HfO_{11} and YbMS/$Yb_4Hf_3O_{12}$ systems, and argued that mobility of the diffusing species is enhanced by both grain boundaries and porosity, consistent with the observations reported here. When the SiO_2 thickness consumed via reaction (1) is compared to that measured, Fig. 4.11(b), the total SiO_2 thickness would have been $\sim$0.45 μm thicker than that measured after 2,000 hours of steam cycling. Since the delamination risk of the coating systems scales linearly with the TGO thickness and the difference in the CTE of the layers [97], reducing the thickness of the TGO, and the fraction of high CTE YbMS phase has improved the long-term thermomechanical stability of the coating system.

While we are not able to identify the mechanisms by which the grains near the Si bond coat coarsen, we hypothesize that it is related to the reaction described in Eq. 4.4, in addition to traditional coarsening mechanisms of two-phase systems [158, 159]. As the migration of silica occurs from the TGO to YbMS near the bond coat, the two materials react to from YbDS, as discussed earlier. We posit that the reaction site will begin to nucleate, and if energetically favorable, will be consumed by a larger YbDS grain in the vicinity. Coarsening of YbDS grains near the Si bond coat has significant implications for the growth of the TGO. Wada *et al.* [152] have shown that oxygen diffusion pathways are enhanced along grain boundaries in polycrystalline YbDS. Larger grains of the YbDS phase near the Si bond coat may therefore delay transport of oxidizing species through this region of the topcoat, reducing the growth rate of the TGO layer and contributing to the observed parabolic reaction with YbMS.

Additional considerations in CTE must be made for this dynamically evolving system. As mentioned previously, it is preferable for YbDS to be in close contact with that of the Si bond coat due to a similarity in CTE between the two materials. Because the region near the Si bond coat preferentially forms YbDS over time, the CTE between adjacent media in the silicate top coat and Si bond coat are better matched as the coating is cycled.

While we have measured the thermal conductivities in the plane of the YbDS coating, the associated temperature gradients experienced by a turbine blade will be perpendicular to our measurements. Additionally, our measured thermal conductivities for YbMS and YbDS were all performed at ambient temperature, and will not be the thermal conductivity at elevated temperatures typically experienced in a gas-turbine engine. Based on the crystalline nature of these materials, one would expect a reduction in the thermal conductivity as the ambient temperature is increased due to an increase in anharmonic phonon-phonon scattering. A variety of experimental and theoretical works have observed this trend in YbMS [105, 149] and YbDS [121, 126]. The majority of these experimental works, however, employ laser flash to measure the thermal diffusivity of these materials up to 1600 K. As the characteristic laser spot size in the laser flash technique is several orders of magnitude larger than those used here, they inherently average over multi-phase systems where grain and phase boundaries all contribute to an average thermal conductivity of their specimen, and does not provide the intrinsic thermal conductivity of YbDS or YbMS alone. As a result of this, we choose to investigate the temperature gradients that such coatings would endure at elevated temperatures based on the theoretically calculated thermal conductivity in the high temperature limit.

The theoretical minimum thermal conductivity in the high temperature limit has extensively been discussed by Clarke [106]. Using this formalism, Zhou *et al.* [126] have estimated a lower limit of 1.18 W m^{-1} K^{-1} for YbDS, while Xiang *et al.* [149] have estimated this to be 0.74 W m^{-1} K^{-1} for YbMS. Even at elevated temperatures, the thermal conductivity of YbDS theoretically exceeds that of YbMS. Using these theoretical high temperature thermal conductivity values, we calculate the nominal temperature distributions based on the heat-conduction equation in the steady-state regime. We model these temperature gradients as a function of cycling time to exemplify the impact of the compositional variation on the net temperature differential of the coating. Specific details of the simulation can be found in Appendix B2, but includes the volatilization of YbDS at

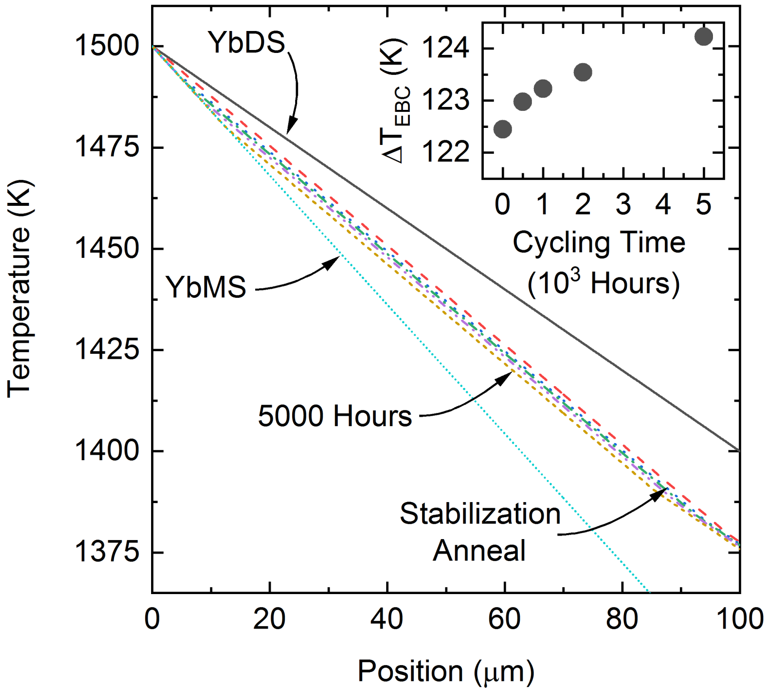

Figure 4.13. Calculated temperature drops across a typical 100 μm ytterbium silicate EBC, accounting for SiO_2 volatilization from YbDS at the surface of the coating, mixing of YbMS and YbDS, and an increase in YbDS fraction near the Si bond coat. Temperature calculations include an EBC composed entirely of YbDS (black line) and YbMS (cyan short dotted line), the stabilization annealed coating (red dashed line), and coatings cycled for 500 (blue dotted line), 1250 (green dashed-dotted line), 2000 (magenta dashed-dotted-dotted line), and 5000 (beige short dashed line) hours. The inset shows the total temperature drop arising from the implementation of the EBC as a function of cycling time.

the surface of the coating and the formation of YbMS, the presence of YbMS in YbDS in the middle of the coating, and YbDS enrichment near the Si bond coat. We do not include the TGO or the Si bond coat in our calculations. For reference, we also calculate the temperature gradients formed if the EBC were comprised of either YbDS or YbMS.

The results of our calculations, Fig. 4.13, indicate a system composed of pure YbDS exhibits the smallest temperature change across the coating at 100 K, while the largest temperature difference of 160 K was achieved with pure YbMS. The temperature difference across the stabilization annealed specimen, which was modeled approximately as a composite with equal distributions of YbMS and YbDS, shows a temperature difference of ~122 K. This temperature differential is larger than a pure YbDS EBC, which has better CTE match to the α-SiC substrate, but smaller than a pure YbMS EBC, which has superior steam volatility resistance but has a high CTE mismatch to the α-SiC substrate. As the EBC is cycled further, and YbMS forms at the surface of the coating while YbDS is enriched near the Si bond coat, the temperature differential increases slightly, extrapolated to $\sim$ 124 K at 5000 hours of cycling time as indicated via the inset of Fig. 4.13. This marginal increase in temperature differential can be attributed to the volatilization of YbDS at the surface of the coating, as the formation of YbMS is coupled with its lower thermal conductivity. The higher thermal conductivity YbDS serves to counteract this effect near the Si bond coat, effectively creating a constant temperature differential across the EBC as a function of cycling time. These results are fortified with the improved steam volatility resistance of YbMS at the surface of the coating and improved CTE match of YbDS that forms near the Si bond coat to the α-SiC substrate. Combined, these factors allow the coating to be more environmentally protective and thermomechanically stable, all while offering thermal insulation comparable to a TBC.

4.2.5 Conclusion

The associated microstructure and thermal characteristics of a top coat EBC has drastic implications on the performance and longevity of turbine components that implement such an EBC. The steam volatility resistant YbMS and CTE-matched YbDS are ideal constituents that should be readily implemented in such systems. As-deposited, the top coat contains amorphous and metastable constituents, and is not ideal for insertion into the hot section of a gas-turbine engine. Upon a stabilization anneal, crystallization throughout the coating is observed, which improves the CTE match to the underlying SiC. The coating consists of a YbDS matrix with YbMS interspersed throughout the coating, suggesting that an improved distribution is possible. As the steam-cycling process extends to prolonged periods, an increase in the YbDS concentration is found near the Si bond coat, while the volatilization of YbDS at the surface of the coating results in the formation of YbMS, which has a higher steam volatility resistance. After 2000 cycling hours, this volatilized region thickens to $\sim$15 μm, and a region free of YbMS is observed near the bond coat. This is further confirmed via the associated thermal conductivity micrographs, where the lowest thermal conductivities in the cross-section of the coating are found at the exposed portion, and the highest are found near the Si bond coat. The increased fraction of YbDS near the Si bond coat enhances the CTE match with the underlying α-SiC and reduces oxygen grain boundary diffusion as grain coarsening occurs for prolonged cycling times. The implementation of a YbMS/YbDS top coat EBC layer has several distinct advantages that make it a strong choice for the use on SiC CMCs.

4.3 Summary

In this chapter, I delved into the thermal conductivity characteristics of the rare-earth disilicate top coat of an EBC. I examined the anisotropic thermal conductivity associated with YDS, which exhibits an approximately 50% increase in thermal conductivity from the [001] and [010] to [100] directions at room temperature. Extraction of the orientational thermal conductivity was achieved through a micron-scale thermal conductivity mapping technique utilizing TDTR. This was first time extraction of the thermal conductivity tensor components of a material had been performed in the literature, and also provided the experimental basis for future thermal conductivity mapping works in this dissertation. Eventually, this included an understanding of the thermal conductivity distribution in a cycled EBC component, from its as-deposited state to being cycled for 2000 hours in a steam environment. Performing these measurements also provided insight into the reaction between YbMS and SiO_2 in the TGO, which formed a higher thermal conductivity, YbDS-rich region near to the Si bond coat. Measurements like these are essential for understanding the evolving temperature profile that a gas-turbine engine would experience a cycling hours reach several thousands of hours.

Chapter 5

Identifying Cristobalite Formation in Environmental Barrier Coating Systems

5.1 Spatially Resolved Thermal Conductivity Measurements of Devitrified Fused Silica

The work presented in this section has previously been published in *Scripta Materialia* [168] via collaborations with Rolls-Royce Inc. and the *Opila Research Group*. From the *ExSiTE Lab*, John Gaskins aided in thermal conductivity measurements, while Albert Tomko aided in interpreting the acquired Raman spectra. Robert Golden and Gregory Harrington of Rolls-Royce Inc. performed thermal aging of the fused silica specimens. Experimental guidance was provided by Elizabeth Opila, Adam Chamberlain, and Patrick Hopkins.

5.1.1 Background

Silicon carbide based ceramic matrix composites (SiC CMCs) have entered service as hot section components in gas turbine engines to increase engine efficiency and subsequently reduce emissions. In a combustion environment, SiC CMCs react with water vapor and form a volatile silicon hydroxide gas species ($Si(OH)_4$) [93, 94]. This reaction leads to high recession rates of SiC CMCs which necessitates the use of environmental barrier coatings (EBCs) in order to limit the exposure of SiC CMCs to this reaction. The EBC is multilayer system that typically consists of silicon layer applied directly to the CMC and top coat that has improved stability in the combustion environment. During service, H_2O (g) and O_2 (g) diffuse through the EBC and oxidize the silicon bond coat, resulting in the formation of a protective amorphous silicon dioxide (a-SiO_2) thermally grown oxide (TGO) [95, 141]. For long term applications it is desirable to maintain the amorphous TGO; however, the operating temperatures and thermal cycling events of the turbine engine cause the TGO to crystalize into the β-cristobalite polymorph of SiO_2 [97]. The $\beta \rightarrow \alpha$ cristobalite transformation that occurs at $\sim$ 220 - 270°C upon cooling is accompanied by a 3-7% volume decrease that results in cracking of the TGO layer [90–92]. The continuous cracking of the TGO layer during service eventually leads to spallation of the EBC [95, 96].

Presently, monitoring the formation of crystallized portions of amorphous SiO_2 has proven difficult. While analysis using scanning electron microscopy (SEM) and optical microscopy techniques can identify vertical cracks in the TGO which typically result from the β- to α-cristobalite transformation, quantifying the volume fraction of cristobalite is difficult. Electron backscatter diffraction (EBSD) is ideal for identifying crystalline vs. amorphous regions in the TGO, however specimen preparation required for this technique can be challenging [169], and generally lacks throughput. While Raman spectroscopy provides a benchmark to identify between the two materials, it lacks the high throughput imaging capabilities as integration of the entirety of the spectra must be performed for a given pixel. The mechanisms of formation and identification of crystalline forms of SiO_2 is paramount to understand the mechanical failure of TGOs. Ultimately this knowledge will drive design and failure criteria for coating systems that form amorphous silica TGOs. In the following study a thermal conductivity mapping procedure is proposed, which takes advantage of the quantifiable differences in thermal conductivity between the varying phases, while offering spatial resolution on the order of several micrometers and allowing for the delineation between a-SiO$_2$ and α-cristobalite.

The thermal conductivity of a-SiO$_2$ silica is well documented in the literature, and typically ranges between 1 and 1.4 W m^{-1} K^{-1} at room temperature [170–173]. On the other hand, that of α-cristobalite is not as well documented, but is found to range between 3.2 and 5.15 W m^{-1} K^{-1} [174–176]. In general, the thermal conductivity of crystalline solids is larger than those of their amorphous counterparts due to the presence of long-wavelength phonons as the primary heat carriers as compared to more localized modes in amorphous materials that transfer heat via much shorter range vibrational interactions [177]. Despite differences in thermal conductivity, the specific heat capacities remain the same at 741 J g^{-1} K^{-1} [178]. Accounting for the differences in densities (2.20 g cm^{-3} for a-SiO$_2$ [66] and 2.32 g cm^{-3} for α-cristobalite [174]), the volumetric heat capacities are 1.63 and 1.72 MJ m^{-3} K^{-1} for a-SiO$_2$ and α-cristobalite, respectively. Thus, differences in densities between these amorphous and α-cristobalite phases of SiO$_2$ do not explain the differences in thermal conductivities. The goal of this work is to study the thermal conductivity of α-cristobalite in partially- and fully-devritrified amorphous silica. Using a local measurement technique based on time domain thermroreflectance, thermal conductivity of thermally aged a-SiO$_2$ was spatially mapped to understand the fraction of α-cristobalite present. Unlike more macroscopic measurements of this crystalline silica phase, local measurements are less prone to obfuscation of the thermal conductivity measurements due to cracking, as these regions can be spatially avoided in the thermal conductivity measurements. Thus, this work provides more robust measurements of the thermal conductivity of fully dense α-cristobalite, in addition to demonstrating the ability to detect the emergence of this crystalline silica phase in a thermally aged TGO.

5.1.2 Materials & Methods

To observe various levels of devitrification of amorphous silica, high purity a-SiO$_2$ samples (99.995% pure; Quartz Scientific Inc., Fairport Harbor, OH) were used in this study. Samples were isothermally exposed at 1316 °C for 100 and 300 hours in a 90% H$_2$O

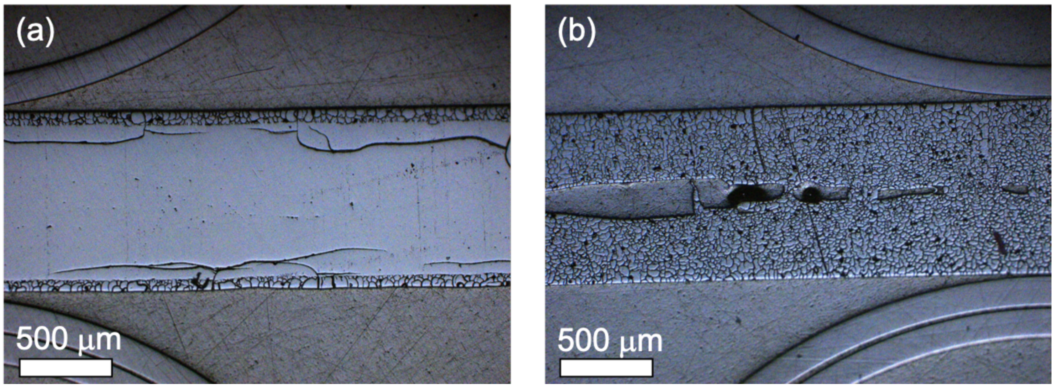

Figure 5.1. Optical micrographs of cross-sectioned SiO_2 specimens thermally aged at (a) 100 hours and (b) 300 hours at 1316 °C.

- 10% air environment in an alumina tube furnace. Samples were inserted and removed from the tube furnace at temperature. Exposed samples used for time-domain thermoreflectance (TDTR) characterization were mounted in epoxy, cross-sectioned and polished to a 1 micrometer finish with diamond; the RMS roughness were ~5 nm as measured via mechanical profilometry. Plan-view optical micrographs of the two samples are found in Figs. 5.1(a) and (b). The exposure to high temperature has a significant effect on the devitrification of the amorphous silica, as evidenced by the noticeable crack formation in Figs. 5.1(a) and (b). For the 100 hour sample, complete devitrification of the glass slide does not occur, and cracks begin to form at the edges of the sample. Cracking occurs throughout the sample exposed for 300 hours.

To confirm the formation of α-cristobalite, Raman spectroscopy was performed on the as-received a-SiO_2 and a reference a-SiO_2 slide isothermally aged at 1316 °C for 100 hours. In their unpolished states, a-SiO_2 remains transparent while α-cristobalite becomes opaque due to cracking. Each specimen was selectively analyzed to confirm the formation of α-cristobalite resulting from the thermal aging process. Excitations were performed at 514 nm, and the acquired Raman spectra are shown in Fig. 5.2 for the two specimens. Figure 5.2(a) shows the Raman spectra for a-SiO_2, which displays numerous broad features associated with the lack of long-range crystalline order. Further, the defect lines, D_1 and D_2, associated with rings in the a-SiO_2 structure, can be clearly observed at ~500 and

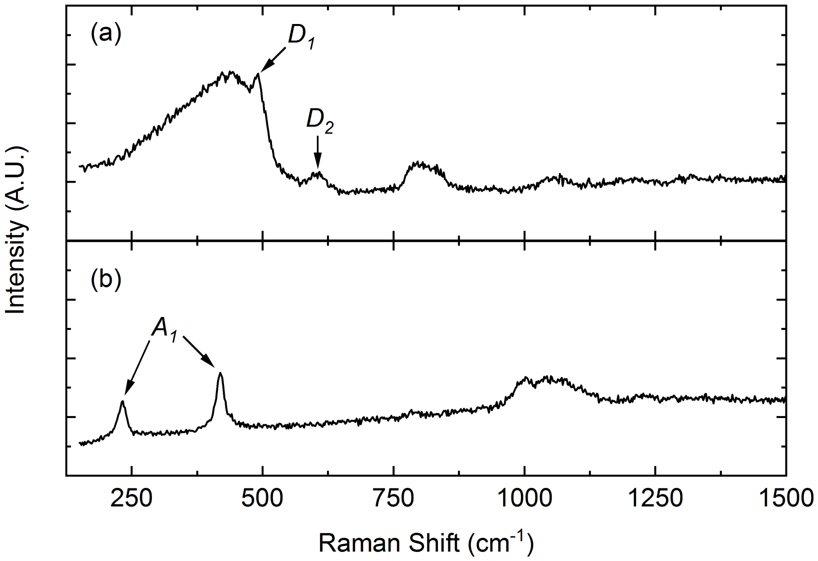

Figure 5.2. Raman spectra of the (a) as-received a-SiO$_2$ slide and (b) reference sample thermally aged at 1316 °C for 100 hours. The Raman spectra are indicative of primarily amorphous silica in the as-received glass slide and α-cristobalite in the thermally aged reference sample. Signatures of defect modes are labeled in (a) as D_1 and D_2, while those of optical modes are labeled in (b) as A_1.

$\sim$600 cm^{-1}, respectively [179]. Both these peaks are labeled Fig. 5.2(a). Similarly, the α-cristobalite Raman spectrum in Fig. 5.2(b) exhibits a sharp peak at $\sim$421 cm^{-1} due to its six-membered ring structure [180]; this peak is well-defined due to the crystallinity of the sample. Note, another defining peak is present at $\sim$233 cm^{-1}, and is in excellent agreement with prior literature [181]. Both of these peaks arise due to the optical vibrations present in α-cristobalite [182], and are labeled as A_1 in Fig. 5.2(b). The use of Raman to identify the formation of α-cristobalite at various depths from the edge of the TGO has been shown previously [97]. While this technique identifies the existence of α-cristobalite and offers diffraction-limited spatial resolution, it lacks high throughput imaging capabilities due to integration times associated with each pixel. To further characterize the formation of α-cristobalite, a nominal 80 nm Al film was deposited on the specimens, and TDTR was performed to spatially probe the sample surface in an effort to determine the fraction of

α-cristobalite present based on their respective thermal properties.

TDTR is an optical pump-probe technique that is widely used to characterize the thermal properties of bulk samples and thin films [57, 70, 111, 117]. The technique relies on an Ti:Sapphire oscillator with an 80 MHz repetition rate and sub-picosecond pulses. A two-tint setup was employed, where the 808.5 nm output of the oscillator is spectrally separated into a high-energy pump path and a low energy probe path [183]. The pump is electro-optically modulated at 8.4 MHz, creating a frequency-dependent heating event at the sample surface. The probe is mechanically delayed in time and monitors the thermoreflectance at the sample surface. By monitoring the in-phase (V_{in}) and out-of-phase (V_{out}) voltages, and relating the ratio of the two, $-V_{in}/V_{out}$, to the solution to the radially symmetric heat diffusion model [57, 77, 111, 112], various thermal properties can be extracted. An example of the data are shown in Fig. 5.3, where data and best-fits are shown for spots probed on α-cristobalite and a-SiO_2 portions on the sample exposed at 1316 °C for 100

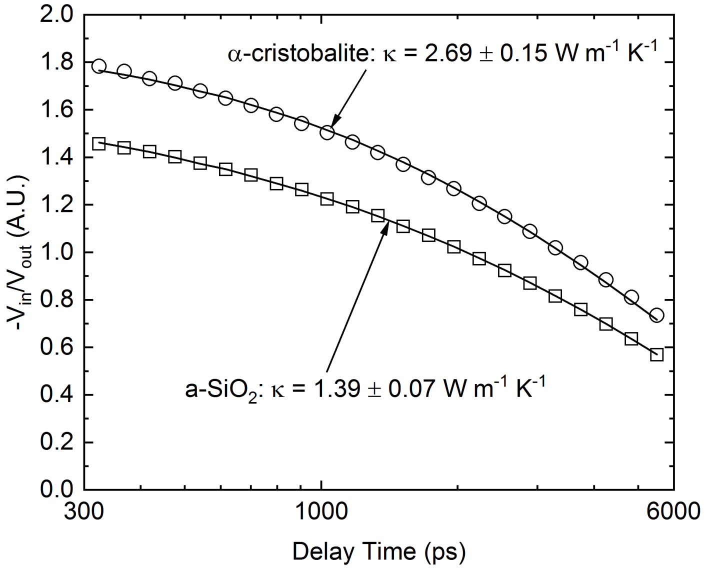

Figure 5.3. TDTR ratio of in-phase (V_{in}) to out-of-phase (V_{out}) data and model used to extract the thermal conductivity of amorphous and crystalline regions in the specimen annealed at 1316 °C for 100 hours. The open squares and circles are the raw data for the amorphous and crystalline regions respectively, while the solid lines are the best-fits.

hours. Picosecond acoustics were utilized to derive the thickness of the coated Al layer using the longitudinal speed of sound of 6.24 nm ps^{-1} [63, 66, 184]. The volumetric heat capacity of α-cristobalite and a-SiO_2 were taken to be 1.72 and 1.63 MJ m^{-3} K^{-1}, respectively, as discussed earlier. In all, the thermal conductivity of α-cristobalite and a-SiO_2 are found to be 2.69 ± 0.15 and 1.39 ± 0.07 W m^{-1} K^{-1}, respectively, when performing full TDTR measurements on crystalline and amorphous regions in the sample exposed at 1316 °C for 100 hours. In these and the following measurements, the $1/e^2$ pump and probe radii are $\sim$4.5 and $\sim$3.8 μm, respectively. At these spot sizes, the thermal conductivity of our Al transducer and spot sizes provide a negligible contribution to uncertainty in the extracted thermal conductivity. The uncertainty associated with the reported values reflects multiple measurements over amorphous and crystalline regions, as well as an uncertainty of 2 nm in our Al transducer layer.

5.1.3 Results & Discussion

The delineation between a-SiO_2 and α-cristobalite, beyond the cracking observed in Figs. 5.1(a) and 5.1(b), is difficult based on the contrasts in conventional optical and scanning electron techniques. The optical contrast in a-SiO_2 vs. α-cristobalite shown in Figs. 5.1(a) and 5.1(b) is negligible, and one would expect a similar lack of contrast from scanning electron micrographs based on the similarities in atomic density. Variations in thermal conductivity are much more tractable based on the large difference between the two phases. Based on acquisition parameters used in this work, the signal to noise ratio of $-V_{in}/V_{out}$ is approximately 25:1, and thus differences in thermal conductivity, and therefore crystallinity, can confidently be observed on the order of 20%.

From a practical standpoint, interrogating a location on a sample using TDTR is time consuming as it is necessary to map out the entire thermal decay curve which often takes several minutes. Various works in the literature have proposed spatially mapping the thermal properties of a given system using pump-probe techniques [72, 154], and have specifically shown its applicability on thermal barrier coating systems [155]. This work imple-

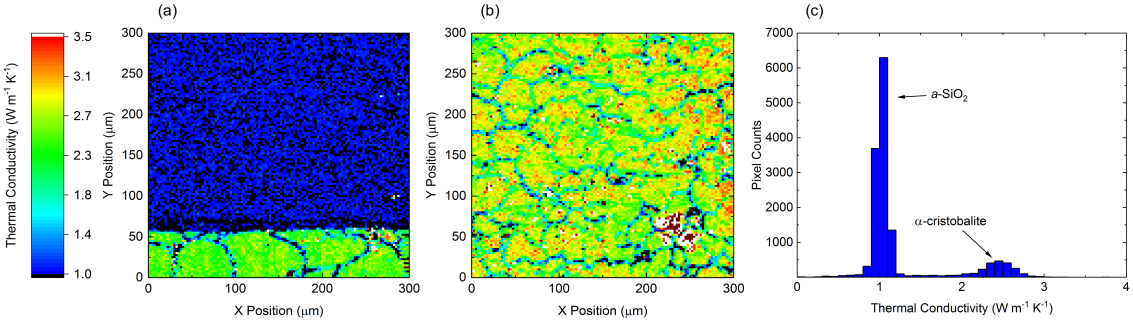

Figure 5.4. Thermal conductivity maps of samples annealed for (a) 100 hours, and (b) 300 hours at 1316 °C. For (a), the map was chosen nearest to the edge of where the sample was embedded into the epoxy, encompassing most of the polycrystalline region possible. In (b), a spot closer to the sample center was chosen. In both maps, a step size of 2.5 μm was chosen. (c) Thermal conductivity distribution from thermal conductivity map in (a). The histogram shows a clear differentiation between the amount of a-SiO$_2$ and α-cristobalite based on the two thermal conductivity distribution peaks, representative of the respective thermal conductivities of the constituent materials.

ments a similar technique. By mounting the sample on a 2-axis stage, the sample is rastered across regions of interest to spatially understand the thermal conductivity in those regions. Due to the fact that the thermal conductivity of a-SiO$_2$ and α-cristobalite are relatively low, the sensitivity to the boundary conductance between the Al and underlying material is low, allowing a single data point to be taken as an accurate representation of the thermal conductivity of the spot of interest. A pump-probe delay time of 2 ns was adopted, which ensures the results are not influenced by the thermal relaxation time of aluminum while still offering large sensitivity to thermal conductivity of the underlying silica of interest [72, 155].

Thermal conductivity maps of the two specimens can be seen in Fig. 5.4, where the pixel size is 2.5 μm. It should be noted that the pixel size as used here is dictated by the movement of the travel stage and adjacent pixels, and because of the size of the spot, will inherently sample adjoining pixels. The ratio, -V$_{\text{in}}$/V$_{\text{out}}$, is analyzed assuming an average of the volumetric heat capacities of amorphous silica and α-cristobalite for the sample exposed for 100 hours, while that of α-cristobalite is chosen for the sample exposed at 300 hours. Maps are originated close to the edge of the epoxy-embedded sample that was exposed at 100 hours to encapsulate as much α-cristobalite as possible, while a spot near the center of the sample aged for 300 hours was chosen. Examining Fig. 5.4(a), a clear difference in thermal conductivity can be observed between the polycrystalline and amorphous regions. For the sample exposed for 100 hours, the thermal conductivity of the amorphous and crystalline regions are determined to be $\sim$1.05 and $\sim$2.50 W m^{-1} K^{-1}. The departure of these values from those discussed earlier can be attributed to the volumetric heat capacity assumed in the analysis. In Fig. 5.4(b), due to complete devitrification, only the thermal conductivity of α-cristobalite is observed, and a value of 2.75 W m^{-1} K^{-1} is recovered.

Acquisition time of the image is largely dependent on the integration time and filter order of the lock-in amplifier. A time constant of 4 ms and a low-pass filter with a rolloff of 12 dB/oct is used to expedite the mapping process, which correlates to a time per pixel on the order of $\sim$25 ms when each pixel contains 1% of the information from the previous. For a 120 $\times$ 120 pixel image, this corresponds to $\sim$10 minutes of acquisition time when accounting for additional waiting considerations. Because the analysis requires solving the heat diffusion equation at a single pump/probe delay time, converting from the ratio (-V_{in}/V_{out}) to thermal conductivity takes less than 10 seconds for 14,400 data points. While thermal conductivity imaging using TDTR can be slower than other techniques that monitor temperature (e.g., full-field spectroscopy [185] and scanning thermal microscopy [186, 187]), the ability to extract relevant thermophysical properties beyond just temperature makes the technique unique. Indeed, scanning thermal microscopy offers the capability to extract thermal conductivity on the order of milliseconds per pixel with submicron spatial resolution [188, 189], but requires additional sources of uncertainty to be accounted for, including the goodness of the contact, ballistic conduction via ambient air [190], and the presence of a water meniscus [191], in addition to the complexity of the tip-sample heat transfer process. These sources of uncertainty are not applicable to TDTR.

To better highlight the differences in thermal conductivity, a histogram of the thermal conductivity map from Fig. 5.4(a) was plotted. A clear difference in the measured thermal conductivity of the two systems is observable in Fig. 5.4(c). Viewing the thermal conductivity distribution in this way is paramount for understanding the fraction of devitrified silica converted over a particular area. This thermal conductivity technique can be employed to quantify the volume fraction of α-cristobalite in the TGO and relate the volume fraction to coating adherence and/or failure metrics (i.e., bond strength, cycles to failure, etc.).

In summary, an alternative methodology was presented for the identification of α-cristobalite that is present as a devitrified SiO_2 TGO that forms on silicon bond coats in EBC systems for SiC CMCs. Spatial mapping of the thermal conductivity allows for delineation between α-cristobalite and a-SiO_2 based on the magnitude of the respective thermal conductivities. This method alleviates issues surrounding current methods for identification of α-cristobalite in gas-turbine engine coatings and offers a path forward toward further understanding failure mechanisms in these coating systems. Specifically, understanding the fraction of α-cristobalite in a thermally grown oxide presents itself as a quantifiable metric to understand the tolerance level at which α-cristobalite formation helps drive failure in these coatings. Future research will be devoted to the application of this work in relevant coating systems.

5.2 Identifying Devitrification in Thermally Grown Oxides

The work presented in this section is in preparation for publication as a result of collaborations with Rolls-Royce Inc. Gregory Harrington and Robert Golden of Rolls-Royce Inc. performed thermal cycling and scanning-electron characterization of the specimens, while John Gaskins of the *ExSiTE Lab* aided in interpreting thermal conductivity measurements. Experimental guidance was provided by Adam Chamberlain and Patrick Hopkins.

5.2.1 Background

In the previous section, we addressed the formation of α-cristobalite in an idealized system–a fused silica slide that was aged in a steam environment such that devitrification occurred at the exposed portions. This led to the formation of α-cristobalite, and was accompanied with significant cracking–similar to what would occur to the thermally grown oxide (TGO) of an environmental barrier coating (EBC) in the hot section of a gas turbine engine. However, the oxide in the latter is typically covered via a rare-earth disilicate top-coat [15, 22]. Thus, oxidizing species do not directly interact with the TGO, but must diffuse through this top coat before reaching the Si bond coat. This diffusion occurs via grain boundaries, porosity, as well as through the top-coat material itself [166]. The pertinent length scales are also vastly different. In the previous section, devitrification occurred on the order of $\sim$50 μm after just 100 hours of aging, and several hundreds of microns after 300 hours of aging. In a typical EBC system, TGO growth can be just a few μm after several thousand hours of cycling [95].

5.2.2 Materials & Methods

To investigate the formation of α-cristobalite in relevant EBC systems, a Si bond coat was applied via atmospheric plasma spray (APS) deposition to three substrates, two of which were SiC/SiC melt-infiltrated ceramic matrix composites (CMCs), while the other was a SiC substrate. We will refer to the two specimens deposited on the CMC as specimens S1 and S2, with the one being deposited on the SiC substrate being specimen S3. The thickness of the applied Si bond coat was $\sim$75 μm in thickness across all specimens. This was followed by the application of a YbDS layer, also applied via APS. Specimens S1 and S3 were cycled for 300 1-hours at 1375 °C in a steam environment (90 mol% H_2O/10 mol% O_2). Specimen S2 was cycled for 300 1-hours at 1316 °C, also in a steam environment, but was annealed for an additional 100 hours at 1000 °C in O_2 to induce partial devitrification.

Representative SEM micrographs of all specimens can be seen in Fig. 5.5, in which the

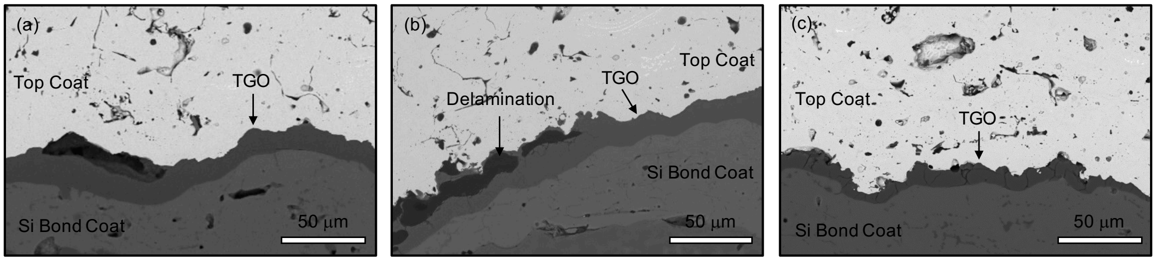

Figure 5.5. SEM BSE micrographs of EBC systems examined in this work. All specimens consisted of a YbDS top coat and a silicon bond coat with an intermediate TGO layer. Specimens (a) and (b) were deposited on a SiC/SiC CMC substrate, while specimen (c) was deposited on a SiC substrate. (a) System subjected to 300 cycles at 1375 °C in a steam environment. (b) System subjected to 300 cycles at 1316 °C in a steam environment, followed by a 1000 hour anneal at 1000 °C in air. (c) System subjected to 300 cycles at 1375 °C.

YbDS top coat, TGO, and Si bond coat have been identified when present. The delineation between these layers can easily be made via the contrast of the SEM BSE micrographs. In Fig. 5.5(a), the TGO appears smooth, suggesting that it has remained amorphous despite undergoing 300 1-hour cycles at elevated temperatures in a steam environment. The thickness was $\sim$15 μm, and no visible cracking was observed, consistent with the lack of devitrification. In the specimen shown in Fig. 5.5(b), which had undergone the same cycling procedure as the specimen in (a) but at 1316 °C and with an additional 100 hour anneal at 1000 °C in air, partial delamination specimen is observed. These findings are consistent with those of Richards *et al.* [95], who observed edge lifting of the top coat following several thousand hours of steam-cycling due to the formation of cristobalite and its corresponding $\beta \rightarrow \alpha$ transition at $\sim$240 °C. Some cracking is observed in the TGO, however, most of this cracking is situated closest to the edge beginning to delaminate. The thickness of the TGO in this specimen was $\sim$10 μm in regions away from the delamination. The specimen shown in Fig. 5.5(c) had been cycled under identical conditions to that shown in Fig. 5.5(a), but the system was deposited onto a SiC substrate as opposed to a SiC/SiC CMC. The thickness of the TGO layer was thinner than in Fig. 5.5(a) and (b), varying between $\sim$3 and 10 μm. Significant vertical cracking was observed, consistent with devitrification of the TGO layer.

Specimen	Substrate	Cycling Procedure	Post Anneal	TGO Thickness (μm)	TGO Characteristics
S1	SiC/SiC CMC	300 Hours @ 1375 °C		14.5 ± 3.6 μm	Smooth
S2	SiC/SiC CMC	300 Hours @ 1316 °C	100 Hours @ 1000 °C	10.4 ± 3.1* μm	Smooth, vertical cracking at edge
S3	SiC	300 Hours @ 1375 °C		6.5 ± 2.5 μm	Vertically Cracked

Table 5.1. Summary of specimens examined in this work, their cycling procedures, alongside thicknesses and observed qualities of the TGO layers.

*In region not delaminated.

The TGO characteristics of each specimen are summarized in Table 5.1. In specimen S1, the TGO is smooth and lacks cracks that would be observed in the SEM micrograph. In specimen S2, some vertical cracking is observed at the edge of the specimen, suggesting devitrification of the oxide layer. This is especially true in porous regions–regions away from this porosity are apparently smooth, implying that devitrification has not occurred. In specimen S3, vertical cracking is observed throughout the TGO layer. This vertical cracking is suggestive of the fact that the TGO is in its crystalline α-cristobalite form, but is not definitive. While the formation of α-cristobalite has been identified in similar systems using Raman spectroscopy [97], understanding the devitrification characteristics over larger scales is cumbersome using this technique, as spectral integration can take on the order of minutes per pixel. Recently, we have developed an imaging technique that monitors the thermal conductivity of a devitrified fused silica specimen, allowing us to delineate between amorphous and crystalline phases based on their respective thermal conductivities [168]. In this work, we determine the fraction of cristobalite in the TGOs of each of the specimens presented thus far via the same thermal conductivity imaging technique.

The imaging technique utilizes time-domain thermoreflectance (TDTR), and optical pump/probe technique, to determine the local TGO thermal conductivity using micrometer spatial resolution. Briefly, the output of a Ti:Sapphire oscillator emanating $\sim$100 fs pulses at 80 MHz is energetically split into pump and probe paths. The pump is electro-optically modulated at 8.4 MHz, which creates a frequency-dependent heating event at the sample surface. The probe, which is unmodulated, is mechanically delayed in time, and is coaxially aligned with the pump to monitor the temperature-dependent reflectivity at the sample surface. The cooling curve is compared to the radially symmetric heat diffusion equation [57, 112], which we use to extract the relevant thermophysical parameter. In this case, the relevant parameter is the thermal conductivity of the TGO layer, and its spatial variation.

Typical measurements using TDTR monitor the time-varying response at the sample surface. To extend this to a spatial setting, where local variations in thermal conductivity can now be probed, we utilize a 3-axis stage to raster the specimen relative to the incident

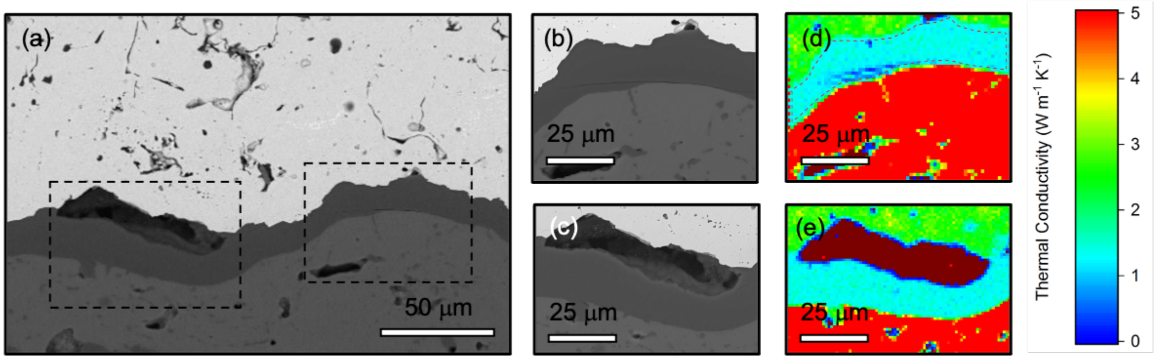

Figure 5.6. Specimen S1 thermal characterization. (a) SEM BSE micrograph of specimen S1. (b) and (d) show higher magnification micrographs of those outlined in (a). (d) and (e) show thermal conductivity micrographs of regions corresponding to (b) and (c), respectively.

pump and probe beams. The z-axis–the axis perpendicular to the incident pump and probe beams–is adjusted at each position so that the sample surface remains in focus for the duration of the micrograph. Using a 50× objective lens, the effective $1/e^2$ pump/probe radii is $\sim$1.4 μm.

5.2.3 Results & Discussion

Thermal characterization of specimen S1 is presented in Fig. 5.6. In particular, Fig. 5.6(a) shows the SEM BSE micrograph from Fig. 5.5, for reference. Higher magnification micrographs of the same region are shown in Figs. 5.6(b) and (c), where the smooth nature of the TGO layer can be more readily observed. Thermal conductivity micrographs with a step size of 0.5μm were acquired over the same regions shown in Fig. 5.6(b) and (c), and are shown in (d) and (e), respectively. The YbDS topcoat, TGO, and Si bond coat can all be delineated by their thermal conductivities in Figs. 5.6(d) and (e). The thermal conductivity of the TGO is in the range of $\sim$1.2–1.4 W m^{-1} K^{-1}, and is consistent with literature values for aSiO$_2$ at room temperature [170–173]. Thus, it is likely that for the conditions under which specimen S1 was fabricated and cycled, the TGO has remained amorphous, which is beneficial for the long-term cycling of coatings with a similar structure.

Low- and high-resolution SEM BSE micrographs of specimen S2 can be found in Fig.

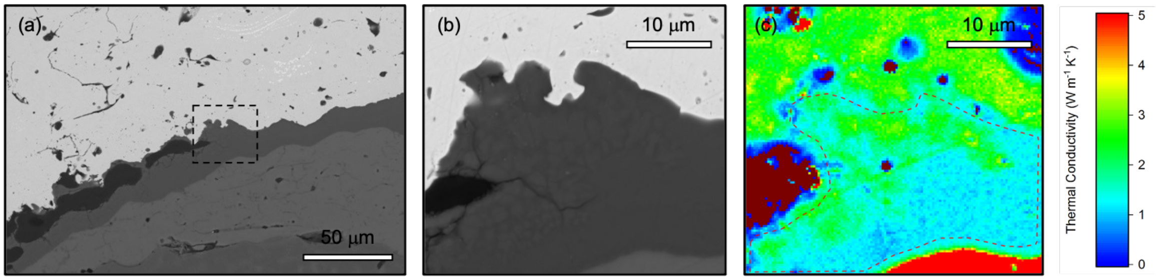

Figure 5.7. Specimen S2 thermal characterization. (a) SEM BSE micrograph of specimen S2. (b) Higher magnification micrograph of that outlined in (a). (c) Thermal conductivity micrograph of the region corresponding to (b).

5.7(a) and (b), respectively. In Fig. 5.7(a), some edge delamination can be seen on the left side of the micrograph. At the extent of this edge delamination, as seen in Fig. 5.7(b), some cracking is observed. Additionally, in this region, some contrast within the TGO itself can be seen. While we are not sure of the exact reason for such contrast, we hypothesize that it is related to the inclusion of trace amounts of impurity materials upon devitrification. Indeed, sulfur segregation has been observed at the metal/oxide interface of NiAl single crystals in contact with an Al_2O_3 TGO [192, 193], and metal impurities have been found to influence the composition of the TGO when cycled for prolonged periods at elevated temperatures [194–196]. Additionally, due to the differences in density between $aSiO_2$ [66] and α-cristobalite [174], we expect this to also influence the phase contrast in the BSE micrograph.

The thermal conductivity micrograph of the same region shown in Fig. 5.7(b) can be seen in Fig. 5.7(c). Visually, the region looks similar to that of specimen S1–it is possible to delineate between the top coat, TGO, and bond coat layers based on their respective thermal conductivities. When compared to the BSE micrograph, correlations in the TGO can be made between contrast in the BSE micrograph and thermal conductivity micrograph. In particular, areas of lighter contrast in (b) correspond to regions of higher thermal conductivity in (c), on the order of that of α-cristobalite. Likewise, darker areas of contrast in (b) correspond to lower thermal conductivities in (c), in agreement with $aSiO_2$. Thus, we posit that the regions of lighter contrast are α-cristobalite nucleation sites.

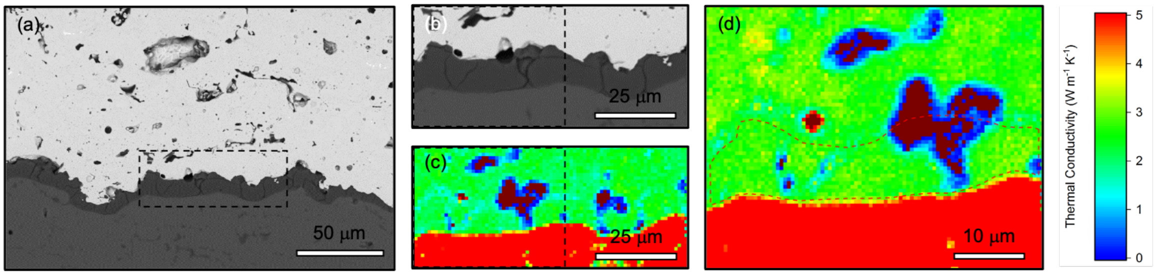

Figure 5.8. Specimen S3 thermal characterization. (a) SEM BSE micrograph of specimen S3. (b) Higher magnification micrograph of that outlined in (a). (c) Thermal conductivity micrograph of the region corresponding to (b). (d) Thermal conductivity micrograph with higher pixel density of the regions outlined in (b) and (c).

Finally, the thermal characterization performed on specimen S3 can be found in Fig. 5.8. The BSE micrograph is shown in Fig. 5.8(a), for reference, where a higher magnification micrograph of the dashed region can be found in Fig. 5.8(b). The thermal conductivity micrograph corresponding to Fig. 5.8(b) can be found in Fig. 5.8(c). Despite the large contrast observed in the BSE micrograph, in which one can clearly observe the top coat, TGO, and bond coat, there is minimal contrast between the top coat and TGO in the thermal conductivity micrograph. The thermal conductivity of the top-coat is consistent with those in specimens S1 and S2, at $\sim$2.8–3 W m^{-1} K^{-1}. The thermal conductivity in the TGO layer is uniform, and higher than that observed in specimen S1 with a value of $\sim$2.8–3 W m^{-1} K^{-1}. The higher thermal conductivity is consistent with that of α-cristobalite, and suggests that the entirety of the TGO layer has been devitrified. A higher magnification thermal conductivity micrograph of regions demarcated in Figs. 5.8(b) and (c) can be seen in Fig. 5.8(d), where some of the finer features of the TGO region can be observed.

To better visualize the differences in the thermal conductivity of the TGO regions specifically and to indicate the differing characteristics of each, regions in Figs. 5.6(d), 5.7(c), and 5.8(d) have been demarcated by red dashed lines and thermal conductivity histogram of these regions can be found in Fig. 5.9. Figure 5.9(a) shows the thermal conductivity distribution of the region demarcated for sample S1. The thermal conductivity of this region is in the range of 1.2–1.4 W m^{-1} K^{-1}, in good agreement with the thermal conductivity of aSiO$_2$, and suggestive of the fact that the TGO has remained amorphous.

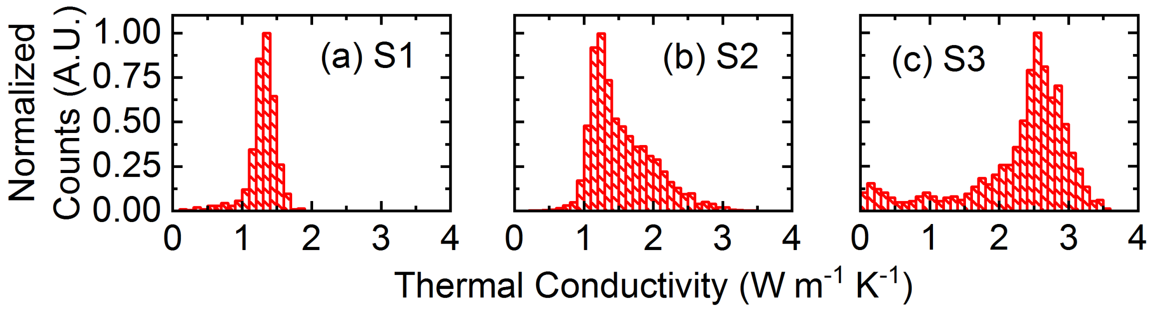

Figure 5.9. Thermal conductivity distributions of specimens (a) S1, (b) S2, and (c) S3 in regions demarcated by the red dashed lines of Figs. 5.6(d), 5.7(c), and 5.8(d), respectively.

The thermal conductivity distribution for the region in specimen S2 can be found in Fig. 5.9(b). The thermal conductivity of this region spans from ∼1–2.5 W m^{-1} K^{-1}. The largest number of counts in the distribution occurs in the range of 1.2–1.4 W m^{-1} K^{-1}, again consistent with the thermal conductivity of $aSiO_2$. There is, however, significant shouldering present in the distribution, extending it to ∼2.5 W m^{-1} K^{-1}. The fact that the distribution does not show significant thermal conductivity counts around 2.5 W m^{-1} K^{-1} suggests that partial devitrification of the layer has likely occurred and that our laser spot size is spatially averaging over regions containing both $aSiO_2$ and α-cristobalite. To better quantify the fraction of devitrified TGO, we perform a deconvolution of the histogram shown in Fig. 5.9(b). The deconvolution assumes that two gaussian distributions are present, each with their own respective centroids and standard deviations. As a result of the spatial averaging of the thermal conductivity due to our laser spot size being larger than the feret diameter of α-cristobalite in the TGO, we fix the centroid of one gaussian to be 1.8 W m^{-1} K^{-1}, which is roughly the mean of the thermal conductivity of $aSiO_2$ and α-cristobalite. In doing so, we find that the fraction of the TGO that is devitrified to be ∼30%. This is in good agreement when determining this fraction via pixel counting statistics of the same region in the SEM BSE micrograph, which results in a fraction of ∼33%. We note, however, that the contrast in the thermal conductivity micrograph is far greater than that in the SEM BSE micrograph, and thus better merits its use.

The thermal conductivity distribution for specimen S3 is shown in Fig. 5.9(c). In this distribution, a significant portion of the counts are present in the range of 2–3 W m^{-1} K^{-1}.

This thermal conductivity is consistent with that of α-cristobalite, and indicates that the entirety of the layer is fully crystalized. Minor thermal conductivity counts are present in the range of 0–2 W m^{-1} K^{-1}. When further examining the SEM BSE micrograph of the same region, however, it is evident that a reduced thermal conductivity is measured in regions in which cracks are present. As TDTR is a laser-based technique in which only a specular surface can be probed so that we monitor temperature as opposed to extraneous additions to our signal, regions near these cracks should be discounted from the analysis. As the thermal conductivity is predominantly reduced near these regions, producing counts in the range of 0–2 W m^{-1} K^{-1}, removing these counts results in a thermal conductivity distribution that is nominally in the range of 2–3 W m^{-1} K^{-1}.

In all, this work examined the formation of α-cristobalite in the TGO of a relevant EBC system that would be implemented on a CMC turbine blade. The results indicate that the thermal conductivity is indicative of the amorphous/crystalline state of the TGO, with spatial resolution on the order of $\sim$2 μm. For systems with amorphous and crystalline TGOs, the ability to monitor devitrification can easily be made via the thermal conductivity distributions in the TGO region. When only partial devitrification has occurred, spatial averaging of the thermal conductivity limits the ability to appropriately delineate between the two phases. Even so, the characteristics of an amorphous TGO compared to a partially devitrified one are sufficient such that the delineation between the two can be made. Our results suggest that monitoring the devitrification of a TGO is possible via probing the local thermal conductivity when standard characterization techniques are unable to adequately determine its crystalline state.

5.3 Summary

In this chapter, I showed that local thermal conductivity measurements can be used to diagnose the crystalline state of a material. This was done by first examining the change in thermal conductivity of an $aSiO_2$ slide that had been steam cycled to devitrification and the formation of α-cristobalite. Upon realizing the fact that the delineation of the two phases could be made via their thermal conductivity, measurements were performed on a relevant EBC system. As the pertinent length scale was significantly smaller than the $aSiO_2$ slide, this required much higher resolution. The measurements were performed on EBC systems with an amorphous, partially devitrified, and fully devitrified TGO, and the results were in good agreement with the TGO characteristics as observed by standard microscopy techniques.

Chapter 6

Heat Transfer at Au Contacts with a TiO_x Wetting Layer

6.1 Stoichiometric Effects on the Thermal Conductance at Au Contacts with a TiO_x Wetting Layer

The work presented in this section has previously been published in *Applied Physics Letters* [197], brought to fruition through collaboration with the *Surface Materials Characterization for Devices Group* at UVa. Keren Freedy, in particular, performed sample preparation as well as the necessary X-ray photoelectron spectroscopy characterization and interpretation to determine the stoichiometry of the TiO_x adhesion layers. Experimental guidance was provided by Stephen McDonnell and Patrick Hopkins.

6.1.1 Background

The thermal resistances across heterogeneous material interfaces are well known to influence heat dissipation mechanisms in materials and devices with characteristic length scales approaching the Kapitza length, l_K, defined by $l_\text{K} = \kappa R_\text{K} = \kappa / h_\text{K}$. In this equation, κ is the thermal conductivity of a material adjacent to the interface, R_K is the thermal boundary resistance ("Kapitza resistance") [26], and $h_{\mathrm{K}} = 1/R_{\mathrm{K}}$ is the thermal boundary conductance [54, 198–201]. Historically, understanding of the phonon transport mechanisms driving the thermal boundary conductance across interfaces has relied on the concept of energy transmission driven by the relative dissimilarities of the acoustic properties [202, 203] or phonon densities of states [54] intrinsic to the bulk of the two materials comprising the interface. More recently, defects and atomic disorder in the form of substrate roughness [204, 205], dislocations [206], atomic diffusion [207], nanoscale or molecular defects [208, 209], and structurally disordered thin films (with thicknesses $d \ll l_{\mathrm{K}}$) [204, 210–213] at and near the interface has been shown to decrease h_{K} as compared to the corresponding "perfect" interface [199].

Under certain conditions, the inclusion of additional interfacial moieties in the form of point defects or thin films can be used to increase the thermal boundary conductance (decrease the thermal boundary resistance). For example, our recent work has shown that point defects generated from ion irradiation can lead to increases in thermal boundary conductance [210] by creating a spatial gradation of vibrational properties, similar to the so-called "vibrational bridge" effect that was computationally observed via molecular dynamics [214, 215]. As another example, the inclusion of surface adsorbates [216–218], molecules [219, 220], and adhesion layers [65] between a film and substrate have been shown to increase the thermal boundary conductance across the interface. In this case, the placement of these interfacial moieties have led to stronger bonding across an otherwise relatively weakly bonded interface. The increase in bond strength then leads to an increase in thermal boundary conductance due to high frequency phonons coupling energy from the one side of the interface to the other [221, 222].

However, as previously mentioned, while interfacial adhesion layers and "defects"/moieties could lead to increases in the relative h_{K} due to bonding, the increase in interfacial disorder or additional interfaces (e.g., adhesion layers) could also lead to decreases in h_{K}, and this interplay between the interfacial region increasing vs. decreasing the thermal boundary conductance is relatively unstudied. For example, when molecules have been used to increase the bonding at film/substrate interfaces, and thus increase h_K, the intrinsic thermal resistance of the interfacial molecule at the junction is assumed negligible [219, 220] (i.e., heat flow through the molecule is ballistic) [223, 224]. A large enough molecule at a film/substrate interface that exhibits diffusive thermal transport can lead to reductions in h_K [208, 225], thus counteracting any benefit of increased adhesion on thermal boundary conductance. This interplay is poorly understood, and has pronounced impact on our understanding of the intertwined role of defects and adhesion layers on the thermal boundary conductance across interfaces, along with the ability to assess and validate concepts and theories of thermal boundary conductance at strongly bonded interfaces.

Thin titanium (Ti) and TiO$_x$ adhesion layers have been predominantly used in thin film manufacturing to increase interfacial bonding to a dielectric substrate. This is due to the fact that the typical Ti adhesion layer allows for an ameliorated adherence of other metal films, such as Au, Pt, Ni, Al, etc., to these dielectric materials. The use of of these adhesion layers covers a wide array of applications, including metal contacts in electronic devices, lithium ion thin film microbatteries [226, 227], split-ring resonators [228–230], and even plasmon damping [231, 232]. The influence of Ti adhesion layers has also been examined for its effects on thermal transport in thin gold films on various substrates [65, 233, 234]. As interfaces can become the dominant resistors in thin film systems, their thermal management is paramount in multilayer geometries and thus, understanding the growth and chemistry mechanisms that influence adhesion layers requisite to their thermal performance is of the utmost importance.

In this work, we describe the results of a series of measurements across gold/non-metal substrate interfaces (amorphous silica (SiO_2), crystalline silica (quartz), sapphire (Al_2O_3), and magnesium oxide (MgO)) with TiO$_x$ adhesion layers ranging in oxygen stoichiometries from $0 \leq x \leq 2.85$. We achieve this range of oxygen stoichiometries through the fabrication of two different sets of Au/TiO$_x$/substrate samples, one evaporated under high vacuum (HV) using different Ti deposition rates and the other evaporated under ultrahigh vacuum (UHV). In the UHV conditions, we identify the role of Ti film thickness on the thermal boundary conductance, while the HV-deposited Ti demonstrates a clear dependency on oxygen composition and hence deposition conditions. In general, our results suggest that thin Ti layers with relatively low oxygen compositions are best suited to maximize the thermal boundary conductance.

6.1.2 Materials & Methods

In the first part of this study, we fabricate the Au/TiO$_x$/substrate samples with electron-beam evaporation in HV. For the TiO$_x$ layers, we evaporate Ti at 0.1, 0.5, and 1.0 Å/s in separate runs on two sets of quartz, aSiO$_2$, MgO, and Al$_2$O$_3$ substrates. Prior to this, the quartz, aSiO$_2$, Al$_2$O$_3$ were sonicated in isopropanol, acetone, and methanol for 5 minutes each, and then placed in a MARCH O$_2$ Plasma Etcher for 10 minutes. The MgO substrate was spin-cleaned with isopropanol, acetone, and methanol. After cleaning, the samples were immediately placed in the electron beam evaporator, and pumped down to $\sim 10^{-6}$ Torr. Following the 3 nm Ti evaporation, we evaporate 3 nm of Au at 0.2 Å/s without breaking vacuum. The evaporator was then vented, and one of each substrate was removed to be analyzed via x-ray photoelectron spectroscopy (XPS). The evaporator was then pumped down to $\sim 10^{-6}$ Torr once again, and an additional 47 nm Au was deposited at 1 Å/s. All depositions were performed with a rotation speed of 17 RPM. XPS was used in determining the composition of the underlying TiO$_x$ interface in the thinner sample set. X-ray reflectivity (XRR) was used to determine a thickness of ∼50 nm Au on the thicker sample sets. As a comparison, we also evaporate 50 nm of Au on the various substrates without an adhesion layer.

XPS data were acquired with a monochromated X-ray source at a pass energy of 50 eV in a UHV system described elsewhere [235]. Figure 6.1(a) shows XPS spectra of the O 1*s* core level in three distinct Ti films deposited on SiO$_2$ substrates at different deposition rates. The O 1*s* spectra are each comprised of two features: a peak at ∼530.5 eV, corresponding to Ti-O bonds [236], and a broader feature at the high binding energy shoulder which is attributed to hydrocarbon species. This higher binding-energy feature decreases

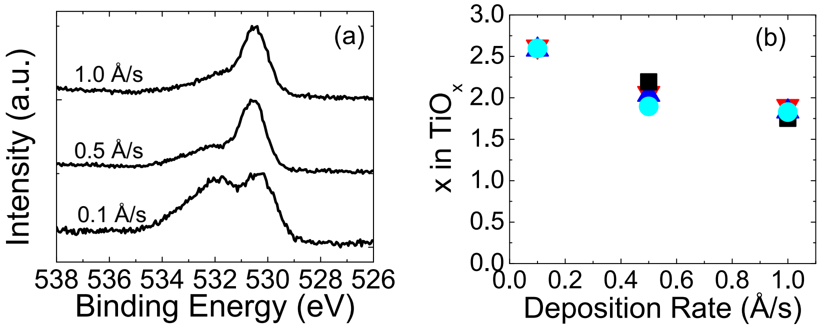

Figure 6.1. (a) O 1*s* core level binding energies of the Ti adhesion layer on an SiO_2 substrate and (b) Oxygen content in TiO_x adhesion layer as a function of Ti deposition rate for quartz (squares), SiO_2 (circles), Al_2O_3 (downward facing triangles), and MgO (upward facing triangles). The value of the Ti deposited on the quartz substrate at 0.1 Å/s could not be recovered due to sample size restrictions in XPS analysis for (b).

in intensity relative to the Ti-O state as deposition rate is increased. Deconvolution of the spectra indicates that at 0.1 A/s, 46% of the total oxygen signal is from Ti-O bonds. This value increases to 71% and 76% at 0.5 and 1 Å/s, respectively. The deposition rate determines the impingement rate of Ti atoms on the surface of the substrate relative to the impingement rate of residual gases in the chamber [237]. A cleaner interface results as Ti atoms arrive at a faster rate allowing less opportunity for the physisorption of contaminants. Due to the constant partial pressure of oxidizing species under HV deposition conditions, the resulting Ti film is always comprised primarily of oxide regardless of the deposition rate. The oxygen composition as a function of Ti deposition rate of these high vacuum-evaporated interfaces determined via our XPS analysis is shown in Fig. 6.1(b). Note: this only accounts for oxygen that is bonded to the Ti in the adhesion layer. We use time-domain thermoreflectance (TDTR) to measure h_K across the Au/substrate interfaces, the details of which are discussed in Appendix B3 [57, 111, 112]. Values for h_K are presented only for quartz, MgO, and Al_2O_3 substrates due to a lack of sensitivity in $aSiO_2$ samples.

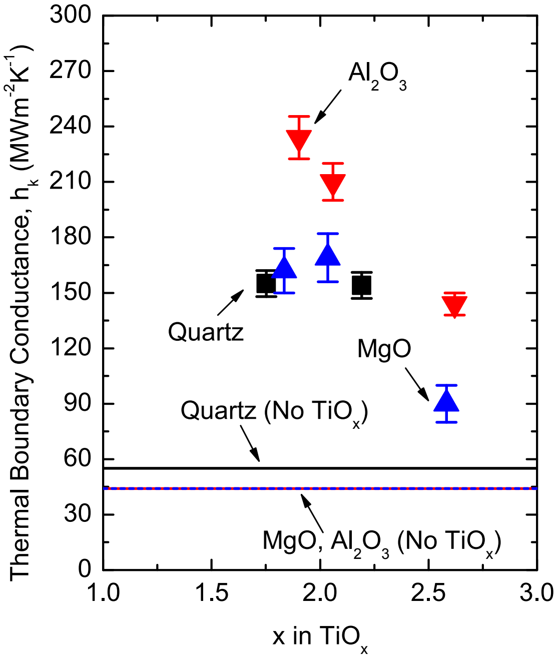

Figure 6.2. Thermal boundary conductances across Au/TiO$_x$/substrate deposited using electron-beam evaporation under high vacuum. The thermal boundary conductance of the quartz sample with Ti deposited at 0.1 Å/s is not shown because the stoichiometry could not be determined due to sample size limitations. Despite this, h_K was determined to be 130 MW m^{-2} K^{-1} for that sample, relatively consistent with the other quartz substrate samples.. The lines are the measured data from the Au/substrate samples with no TiO$_x$ adhesion layers.

6.1.3 Results & Discussion

The Au/TiO$_x$/substrate thermal boundary conductances as a function of x in TiO$_x$ is plotted in Fig. 6.2 for the 3 nm evaporated TiO$_x$ layers. As expected, the measured thermal boundary conductances across the Au/TiO$_x$/substrate interfaces are higher than the Au/substrate interfaces without the adhesion layer (in most cases, more than a factor of three higher), which is most likely a consequence of increased adhesion between the Au and substrate and consistent with previous results [65]. In general we observe a reduction in h_K with an increase in oxygen composition in the TiO$_x$ layer for the MgO and Al$_2$O$_3$ substrates. Since the oxygen composition is directly related to the deposition rate in our evaporator, an initial qualitative conclusion is that under typical HV conditions, the deposition rate of evaporated Ti will result in TiO_x with varying x, and a higher oxygen composition in this evaporated adhesion layer leads to a lower h_K across the Au/TiO_x/MgO and Au/TiO_x/Al_2O_3 interfaces. While still in most of these cases the TiO_x offers an improved h_K as compared to the thermal boundary conductance across the Au/substrate interface with out the adhesion layer, for the case of the largest oxygen composition $x = 2.85$, the impact of the adhesion layer loses its benefit in terms of increasing h_K. The thermal boundary conductance across this Au/$TiO_{2.85}$/MgO interface is about a factor of two higher than the Au/MgO case, while for lower oxygen compositions in the evaporated TiO_x adhesion layer, the improvement in thermal boundary conductance is a factor of three to five times higher.

Another feature we observe in Fig. 6.2 is that the thermal boundary conductance across the Au/TiO_x/quartz is independent of x. There could be several mechanisms at play that cause this different trend in h_K vs. x for the quartz substrate as compared to the MgO and Al_2O_3, including reduction of the deposited Ti and differing TiO_x film qualities and morphologies. The variabilities and vacuum levels of this (and most) evaporators prevent us from making more quantitative conclusions on these particular samples beyond our initial qualitative conclusion related to the processing, chemical composition and thermal boundary conductance, discussed above. However, we gain more insight into this relationship by repeating this study with UHV-grown titanium adhesion layers. In this case, due to the UHV conditions in our chamber, the reduced physisorption of foreign species is correlated to a decrease in oxidized Ti at the substrate.

The Ti adhesion layers were deposited in UHV (7.5×10^{-10} Torr) via electron-beam evaporation on the same aforementioned substrates using identical cleaning procedures. Samples were subsequently coated with a thin layer of gold *in situ* to prevent oxidation of the underlying Ti layer [237]. The gold is deposited until the XPS signal of the substrate is buried, and its thickness is later confirmed with XRR. The samples were immediately transferred to the HV evaporator and pumped down to pressures $\sim 10^{-6}$ Torr to be deposited with a thicker Au layer (47 nm). A comparison of the Ti 2p spectra for Ti deposited at 1.0 Å/s in HV and Ti deposited at < 0.1 Å/s under UHV is shown in Fig. B19 of Appendix B3.

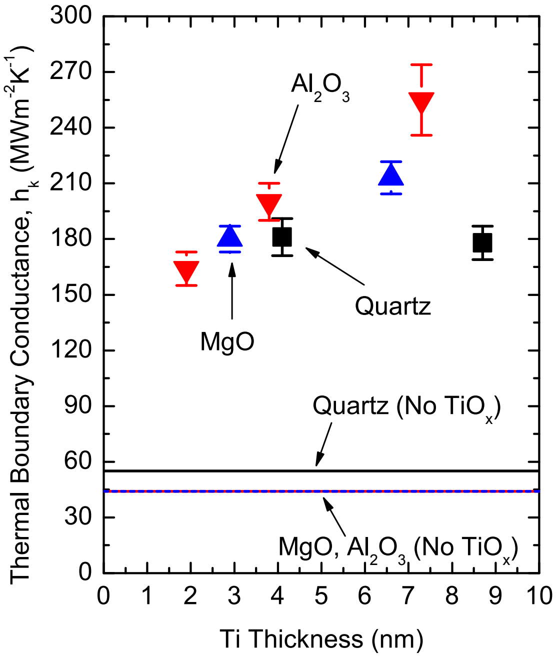

Figure 6.3. Thermal boundary conductances at Au/Substrate interfaces with a Ti adhesion layer despoited via electron-beam evaporation in UHV as a function of Ti thickness. The lines are the measured data from the Au/substrate samples with no Ti adhesion layer.

In the HV-deposited sample, metallic Ti accounts for only 6% of the total Ti signal and the remainder is from TiO_2. In contrast, Ti deposited in UHV appears purely metallic.

The measured thermal boundary conductances as a function of Ti layer thickness are shown in Fig. 6.3. In the cases of Al_2O_3 and MgO, there is a clear increase in h_K with increasing Ti thickness. On the other hand, as the thickness of the Ti increases on the quartz substrate, the thermal boundary conductance remains relatively constant. An increase in thermal boundary conductance (decrease in thermal boundary resistance) with an increase in film thickness suggests that the Ti film is not in a fully thermally diffusive regime, suggesting at least partially ballistic electron and/or phonon transport from the Au scattering at the substrate surface without scattering and losing energy in the Ti layer. This is the case in Al_2O_3 and MgO for the Ti thicknesses presented here. However, to explain the phenomena observed in the quartz substrate, we must examine the free energies of the Mg-O, Al-O, and Si-O bonds. As the Ti-O bond has a smaller free energy (-825 kJ mol^{-1}) compared to

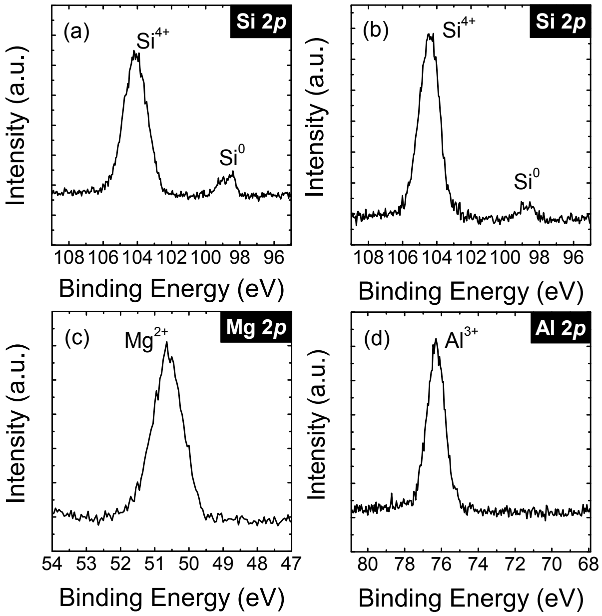

Figure 6.4. Si $2p$ spectra of (a) SiO_2 and (b) quartz, (c) Mg $2p$ spectra of MgO, and (d) Al $2p$ spectra of Al_2O_3 after depositing a thin layer of Ti in UHV. (a) and (b) exhibit the reaction of Ti with oxygen from these substrates, leading to the appearance of the Si^0 chemical state, while the lack of Mg^0 and Al^0 states in (c) and (d), respectively, suggest no reaction of Ti with oxygen from these substrates.

Mg-O (-1150 kJ mol^{-1}) and Al-O (-1050 kJ mol^{-1}) bonds at room temperature [238], Ti near the substrate will not break these bonds to form TiO_x. On the other hand, the free energy associated with the Ti-O bond is smaller than that of Si-O (-810 kJ mol^{-1}), suggesting that Si-O bonds near the interface are breaking to form TiO_x. This is confirmed via XPS, shown in Fig. 6.4, the data of which exhibits bond scission in SiO_2 and quartz substrates, but not in MgO and Al_2O_3. The Si $2p$ spectra shown in Fig. 6.4(a) and (b) indicate that in UHV, Ti reacts with oxygen from the substrate which leads to the appearance of the Si^0 chemical state.

With this additional information, we revisit h_K in the HV evaporated quartz samples. Regardless of deposition rate, the conductance across the Au/TiO_x/quartz interface is not altered significantly across oxygen stoichiometries. Based on XPS data from UHV grown samples, Ti deposited onto quartz and SiO_2 break the Si:O bond to form Ti:O, presenting similar bonding across the Au/Ti/quartz interface. This is confirmed further in the Ti grown under UHV conditions on quartz, whereby h_K is not altered significantly. We currently do not understand why increasing the thickness of the Au/TiO$_x$/quartz interface does not decrease the resistance. However, we note that since the UHV grown TiO$_x$ is not a pure metal, an increased contribution from vibrational transport will most certainly be playing a role compared to the pure Ti case.

There are a variety of factors that could alter our presented values for thermal boundary conductances at these interfaces. Differences in UHV and HV deposition parameters, for example, have the potential to alter the structure of the TiO$_x$ adhesion layer. In turn, differences in structure can alter measured thermal boundary conductances, which could explain differences across deposition rates in HV-deposited adhesion layers and the increase in h_K for UHV samples. Additionally, we cannot confirm that a conformal adhesion layer was deposited with a constant thickness. Indeed, we account for the uncertainty of the thickness of the Ti adhesion layer in our analysis of thermal boundary conductance, but this does not account for islanding or other complications arising due to electron-beam evaporated metals. This, along with the quality of the Ti layer, could be playing a role in explaining the thickness trends in h_K in UHV-grown samples. Thus, we cannot comment on the specific mechanisms governing h_K for UHV Ti. We can conclude, however, that Ti adhesion layers deposited in UHV in general improve heat management compared to their HV counterparts, especially as the deposition rate of the Ti is lowered.

In summary, we report on a series of measurements demonstrating the role of oxygen stoichiometry on the thermal boundary conductance across Au/TiO$_x$/substrate interfaces. Under HV conditions, where the evaporated Ti oxidizes upon reaching the substrate, we show that slower deposition rates correspond to a higher oxygen content in the TiO$_x$ layer, which results in a lower thermal boundary conductance across the Au/TiO$_x$/substrate interfacial region. Under UHV conditions, pure metallic Ti is deposited on the substrate surface. In the case of quartz substrates, the metallic Ti reacts with the substrate and getters oxygen leading to a TiO$_x$ layer. In the case of the Al$_2$O$_3$ and MgO cases, we demonstrate that h_K is dependent on the thickness of the adhesion layer. In general, our results suggest that

Ti layers with relatively low oxygen compositions are best suited to maximize the thermal boundary conductance.

See Appendix B3 for details including the choice of adhesion layer deposition rates, calculation of the adhesion layer stoichiometries and thicknesses, a description of TDTR, and a comparison of the XPS spectra of Ti deposited in HV and UHV.

6.2 Band alignment and defects influence the electron-phonon heat transport mechanisms across metal interfaces

The work presented in this section has previously been published in *Applied Physics Letters* [239], with contributions from the *Surface Materials Characterization for Devices Group* and *ExSiTE Lab* at UVa, as well as the *Laboratory of Quantum Dynamics* at USC. From the *Surface Materials Characterization for Devices Group*, Keren Freedy and Maria Sales performed sample preparation and X-ray photoelectron characterization and interpretation. Albert Tomko from the *ExSiTE Lab* aided in coding the two-temperature model for data interpretation, while Teng-Fei Lu from the *Laboratory of Quantum Dynamics* performed real-time time-dependent density functional theory calculation of Au/Ti$_x$O$_y$ systems. Experimental and theoretical guidance were provided by Oleg Prezhdo, Stephen McDonnell, and Patrick Hopkins.

6.2.1 Background

The interaction between excited electrons and phonons is fundamental to the functionality of a range of devices and technologies, such as photovoltaics [240–243], catalysis [244, 245], and optoelectronics [246–249]. Photovoltaics, in particular, rely on the lack of recombination of charge carriers prior to reaching electrodes, and thus a low electron/hole-phonon coupling rate is necessary for optimizing efficiency. As a result of this condition, TiO$_2$ is ubiquitously used in the photovoltaic industry due to its low recombination rate, wide band gap, and higher conduction band edge energy [250, 251]. In perovskite solar cells, TiO_2 layers have been implemented adjacent to the photoactive perovskite to facilitate fast electron transport to the transparent conducting oxide and maximize efficiency by reducing electron-phonon coupling [252].

Unsurprisingly, defects present in TiO_2 layers have been shown to inhibit the maximum attainable quantum efficiency, η, of solar cells. In one study, η was reduced by more than a factor of two in TiO_2 films containing oxygen vacancies [253]. In another, oxygen vacancies were correlated to second order scattering modes, alongside the presence of Ti^{4+}/Ti^{3+} mixed states [254]. Both of these factors decreased η by a factor of $\sim$2–4 as a result of an increase in the charge recombination rate as a result of an increased number of coupling pathways [255]. Further, Radecka *et al.* [256] have examined stoichiometry influences in oxygen deficient TiO_{2-x} films, where an increase in oxygen deficiency was correlated with a reduction in charge carrier mobility. Sharma *et al.* [257] have also shown that non-stoichiometry reduces η by a factor of two. Clearly, the defect concentration is integral in the performance of photovoltaic devices, impacting electron-phonon coupling, and must be accounted for during the fabrication process.

In this work, we study the effects of oxygen stoichiometry in TiO_x layers on electron-phonon coupling and resulting energy transport mechanisms, schematically illustrated in Fig. 6.5(a). This is accomplished by implementing ultrafast pump-probe spectroscopy to examine the non-equilibrium carrier dynamics of $Au/TiO_x/Al_2O_3$ systems, and quantifying the electron-phonon coupling factor, g, of thin TiO_x layers whose stoichiometry and thickness range from x = 0–2.62 and d = 0–4 nm, respectively. Additionally, we determine the efficiency of electron thermal transport across the Au/TiO_x interfacial region, quantified by the electron-electron thermal boundary conductance [56, 258, 259]. We find that both of these transport mechanisms are heavily influenced by the stoichiometry of the TiO_x layer, where residual metallic Ti^0 allows for more efficient electron-phonon coupling in the adhesion layer and electron energy transport at the Au/TiO_x interface as a result of the better band alignment between the Au and TiO_x, as quantified by time-dependent density functional theory.

Energy transport from a photonically excited electronic system of a metal contact to the phononic system of a dielectric substrate through an adhesion layer consists of numerous energy transport mechanisms within and between layers at ultrafast ($<$ 1000 ps) timescales. First, energy is deposited into the electronic system of the top metal contact via photon absorption. Electrons in this layer will traverse through the layer and scatter with a phonon at an average length scale of the mean free path. At the Au/TiO$_x$ interface, the efficiency of electron interfacial energy transport can be described by the electron diffuse mismatch model (EDMM) [56]. In short, the electron-electron interfacial conductance, G_{ee}, is proportional to the average electron temperature on either side of the interface, $T_{e,avg}$, via the ratio of the electronic densities of states and Fermi velocities, Γ. As electrons traverse the Au/TiO$_x$ interface, they couple to the lattice in the TiO$_x$ layer, increasing its temperature. This creates a temperature disparity between the top Au contact and underlying dielectric substrate in the electronic and lattice systems. Ultimately, this results in an indirect heating of the Au lattice temperature as a result of the mismatch in electron-phonon coupling with the TiO$_x$ layer which can be probed using ultrafast pump/probe spectroscopy.

6.2.2 Materials & Methods

To explore the effects of oxygen stoichiometry and thickness on electron-phonon coupling in TiO$_x$, as well as electron energy transfer at the Au/TiO$_x$ interface, we monitor the sub-picosecond to nanosecond excitation and relaxation processes of Au/TiO$_x$ samples with time-domain thermoreflectance. The specific samples and characterization of these samples are detailed in our prior work [197]. Briefly, 4 nm layers of TiO$_x$ were deposited in a high vacuum (HV) environment ($\sim 1 \times 10^{-6}$ Torr) at 0.1, 0.5, and 1.0 Å/s on a set of Al_2O_3 substrates. Due to the HV conditions during evaporation, the deposition resulted in TiO$_x$ with varying x based on the Ti deposition rate when assuming a consistent codeposition of oxidizing species across all specimens during the deposition procedure [197]. This TiO$_x$ adhesion layer was capped with $\sim$3 nm Au, and one of the substrates was re-

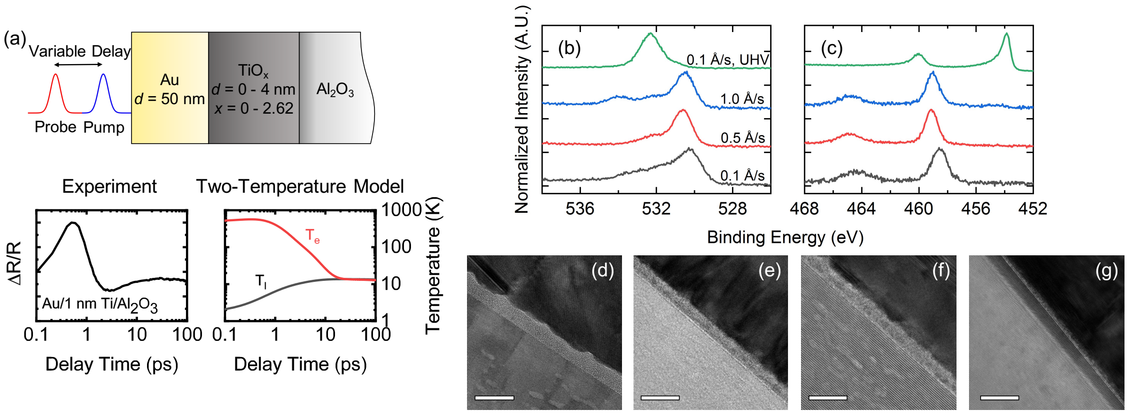

Figure 6.5. (a) Optical pump/probe experiment for determining energy transfer mechanisms in Au/TiO$_x$ structures. T_e and T_l are the surface temperature excursions of the electronic and lattice systems, respectively, in Au/1 nm Ti/Al$_2$O$_3$ as determined via the two-temperature model. (b) O 1s and (c) Ti 2p spectra of TiO$_\text{x}$ adhesion layers deposited in HV and UHV. TEM micrographs of adhesion layers deposited at (d) 0.1, (e) 0.5, and (f) 1.0 Å/s in HV and at (g) 0.1 Å/s in UHV. In (d)-(g), the scale bar is 5 nm.

moved from the chamber for characterization via x-ray photoelectron spectroscopy (XPS). The other was pumped down once again, and capped with an additional ~50 nm Au to facilitate thermal measurements via time-domain thermoreflectance [260, 261]. For comparative purposes, we fabricate systems without an adhesion layer (i.e., just 50 nm Au on Al$_2$O$_3$), as well as one with a 1 nm Ti adhesion layer deposited at ~0.1 Å/s in ultra-high vacuum (UHV) capped with 50 nm Au. The thickness of the Au layer for all these specimens, ~50 nm, is ideal in maximizing sensitivity to measurements of the electron-phonon coupling factor, g, and the electron-electron thermal boundary conductance, Γ, while minimizing additional optical thermoreflectance responses from the underlying TiO$_x$ layer that can obfuscate analysis (c.f., Appendix B4).

XPS spectra of the specimens with a TiO$_x$ adhesion layer are shown in Fig. 6.5 for the (b) O 1s and (c) Ti 2p spectra of the TiO$_x$ adhesion layers. Spectral deconvolution was performed on both spectra in order to determine (1) the fraction of oxygen that reacted with Ti to form TiO$_x$ during the deposition process, and (2) the fraction of unreacted Ti present in the layer, Ti^0. At 0.1 Å/s, approximately ~50% of the oxygen present in the adhesion layer comes directly from TiO$_x$, with the other ~50% coming from hydrocarbon and hydroxide species. On the other hand, oxygen from TiO$_x$ comprised ∼75% of the oxygen present in specimens deposited at 0.5 and 1.0 Å/s. At 0.1 Å/s in UHV, no oxygen originating from Ti-O bonds was found–the signature at ∼532 eV is of the Al$_2$O$_3$ substrate, and is detectable due to the thinness of the layer (1 nm). From the Ti 2p spectra, Fig. 6.5(c), spectral deconvolution indicates that the composition of Ti present at 0.1 and 0.5 Å/s is entirely of reacted Ti, Ti^{4+}. At 1.0 Å/s, however, the small signature at ∼455 eV indicates that approximately 4% of the layer comprised of unreacted Ti, Ti^0. In all, the O:Ti ratios of the TiO$_x$ layers deposited in HV, when accounting for only O-Ti features, were 2.62, 2.06, and 1.90 for specimens deposited at 0.1, 0.5, and 1.0 Å/s, respectively, while the specimen deposited in UHV appears purely metallic.

Shown in Fig. 6.5(d)-(g) are TEM micrographs of each specimen at the Au/TiO$_x$/Al$_2$O$_3$ interfacial regions. All samples deposited in HV show a consistent thickness of 3-4 nm and no signs of island formation. For the specimen deposited in UHV, Fig. 6.5(g), the thickness of the adhesion layer is consistent with that determined via XPS, ∼1 nm. In the specimens deposited in HV, there is a noticeable difference in structure between the samples deposited at 0.1 Å/s and those deposited at 0.5 and 1.0 Å/s. At 0.1 Å/s, the adhesion layer is completely amorphous, while at 0.5 and 1.0 Å/s, the interfacial layers show pockets of crystallinity. We are unsure of the exact reasons for the amorphous nature of the adhesion layer deposited at 0.1 Å/s in HV. Considering that the layer deposited at approximately the same deposition rate in UHV was crystalline, we hypothesize that the co-deposition of oxidizing species in HV played some role in the crystallization kinetics during the deposition of the layer.

We measure the ultrafast electron thermal transport mechanisms of the Au/TiO$_x$ samples with time-domain thermoreflectance (TDTR), an optical pump/probe technique. See Appendix B4 for additional details regarding TDTR. The acquired thermal decay is typically compared to the heat diffusion equation; however, at short, ultrafast timescales, where the dynamic interplay between electrons and phonons is most prevalent, the two-temperature model [52] (TTM) is implemented. Governed by the coupled partial differential equations,

$$\begin{aligned} C_e \frac{\partial T_e}{\partial t} &= \nabla \cdot (\kappa_e \nabla T_e) - g(T_e - T_l) + S(x,t) \\ C_l \frac{\partial T_l}{\partial t} &= \nabla \cdot (\kappa_l \nabla T_l) + g(T_e - T_l), \end{aligned} \tag{6.1}$$

the TTM considers both electrons and phonons as separate carriers of heat. In these equations, C_e and C_l are the electronic and lattice heat capacities, respectively, T_e and T_l are the electronic and lattice temperatures, κ_e and κ_l are the electronic and lattice thermal conductivities, and. g is the electron-phonon coupling factor. In the Au capping and TiO$_x$ adhesion layers, the electronic heat capacities are defined such that $C_e = \gamma T_e$, where γ is the electron heat capacity coefficient [43, 262]. $S(x,t)$ is the source term, which deposits energy into the electronic system, defined as such:

$$S(x,t) = -0.94 \frac{1-R}{t_p} J \cdot \exp[-2.77(\frac{t}{t_p})^2] \frac{dI}{dx}. \tag{6.2}$$

In this equation, J is the fluence, R is the surface reflectivity, t_p is the duration of the pump pulse, and x and t are the space and time variables, respectively. $\frac{dI}{dx}$ is the spatial derivative of the light intensity distribution in the sample, calculated using a transfer matrix method with the indices of refraction, n, at our pump wavelength of 400 nm.

Equations 6.1 and 6.2 are solved numerically using the Crank-Nicolson method [79]. Unless otherwise stated, all inputs into the model can be found in Table 6.1. For the Au/Al_2O_3 system, we fit for g of the Au film and the phonon conductance at the Au/Al_2O_3 interface. In systems with a TiO$_x$ adhesion layer, we fit for g of the adhesion layer, Γ at the Au/TiO$_x$ interface, as well as the phonon conductance at the TiO$_x$/Al_2O_3 interface. See Appendix B4 for additional details regarding the modeling and fitting procedure.

Table 6.1. Parameters utilized in TTM modeling and fitting. For each layer, d is the thickness, C_l is the lattice heat capacity, γ is the electronic heat capacity coefficient, κ_e and κ_l are the electronic and lattice thermal conductivities, respectively, g is the electron-phonon coupling factor, n is the complex refractive index, and dn/dT is the temperature derivative of the complex index of refraction. Fitting parameters are designated by **F** in Au, Au/TiO$_x$, and Au/Ti systems. In Au/TiO$_x$ and Au/Ti systems, we also fit for Γ, the proportionality constant for the electron-electron thermal conductance.

	Au	TiO$_x$	Ti	Al$_2$O$_3$
d (nm)	50*	4	1	
C_l (MJ m^{-3} K^{-1})	2.49^a	2.83^a	2.36^a	3.06^a
γ (J m^{-3} K^{-2})	63^b	329^b	329^b	
κ_e (W m^{-1} K^{-1})	276^x	1^d	10^a	
κ_l (W m^{-1} K^{-1})	3^e	1	2^a	35
g (10^{16} W m^{-3} K^{-1})	2.8 ± 0.7			
n (400 nm)	$1.47{+}i1.95^f$	2.37^g	$2.09{+}i2.96^f$	1.79^h
n (800 nm)	$0.15{+}i4.91^f$	2.10^g	$3.14{+}i4.01^f$	1.76^h
$dn/dT \times 10^4$ (800nm)	2.1^i	2.1^i	2.1^i	

*Measured using x-ray reflectivity.
[a] Ref. 66
[b] Ref. 43
[x] Determined using four-point probe and the Wiedemann-Franz law.
[d] Ref. 263
[e] Ref. 49
[f] Ref. 264
[g] Ref. 265
[h] Ref. 266
[i] Ref. 62

6.2.3 Results & Discussion

Figure 6.6 shows the acquired ultrafast reflectivity and best fits for the Au/TiO$_x$ systems in the range of x = 0–2.62, alongside Au for reference. The response of TiO$_{2.06}$ was not included because of its similarity to TiO$_{1.90}$. At short time scales (< 4 ps), a sharp increase in the reflectivity followed by its decay is observed across all specimens due to the dynamic electron temperature following excitation. At longer time scales (> 4 ps), the response de-

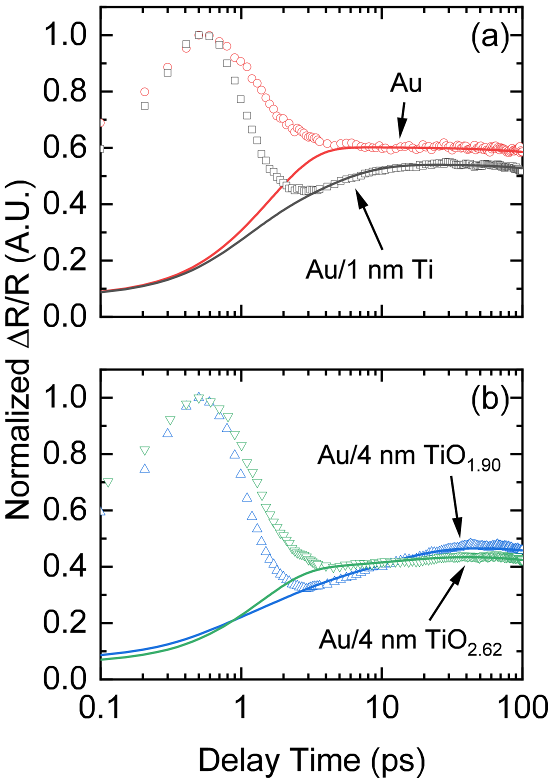

Figure 6.6. Ultrafast data and TTM best fits ($>$ 3 ps) for (a) Au and Au/1 nm Ti and (b) Au/4 nm TiO$_x$ systems.

pends on the composition of the adhesion layer. For the system lacking an adhesion layer, the reflectivity is approximately constant and decays slightly. On the other hand, systems with an adhesion layer exhibit a rise in reflectivity compared to that at ~3 ps. Both the rate at which this rise occurs and its final magnitude depend on the stoichiometry of the underlying adhesion layer, and is characteristic of electron energy transport and the mismatch of electron-phonon coupling factors in metal/metal [82, 83, 233] and metal/semiconductor [267] systems.

The extracted g and Γ for all systems are presented in Fig. 6.7(a) and (b), respectively. For systems with a TiO$_x$ adhesion layer, we cannot distinguish between the intrinsic transport characteristics of g and Γ and those due to the nanometer roughness at the Au/TiO$_x$ interface. Our reported values therefore reflect both intrinsic transport mechanisms within the TiO$_x$ and at the Au/TiO$_x$ interfaces, as well as the contribution from any extrinsic ef-

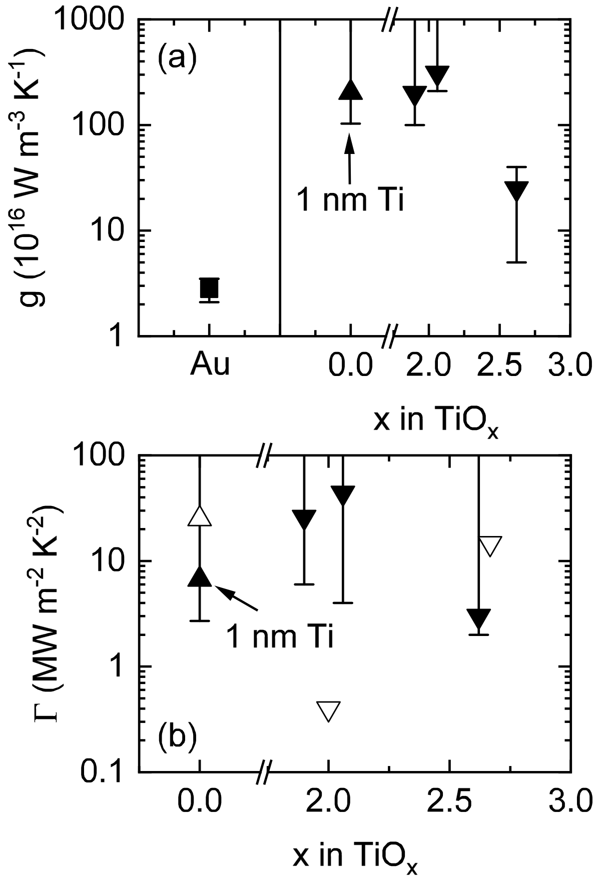

Figure 6.7. Experimentally determined (a) electron-phonon coupling (g) of TiO$_x$ wetting layers and (b) coefficient of electron-electron thermal conductance (Γ) at Au/TiO$_x$ interfaces. Filled symbols are experimentally determined, while open symbols are predicted by the electronic diffuse mismatch model (EDMM).

fects as a result of the roughness at the Au/TiO$_x$ interfacial region. We determine the electron-phonon coupling factor of Au to be $2.8 \pm 0.7 \times 10^{16}$ W m^{-3} K^{-1}, in reasonable agreement with previously reported values [268–271]. The predicted value for the electron-phonon coupling factor in Ti is $\sim 150 \times 10^{16}$ W m^{-3} K^{-1} at room temperature [43]. This large value, coupled with the small thickness, d, of the adhesion layer results in a large electron-phonon conductance in the Ti layer, gd. As a result, we set a lower limit on the electron-phonon coupling factor of Ti, as values above 100×10^{16} W m^{-3} K^{-1} offer comparable fits to our data. We find g of the oxygenated adhesion layers with stoichiometries

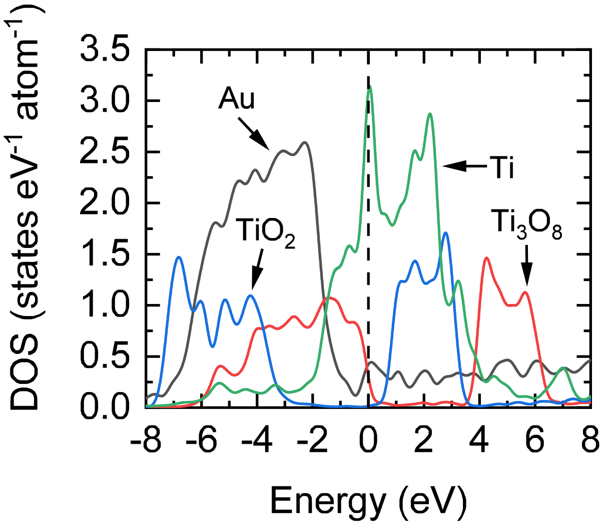

Figure 6.8. Electron density of states (DOS) of Au, Ti, TiO_2, and Ti_3O_8 from Lu *et al.* [272]. Reproduced with permissions from J. Phys. Chem. Lett. 11, 4 (2020). Copyright 2020 American Chemical Society [272].

$TiO_{1.90}$ and $TiO_{2.06}$ to be similar to that of the 1 nm pure Ti layer, $> 100 \times 10^{16}$ W m^{-3} K^{-1}. This high g in a highly defected TiO_x layer is likely due to the fact that residual, unreacted Ti is present in these films, allowing for a low resistance pathway from the Au to TiO_x adhesion layer. Indeed, we observe that $\sim$4% of the Ti in $TiO_{1.90}$ layer consists of unreacted Ti^0. We note that while the presence of Ti^0 cannot be confirmed via XPS in the specimen with a stoichiometry of $TiO_{2.06}$, g for this layer is still comparable to that of pure Ti. This suggests that fractions of Ti less than the detectable limits of XPS ($\sim$0.5–1%) are still able to significantly impact the transport processes in these systems. Once the oxygen concentration of the adhesion layer is greatly increased, reaching a stoichiometry of $TiO_{2.62}$, no residual Ti^0 can be confirmed, and this low resistance pathway is not present. We find that g for the $TiO_{2.62}$ layer is $\sim$25 $\times 10^{16}$ W m^{-3} K^{-1}, suggesting that coupling still occurs in the $TiO_{2.62}$ layer at a rate that exceeds that of the Au film.

Figure 6.7(b) shows the results for the electronic thermal conductance coefficient, Γ. As with g in the 1 nm Ti adhesion layer, the incredibly high electron-electron conductance at the Au/Ti interface makes g and Γ difficult to quantify. Indeed, the electronic diffuse-mismatch model predicts Γ to be 25 MW m^{-2} K^{-2}, or an equivalent conductance of nearly 7.5 GW m^{-2} K^{-1} at room temperature. We can thus only place a lower bound on Γ, as equivalent fits in our model are found for when $\Gamma > 2$ MW m^{-2} K^{-2}. EDMM calculations of Γ, shown as open symbols in Fig. 6.7(b), using the electron density of states (DOS) from Fig. 6.8, exemplify the importance of stoichiometry in these models. In particular, due to the presence of Ti^0 in our TiO$_x$ films, our measured Γ exceeds the theoretical value for Au/TiO$_2$ by an order of magnitude. Additionally, the measured lower bound for Γ in TiO$_{2.62}$, which has a stoichiometry that is close to Ti$_3$O$_8$, is in reasonable agreement with the EDMM predicted value for Au/Ti$_3$O$_8$.

To better understand the reasons for our measured g and Γ, we focus on examining stoichiometric effects in Au/Ti$_x$O$_y$ on electron-phonon relaxation times using real-time time-dependent density functional theory (TDDFT) [272], the simulation details of which can be found in Appendix B4. In Fig. 6.9, we plot the (a) picosecond pump/probe dynamics of our Au/TiO$_x$ systems alongside the (b) electron energy decay of Au/Ti$_x$O$_y$ calculated using TDDFT in Ref. 272. Because the short-time response of our acquired data are indicative of the electron temperatures of Au and TiO$_x$ in our specimens, we normalize the data such that the signal decays to 0 at 3 ps for comparative purposes only. This approximately reflects the time at which the energy of the excited electrons have decayed to 0 eV, allowing us to make direct comparisons to the TDDFT predictions. We also adjust the 0 time delay to the maximum of the acquired signal.

We find that the measured relaxation times of our Au/TiO$_x$ systems are in qualitative agreement with those derived from TDDFT. In Au and Au/TiO$_{2.62}$ systems, we determine relaxation times of $\sim$650 fs. For Au/TiO$_x$ systems for x = 0, 1.90, and 2.06, the relaxation time is faster, $\sim$420 fs. Our measured relaxation times reflect electron-electron as well as electron-phonon interactions. Lu *et al.* [272] determined relaxation times of 2.75, 2.85, 1.99, and 0.75 ps for Au, Au/Ti$_3$O$_8$, Au/TiO$_2$, and Au/Ti systems, respectively. We cannot make direct comparisons to Ref. 272 due to the fact that they do not account for electron-electron interactions and the simulation is not able to capture all electronic and phononic

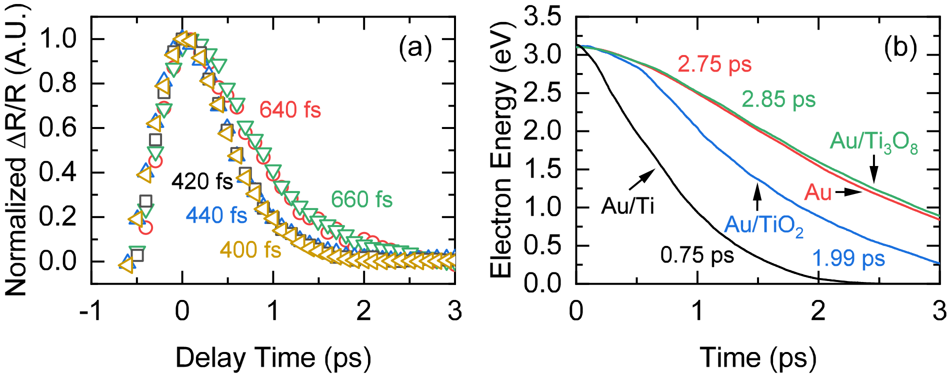

Figure 6.9. (a) Normalized ultrafast response of Au films with a TiO$_x$ wetting layer. Red circles are for the Au system, green down-facing triangles are for the Au/TiO$_{2.62}$ system, gold left-facing triangles are for the Au/TiO$_{2.06}$ system, blue up-facing triangles are for the Au/TiO$_{1.90}$ system, and black squares are for the Au/1 nm Ti system. (b) Electron relaxation dynamics from Lu *et al.* [272] for Au/Ti$_x$O$_y$ systems. Reproduced with permissions from J. Phys. Chem. Lett. 11, 4 (2020). Copyright 2020 American Chemical Society [272].

states due to its size. However, we find that our derived relaxation times trend well with those of Lu *et al.* [272] when considering the minute differences in stoichiometry.

The reason for the decreased relaxation time in Au/TiO$_x$ systems for $x = 0$, 1.90, and 2.06 is influenced by a variety of factors, including (1) the presence of Ti^0, (2) the excited electron energy relative to the Fermi energy, and (3) the relative position of the Fermi energy in Au to the conduction and valence bands of TiO$_x$.

Primarily, Ti^0 atoms present in TiO$_{1.90}$ and TiO$_{2.06}$ accelerate the relaxation time due to the higher g of Ti. As the fraction of Ti^0 in these layers is small as confirmed via XPS, and the composition is nominally TiO$_2$, lighter Ti and O atoms in TiO$_2$ move faster to help increase electron-phonon coupling compared to Au. Indeed, inspection of the nonadiabatic electron-phonon coupling matrix element, $i\hbar\langle\Phi_j|\nabla_R|\Phi_k\rangle \cdot d\boldsymbol{R}/dt$, which describes the transition between electronic states j and k by coupling to phonons, is proportional to the phonon velocity, $d\boldsymbol{R}/dt$ [273].

Additionally, the alignment of the TiO$_x$ energy levels with respect to the Au Fermi energy influences charge-phonon relaxation, see Fig. 6.8. For an accelerated relaxation process to occur, the energy of excited electrons in the Au must fall outside of the TiO$_x$ bandgap so that they may interact with those in the adhesion layer. As the incident photon energy (3.1 eV) generates the same number of electrons and holes, an equivalent number of conductance and valence band orbitals will be involved in the photoexcitation process. Since the hole DOS is larger than the electron DOS in Au, the generation of a particular number of hole states requires a smaller energy range compared to the same number of electron states. Thus, as a result of this asymmetry in DOS, the photoexcitation process covers a broader range of electron state energies, and electrons therefore accommodate the majority of the incident photon energy. Excited electrons in the Au will therefore be above the bandgap of TiO$_2$, increasing coupling.

Further, the Au Fermi energy is within $\sim$1 eV of the conduction band (CB) minimum of TiO$_2$, resulting in a resonance of the TiO$_2$ CB states and Au electrons near the Fermi energy and increasing electron-phonon relaxation. The Au Fermi energy is also within $\sim$0.5 eV of the valence band (VB) maximum for Ti$_3$O$_8$, whose stoichiometry is close to TiO$_{2.62}$. At this stoichiometry, electrons excited to 3.1 eV above the Au Fermi energy fall within the band gap of of the adhesion layer, and thus electron-phonon coupling is subdued due to the fact electrons in the TiO$_{2.62}$ layer cannot participate in the process resulting in a comparable relaxation time to the system lacking an adhesion layer.

In summary, we performed ultrafast pump/probe measurements for the determination of the electron-phonon coupling factors of thin TiO$_x$ layers and the associated electron-electron conductance across the Au/TiO$_x$ interface. Our results are indicative of the fact that even a small fraction of unreacted Ti in TiO$_x$ adhesion layers has a significant impact on the associated energy transfer mechanisms across Au/TiO$_x$ interfacial regions. TiO$_x$ layers with stoichiometries close to TiO$_2$, when unreacted Ti is still present, offer comparable electron-phonon coupling factors and electron-electron thermal boundary conductances to that of pure Ti. The data are in agreement with real-time TDDFT calculations, and the results provide fundamental insight to applications requiring the use of metal oxide nanoscale films and interfaces in systems where charge relaxation plays a significant role in optimizing efficiencies.

See Appendix B4 for a description of TDTR, experimental insight into the electron-phonon relaxation length scales, parameters used in two-temperature modeling, and a description of density functional theory calculations.

6.3 Summary

In this chapter, we examined the foundational component to the integration of metal contacts in nanoelectronic devices: the adhesion layer. Specifically, we examined Au contacts with a TiO$_x$ adhesion layer, whose stoichiometry was varied from x = 0–2.62 in an effort to elucidate the energy transport mechanisms from the Au contact into the substrate. In the first half of the chapter, this was viewed from a pure conductance standpoint, in which the interfacial conductance at the Au/TiO$_x$/substrate interface was examined. Both the adhesion layer and substrate stoichiometries determined this interfacial conductance, where oxygen-rich TiO$_x$ films reduced the conductance to that without an adhesion layer. When energetically favorable, Ti atoms in the adhesion layer will react with the substrate to form TiO$_x$, impeding transport from the metal to the substrate. In the second half of the chapter, the two-temperature model was used in determining the electron-phonon coupling of the adhesion layer alongside the interfacial electron-electron conductance at the Au/TiO$_x$ interfacial regions. As these adhesion layers were not stoichiometric TiO$_2$ and Ti$_3$O$_8$, residual Ti^0 present in these systems increased electron-phonon coupling of the layer to that of pure Ti. Electron energy transmission was found to be high across all specimens with an adhesion layer, regardless of stoichiometry. The relaxation dynamics were compared to calculations made by real-time time-dependent density functional theory, and were found to be in good agreement with one another when considering stoichiometry.

Chapter 7

Summary and Future Outlook

Heat transfer processes in a gas turbine engine are vastly different from those in nanoscopic devices. While the structure and functionality may be similar in such applications, the heat transfer processes must be examined from a macroscopic and nanoscopic perspective. In this dissertation, an emphasis was placed on the thermal characterization of these applications using time-domain thermoreflectance (TDTR). Doing so allowed for the understanding of the heat transfer processes of barrier coating components as well as the methodologies of interfacial transport in an Au/substrate system with a TiO_x adhesion layer. In barrier coating materials, I specifically examined the anisotropic thermal properties of β-$Y_2Si_2O_7$, as well as the spatially-varying thermal conductivity of a steam cycled β-$Yb_2Si_2O_7$ coating. This was performed using TDTR mapping approach, and indicate that spatial inhomogeneity and anisotropy have the potential to influence the temperature gradient induced via such a coating. The mapping approach was also applied to the characterization of α-cristobalite formation in thin TGO layers, demonstrating the throughput and resolution of TDTR. In the nanoscopic regime, interfacial conductance and electron-phonon coupling were examined in Au/substrate systems with a TiO_x adhesion layer. The results were examined from the perspective of carrier equilibrium and carrier non-equilibrium. In all, these studies exemplify the multifunctional capabilities of TDTR. A summary of each chapter is presented below.

7.1 Summary

In Chapter 2, thermal transport concepts were presented as a foundation of the experiments to be performed in this dissertation. The thermal conductivity was first discussed from a continuum and subcontinuum perspective. In the continuum limit, I discussed the tensorial representation of the thermal conductivity. An understanding of this representation was necessary for determining the anisotropic thermal conductivity of β-$Y_2Si_2O_7$, performed in Chapter 4. Defining the thermal conductivity in this way is also applicable to a variety of other anisotropic materials. In the subcontinuum limit, however, an emphasis was placed on thermal conduction from the perspective of material carriers, namely electrons and phonons. The heat capacities, velocities, and mean free paths of each carrier were discussed, all in the framework of the kinetic theory of gasses. Because considerations of interfaces must be made in this subcontinuum limit, interfacial transport at dielectric/dielectric, metal/metal, and metal/dielectric interfaces were defined. These modalities of thermal transport were essential for characterizing transport in Au/TiO_x systems found in Chapter 6.

In Chapter 3, I discussed the metrology pertinent to this dissertation. The primary focus here was time-domain thermoreflectance, as it was implemented in all experiments. The associated heat transfer analysis was examined from two perspectives: carrier equilibrium and carrier non-equilibrium. The former was most pertinent for the extraction of the thermal conductivities of barrier coating materials in Chapter 4, monitoring crystallinity in thermally grown oxides in Chapter 5, and measuring interfacial conductances in Chapter 6. For carrier non-equilibrium, I presented the two-temperature model formalism whereby the temperature excursions for both electrons and phonons must be accounted for. Finally, the fundamentals for the extension of time-domain thermoreflectance to spatially probe thermal properties was presented. This enabled large-scale thermal property images with micrometer resolution.

In Chapter 4, the main focus was acquiring thermal conductivity micrographs to characterize EBC components. Specifically, the anisotropic thermal conductivity of β-$Y_2Si_2O_7$, the crystal structure of which is monoclinic, was assessed. This was accomplished by correlating thermal conductivity micrographs to electron backscatter diffraction micrographs, where Euler angles in the latter were used to determine the orientations of numerous crystallites relative to the measurement configuration. In this way, the thermal conductivity of β-$Y_2Si_2O_7$ was found to vary between 5 and 7 W m^{-1} K^{-1} depending on its orientation. Extending these measurements to a relevant coating system, the latter portion of the chapter was devoted to measuring the spatially varying thermal conductivity of an EBC with a β-$Yb_2Si_2O_7$ topcoat. Measurements performed at 0, 500, and 2000 cycling hours reveal that the thermal conductivity of the system evolves dynamically, owing to the reactions between steam and the topcoat at the exterior of the coating and between the topcoat and thermally grown oxide. Further characterization of the microstructure via electron-backscatter diffraction indicated that significant grain coarsening occurs as the system is cycled to 2000 hours.

Chapter 5 featured the continuation of the characterization of EBC systems. In this chapter, however, emphasis was not placed on measurements of thermal conductivity with respect to the insulating characteristics of a coating, but rather as a diagnostic tool for the formation of α-cristobalite in the thermally grown oxide of an EBC. A case study was performed to ensure that the delineation between α-cristobalite and $aSiO_2$ could be made based on their associated thermal conductivities. Indeed, this study revealed that the thermal conductivity of α-cristobalite was approximately twice that of $aSiO_2$ at $\sim$2.7 W m^{-1} K^{-1}. Knowing this, an emphasis was placed on characterizing a relevant EBC system in which varying degrees of crystallinity existed in the thermally grown oxide layer. Several specimens were examined, including ones with entirely amorphous, entirely crystalline, and partially crystalline thermally grown oxide layers. In the specimen with an amorphous TGO layer, the thermal conductivity of the TGO was consistent with that of $aSiO_2$. A clear delineation could also be made between all pertinent layers of the EBC based on the thermal conductivities of each layer. In the crystalline TGO layer, the thermal conductivity was consistent with that of α-cristobalite, determined in the case study in the first half of the chapter. Finally, a partially crystalline specimen was examined, and the fraction of crystallinity was assessed based on the thermal conductivity distribution within the TGO layer.

In Chapter 6, I delved into the subcontinuum limit by examining the Au/TiO$_x$ system. By fabricating these systems under a variety of deposition conditions, the stoichiometry of the TiO$_x$ layers was varied between 0 and 2.62, with thicknesses varying from 0 to 9 nm. The interfacial conductances were then probed using time-domain thermoreflectance, where a correlation was made to the stoichiometries and thicknesses of the wetting layers. Specifically, as the adhesion layer became more oxygenated, the interfacial conductance was decreased, and as the thickness of the adhesion layer increased for $x = 0$, the interfacial conductance decreased. In specimens deposited on quartz, the interfacial conductance was approximately constant in this parameter space, owing to the fact that the SiO$_2$ substrate interacts with Ti to form TiO$_x$. In the second half of the chapter, the mechanisms by which energy was transported into the substrates was assessed. Specifically, short delay times ($<$ 1000 ps) in the time-domain thermoreflectance response were analyzed under the two-temperature formalism, outlined in Chapter 3. This enabled the extraction of the electron-phonon coupling factor of the wetting layers. Despite the stoichiometries of many of the systems being near TiO$_2$, small amounts of Ti^0 defects resulted in a measured electron-phonon coupling factor comparable to pure Ti adhesion layers deposited in UHV. When the system consisted of heavily oxygenated TiO$_x$, a much lower electron-phonon coupling factor was extracted. Ultimately, the extracted electron-phonon coupling factors for each adhesion layer were directly correlated to their respective interfacial conductances, suggesting that the net conductance across the interface is largely mediated by the electron-phonon coupling factor of the interfacial region.

7.2 Future Outlook

This dissertation is by all means not all-encompassing in terms of the thermal characterization of environmental/thermal barrier coating components or Au contacts with an adhesion layer. The studies are highly specific to a given material system, and while relations can be made to additional, similar material systems, differences in microstructure, phase, stoichiometry, etc., ultimately necessitate additional studies. Additionally, the conditions under which these experiments were performed ares fundamentally different than those in which a coating or device may be implemented. As such, there are several future avenues in which one could expand on each of the experiments presented in this dissertation:

- **High temperature thermal conductivity measurements:** In Chapter 4, the anisotropic thermal conductivity of β-$Y_2Si_2O_7$ was assessed, and the spatially varying thermal conductivity of a β-$Yb_2Si_2O_7$ EBC was examined as a function of cycling time. In both of these experiments, measurements were performed at room temperature and the extracted data, thus, do not reflect those at the typical operating temperature of the hot section of a gas-turbine engine. Recently, through working with various colleagues, I have begun to make high temperature measurements exceeding 1000 °C by judiciously controlling experimental parameters. In practice, each of the studies performed in Chapter 4 could be performed at elevated temperatures, revealing the (1) anisotropic and (2) spatially-varying thermal conductivity of these materials at temperatures relevant to their typical operating environments.

- ***In situ* characterization of thermally grown oxides:** In Chapter 5, I characterized the thermally grown oxide of a relevant EBC system. All these measurements were performed *ex situ*, requiring significant sample preparation and ultimately increasing the requisite time to perform measurements. Specifically, the cross-sectioning necessary to probe the thin TGO layer does not allow for its characterization *in situ*. Thus, a push must be made to characterize the TGO layer from the plan-section of an EBC system. In Chapter 3, I discussed a little bit about the implementation of

SSTR, and how it is fundamentally different than TDTR in that the volume probed is much larger. As such, SSTR is more sensitive to subsurface features than TDTR. With sufficiently large spot sizes and power, one could probe the plan-section of an EBC to gain insight into the characteristics of the underlying TGO layer.

- **Infrared/ultraviolet pump/probe measurements of metal/dielectric contacts with a thin adhesion layer:** In Chapter 6, measurements of interfacial conductance and electron-phonon coupling were performed in Au/dielectric systems with a thin TiO_x adhesion layer. In the latter half of the chapter, the ultrafast portion of the data acquired via TDTR was analyzed using the two-temperature model, which interprets the electrons and lattice subsystems having two distinct temperature profiles. However, at a probe wavelength of 800 nm, the magnitude of the reflectivity is dictated by both electronic and lattice subsystems. As the analysis was contingent on just the lattice subsystem to determine the reflectivity, there inherently exists uncertainty in the data at shorter pump/probe delay times, < 5 ps. This is due to the fact that both the temperatures of the electronic and lattice systems are sufficiently high to contribute to the reflectivity. As such, an experimental means of examining the temperatures of each carrier would be foundational in the understanding of the dynamics of the system. Recently, developments have been made in our lab to specifically probe the electronic and lattice temperatures using tunable infrared and ultraviolet pump/probe systems. As a result of the breadth of wavelengths available between these systems, these measurements are able to delineate between electron and lattice temperature excursions. In conjunction with two-temperature model analysis, these measurements have the potential to offer additional insight into the carrier dynamics in metal/substrate systems with a thin wetting layer.

Appendix A

Published Work

As part of my dissertation, I have published 7 first author publications [71, 86, 124, 157, 168, 197, 239] and 1 co-first author publication [274] in peer-reviewed journals. With the help of Dr. Braun and Dr. Hopkins, I published a Perspective in the *Journal of Applied Physics* [157], which became one of the most read Editor's picks of 2019. Five of my first-author publications have been included in this document [86, 124, 168, 197, 239], while select sections from the Perspective were included in Chapter 2 [157]. In addition to these contributions, I have also contributed to 17 peer-reviewed publications as a coauthor [267, 275–278, 278–289]. In reverse chronological order, these first author, co-first author, and coauthor contributions are as follows:

25. **Olson, D. H.**, Sales, M. G., Tomko, J. A., Lu, T. F., Prezhdo, O. V., McDonnell, S. J., and Hopkins, P. E., "Band alignment and defects influence the electron-phonon heat transport mechanisms across metal interfaces," *Applied Physics Letters*, vol. 118, no. 16, pp. 1–7, 2021

24. Fields, S. S., **Olson, D. H.**, Jaszewski, S. T., Fancher, C. M., Smith, S. W., Dickie, D. A., Esteves, G., Henry, M. D., Davids, P. S., Hopkins, P. E., and Ihlefeld, J. F., "Compositional and phase dependence of elastic modulus of crystalline and amorphous $Hf_{1-x}Zr_xO_2$ thin films," *Applied Physics Letters*, vol. 118, no. 10, 2021

23. Aryana, K., Gaskins, J. T., Nag, J., Stewart, D. A., Bai, Z., Mukhopadhyay, S., Read, J. C., **Olson, D. H.**, Hoglund, E. R., Howe, J. M., Giri, A., Grobis, M. K., and Hopkins, P. E., "Interface controlled thermal properties of ultra-thin chalcogenide-based phase change memory devices,"

Nature Communications, vol. 12, 2021

22. Tomko, J. A., Runnerstrom, E. L., Wang, Y. S., Chu, W., Nolen, J. R., **Olson, D. H.**, Kelley, K. P., Cleri, A., Nordlander, J., Caldwell, J. D., Prezhdo, O. V., Maria, J. P., and Hopkins, P. E., "Long-lived modulation of plasmonic absorption by ballistic thermal injection," *Nature Nanotechnology*, vol. 16, pp. 47–51, 2021

21. **Olson, D. H.**, Deijkers, J. A., Quiambao-Tomko, K., Gaskins, J. T., Richards, B. T., Opila, E. J., Hopkins, P. E., and Wadley, H. N. G., "Evolution of microstructure and thermal conductivity of multifunctional environmental barrier coating systems," *Materials Today Physics*, vol. 17, 2021

20. Zhang, F., Zheng, B., Sebastian, A., **Olson, D. H.**, Liu, M., Fujisawa, K., Pham, Y. T. H., Jimenez, V. O., Kalappattil, V., Miao, L., Zhang, T., Pendurthi, R., Lei, Y., Elías, A. L., Wang, Y., Alem, N., Hopkins, P. E., Das, S., Crespi, V. H., Phan, M. H., and Terrones, M., "Monolayer Vanadium-Doped Tungsten Disulfide: A Room-Temperature Dilute Magnetic Semiconductor," *Advanced Science*, vol. 7, no. 24, pp. 1–9, 2020

19. Liu, H., Grasseschi, D., Dodda, A., Fujisawa, K., **Olson, D. H.**, Kahn, E., Zhang, F., Zhang, T., Lei, Y., Branco, R. B. N., El'ias, A. L., Silva, R. C., Yeh, Y.-T., Maroneze, C. M., Seixas, L., Hopkins, P., Das, S., de Matos, C. J. S., and Terrones, M., "Spontaneous chemical functionalization via coordination of Au single atoms on monolayer MoS_2," *Science Advances*, vol. 6, no. 49, 2020

18. Rasel, M. A. J., Giri, A., **Olson, D. H.**, Ni, C., Hopkins, P. E., and Feser, J. P., "Chain-Length Dependence of Thermal Conductivity in 2D Alkylammonium Lead Iodide Single Crystals," *ACS Applied Materials and Interfaces*, vol. 12, no. 48, pp. 53705–53711, 2020

17. Zhu, T., **Olson, D. H.**, Hopkins, P. E., and Zebarjadi, M., "Heat diffusion imaging: In-plane thermal conductivity measurement of thin films in a broad temperature range," *Review of Scientific Instruments*, vol. 91, no. 11, 2020

16. Giri, A., Chou, S. S., Drury, D. E., Tomko, K. Q., **Olson, D. H.**, Gaskins, J. T., Kaehr, B., and Hopkins, P. E., "Molecular tail chemistry controls thermal transport in fullerene films," *Physical Review Materials*, vol. 4, no. 6, pp. 1–8, 2020

15. Freedy, K. M., Zhu, T., **Olson, D. H.**, Litwin, P. M., Hopkins, P. E., Zebarjadi, M., and McDonnell, S. J., "Interface chemistry and thermoelectric characterization of Ti and TiO_x contacts to MBE-grown WSe_2," *2D Materials*, vol. 7, no. 4, 2020

14. **Olson, D. H.**, Avincola, V. A., Parker, C. G., Braun, J. L., Gaskins, J. T., Tomko, J. A., Opila,

E. J., and Hopkins, P. E., “Anisotropic thermal conductivity tensor of β-$Y_2Si_2O_7$ for orientational control of heat flow on micrometer scales,” *Acta Materialia*, vol. 189, pp. 299–305, 2020

13. Aryana, K., Gaskins, J. T., Nag, J., Read, J. C., **Olson, D. H.**, Grobis, M. K., and Hopkins, P. E., “Thermal properties of carbon nitride toward use as an electrode in phase change memory devices,” *Applied Physics Letters*, vol. 116, no. 4, 2020

12. **Olson, D. H.**, Gaskins, J. T., Tomko, J. A., Opila, E. J., Golden, R. A., Harrington, G. J., Chamberlain, A. L., and Hopkins, P. E., “Local thermal conductivity measurements to determine the fraction of α-cristobalite in thermally grown oxides for aerospace applications,” *Scripta Materialia*, vol. 177, pp. 214–217, 2020

11. **Olson, D. H.**, Braun, J. L., and Hopkins, P. E., “Spatially resolved thermoreflectance techniques for thermal conductivity measurements from the nanoscale to the mesoscale,” *Journal of Applied Physics*, vol. 126, no. 150901, pp. 47–55, 2019

10. Freedy, K. M., **Olson, D. H.**, Hopkins, P. E., and McDonnell, S. J., “Titanium contacts to MoS_2 with interfacial oxide: Interface chemistry and thermal transport,” *Physical Review Materials*, vol. 3, no. 10, pp. 1–7, 2019

9. Rosul, M. G., Lee, D., **Olson, D. H.**, Liu, N., Wang, X., Hopkins, P. E., Lee, K., and Zebarjadi, M., “Thermionic transport across gold-graphene-WSe_2 van der Waals heterostructures,” *Science Advances*, vol. 5, no. 11, 2019

8. Braun, J. L., **Olson, D. H.**, Gaskins, J. T., and Hopkins, P. E., “A steady-state thermoreflectance method to measure thermal conductivity,” *Review of Scientific Instruments*, vol. 90, no. 2, 2019

7. Tomko, J. A., **Olson, D. H.**, Giri, A., Gaskins, J. T., Donovan, B. F., O’Malley, S. M., and Hopkins, P. E., “Nanoscale Wetting and Energy Transmission at Solid/Liquid Interfaces,” *Langmuir*, vol. 35, pp. 2106–2114, 2019

6. **Olson, D. H.**, Rost, C. M., Gaskins, J. T., Szwejkowski, C. J., Braun, J. L., and Hopkins, P. E., “Size effects on the cross-plane thermal conductivity of transparent conducting indium tin oxide and fluorine tin oxide thin films,” *IEEE Transactions on Components, Packaging and Manufacturing Technology*, vol. 9, no. 1, pp. 51–57, 2019

5. Braun, J. L., Rost, C. M., Lim, M., Giri, A., **Olson, D. H.**, Kotsonis, G. N., Stan, G., Brenner, D. W., Maria, J. P., and Hopkins, P. E., “Charge-induced disorder controls the thermal conductivity

of entropy-stabilized oxides," *Advanced Materials*, vol. 30, no. 51, pp. 1–8, 2018

4. Giri, A., King, S. W., Lanford, W. A., Mei, A. B., Merrill, D., Li, L., Oviedo, R., Richards, J., **Olson, D. H.**, Braun, J. L., Gaskins, J., Deangelis, F., Henry, A., and Hopkins, P. E., "Interfacial Defect Vibrations Enhance Thermal Transport in Amorphous Multilayers with Ultrahigh Thermal Boundary Conductance," *Advanced Materials*, vol. 30, no. 44, pp. 1–6, 2018

3. **Olson, D. H.**, Freedy, K. M., McDonnell, S. J., and Hopkins, P. E., "The influence of titanium adhesion layer oxygen stoichiometry on thermal boundary conductance at gold contacts," *Applied Physics Letters*, vol. 112, no. 171602, 2018

2. Tomko, J. A., **Olson, D. H.**, Braun, J. L., Kelliher, A. P., Kaehr, B., and Hopkins, P. E., "Substrate thermal conductivity controls the ability to manufacture microstructures via laser-induced direct write," *Applied Physics Letters*, vol. 112, no. 5, 2018

1. Donovan, B. F., Tomko, J. A., Giri, A., **Olson, D. H.**, Braun, J. L., Gaskins, J. T., and Hopkins, P. E., "Localized thin film damage sourced and monitored via pump-probe modulated thermoreflectance," *Review of Scientific Instruments*, vol. 88, no. 5, 2017

Appendix B

Supplementary Data

B1 Anisotropic Thermal Conductivity of Yttrium Disilicate

B1.1 Scanning Electron and Electron-Backscatter Diffraction Micrographs

Scanning electron micrographs of the three regions examined in this work are shown in Fig. B1. Two sets of FIB marks were placed on the sample in order to view the areas under under our optical setup prior to TDTR mapping, as well as to allow for SEM, EBSD, and thermal map overlays for identification of grains between the three techniques. Electron backscatter diffraction (EBSD) micrographs were taken to identify the phase of the grains, as $Y_2Si_2O_7$ exhibits numerous polymorphs. Figure B2 shows phase images for each of the three regions, which are mainly composed of the β polymorph of $Y_2Si_2O_7$. We note that the γ phase of the disilicate is present in region I, however we do not include this grain in our analysis of the thermal conductivity tensor of β-$Y_2Si_2O_7$.

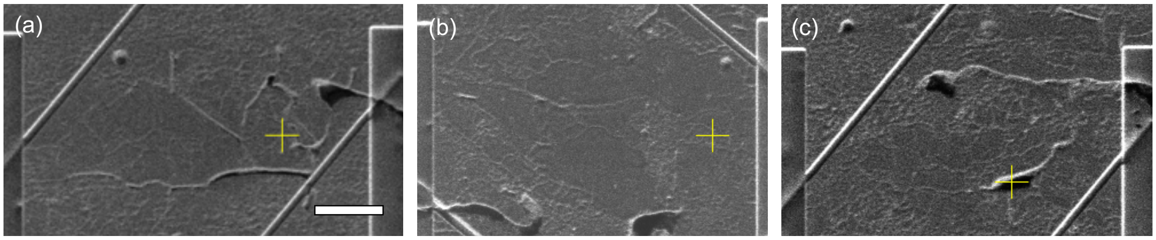

Figure B1. Scanning electron micrographs of the FIBed regions, prior to TDTR mapping. Figures (a), (b), and (c) correspond to mapped regions I, II, and III, respectively. Two sets of FIB marks, thin diagonally and thick vertically oriented, were used to help identify the location of grains within regions. The scale bar shown in (a) is 10 μm.

B1.2 Time-Domain Thermoreflectance Analysis

We use time-domain thermoreflectance (TDTR) to spatially monitor and determine the thermal conductivity of β-$Y_2Si_2O_7$. In our two-tint system, we spectrally separate the output of an 80 MHz Tsunami Ti:Sapphire oscillator centered at 808.5 nm into pump and probe paths. The pump path is amplitude modulated by an electro-optic modulator, and creates a frequency-dependent heating event at the surface of the sample. The probe is mechanically delayed in time, and monitors the thermoreflectance at the sample surface due to the pump heating event. We fix the modulation of the pump to 8.4 MHz, which allows us to maintain one-dimensionality in our analysis at the spot sizes used in this study. We fit the TDTR scan to the radially symmetric heat diffusion equation assuming the parameters shown in Table B1. The thermal conductivity of the Al transducer is determined by applying the Wiedemann-Franz Law to electrical resistivity measurements made via four-point probe measurements on a reference sample placed in the aluminum deposition at the same time as the samples of interest. The room temperature heat capacity values for aluminum are taken from the literature [66]. The thickness is extracted from the picosecond acoustics response at short time scales, shown in Fig. B3(a). Points are chosen assuming an interfacial layer with that of low stiffness, according to Hohensee *et al.* [290]; the acoustic response is uncharacteristic of what is typically observed at a metal/nonmetal interface. The heat capacity of fully dense β-$Y_2Si_2O_7$ is taken to be 2.14 ± 0.12 MJ m^{-3} K^{-1} based on values

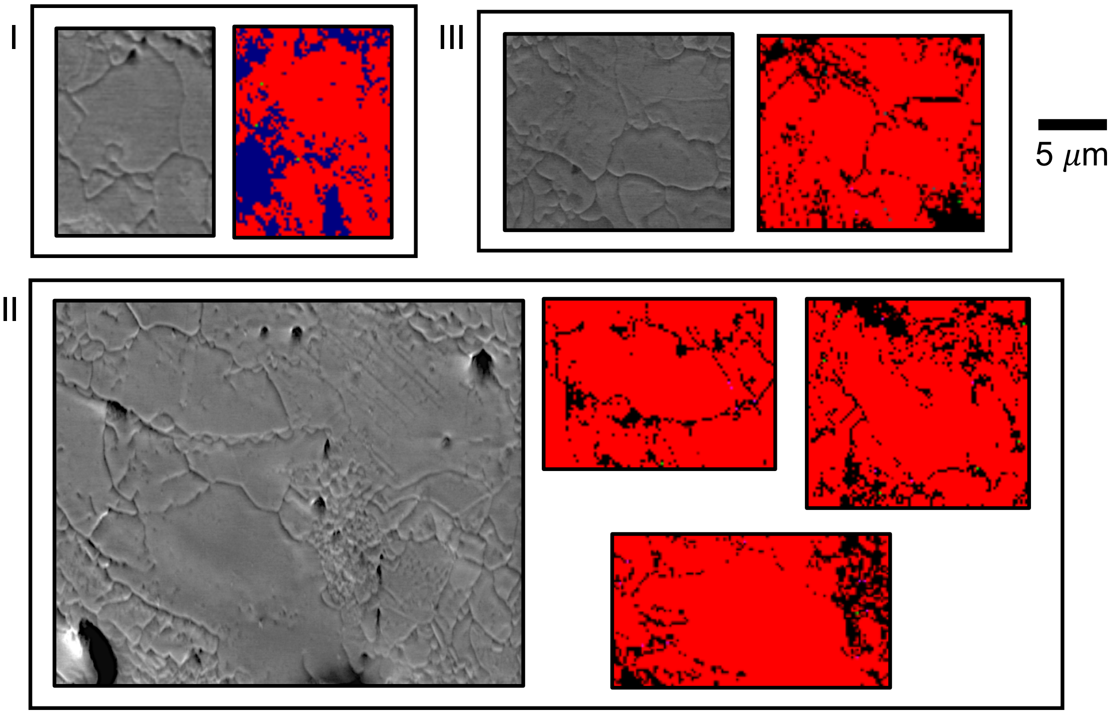

Figure B2. EBSD micrographs of the phases present in the mapped regions which are primarily γ- and β-$Y_2Si_2O_7$, represented by blue and red, respectively.

found in the literature [101, 121, 291]. From archimedes density tests we find that our sample is 90% dense, and adjust the volumetric heat capacity used in our analysis accordingly. A representative TDTR curve can be seen in the inset of Fig. B3(a), where we fit for the thermal conductivity of β-$Y_2Si_2O_7$ and the conductance at the Al/β-$Y_2Si_2O_7$ interface.

In order to perform high throughput thermal conductivity mapping, the delay time is fixed depending on the thermal boundary conductance at the Al/β-$Y_2Si_2O_7$ interface. We choose the pump-probe delay time such that the sensitivity to this conductance is near zero,

Layer	Volumetric Heat Capacity (MJ m^{-3} K^{-1})	Thermal Conductivity (W m^{-1} K^{-1})	Thickness (nm)
Al Transducer	2.42	111 $\pm$ 7	82 $\pm$ 2
β-$Y_2Si_2O_7$	1.92 $\pm$ 0.1	**F**	-

Table B1. Parameters for TDTR analysis. The effective pump/probe radii is 1.6 μm with an uncertainty 0.08 μm, while the thermal boundary conductance at the Al/disilicate interface is dependent on the region probed, as described in the text. The fitting parameter of interest is designated by **F**.

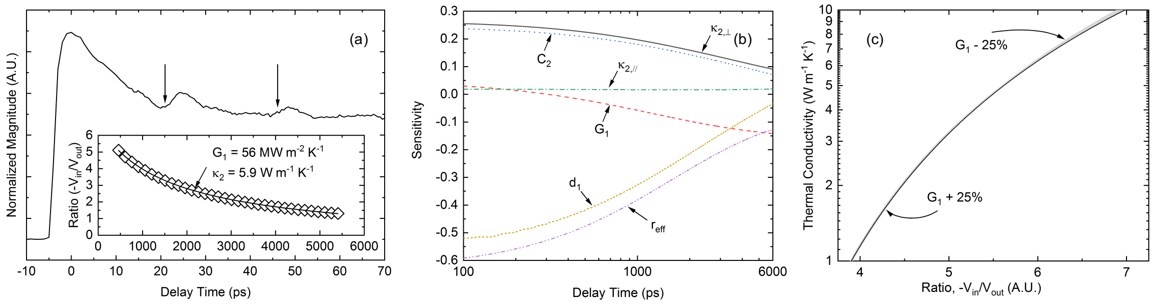

Figure B3. (a) Representative short- and long-time thermoreflectance signals from a region II grain. The arrows denote points which were used to extract the thickness of the Al transducer, while the inset shows the data and best fit used to obtain baseline thermal properties. (b) Sensitivity analysis corresponding to the thermal fitting curve from (a). A delay time is chosen such that sensitivity to the thermal boundary conductance is near zero, occurring at ∼350 ps, in order to maximize our sensitivity to the cross-plane thermal conductivity. The remaining variables are known and uncertainty in these values is propagated into the error analysis as shown in the values in Table B2. (c) Thermal conductivity correlation curve, showing the relation between the extracted ratio signal ($-V_{in}/V_{out}$) and thermal conductivity in black for G_1 = 43 MW m^{-2} K^{-1}. Included in gray are variations in the correlation curve when accounting for a 25% variation in G_1.

and correlate the ratio at a single delay time to the thermal conductivity in order to extract the thermal conductivity. Sensitivity curves are shown in Fig. B3(b) for a spot in Region II. The sensitivity of the ratio is defined as [56]

$$S_\alpha = \frac{\partial \ln(-\mathrm{V_{in}}/\mathrm{V_{out}})}{\partial \ln(\alpha)}, \tag{B1}$$

where S_α is the sensitivity to the parameter α. We compute the sensitivity of our model to the thickness of the aluminum (d_1), the boundary conductance between the aluminum and β-$Y_2Si_2O_7$ (G_1), the in-plane ($\kappa_{2,//}$) and cross-plane ($\kappa_{2,\perp}$) thermal conductivity of the β-$Y_2Si_2O_7$ relative to the measurement orientation, the heat capacity of the β-$Y_2Si_2O_7$ (C_2), and the effective pump/probe radius, r_{eff}. For regions I, II, and III, the measured conductances are 43 ± 2, 56 ± 3, and 41 ± 3 MW m^{-2} K^{-1}, respectively. Thus, the sensitivity where G_1 is near zero for regions I, II, and III correlates to ∼350, ∼180, and ∼460 ps, respectively. This is specifically shown in Fig. B3(b) for region II, where G_1 crosses zero sensitivity at ∼350 ps. These are the pump-probe delay times that we choose for each of

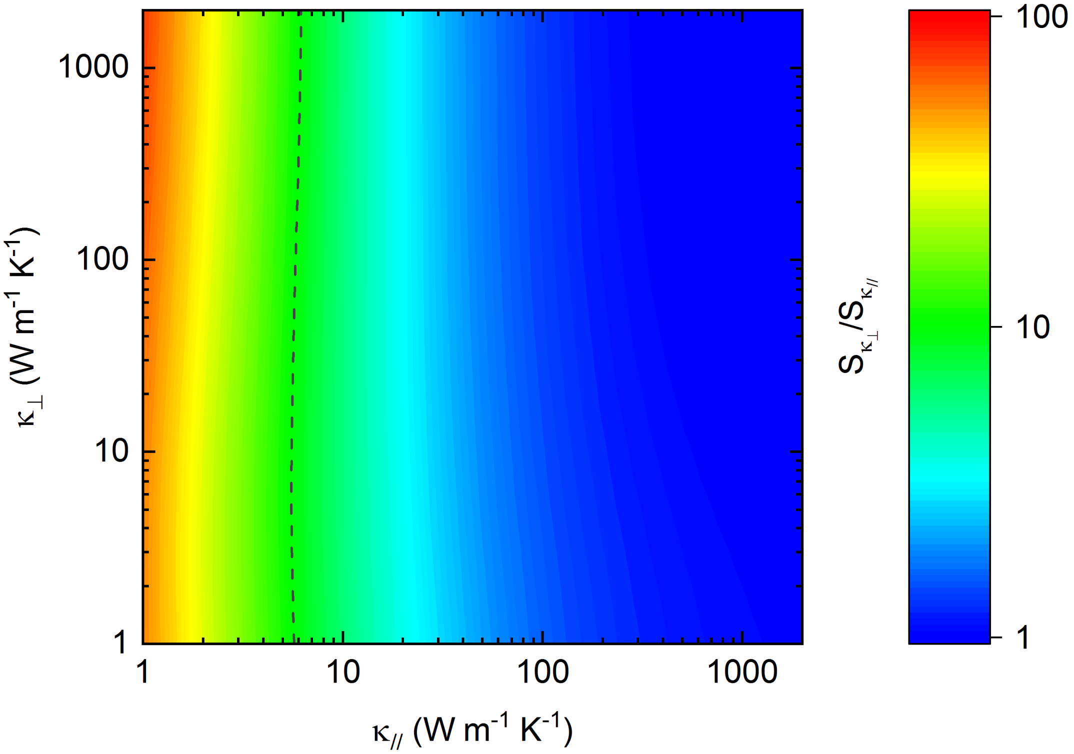

Figure B4. Relative sensitivity of the cross-plane thermal conductivity ($S_{\kappa_\perp}$) to the in-plane thermal conductivity ($S_{\kappa_{//}}$) of our system for a range of conductivity pairs. The contour line is drawn for $S_{\kappa_\perp}/S_{\kappa_{//}}$ = 10.

the thermal conductivity micrographs associated with those regions such that changes in the measured ratio signal are indicative primarily of changes in thermal conductivity, not the conductance at the Al/β-$Y_2Si_2O_7$ interface. This is visually represented in the thermal conductivity correlation curve, shown in Fig. B3(c). The black line correlates the extracted ratio from the experiment to the thermal conductivity of the disilicate. The bounds for varying the thermal conductance by ± 25% are shown in grey, and indicate that even moderate perturbations of G_1 do not significantly impact our extracted thermal conductivity. The relative sensitivity of $\kappa_\perp$ to $\kappa_{//}$ of the substrate are shown in Fig. B4 for thermal conductivities ranging from 1-2000 W m^{-1} K^{-1}. In the event that the $\kappa_{//}$ is very high, extraction of $\kappa_\perp$ becomes more difficult as the sensitivity to $\kappa_\perp$ is thwarted by that of $\kappa_{//}$.

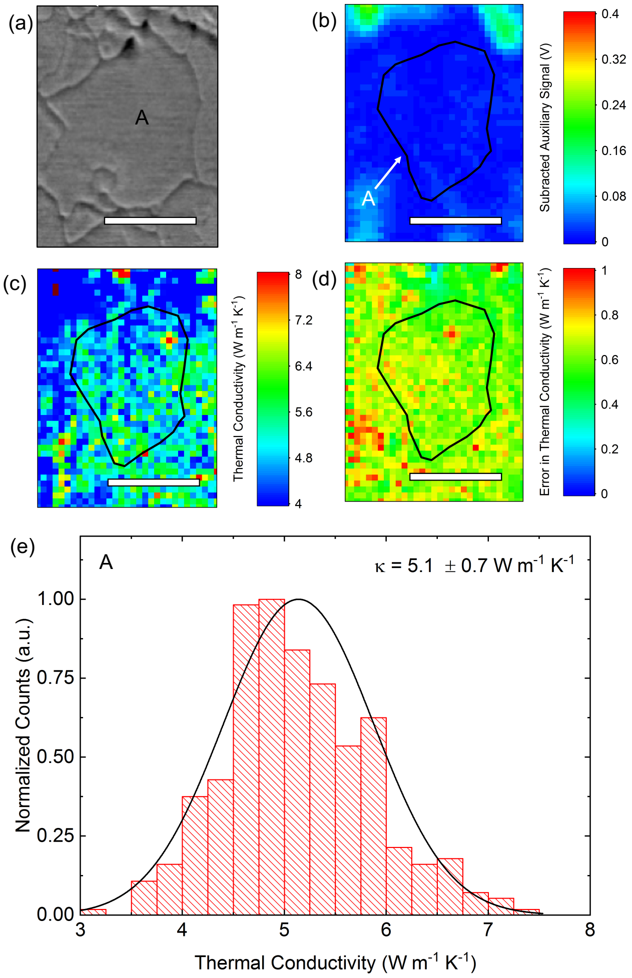

Figure B5. Thermal conductivity analysis of the grain present in region I. The SEM micrograph in (a) shows the region comprising the grain of interest. The subtracted auxiliary signal (b), thermal conductivity map (c), and error in thermal conductivity (d) micrographs are shown for grain A. Grain A is labeled in (b) along with its thermal conductivity distribution in (f). In (b)-(d), the step size is 0.25 μm, and the scale bars in (a)-(d) are 5 μm.

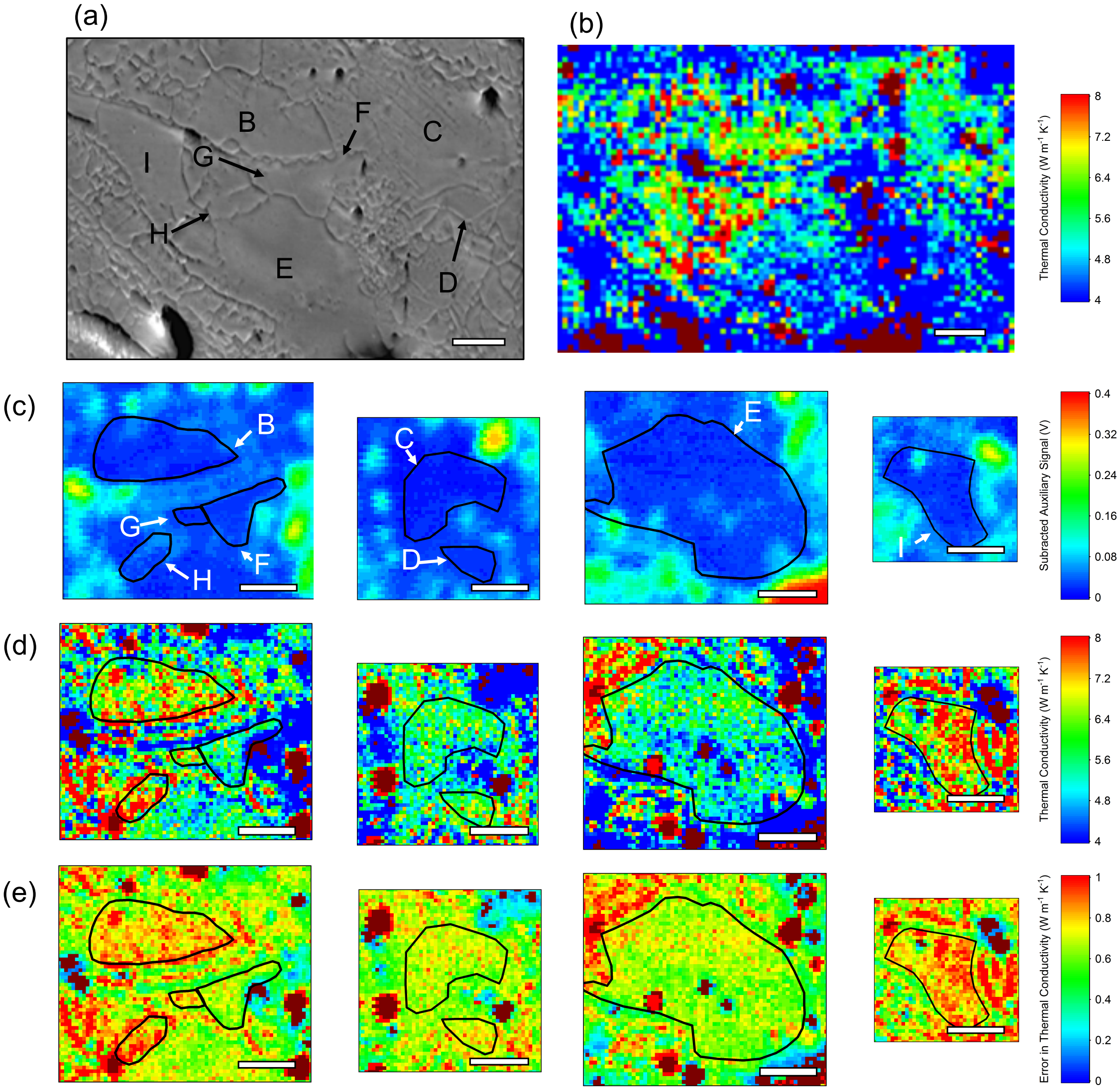
(a)
B
F
C
I
G
H
E
D
(b)
Thermal Conductivity (W m-1 K-1)
8
7.2
6.4
5.6
4.8
4
(c)
B
C
E
G
F
H
D
I
Subracted Auxiliary Signal (V)
0.4
0.32
0.24
0.16
0.08
0
(d)
Thermal Conductivity (W m-1 K-1)
8
7.2
6.4
5.6
4.8
4
(e)
Error in Thermal Conductivity (W m-1 K-1)
1
0.8
0.6
0.4
0.2
0

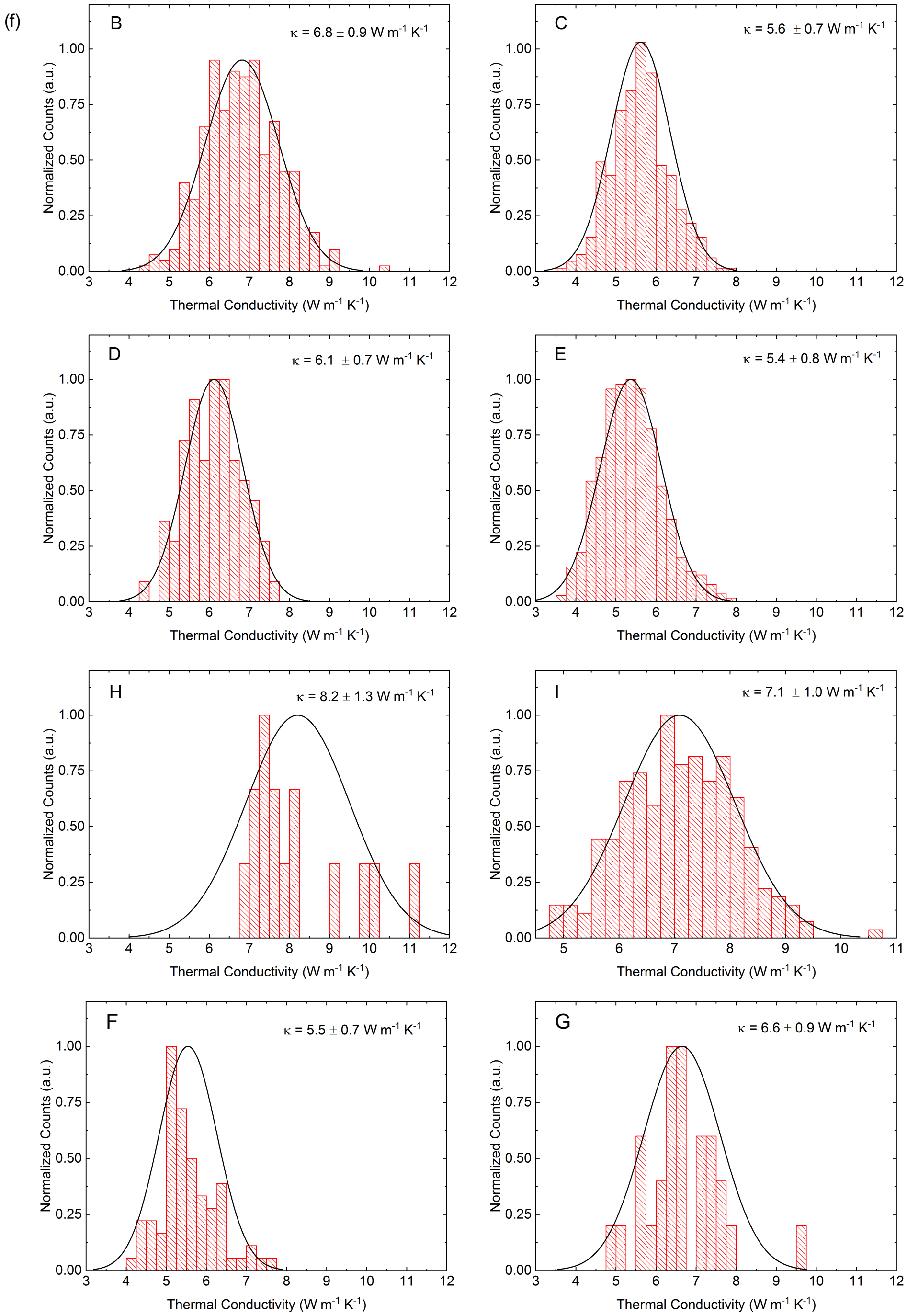

Figure B6. Thermal conductivity analysis of grains present in region II. The SEM micrograph of the region comprising grains B-I is shown in (a) along with the coarse thermal conductivity map (b) with step size of 0.5 μm. The scale bar in both is 5 μm. The subtracted auxiliary signal (c), thermal conductivity map (d), and error in thermal conductivity (e) micrographs are shown for grains B-I. Grains B-I are labeled in (c), and their thermal conductivity distributions are shown in (f). In (c)-(e), the step size is 0.25 μm, and the scale bar is 4 μm.

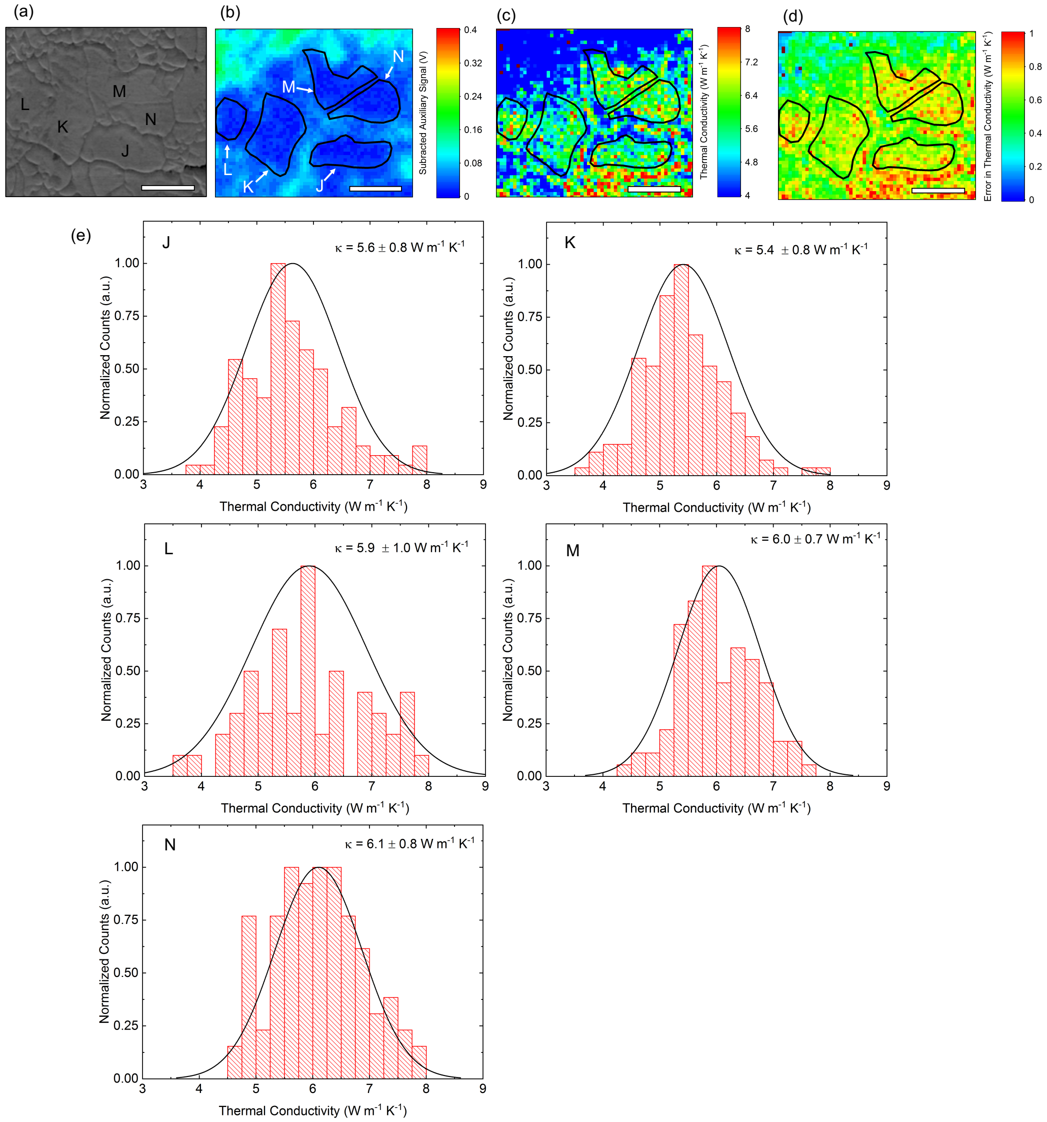

Figure B7. Thermal conductivity analysis of grains present in region III. The SEM micrograph of the region comprising grains J-N is shown in (a). The subtracted auxiliary signal (b), thermal conductivity map (c), and error in thermal conductivity (d) micrographs are shown for grains J-N. Grains J-N are labeled in (b), and their thermal conductivity distributions are shown in (e). In (b)-(d), the step size is 0.25 μm, and the scale bar in (a)-(d) is 5 μm.

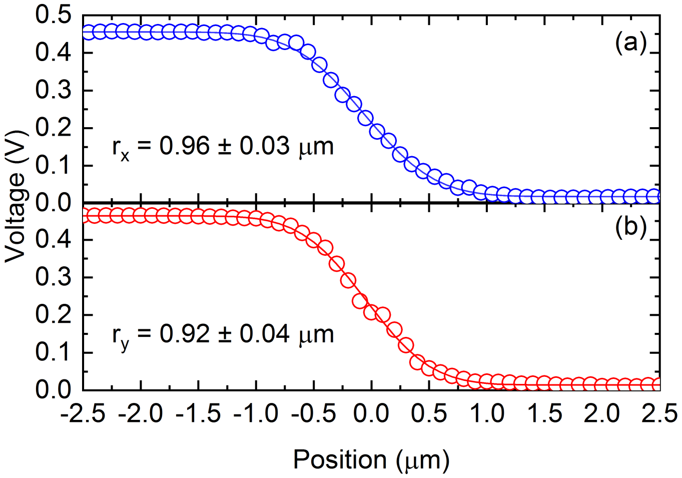

Figure B8. Knife edge measurements for the (a) x- and (b) y-dimensions of the probe. Dimensions are labeled as r_x and r_y for the radius in the x- and y-dimensions, respectively.

All thermal conductivity images used to extract the thermal conductivity of particular grains were taken with a step size of 0.25 μm, unless otherwise specified. We further selectively analyze regions where the probe auxiliary signal, subtracted from the reference beam in our balanced photodetector scheme, is $\leq$ 0.03 V. This is done to identify areas on the sample surface that are specularly reflecting the probe beam which are indicative of areas that do not have small artifacts such as stray dust or debris that would diffusely scatter incoming light. The details of the thermal map analysis are shown in Figs. B5-B7, along side SEM micrographs for reference.

We use the convention of Wei *et al.* [72] for the determination of the uncertainty in our measured thermal conductivities. Specifically, we employ this analysis with errors of 5% in the pump/probe radii, 7% in the thermal conductivity of the Al transducer, 2.5% in the thickness of the Al transducer, 5% in the boundary conductance at the Al/disilicate interface, and 5% in the volumetric heat capacity of the disilicate. At this modulation frequency, we take into account an error in the phase of 0.2 mrad. Our most sensitive parameter is that of the pump/probe radii. While we fit for the effective pump/probe radii in our initial analysis, we also perform knife edge measurements in a reflection configuration

Region	Grain Identifier	κ_{theory} (W m^{-1} K^{-1})	κ_{mean} (W m^{-1} K^{-1})	$\delta\kappa_{\text{spatial}}$ (W m^{-1} K^{-1})	$\delta\kappa_{\text{calculated}}$ (W m^{-1} K^{-1})	$\delta\kappa_{\text{total}}$ (W m^{-1} K^{-1})
I	A	5.9	5.1	0.7	0.6	1.0
II	B	6.6	6.8	0.9	0.8	1.2
	C	5.3	5.6	0.7	0.7	1.0
	D	6.1	6.1	0.7	0.7	1.0
	E	5.5	5.4	0.8	0.7	1.0
	F	5.3	5.5	0.7	0.7	1.0
	G	6.3	6.6	0.9	0.8	1.2
	H	7.2	8.2	1.3	0.9	1.6
	I	6.0	7.1	1.0	0.8	1.3
III	J	5.9	5.6	0.8	0.7	1.1
	K	5.6	5.4	0.8	0.7	1.0
	L	6.7	5.9	1.0	0.7	1.2
	M	6.6	6.0	0.7	0.7	1.0
	N	6.5	6.1	0.8	0.7	1.1

Table B2. Mapping region, grain identifier, thermal conductivity calculated from Eq. B8 and the derived tensor components from the main text (κ_{theory}), mean thermal conductivity from measurements (κ_{mean}), error in thermal conductivity due to spatial variations ($\delta\kappa_{\text{spatial}}$), error in thermal conductivity calculated via Eq. B2 ($\delta\kappa_{\text{calculated}}$), and total error in thermal conductivity ($\delta\kappa_{\text{total}}$).

to extract the radius of the probe. Measurements are shown in Fig. B8, where the measured probe dimensions are 0.96 x 0.92 μm in radius. An uncertainty of 5% is obtained from multiple measurements along various regions of our photolithographically fabricated knife-edge sample. This yields an effective pump radius of 1.29 μm. The final uncertainty at each point in the thermal conductivity map is determined via the equation

$$(\frac{\delta_\kappa}{\kappa})^2 = (R\frac{\delta_\phi}{S_\kappa})^2 + \sum(\frac{S_\alpha}{S_\kappa}\frac{\delta_\alpha}{\alpha})^2. \tag{B2}$$

In this equation, the final uncertainty in thermal conductivity δ_κ is dependent on the sensitivity to thermal conductivity S_κ and additional parameters described previously as S_α. We take the error in phase as $R\frac{\delta_\phi}{S_\kappa}$, where R is the ratio signal in the map. We add this uncertainty with the distribution of thermal conductivities measured for each grain in quadrature to report the final uncertainty. A summary of the mean thermal conductivities, κ_{mean}, and standard deviation of the distribution extracted from the selected region of each grain, $\delta\kappa_{\text{spatial}}$, are shown in Table B2. Also shown in the Table are the error in thermal conductivities calculated via Eq. B2, $\delta\kappa_{\text{calculated}}$. The final uncertainty is calculated via the square root of the sum of the squares of $\delta\kappa_{\text{spatial}}$ and $\delta\kappa_{\text{calculated}}$ (i.e., $\delta\kappa_{\text{total}} = \sqrt{\delta\kappa^2_{\text{spatial}} + \delta\kappa^2_{\text{calculated}}}$).

Shown in Fig. B9 are numerical calculations to the radially symmetric heat diffusion equation for both the in- and cross-plane thermal penetration depths [77]. At low modulation frequencies, the cross-plane thermal penetration depth approximately follows the 1/e^2 pump radius, while the in-plane thermal penetration depth is enhanced due to heat spreading in the Al transducer. At high modulation frequencies, the cross-plane penetration depth approaches the commonly accepted equation for thermal penetration

$$\sqrt{\frac{\kappa}{\pi C f}}, \tag{B3}$$

where f is the modulation frequency and κ and C reflect the thermal conductivity and heat capacity of β-$Y_2Si_2O_7$. The in-plane thermal penetration depth, on the other hand, approximately follows $f^{-0.1}$, and deviates significantly from Eq. B3 when κ and C reflect the thermal conductivity and heat capacity of the Al transducer.

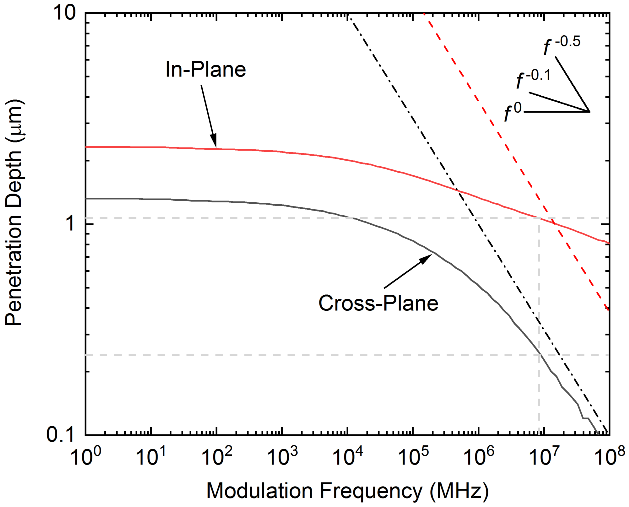

Figure B9. Numerically calculated in- and cross-plane 1/*e* thermal penetration depths for Al/β-$Y_2Si_2O_7$. The dashed lines correspond to Eq. B3 when calculated using properties of the Al transducer and β-$Y_2Si_2O_7$ crystallite.

B1.3 Derivation of $\kappa(\theta,\phi)$

For the derivation of $\kappa(\theta,\phi)$, we explicitly derive the thermal conductivity magnitude from the direction cosines of the orientation. This derivation is not unlike that of Jaing *et al.* [292]. From Fourier's law of heat conduction, the heat flux is related to the temperature gradient by the thermal conductivity:

$$\mathbf{q} = -\widetilde{\mathbf{K}}\nabla \mathrm{T}, \tag{B4}$$

where $\mathbf{q}$ is the heat flux, T is the temperature distribution of the system, and $\widetilde{\mathbf{K}}$ is the thermal conductivity tensor. The thermal conductivity tensor is a second rank tensor defined as

$$\widetilde{\mathbf{K}} = \begin{bmatrix} \kappa_{xx} & \kappa_{xy} & \kappa_{xz} \\ \kappa_{yx} & \kappa_{yy} & \kappa_{yz} \\ \kappa_{zx} & \kappa_{zy} & \kappa_{zz} \end{bmatrix}. \tag{B5}$$

Onsager's principle states that each of the components of the heat flux is linearly proportional to each of the components of the temperature gradient [293], implying $\kappa_{ij} = \kappa_{ji}$ must be true to satisfy these relations. The appearance of these off-diagonal terms in this tensor depend on the symmetry of the crystal. Only in triclinic systems are all the off-diagonal terms maintained, while just κ_{xz} is maintained in a monoclinic system. For systems of higher symmetry, only the diagonal elements are present in the system. The thermal conductivity tensor components are aligned with that of the cartesian coordinate system, where κ_{xx}, κ_{yy}, and κ_{zz} relate the heat flux and temperature gradient in the $\hat{x}$, $\hat{y}$, and $\hat{z}$ directions, respectively. The off-diagonal terms relate the heat flux and temperature gradient in orthogonal directions, i.e., κ_{xz} relates the heat flux in the $\hat{x}$ direction to the temperature gradient in the $\hat{z}$ direction, and vice-versa.

In Einstein notation, the magnitude of the thermal conductivity in a given direction is

$$\kappa(\theta,\phi) = K_{ij} l_i l_j, \tag{B6}$$

where l_1, l_2, and l_3 are the direction cosines [293]. For a unit vector in spherical coordinates, with θ the azimuthal angle and ϕ the polar angle, the direction cosines are the following:

$$\begin{aligned} l_1 &= \sin\phi\cos\theta \\ l_2 &= \sin\phi\sin\theta \\ l_3 &= \cos\phi. \end{aligned} \tag{B7}$$

Evaluating Eq. B6 assuming a thermal conductivity tensor in which all terms are non-zero, the angular dependence of thermal conductivity can be expressed as:

$$\begin{aligned} \kappa(\theta,\phi) = \kappa_{xx}\sin^2\phi\cos^2\theta + \kappa_{yy}\sin^2\phi\sin^2\theta + \kappa_{zz}\cos^2\phi \\ +2\kappa_{xy}\sin^2\phi\cos\theta\sin\theta + 2\kappa_{xz}\sin\phi\cos\theta\cos\phi + 2\kappa_{yz}\sin\phi\sin\theta\cos\phi. \end{aligned} \tag{B8}$$

We note that this result is identical to that of Jiang *et al.* [292]. An effective thermal conductivity can be defined as $\kappa_{eff} = \sqrt[3]{\det(\widetilde{\mathbf{K}})}$, where the cube root arises due to the rank of the tensor.

B1.4 Debye Velocity Calculation

To calculate the directional-dependence of the Debye velocity, we solve the Christoffel equation assuming literature values for the elastic constants of β-$Y_2Si_2O_7$. The elastic tensor is taken from Luo *et al.* [294], and in Voigt notation, takes the form

$$C_{ijnm} = \begin{bmatrix} 303 & 119 & 131 & 0 & -24 & 0 \\ 119 & 207 & 109 & 0 & 42 & 0 \\ 131 & 109 & 203 & 0 & -9 & 0 \\ 0 & 0 & 0 & 71 & 0 & 31 \\ -24 & 42 & -9 & 0 & 105 & 0 \\ 0 & 0 & 0 & 31 & 0 & 72 \end{bmatrix} \text{GPa}. \tag{B9}$$

The Christoffel matrix is further defined by

$$\Gamma_{ij} = q_n C_{inmj} q_m, \tag{B10}$$

where $\boldsymbol{q}$ is a vector with components that are the direction cosines. The product of the density and square of the phase velocity (i.e., $\rho \mathrm{v}_p^2$, where ρ is the density and v_p is the phase velocity) for a given $\boldsymbol{q}$ can be further defined by solving for the eigenvalues of Γ_{ij}. We use the code from Jaeken *et al.* [122] to further extract the directional-dependence of the group velocity, assuming a theoretical density of 4.04 g cm^{-3}. The Debye velocity, v_D, is then calculated via

$$\frac{3}{v_D^2} = \frac{1}{v_l^2} + \frac{1}{v_{t,1}^2} + \frac{1}{v_{t,2}^2}, \tag{B11}$$

where v_l is the longitudinal component and $v_{t,1}$ and $v_{t,2}$ are the two transverse components of the speed.

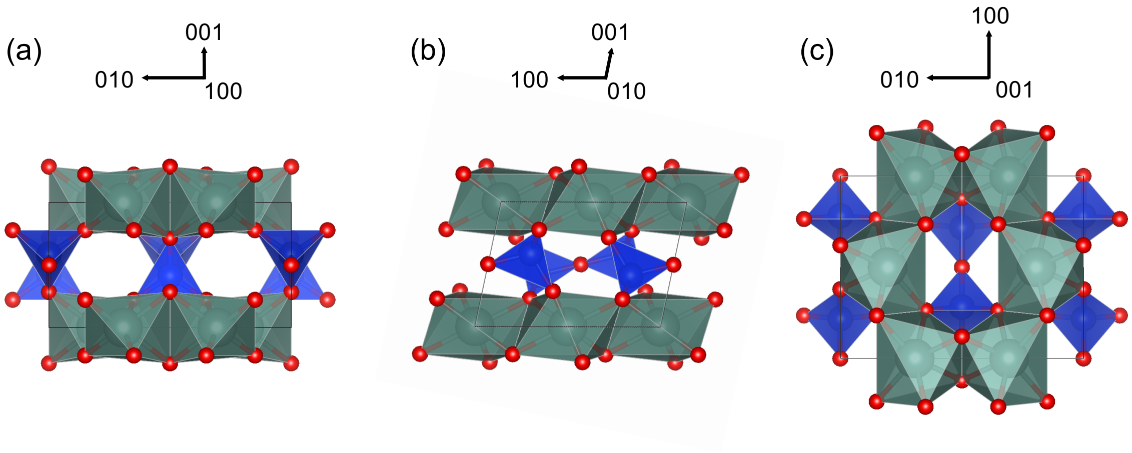

Figure B10. Plan-view orientation images of the monoclinic crystal of β-$Y_2Si_2O_7$ in the (a) (100), (b) (010), and (c) (001) planes. Y, Si, and O are represented by green, blue, and red atoms, respectively, while the YO_6 polyhedra and SiO_4 tetrahedra are designated as green polyhedra and blue tetrahedra, respectively.

B1.5 Orientation Images of β-$Y_2Si_2O_7$

Orientational images of the monoclinic crystal structure of β-$Y_2Si_2O_7$ can be found in Fig. B10. β-$Y_2Si_2O_7$ consists of SiO_4 tetrahedra and YO_6 polyhedra arranged into a layered-like structure. The [100] and [010] directions are similar in structure, less for the additional O shared between two SiO_4 tetrahedra in the [100] direction, while the structure along the [001] direction departs significantly from those of the [100] and [010] directions.

B2 Spatiotemporal Thermal Conductivity Evolution of Steam Cycled Ytterbium Silicate/Silicon Environmental Barrier Coatings

B2.1 Atmospheric Plasma Spray Deposition

Powders used for the Si bond coat were S1-122 electronics grade powder (Micron Metals), with a particle diameter range of 28-129 μm. Ytterbium silicate powders (YbDS and YbMS, Treibacher Industrie Inc.) in fused-crushed form with irregular/angular morphology and a particle diameter of 20-50 μm were used for plasma spraying of the top-coat. The plasma spray conditions were chosen to ensure complete particle melting but sought to avoid overheating which has been linked to rapid loss of SiO_2 from the YbDS coatings [130, 153]. To compensate for the low molten particle temperature (which promotes low density, high permeability coatings) [130, 153], the depositions were conducted in a furnace set at 1200 °C so that the hot substrate surface prolonged the time for droplet solidification after impingement, thereby extending the radial distance of droplet flow over the surface, d, resulting in a high density coating of low oxidizer permeability. Oxidation of the samples during deposition was inhibited by the use of an argon flow (21:1 Ar_2:H_2 at 20 slm) furnace where the substrate was held at 1200 °C during deposition. A $\sim$50 μm thick Si layer and $\sim$100 μm thick YbDS layer were deposited using the plasma spray parameters

APS Layer	Thickness (μm)	Torch Power (kW)	Arc Current (A)	Primary Ar (slm)	Secondary H_2 (slm)	Powder Feed Rate (g/min)	Ar Carrier Gas Flow Rate (slm)
Si	$\sim$50	22.7	500	77.87	0.94	31.0/upper	5.9
Yb_2Si_2O7	$\sim$100	11.2	275	84.95	0.94	41.5/lower	5.9

Table B3. APS parameters used for the deposition of the YbDS-silicon EBC.

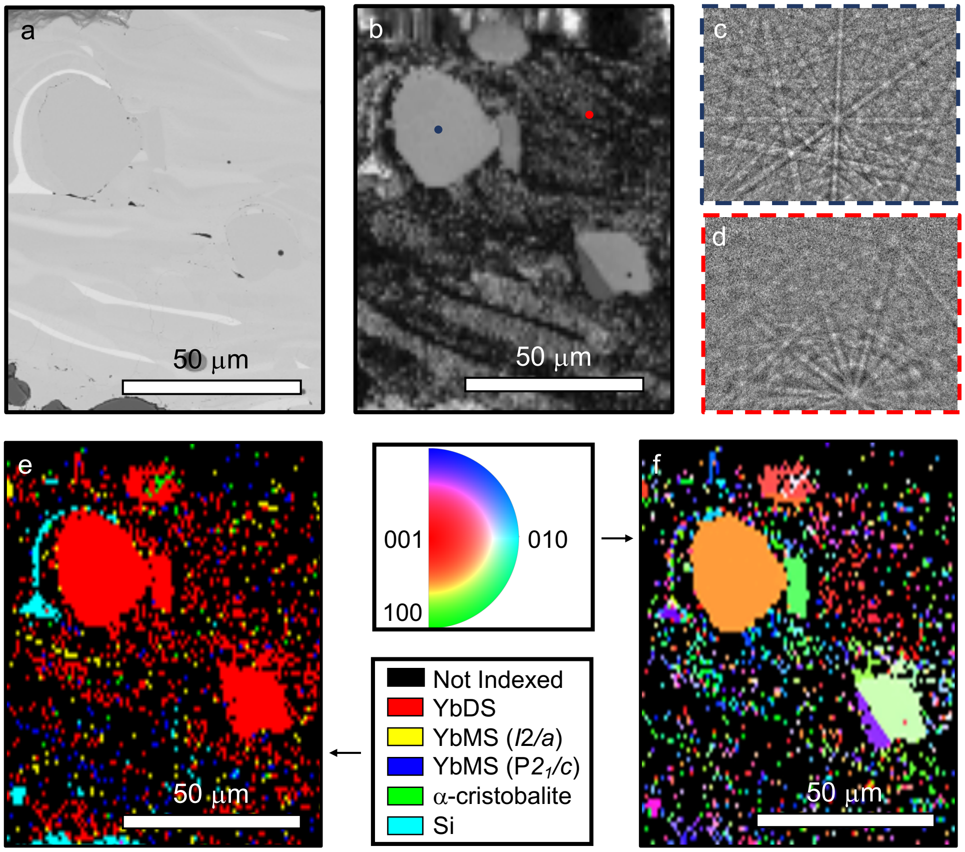

Figure B11. As-deposited specimen. (a) BSE-mode electron micrograph, showing the phase contrast of the coating. (b) EBSD band-contrast micrograph and (c,d) corresponding diffraction patterns from the blue and red dots in (b). (e) EBSD phase contrast micrograph showing that the large crystalline splats are of the YbDS phase, and the lack of heterogeneity present in the system. (f) Inverse pole figure (IPF) Z micrograph showing the differences in grain orientation of the crystalline splats present in the coating.

indicated in Table B3. Both sides of the α-SiC substrates were coated using this method. Samples were stabilization annealed at 1250 °C for 24 hours, and then thermally cycled in a 90 vol % H_2O/10 vol % O_2 environment.

B2.2 Electron-Backscatter Diffraction Characterization

EBSD: As-Deposited Specimen

EBSD band-contrast micrographs for the as-deposited specimen can be found in Fig. B11. For reference, we also show the SEM BSE micrograph in Fig. B11(a). The band-contrast micrograph in (b) shows the presence of large crystallites in a amorphous/nanocrystalline

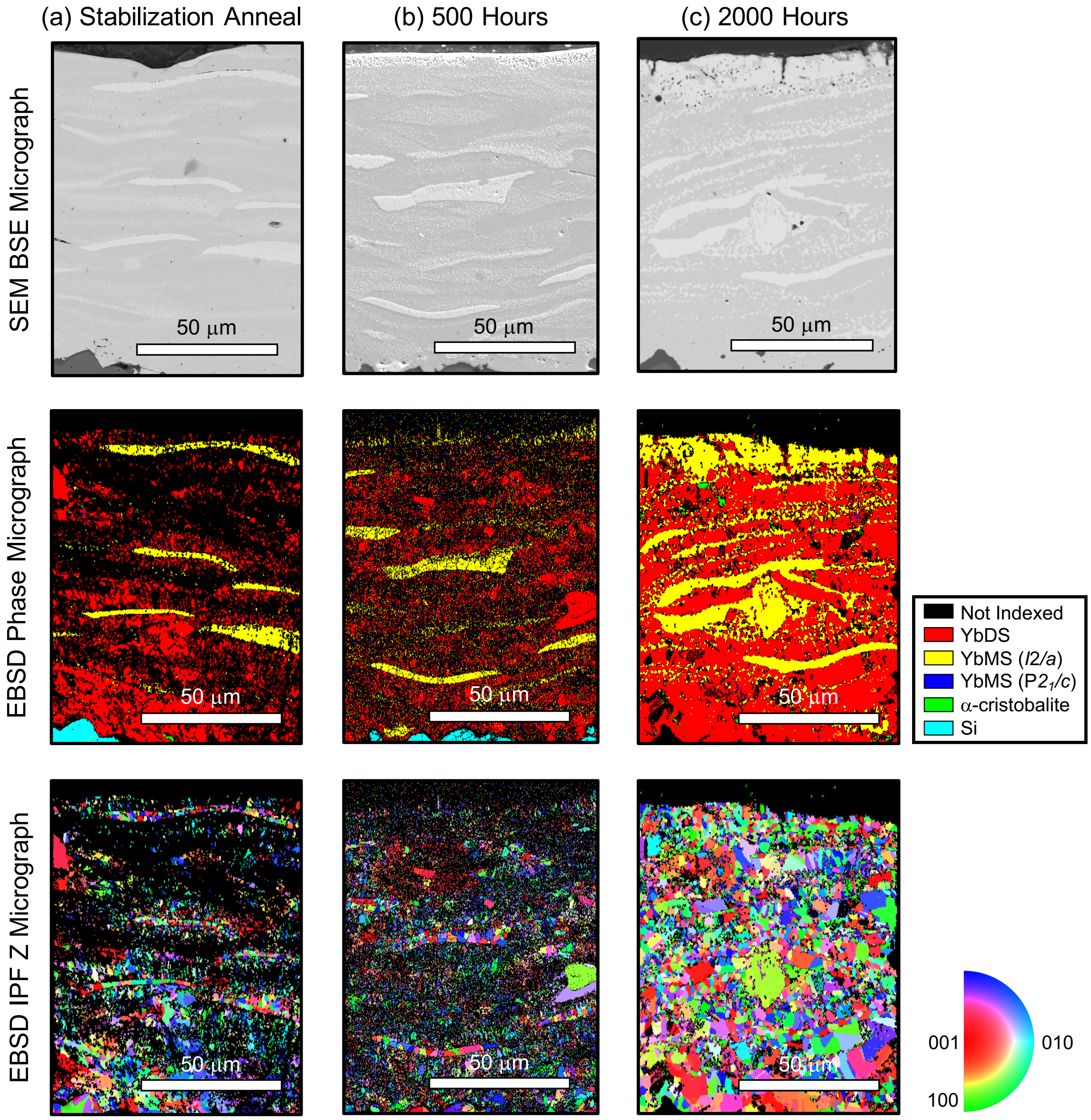

Figure B12. SEM BSE, EBSD phase, and EBSD IPF Z micrographs for specimens in their stabilization annealed states and after cycling in a steam environment for (b) 500 and (c) 2000 hours. EBSD micrographs were acquired using a 0.25 μm step size. The IPF Z legend is for a monoclinic structure, and is thus applicable for YbDS and YbMS phases present in the system.

matrix. Based on the step size used in the micrographs (1 μm), we are unable to resolve grains with dimensions smaller than this. Nonetheless, the large crystallites are highly diffractive while the matrix shows some diffraction in the patterns found in Fig. B11(c) and (d), respectively. The phase contrast micrograph in Fig. B11(e) shows that the large crystallites are of the YbDS phase. Additionally, the micrograph exemplifies that the coating is not entirely comprised of YbMS or YbDS – trace amounts of Si and α-cristobalite appear to be present. For the large YbDS crystallites, the inverse pole figure (IPF) Z micrograph shows the relative orientation between each crystallite.

EBSD: Stabilization Annealed, 500, 2000 Hour Specimens

EBSD characterization for the stabilization annealed specimen, as well as specimens cycled for 500 and 2000 hours can be found in Figs. B12(a), (b), and (c), respectively. Specifically, Fig. B12 shows BSE-mode SEM micrographs, EBSD phase contrast micrographs, and EBSD inverse pole figure (IPF) Z micrographs, which represent the orientation of grains normal to the EBSD measurement orientation. Good agreement in phase contrast can be found between the SEM BSE micrograph contrast and EBSD phase contrast micrographs. We do not observe significant texturing in any portion of the coating as a function of cycling time. The EBSD band contrast micrograph for the specimen cycled for 2000 hours can be found in Fig. B13.

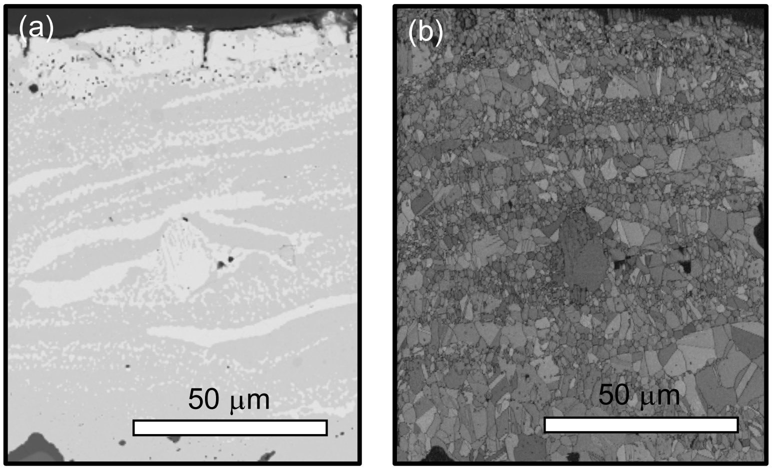

Figure B13. (a) SEM BSE and (b) EBSD band contrast micrographs of the specimen cycled for 2000 hours.

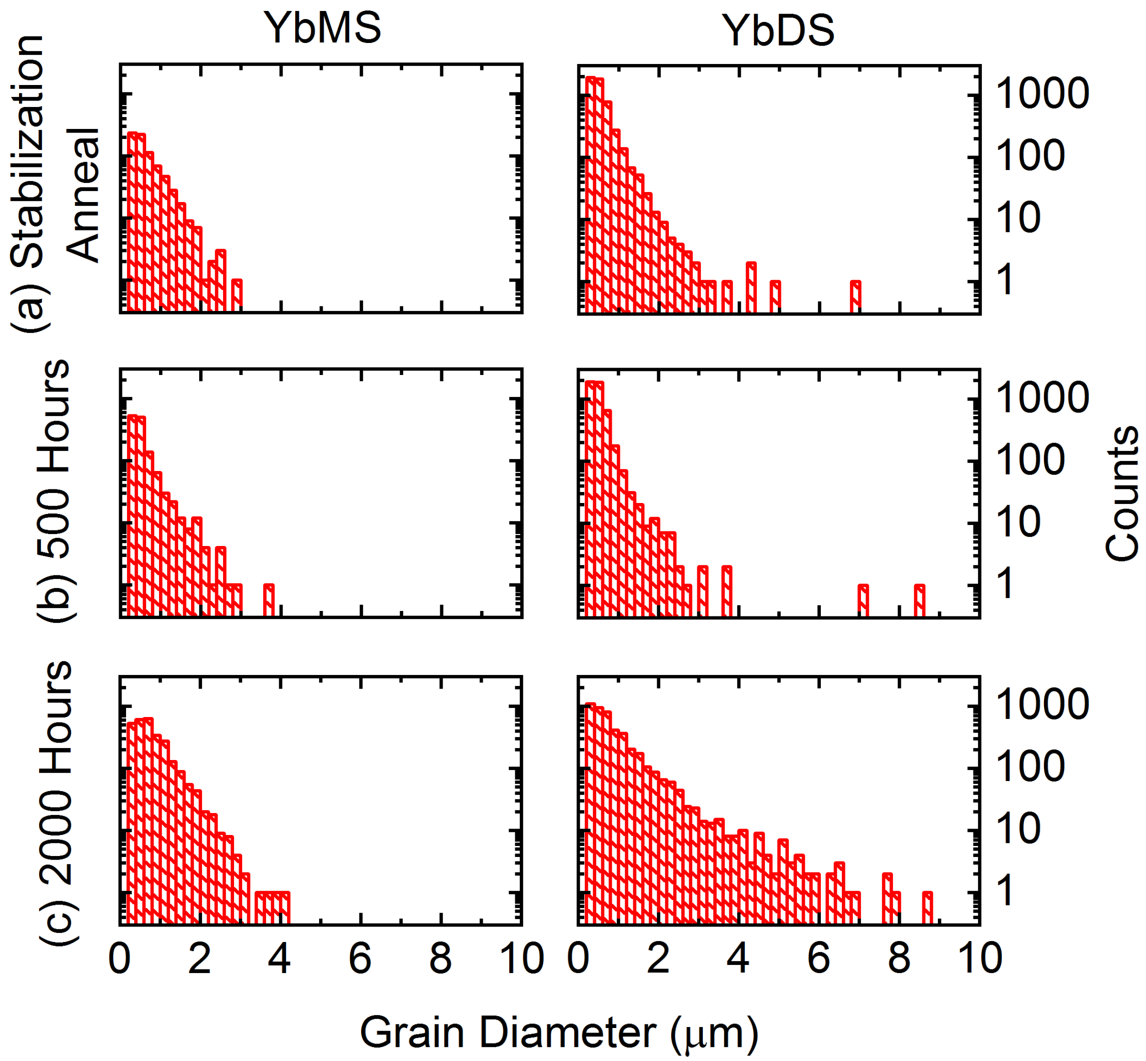

Figure B14. YbMS and YbDS grain size distributions for the (a) stabilization annealed specimen and specimens cycled for (b) 500 and (c) 2000 hours.

Grain Size Distributions

Grain size distributions for YbMS and YbDS in each of the specimens can be found in Fig. B14, which shows these distributions for (a) the stabilization annealed specimen and specimens cycled for (b) 500 and (c) 2000 hours. For the stabilization annealed specimen, YbMS grain sizes were small, generally on the order of ∼2 μm or less, with $<$ 10 grains in the 2–3 μm range. The YbDS grains were of similar size, although grain sizes extended to ∼5 μm. Similar distributions can also be observed after cycling for 500 hours, Fig. B14(b). Some coarsening was observed for both silicates in the 2–3 μm range, although the distributions remained nominally the same due to the early cycling times. After 2000 hours of cycling, Fig. B14(c), significant coarsening was observed for both YbMS and YbDS constituents. In YbMS, a greater fraction of the grains had diameters of 1–3 μm, while those of YbDS increased significantly in the 1–6 μm regime, with several grains reaching 6–8 μm.

B2.3 Phase Profile Determination

We determine the YbDS and YbMS phase profiles for each of the specimens presented in the main document using pixel counting statistics in a custom MATLAB program. There is sufficient contrast between YbMS and YbDS in the BSE micrographs, and this contrast is in excellent agreement with the EBSD phase contrast micrographs, as shown in Fig. B12. Ideally, we would utilize the EBSD phase data to create the phase profiles shown in Fig. 4.7 of the main document. However, the resolution used to acquire this data (0.25 μm) was much smaller than that of the BSE micrographs (70 nm).

The MATLAB program functions as follows. First, the grayscale BSE micrograph is imported, and a histogram of the grayscale values are plotted to identify YbDS and YbMS phases, the distributions of which are nominally gaussian. The micrograph is then compartmentalized vertically into 200 sections from the exposed portion of the coating to the bond coat. A gaussian distribution is fitted to the histogram of each compartment at grayscale values of YbDS and YbMS for each micrograph, which yields the phase profile. We note that the profiles calculated only show relative amounts of YbDS and YbMS, and do not include fractions of, for example, porosity and the silicon bond coat as a function of depth.

We also perform pixel counting statistics on our EBSD-acquired micrographs. The phase profiles calculated from BSE and EBSD micrographs can be found in Fig. B15 for the (a) stabilization annealed sample and samples cycled for (b) 500 and (c) 2000 hours. EBSD micrographs are coarser in resolution, and are unable to index YbDS and YbMS when the grain size becomes less than the step size used in our measurement, 0.25 μm.

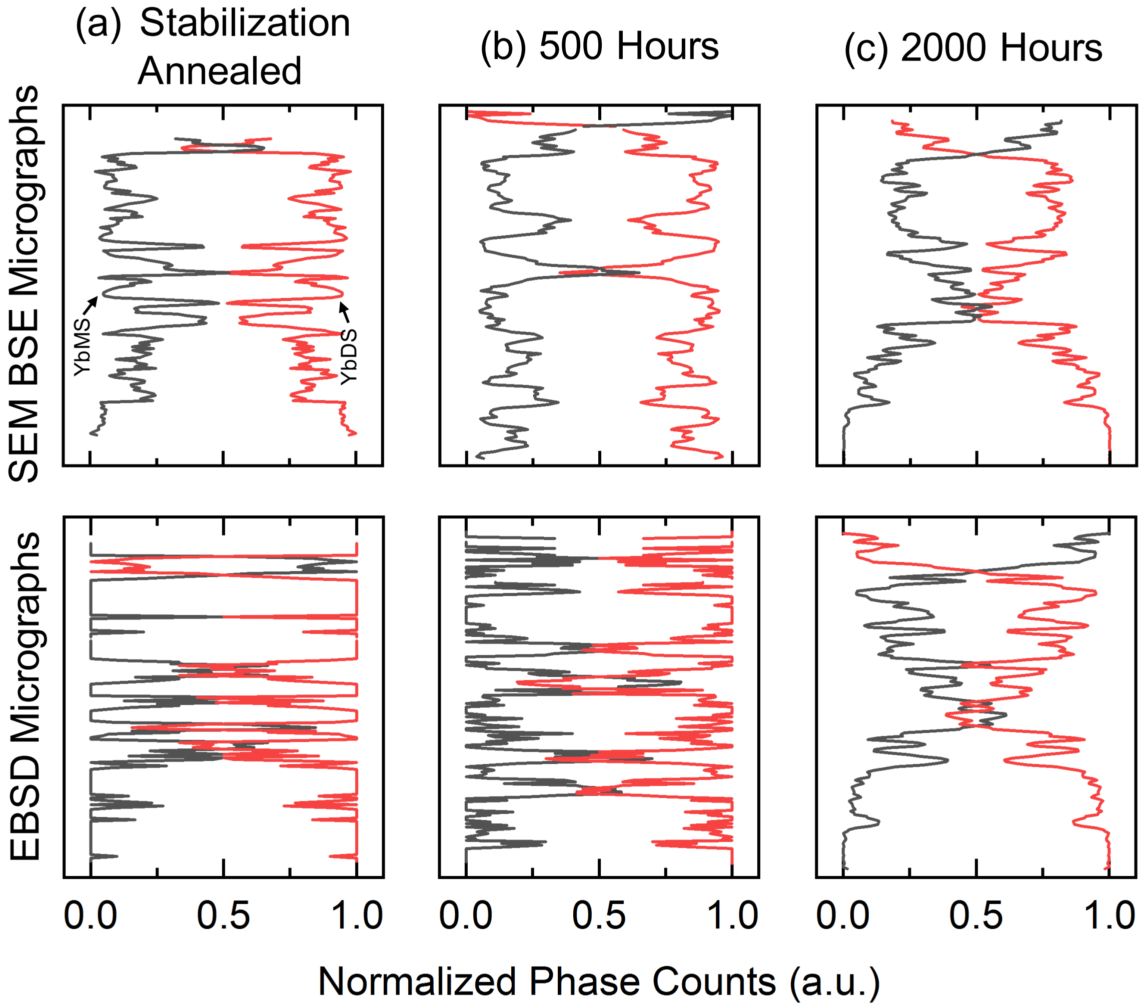

Figure B15. A comparison of YbDS and YbMS phase profiles in (a) the stabilization annealed coating and after cycling for (b) 500 and (c) 2000 hours acquired from pixel counting statistics using SEM BSE and EBSD micrographs.

This is particularly noticeable in the EBSD phase micrographs for the stabilization annealed specimen and the specimen cycled for 500 hours in Figs. B12(a) and (b), respectively. As a result, the acquired phase profiles using the EBSD micrographs appear more discrete, rather than the continuous profiles using the SEM BSE micrographs. As mentioned earlier, however, the generally good agreement between the contrast of YbDS and YbMS in the BSE micrographs and the identification of these two phases in the EBSD phase micrographs merits the use of the SEM BSE micrographs for the determination of the phase profiles.

B2.4 Time-Domain Thermoreflectance

We use time-domain thermoreflectance (TDTR) for the thermal conductivity measurements of the YbDS top-coat layer. An 80 MHz Ti:Sapphire oscillator centered at 808.5 nm (∼12 nm FWHM), is spectrally separated into high- and low-energy pump and probe paths, respectively. The pump is amplitude-modulated via an electrooptic modulator at 8.4 MHz, and creates a frequency dependent heating event at the surface of the specimen coated with Al. The probe is mechanically delayed in time, and monitors the thermoreflectance at the sample surface following the pump heating event. We monitor both the in-phase (V_{in}) and out-of-phase (V_{out}) components of the probe signal via lock-in detection, and compare the ratio of the two ($-V_{out}/V_{out}$) to the radially symmetric heat diffusion equation to extract both the thermal conductivity of the specimen as well as the conductance at the Al/specimen interface. The thickness of the Al transducer are determined by picosecond acoustics, and using the literature value for the speed of sound in Al [66, 184]. While we are not particularly sensitive to the thermal conductivity of our Al transducer, we determine this parameter by codepositing a-SiO_2 and Al_2O_3 reference samples in the same deposition, and using the Wiedemann-Franz law to relate the electrical conductivity to thermal conductivity. The volumetric heat capacity of YbDS and YbMS are calculated based on literature values of density and heat capacity, and are summarized in Table B4. The parameters used in our analysis for the extraction of the thermal conductivity of the coating can be found in Table B5. Note that we utilize the volumetric heat capacity of YbDS in this analysis. For the majority of our measurements, the $1/e^2$ pump and probe radii are 4.5 and 3.5 μm, respectively, when using a 20x objective, except when high-resolution measurements are performed with a 50x objective, in which case the effective pump/probe radii is 1.4 μm.

Material	Density ($g\ cm^{-3}$)	Heat Capacity ($J\ kg^{-1}\ K^{-1}$)	Volumetric Heat Capacity ($J\ cm^{-3}\ K^{-1}$)
β-$Yb_2Si_2O_7$	6.15 [126]	274 [20]	1.69
Yb_2SiO_5	6.92 [105]	352 [295]	2.44

Table B4. Thermophysical parameters of β-$Yb_2Si_2O_7$ and Yb_2SiO_5.

Layer	Thermal Conductivity (W m^{-1} K^{-1})	Volumetric Heat Capacity (J cm^{-3} K^{-1})	Thickness (nm)
Aluminum	115 ± 5	2.42	82 ± 2
β-$Yb_2Si_2O_7$/Yb_2SiO_5	**F**	1.69	–

Table B5. Thermophysical parameters use in the analysis of TDTR data. Fitting parameters are designated by **F**.

Example data are shown in Fig. B16 for a probed region predominantly of the disilicate phase in the 2000 hour specimen. Additional details regarding TDTR and its analyses can be found in the literature.

To spatially profile the thermal conductivity of the coatings at various points in the cycling process, we mount each specimen onto an XY translation stage. The sample is rastered relative to the probe beam so that we do not have to alter the alignment in our laser setup. To perform the raster, we select a single-pump/probe delay time that minimizes

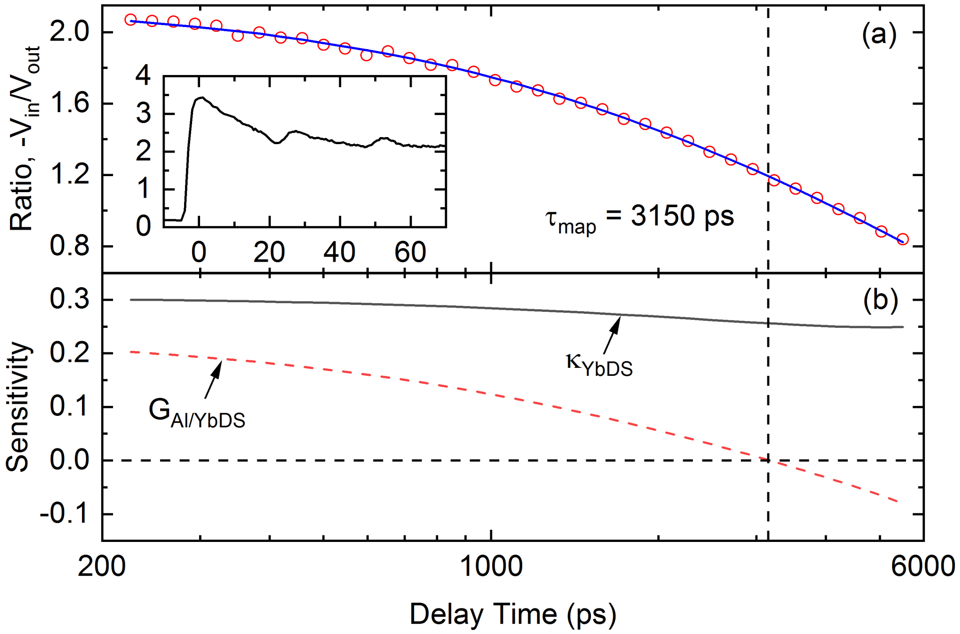

Figure B16. (a) Example TDTR curve on a YbDS-rich region on the specimen cycled for 2000 hours. The inset shows the picosecond acoustic response at shorter time delays, where oscillations were used to extract the thickness of the Al transducer. (b) Sensitivity analysis for the thermal conductivity of YbDS, κ_{YbDS}, and conductance at the Al/YbDS interface, $G_{\mathrm{Al/YbDS}}$. The pump/probe delay time is fixed at 3150 ps, as sensitivity to $G_{\mathrm{Al/YbDS}}$ is zero at this point.

sensitivity to the conductance at the Al/silicate interface. An example of this process is shown in Fig. B16 for the specimen cycled for 2000 hours. First, we perform numerous full TDTR measurements across the region to be probed to extract an expected thermal conductivity and interfacial conductance. We find that the thermal conductivity across various YbDS-rich regions is 5.9 ± 0.4 W m^{-1} K^{-1}, and the conductance at the Al/YbDS interface, $G_{Al/YbDS}$, to be 31 ± 2 MW m^{-2} K^{-1}. Following, we calculate the sensitivity to each of these parameters to -V_{in}/V_{out}, defined by [56]

$$S_\alpha = \frac{d\ln(-V_{in}/V_{out})}{d\ln\alpha}, \tag{B12}$$

where α is the parameter of interest.

Sensitivity to the YbDS thermal conductivity and Al/YbDS interfacial conductance can be found in Fig. B16(b). We perform a linear interpolation to extract the point at which the sensitivity to the conductance goes to zero. Conceptually, this means that small perturbations of $G_{Al/YbDS}$ about its nominal value will not result in large changes in the acquired thermoreflectance signal, and that any variations we observe when rastering across a sample are primarily indicative of changes in thermal conductivity. A summary of the conductances measured across all specimens in this work and their corresponding pump/probe delay times can be found in Table B6.

Cycling Time	Thermal Boundary Conductance ($MW\ m^{-2}\ K^{-1}$)	Delay Time[a] (ps)
As-Deposited	52 ± 2	680
Stabilization Annealed	49 ± 1	890
500 Hours	53 ± 1	830
1250 Hours	52 ± 2	800
2000 Hours	31 ± 2	3150

Table B6. Measured thermal boundary conductance at Al/YbDS coating interface and derived pump/probe delay time for mapping procedure from sensitivity analysis described in the text. [a]For measurements performed with a 20x objective.

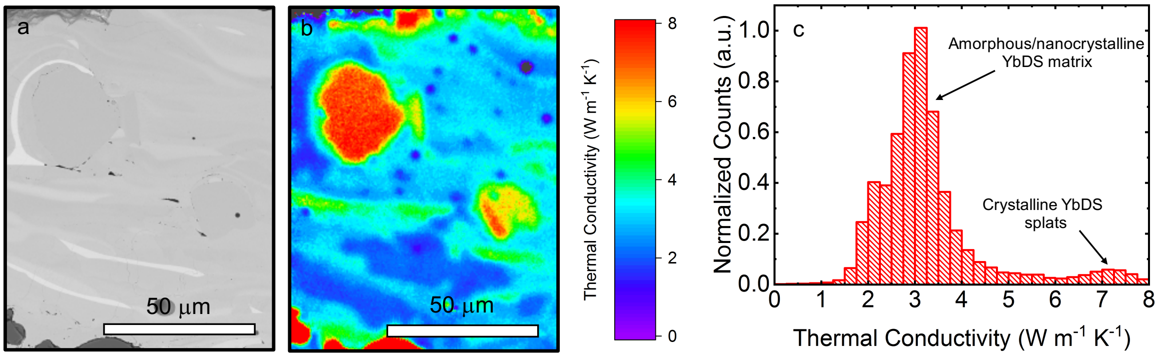

Figure B17. (a) SEM BSE, (b) thermal conductivity micrograph, and (c) thermal conductivity histogram of the as-deposited specimen.

B2.5 Thermal Conductivity Micrograph of As-Deposited Specimen

The thermal conductivity of the as-deposited specimen can be found in Fig. B17, alongside its SEM BSE micrograph. The as-deposited specimen shows a generally low thermal conductivity, less for the high thermal conductivity YbDS crystallites, and is on the order of 2–4 W m^{-1} K^{-1}, see histogram in Fig. B17(c). The low thermal conductivity of the coating can be attributed to its amorphous/nanocrystalline nature, in which heat carriers are more frequently scattered causing a reduction in the thermal conductivity. We attribute the differences in thermal conductivity of YbDS splats to their differing orientations, as β-YbDS is monoclinic in nature. This is also confirmed via the EBSD IPF Z micrograph in Fig. B11(f). We have previously [86] determined the anisotropic thermal conductivity tensor for β-$Y_2Si_2O_7$ (β-YDS). In general, we find good agreement between the anisotropic thermal conductivity of β-YDS and β-YbDS, where a higher thermal conductivity ($\sim$7 W m^{-1} K^{-1}) is observed near to the [100] direction, and a lower thermal conductivity ($\sim$5 W m^{-1} K^{-1}) near to the [010] direction. Unlike in our previous work, there are not a sufficient number of grains to fully recreate the stereographic projection of the thermal conductivity of β-YbDS.

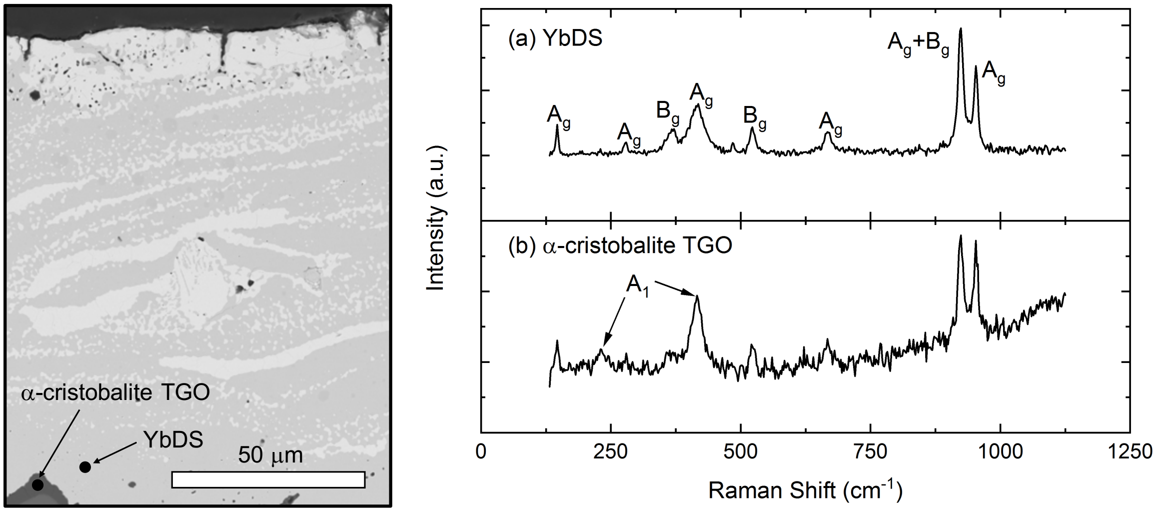

Figure B18. Background-subtracted Raman spectra acquired from (a) YbDS regions and (b) TGO regions of the specimen cycled for 2000 hours.

B2.6 Raman Spectra: 2000 Hours Specimen

Raman spectra for YbDS-rich and TGO regions of the specimen cycled for 2000 hours can be found in Fig. B18. Spectra were acquired using a Renishaw InVia Confocal Raman microscope at an excitation wavelength of 532 nm using a 50× objective. The YbDS spectra shown in (a) show no features indicative of residual YbMS being present in the region near to the silicon bond coat. If YbMS were present in this region, it would manifest itself as additional low wavenumber modes in the 50–200 cm^{-1} range, as indicated by Ogawa *et al.* [296]. Singly degenerate A_g and B_g modes are identified in (a), and the spectra is consistent with previous experimental reports [297]. Raman spectra acquired in the TGO region are shown in Fig. B18(b), with peaks originating from the A_1 optical mode identified at $\sim$416 cm^{-1} and $\sim$230 cm^{-1}. The spectra for α-cristobalite shows strong overlap with YbDS, especially at $\sim$416 cm^{-1}. Additionally, YbDS indicators at longer wavenumbers are also present, suggesting that the Raman interaction volume extends beyond what we observe in the camera. Nonetheless, the α-cristobalite peak at $\sim$230 cm^{-1}, although weak, is consistent with previous reports [97, 168, 180], and the lack of broad features characteristic of an amorphous TGO are not present, confirming devitrification of the TGO.

B2.7 Estimation of Total Silica Formed

To estimate the total amount of silica formed in the TGO, and therefore that lost to the reaction described in Eq. 4.4 of the main document, we begin with the measured thickness the YbDS rich (YbMS free) region at the silicon bond coat. By assuming YbDS consists of an average of 12.5 ± 2.5 mol% YbMS, the number of moles of YbMS reacted can be calculated using the molar volumes of YbDS (V_M = 83.62 cm^3 mol^{-1}) and YbMS (V_M = 65.63 cm^3 mol^{-1}). For each mole of YbMS consumed, one mole of SiO_2 is required to form YbDS, and is therefore the amount lost to the reaction in Eq. 4.4 of the main document. We use the molar volume of β-cristobalite (V_M = 27.64 cm^3 mol^{-1}) for this calculation. The total thickness of the TGO that is formed is the sum of that reacted and that measured via SEM.

B2.8 Temperature Gradient Evolution Calculation

To model the temperature gradients in the steady-regime of a coating system, we begin with Fourier's Law with a thermal conductivity that varies in space:

$$q = -\kappa(x)\frac{dT}{dx}. \tag{B13}$$

Rearranging and performing a cumulative integral with respect to x, we find

$$T(x) - T(0) = -q\int_0^x \frac{1}{\kappa(x')}dx'. \tag{B14}$$

For a coating of thickness $x = L$, the equation can be further simplified to determine the heat flux necessary to induce a nominal temperature drop across the entirety of the coating:

$$q = \frac{T(0) - T(L)}{\int_0^L \frac{1}{\kappa(x')}dx'}. \tag{B15}$$

Coating Layer	Thickness (μm)	Thermal Conductivity (W m^{-1} K^{-1})
YbMS	$179 \times 10^{-3}\sqrt{t}$	0.74
YbDS/YbMS	$100 - (176 + 179) \times 10^{-3}\sqrt{t} - 2.1$	0.96
YbDS	$2.1 + 176 \times 10^{-3}\sqrt{t}$	1.18

Table B7. Thicknesses and thermal conductivities used for the estimation of the thermal gradients experienced by a ytterbium silicate-silicon EBC. Time, t, is in hours.

In our calculations, the heat flux is calculated for a 100 K temperature drop such that the silicon bond coat remains at 1400 K, and is taken as the temperature drop associated with the specimen composed entirely of YbDS. This same heat flux is used for the calculations at longer cycling times.

The growth of the YbMS at the surface of the coating due to the volatilization of YbDS is modeled to grow parabolically at 179 nm $\sqrt{t}$,while that of the YbDS-rich region near to the silicon bond coat is also modeled to grow parabolically at 176 nm $\sqrt{t}$ with an initial thickness of 2.1 μm based on the experimental observations of thickness in our material systems. The thermal conductivities of each layer and their progressions in thickness are tabulated in Table B7.

B3 Thermal Conductance at Au Contacts with a TiO$_x$ Wetting Layer

B3.1 Choice of Ti Deposition Rate

We choose to deposit the Ti adhesion layers in HV at 0.1, 0.5, and 1.0 Å/s for a variety of reasons. The low deposition rates are chosen to reduce the surface roughness for experimental purposes, as a highly reflective surface (RMS roughness <10nm) is necessary for time-domain thermoreflectance measurements. Various pieces in the literature have shown that increasing deposition rate has a profound effect on surface roughness across all films [298, 299]. Additionally, we keep the deposition rates to Å/s and below due to the restrictions of our electron beam evaporator. There is a finite rise time in the chamber to reach a desired deposition rate, and depositing 3 nm of Ti at a higher rate of deposition would have resulted in a non-constant deposition rate, another variable that could influence interfacial conductances. By restricting the deposition rates to 0.1, 0.5, and 1.0 Å/s, the deposition rate of the Ti in the chamber remained closest to their designated values.

B3.2 Calculation of TiO$_x$ Stoichiometry

The O:Ti ratio was calculated using intensities of the O 1s peak (I$_{O1s}$) and the Ti 2p$_{3/2}$ (I$_{Ti2p_{3/2}}$) peak corresponding to Ti-O bonds normalized to their respective relative sensitivity factors (RSF). Intensities were determined from Voigt function fits generated using kolXPD software. The RSF for each core level was calculated using the transmission function for the Scienta Omicron R3000 detector and Hartree-Slater subshell photoionization cross-section energies at 1487 eV [300]. Stoichiometry was determined by

$$\frac{O}{Ti} = \frac{\frac{I_{O1s}}{RSF_{O1s}}}{\frac{I_{Ti2p_{3/2}}}{RSF_{Ti2p_{3/2}}}}. \tag{B16}$$

B3.3 Calculation of Ti Thickness

The thickness of the Ti film was calculated using the integrated intensity of the Ti 2p core level of the thin films measured by XPS (I_{TF}) and the integrated intensity of the Ti 2p core level of an infinitely thick Ti film (I_∞) measured by XPS separately. The equation for the intensity of a thin film reported by Himpsel *et al.* is given as

$$I_{TF} = I_\infty(1 - e^{-\frac{d}{EALcos\theta}}) \tag{B17}$$

where d is the thickness of the thin film, EAL is the effective attenuation length, and θ is the photoelectron take-off angle [301]. The EAL is calculated using the NIST EAL database. In the ScientaOmicron system used in this work, the take-off angle is 45°. Solving for thickness, this yields

$$d = -EALcos\theta(ln(-\frac{I_{TF} - I_{\infty}}{I_{\infty}})). \tag{B18}$$

B3.4 XPS spectra of Ti deposited in HV and UHV

A comparison of the Ti $2p$ spectra for Ti deposited at 1.0 Å/s in HV and Ti deposited at <0.1 Å/s under UHV is shown in Fig. B19. Metallic Ti is indicated by a chemical state at 454.1 eV with a spin orbit splitting of 6.17 eV. TiO_2 has its $2p_{3/2}$peak at 458.8 eV with a spin orbit splitting of 5.54 eV [302].

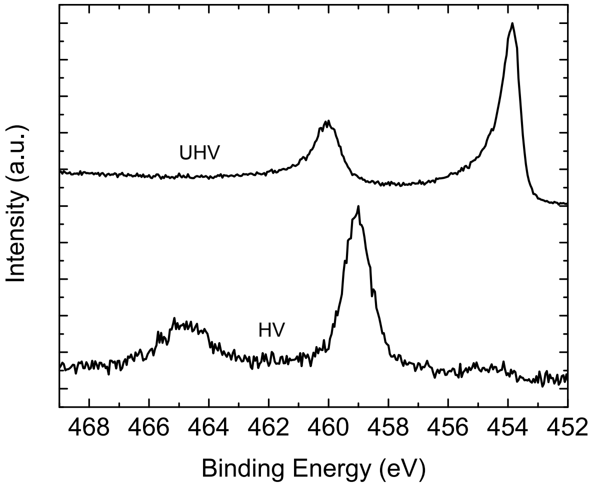

Figure B19. XPS spectra of Ti $2p$ core level of Ti deposited in HV at 1.0 Å/s and in UHV on Al_2O_3.

B4 Band alignment and defects influence the electron-phonon heat transport mechanisms across metal interfaces

B4.1 Time-Domain Thermoreflectance

In time-domain thermoreflectance (TDTR), 100 fs pulses emanate from an 80 MHz Ti:Sapphire oscillator, centered at 800 nm (1.55 eV) with a bandwidth of ∼11.5 nm. In our implementation, we frequency-double the pump to 400 nm (3.1 eV) using a $BiBO_3$ crystal to increase absorption in Au. The probe is mechanically delayed in time to monitor the thermoreflectance at the sample surface. The $1/e^2$ pump and probe radii are 8.0 and 4.5 μm, respectively, with the incident pump fluence being 3.85 J m^{-2} for the Au/TiO_x films and 2.42 J m^{-2} for the Au film. The cross-correlation of the pump and probe pulses at the sample surface is ∼800 fs [303] due to the dispersion induced from various components in the TDTR optical path.

B4.2 Varying Au Thickness in Au/TiO_x Systems

The in-phase reflectivity responses (V_{in}) of Au/TiO_x systems with varying Au thicknesses are presented in Fig. B20. In these specimens, a 5 nm TiO_x layer was deposited in a moderately high vacuum ($< 1 \times 10^{-6}$) Torr at 1.0 Å/s, which ensured at least some fraction of the layer contained Ti^0 according to the main document and our previous study [197]. The thickness of the Au layer was confirmed via X-ray reflectivity. Specimens with an Au capping layer of $<$ 102 nm reveal a significant rerise in the acquired magnitude following initial peak indicative of the electron temperature. Those with very thin Au capping layers, 14 and 24 nm, reveal a sign change at ∼2 ps where the signal goes negative before rerising again. We are unsure for the exact reasons for this, but hypothesize that it is related to the convolution of the Au and Ti thermoreflectance values at the probing wavelength. At the pump wavelength, a significant portion of optical energy is directly coupled to electrons in the Ti based on the optical skin depth of Au, ∼16 nm [264]. As the electron and lattice contribution to thermoreflectance of TiO_x is relatively unexplored, as well as its temperature dependent indices of refraction, we expect the signal acquired by the probe to be influenced by the Ti layer in some capacity. Nonetheless, we do not observe a sign change at thicknesses $\geq$ 49 nm, suggesting that this thickness may be optimal for interpreting the data via the TTM. For this reason, all specimens in the document were coated with an Au layer of ∼50 nm.

The characteristic electron-phonon interaction length is mathematically defined as $\lambda_{ep} =$

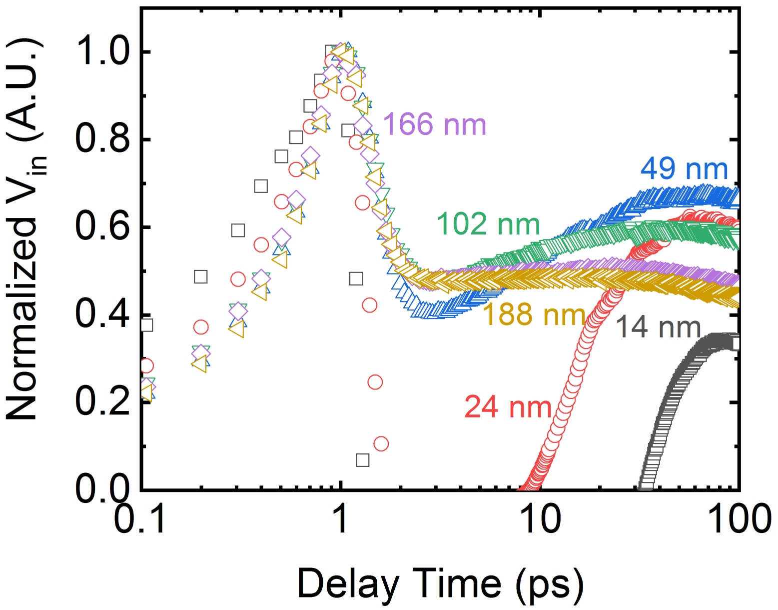

Figure B20. Ultrafast response in Au/TiO$_x$ systems with varying Au thicknesses, labeled.

$\sqrt{\kappa_e/g}$, where κ_e and g are the electronic thermal conductivity and electron-phonon coupling factor, respectively. In bulk Au, $\lambda_{ep} \approx 110$ nm [43]. Thus, performing these measurements with varying Au thickness yields critical insight into the interaction length between these two carriers. At an Au layer thickness of 166 nm, we observe a slight rerise in the signal, which is entirely diminished at 188 nm. At an Au thickness of 102 nm, the magnitude of this rerise is larger than at 166 nm, and at 49 nm the rerise is larger yet. For this rerise to occur, optically excited electrons in the Au layer must propagate through the Au layer without coupling with the lattice so that they can ballistically traverse into the TiO$_x$ layer. Once there, energy is transmitted to the lattice due to the ultrahigh g of the wetting layer, and the lattice temperature differential between the wetting and Au layers results in diffusion of heat via the lattice to the Au film, causing an increase in our acquired signal. If electrons are not able to reach the TiO$_x$ layer, then we would not expect a rerise in the signal. If we account for both the 1/e absorption depth at the pump wavelength, $\delta \approx 16$ nm [264], as well as the characteristic electron-phonon interaction length, the length over which energy is deposited into the Au layer will be $\delta + \lambda_{ep} \approx 126$ nm [271]. We find this value to be consistent with our experimental data, as it is less than the Au thickness at which we observe a diminished rerise in the signal, 166 nm, but larger than at 102 nm where the rerise is still present. Further experiments with finer increments in Au thickness would help to identify λ_{ep} definitively.

B4.3 Two-Temperature Modeling

To model the data acquired via TDTR, we first adjust the zero delay time of our TDTR data to be at approximately halfway of the initial peak to account for the delayed onset of electron thermalization. Spatial and temporal discretizations of 0.5 nm and 50 fs, respectively, are used in simulating the energy deposition. The substrate is modeled to be 100 nm, with a 0.5 nm discretization. The final discretized layer of the substrate is fixed to have an infinite heat capacity to emulate a semi-infinite substrate. The electronic heat capacity of each layer is chosen to be proportional to temperature via the electronic heat capacity coefficient γ, $C_e = \gamma T_e$, which is valid for the range of electronic temperatures in this study. The electron-phonon coupling factor g is approximately independent of lattice and electronic temperatures for low temperature perturbations [43], and is thus chosen to be constant. Interfaces are modeled have thicknesses of 0.5 nm, where the phonon thermal conductance is given an equivalent thermal conductivity for the discretized thickness, and the electronic thermal conductance is the product of the average of the electronic temperatures on either side of the interface and Γ (i.e., $\Gamma T_{\mathrm{e,ave}}$) to be in accordance with electron diffuse-mismatch model [56]. For systems with a wetting layer, we fix the Au/TiO_x phonon conductance to 100 MW m^{-2} K^{-1}. Additionally, for 1 nm pure Ti, we use literature values [304] for the electron and phonon thermal conductivities, adjusted for size effects using kinetic theory. For 4 nm TiO_x films, we assume 1 W m^{-1} K^{-1} for both the phonon thermal conductivity for amorphous TiO_2 films [263]. For the electron thermal conductivity in these films, 1 W m^{-1} K^{-1} is also assumed to account for any Ti^0 that may be present. See Table 6.1 of the main document for all inputs into the model.

In defining the electronic heat capacity, $C_e = \gamma T_e$, we choose to take γ for Ti from Lin et al.'s work [43] in describing those of our TiO_x films. A more rigorous definition of γ, however, depends on the electron density of states at the Fermi level, $D(\varepsilon_F)$, where ε_F is the Fermi energy. The electron heat capacity can be shown to be directly proportional to $D(\varepsilon_F)$ [262]:

$$C_e = \frac{\pi^2}{3} k_B^2 D(\varepsilon_F) T_e = \gamma T_e. \tag{B19}$$

Examining the electron density of states for Ti_xO_y from Fig. 6.8 of the main document, there are several key features to note. At ε_F for Ti, a large electron density exists, which ultimately correlates to a large value of γ for Ti. In stoichiometric TiO_2, the electron density is nearly 0. However, in our TiO_x systems in which $x \approx 2$, the presence of unreacted Ti^0, as confirmed via XPS and our two-temperature modeling, must provide additional states at and near ε_F, thereby increasing γ. Thus, γ of pure Ti is chosen for TiO_x films with $x \approx 2$. With regards to the TiO_x layer with $x = 2.62$, we are unable to rigorously define γ due to the off-stoichiometry of the film. In examining the electron density of states for Ti_3O_8 in Fig. 6.8 of the main document, the number of states at ε_F is comparable to that of Au. This large number of states is the reason for the theoretically efficient electron energy transmission, as described by Γ, at Au/Ti_3O_8 interfaces shown in Fig. 6.7(b) of the main document. Further, $D(\varepsilon_F)$ for Ti_3O_8, being comparable to that of Au, suggests that a value of γ similar to that of Au would best describe γ for Ti_3O_8. However, as the stoichiometry of TiO_x for $x = 2.62$ is not exactly Ti_3O_8, we choose γ of pure Ti to describe our $TiO_{2.62}$ layer to allow for an intercomparison between all TiO_x specimens.

Part of the analysis relies on the interpretation of the electronic and phononic temperatures described by the TTM. In general, the reflectivity is exhibits contributions from the electronic and lattice subsystems [81]:

$$\Delta R = a\Delta T_e + b\Delta T_l. \tag{B20}$$

In this equation, ΔR is the change in reflectivity resulting from perturbations in the electronic and lattice temperatures, ΔT_e and ΔT_l, respectively. The factors a and b are scaling constants that determine the contributions of each of these systems to ΔR. Because the signal acquired in TDTR encompasses contributions from both of these systems, and that the electronic contribution to thermoreflectivity becomes negligible $\sim$3 ps after excitation by the laser pulse near 800 nm for fluences used in this work [82, 83], we choose to interpret the lattice temperature acquired by the TTM and compare it to our measured data 3 ps after excitation. This interpretation accounts for the subsurface temperature profile and its influence on the thermoreflectivity [84], where the temperature at each discrete point beneath the surface contributes to the reflectivity and approximately follows the optical attenuation depth. The weighting function with which we use to interpret this subsurface temperature utilizes the index of refraction, n, of Au and its temperature dependence, dn/dT, at our probing wavelength, 800 nm, using previously reported data [62]. Because temperature dependent indices of refraction are not available for our TiO_x films, nor would there be any reasonable way of determining them without compromising their current stoichiometry, we utilize those from Au in the determination of the weighting function in our analysis.

The dR/dT weighting function assuming the temperature dependent indices of refraction of Au for both the Au and $TiO_{1.90}$ layers is shown in Fig. B21(a) as the black solid line. The weighting function exemplifies the insensitivity of the contribution from the underlying $TiO_{1.90}$ layer, as dR/dT is < 0.05 within this region. As an extreme example, we recalculate this weighting function under the assumption that the temperature dependent indices of refraction in the TiO_x layer are that of Pt [62]. Shown as the dashed red line in Fig. B21(a), this results in a negligible change in the dR/dT weighting function–the majority of the contribution to the probe reflectivity is manifested in the Au capping layer. The probe-averaged temperature rise when utilizing both weighting functions is shown in Fig. B21(b). While a distinction can be made between these responses, we emphasize that we normalize and fit the model to our data beyond 3 ps, and that the rate at which the temperatures rise for each response are similar. Fitting our data under the assumption that the temperature coefficients of the $TiO_{1.90}$ layer are that of Pt provides similar lower bounds to g and Γ compared to when those of Au are used.

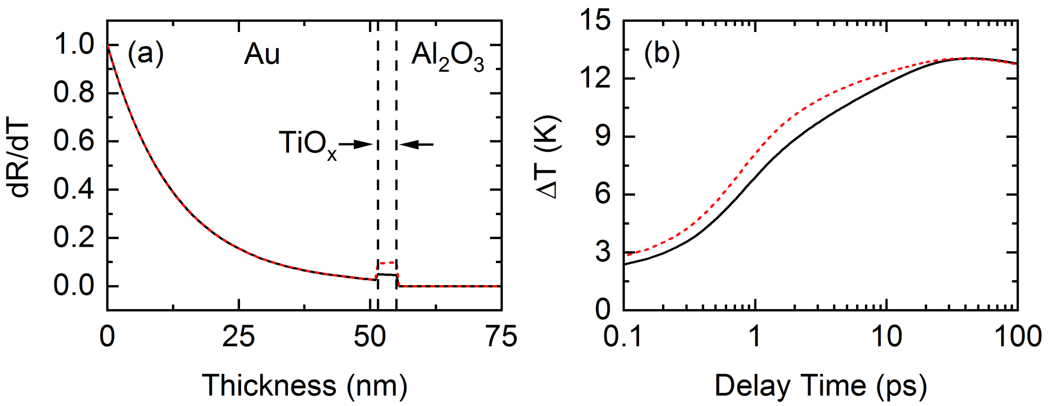

Figure B21. (a) dR/dT weighting function and (b) probe-averaged temperature response of the Au/4 nm $TiO_{1.90}/Al_2O_3$ system under the assumption that the temperature dependent indices of refraction of the $TiO_{1.90}$ layer are that of Au (black solid line) and Pt (dashed red line).

We note that for the time scales over which we determine the parameters of interest, we are not particularly sensitive to the Au/Al_2O_3 and TiO_x/Al_2O_3 phonon conductances in the Au/Al_2O_3 and $Au/TiO_x/Al_2O_3$ systems, respectively, due to the fact that thermal diffusion into the substrate typically occurs beyond ∼100 ps [305]. For the electron-phonon coupling factor of Au, uncertainty is determined by perturbing the pump and probe indices of refraction, the temperature dependent index of refraction of the probe, as well as the fluence by 10% and taking the difference between the newly acquired g and original g and calculating the quadrature. For g and Γ in systems with the TiO_x adhesion layer, we determine the bounds to these values when the sum of the square of the difference between our data and the implemented TTM model (i.e., $\sum(T_d\text{-}T_m)^2$, where T_d is the measured thermoreflectance data and T_m is the TTM model) is $< .02$ for the range over which the data are fitted.

B4.4 Theory and Simulation Details

Time-Domain Density Functional Theory (TDDFT)

In real-time TDDFT, the electron density, $\rho(r,t)$, evolves in time and is obtained by summation over densities of the occupied time-dependent single-electron Kohn Sham (KS) orbitals, $\Psi_n(r,t)$:

$$\rho(r,t) = \sum_{n=1}^{N_e} |\Psi_n(r,t)|^2 \tag{B21}$$

where n = 1, 2, ..., N_e, and N_e is the total number of electrons. The equations of motions are obtained using the time-dependent variational principle applied to the total Kohn-Sham energy. Each evolving KS orbital satisfies the equation:

$$i\hbar\frac{\partial}{\partial t}\Psi_n(r,t) = H[\rho(r,t)]\Psi_n(r,t) \tag{B22}$$

where the Hamiltonian is a DFT functional that depends on the electron density, its gradient, etc. The equations are coupled, because $H[\rho(r,t)]$ depends on all KS orbitals. In order to solve the time-dependent KS (TDKS) equations, Eq. B22, we expand the time-dependent KS orbitals in the basis of adiabatic KS orbitals, $\Phi_k(r;\mathbf{R}(t))$, which are calculated by ground state DFT for the current nuclear coordinates $\mathbf{R}$,

$$\Psi_n(r,t) = \sum_k C_k^n(t)\Phi_k(r;\mathbf{R}(t)). \tag{B23}$$

Such expansion provides an efficient numerical way to solve the time-dependent KS equations, because adiabatic KS orbitals are available from many highly optimized DFT codes, and because the size of the expansion is small compared, for instance, to a grid representation in the position or momentum space. By insertion of Eq. B23 into Eq. B22, one converts the time-dependent KS equations into equations for the expansion coefficients:

$$i\hbar\frac{\partial}{\partial t}c_j^n(t) = \sum_k C_k^n(t)(\varepsilon_k\delta_{jk} + d_{jk}) \tag{B24}$$

where ε_k is energy of the adiabatic KS orbital k, and d_{jk} is the nonadiabatic coupling (NAC) between adiabatic KS orbitals j and k. The NAC arises from atomic motions that change adiabatic orbitals along a nuclear trajectory. We calculate the NAC numerically as the overlap between adiabatic orbitals j and k at sequential time steps:

$$d_{jk} = -i\hbar \frac{\langle \Phi_j | \nabla_R H | \Phi_k \rangle}{\varepsilon_j - \varepsilon_k} \cdot \frac{dR}{dt} = -i\hbar \langle \Phi_j | \nabla_R | \Phi_k \rangle \cdot \frac{dR}{dt} = -i\hbar \langle \Phi_j | \frac{\partial}{\partial t} | \Phi_k \rangle . \tag{B25}$$

The current version of the above scheme is implemented [306, 307] with the Quantum Espresso (QE) package [308].

Non-adiabatic Molecular Dynamics by Surface Hopping

Solution to the time-dependent Schrödinger equation, presently Eq. B22, provides input to surface hopping (SH). SH is needed in order to obtain branching and thermodynamic equilibrium, which are not trivial to achieve when the Schrödinger equation for electrons is coupled to a classical trajectory for atoms. In particular, a classical trajectory cannot branch, in contrast to quantum mechanical wave-packets, and the unitary evolution provided by the Schrödinger equation cannot reach thermodynamic equilibrium which requires coupling to a bath. Fewest switches SH (FSSH) developed by Tully [309] is a very popular and efficient SH strategy. The scheme minimizes the number of hops and defines the SH probability using population fluxes between quantum states. The time-dependent probability of a hop from state j to state k within the time interval dt is given in FSSH by:

$$\begin{gathered} dP_{jk} = \frac{-2Re(A^*_{jk} d_{jk} \dot{\mathbf{R}})}{A_{jj}} dt \\ A_{jk} = c_j c^*_k . \end{gathered} \tag{B26}$$

If the hopping probability dP_{jk} is negative, it is set to zero: a hop from state j to state k is allowed to take place only when the electronic occupation of state k increases and the occupation of state j decreases. A random number distributed uniformly between 0 and 1 is sampled and compared to the hopping probability in order to determine whether the system should remain in the current state or should hop to a new state. When an electronic transition occurs, the original FSSH technique rescales the nuclear velocities along the NAC direction to conserve the total electron-nuclear energy. If there is not enough nuclear ki-

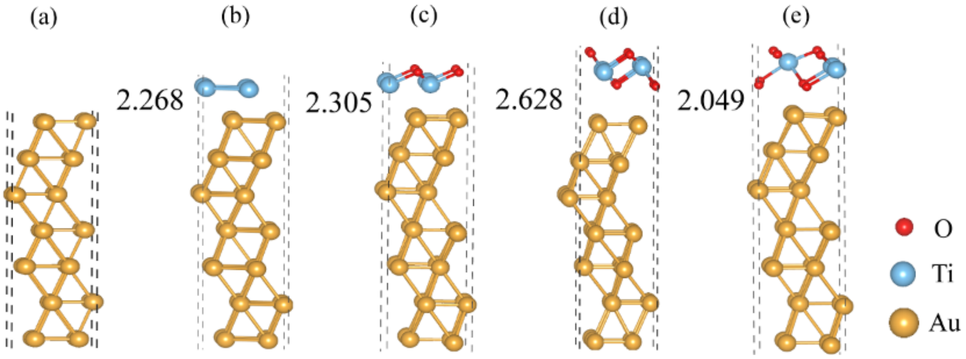

Figure B22. Geometries of (a) pure Au(111) slab, and Au(111) slab with absorbed (b) Ti, (c) Ti_4O_4, (d) Ti_4O_8 and (e) Ti_3O_8 layers at 0 K. The numbers on the left side of the structures indicate the distances between the TiO_x layer and the nearest Au layer.

netic associated with the NAC direction to account for the increase in the electronic energy, the hop is rejected. The velocity rescaling and hop rejection rules give detailed balance between transitions upward and downward in energy, mimicking Boltzmann statistics and leading to quantum-classical thermodynamic equilibrium at long times. Under the classical path approximation, the velocity rescaling and hop rejection are replaced by multiplying the probability to hop upward in energy with the Boltzmann factor, leading to significant computational savings [306, 307].

Simulation Details

The electronic structure calculations, geometry optimization and ground state molecular dynamics were carried out using the QE package. The electronic exchange and correlation interactions were treated using the Perdew-Burke-Ernzerhof (PBE) DFT functional [310]. The interactions of valence electrons with ions were accounted for via the projector augmented wave (PAW) method [311]. The van der Waals (vdW) interactions were included using the DFT-D3 approach. Pure DFT functionals, such as PBE, often underestimate energy gaps due to the self-interaction error. To account for this problem, the DFT+U approach was used, with U = 9.0 eV applied to the 3*d* electrons of the Ti atoms, improving description of the TiO_x electronic structure [312, 313]. A basis set energy cutoff of 40 Ry and a kinetic energy cutoff of 400 Ry for charge density were employed. The simulation cells are shown in Fig. B22. The calculations were performed using a uniform $5 \times 5 \times 1$ k-point grid. Atomic positions were fully relaxed until the calculated Hellmann-Feynman forces were smaller than 0.05 eV/Å. After the structure optimization, repeated velocity rescaling was used to heat the systems to 300 K. Subsequently, 3 ps adiabatic MD trajectories were generated with a 1 fs atomic time step and were used for the NAMD calculations. The first 500 structures were used as initial conditions to perform FSSH, with 1000 random number sequences for each structure, using the PYXAID package.

Bibliography

[1] Fourier, J.-B.-J., “Theorie analytique de la chaleur,” 1822.

[2] Ju, Y. S. and Goodson, K. E., “Phonon scattering in silicon films with thickness of order 100 nm,” *Applied Physics Letters*, vol. 74, no. 20, 1999.

[3] Huxtable, S. T., Abramson, A. R., Tien, C. L., Majumdar, A., Labounty, C., Fan, X., Zeng, G., Bowers, J. E., Shakouri, A., and Croke, E. T., “Thermal conductivity of Si/SiGe and SiGe/SiGe superlattices,” *Applied Physics Letters*, vol. 80, no. 10, pp. 1737–1739, 2002.

[4] Wang, Y., Fujinami, K., Zhang, R., Wan, C., Wang, N., Ba, Y., and Koumoto, K., “Interfacial thermal resistance and thermal conductivity in nanograined $SrTiO_3$,” *Applied Physics Express*, vol. 3, no. 3, pp. 2–5, 2010.

[5] Slack, G. A., “Thermal conductivity of pure and impure silicon, silicon carbide, and diamond,” *Journal of Applied Physics*, vol. 35, no. 12, pp. 3460–3466, 1964.

[6] McConnell, A. D., Uma, S., and Goodson, K. E., “Thermal conductivity of doped polysilicon layers,” *Journal of Microelectromechanical Systems*, vol. 10, no. 3, pp. 360–369, 2001.

[7] Chen, G., *Nanoscale energy transport and conversion: a parallel treatment of electrons, molecules, phonons, and photons*. Oxford University Press, 2005.

[8] Singh, P. and Ravindra, N. M., “Temperature dependence of solar cell performance - An analysis,” *Solar Energy Materials and Solar Cells*, vol. 101, pp. 36–45, 2012.

[9] Lohnert, G. H., Nabielek, H., and Schenk, W., “The fuel element of the HTR-module, a prerequisite of an inherently safe reactor,” *Nuclear Engineering and Design*, vol. 109, no. 1-2, pp. 257–263, 1988.

[10] Martin, D. G., “Considerations pertaining to the achievement of high burn-ups in HTR fuel,” *Nuclear Engineering and Design*, vol. 213, pp. 241–258, apr 2002.

[11] Twaha, S., Zhu, J., Yan, Y., and Li, B., “A comprehensive review of thermoelectric technology: Materials, applications, modelling and performance improvement,” *Renewable and Sustainable Energy Reviews*, vol. 65, pp. 698–726, 2016.

[12] He, R., Schierning, G., and Nielsch, K., “Thermoelectric Devices: A Review of Devices, Architectures, and Contact Optimization,” *Advanced Materials Technologies*, vol. 3, no. 4, 2018.

[13] Langston, L. S., “Powering Ahead,” *Mechanical Engineering*, vol. 133, no. 05, pp. 30–33, 2011.

[14] Clarke, D. R., Oechsner, M., and Padture, N. P., “Thermal-barrier coatings for more efficient gas-turbine engines,” *MRS Bulletin*, vol. 37, no. 10, pp. 891–898, 2012.

[15] Padture, N. P., Gell, M., and Jordan, E. H., “Thermal barrier coatings for gas-turbine engine applications,” *Science*, vol. 296, no. 5566, pp. 280–284, 2002.

[16] Lee, K. N., Fox, D. S., and Bansal, N. P., "Rare earth silicate environmental barrier coatings for SiC/SiC composites and Si_3N_4 ceramics," *Journal of the European Ceramic Society*, vol. 25, pp. 1705–1715, 2005.

[17] Padture, N. P., "Advanced structural ceramics in aerospace propulsion," *Nature Materials*, vol. 15, no. 8, pp. 804–809, 2016.

[18] Lee, K. N., Fritze, H., and Ogura, Y., "Protective Coatings for Gas Turbines," in *The Gas Turbine Handbook*, pp. 419–437, U.S. Department of Energy, NETL, 2006.

[19] DiCarlo, J. A., Yun, H. M., Morscher, G. N., and Bhatt, R. T., "SiC/SiC Composites for 1200°C and Above," *Handbook of Ceramic Composites*, no. December, pp. 77–98, 2006.

[20] Arthur, E. K., Ampaw, E., Azeko, S. T., and Danyuo, Y., "Design of Thermally Reliable Environmental Barrier Coating for a SiC/SiC Ceramic Matrix Composites," *International Journal of Composite Materials*, vol. 3, no. 6, pp. 191–197, 2013.

[21] Hay, R. S. and Mogilevsky, P., "Model for SiC fiber strength after oxidation in dry and wet air," *Journal of the American Ceramic Society*, vol. 102, no. 1, pp. 397–415, 2019.

[22] Spitsberg, I. and Steibel, J., "Thermal and Environmental Barrier Coatings for SiC/SiC CMCs in Aircraft Engine Applications," *International Journal of Applied Ceramic Technology*, vol. 1, no. 4, pp. 291–301, 2010.

[23] Xu, Y., Hu, X., Xu, F., and Li, K., "Rare earth silicate environmental barrier coatings: Present status and prospective," *Ceramics International*, vol. 43, pp. 5847–5855, jun 2017.

[24] Ohji, T. and Singh, M., eds., *Engineered Ceramics: Current Status and Future Prospects*. John Wiley & Sons, Ltd, 2015.

[25] Xu, J., Sarin, V. K., Dixit, S., and Basu, S. N., "Stability of interfaces in hybrid EBC/TBC coatings for Si-based ceramics in corrosive environments," *International Journal of Refractory Metals and Hard Materials*, vol. 49, no. 1, pp. 339–349, 2015.

[26] Kapitza, P. L., "The study of heat transfer in Helium II," *Zhurnal eksperimentalnoi i teoreticheskoi fiziki*, vol. 11, pp. 1–31, 1941.

[27] Rupp, K., "42 Years of Microprocessor Trend Data," 2018.

[28] "Intel Unleashes its First 8-Core Desktop Processor," 2014.

[29] "Computer History Museum."

[30] "4004 single Chip 4-Bit P-Channel Microprocessor," tech. rep., Intel, 1987.

[31] "Core i7-900 Desktop Processor Extreme Edition Series and Intel ® Core i7-900 Desktop Processor Series," tech. rep., Intel, 2010.

[32] Gelsinger, P., "Into the Core...," 2006.

[33] Poensgen, R., "Ein technisches Verfahren zur Ermittlung der Wärmeleitfähigkeit plattenförmiger Stoffe," in *Mitteilungen über Forschungsarbeiten auf dem Gebiete des Ingenieurwesens*, pp. 25–40, Berlin: Springer, 1912.

[34] Healy, J. J., de Groot, J. J., and Kestin, J., "The theory of the transient hot-wire method for measuring thermal conductivity," *Physica B+C*, vol. 82, no. 2, pp. 392–408, 1976.

[35] Gustafsson, S. E., “Transient plane source techniques for thermal conductivity and thermal diffusivity measurements of solid materials,” *Review of Scientific Instruments*, vol. 62, no. 3, pp. 797–804, 1991.

[36] Parker, W. J., Jenkins, R. J., Butler, C. P., and Abbott, G. L., “Flash method of determining thermal diffusivity, heat capacity, and thermal conductivity,” *Journal of Applied Physics*, vol. 32, no. 9, pp. 1679–1684, 1961.

[37] Onsager, L., “Reciprocal Relations in Irreversible Processes. I.,” *Physical Review*, vol. 37, pp. 405–426, 1931.

[38] Onsager, L., “Reciprocal Relations in Irreversible Processes. II.,” *Physical Review*, vol. 38, pp. 2265–2279, 1931.

[39] Soret, C., “Sur l’Etude Experimentale des Coefficients Rotationnels de Conductibilite Thermique,” *Arch. Sci. Phys. Nat.*, vol. 29, pp. 355–357, 1893.

[40] Voigt, W., “Fragen der Kristallphysik I. Uber die Rotatorischen Constanten der Warmeleitung von Apatit und Dolomit,” *Nachr. Ges. Wiss. Goettingen, Math.-Phys. Kl.*, vol. 3, pp. 87–89, 1903.

[41] Wenk, H.-R., Joswig, W., Tagai, T., Korekawa, M., and Smith, B. K., “The average structure of An 62-66 labradorite,” *American Mineralogist*, vol. 65, pp. 8I–95, 1980.

[42] Bunge, H.-J., *Texture Analysis in Materials Science*. Berlin: Akademie-Verlag, 1969.

[43] Lin, Z., Zhigilei, L. V., and Celli, V., “Electron-phonon coupling and electron heat capacity of metals under conditions of strong electron-phonon nonequilibrium,” *Physical Review B*, vol. 77, no. 075133, 2008.

[44] Gall, D., “Electron mean free path in elemental metals,” *Journal of Applied Physics*, vol. 119, no. 8, p. 85101, 2016.

[45] Kaveh, M. and Wiser, N., “Electron-electron scattering in conducting materials,” *Advances in Physics*, vol. 33, no. 4, pp. 257–372, 1984.

[46] Franz, R. and Wiedemann, G., “Ueber die Wärme-Leitungsfähigkeit der Metalle,” *Annalen der Physik*, vol. 165, no. 8, pp. 497–531, 1853.

[47] Lorenz, L., “Über das Leitungsvermögen der Metalle für Wärme und Elektrizität,” *Ann. Phys. Wied. Ann.*, vol. 13, 1881.

[48] Chen, G., “Nonlocal and Nonequilibrium Heat Conduction in the Vicinity of Nanoparticles,” *Journal of Heat Transfer*, vol. 118, no. 3, p. 539, 1996.

[49] Klemens, P., “The Lattice Component of the Thermal Conductivity of Metals and Alloys,” *Australian Journal of Physics*, vol. 7, no. 1, p. 57, 1954.

[50] Kaganov, M., Lifshitz, I. M., and Tanatarov, L. V., “Relaxation between Electrons and the Crystalline Lattice,” *Soviet Physics JETP*, vol. 4, no. 2, pp. 173–178, 1957.

[51] Lifshits, I. M., Kaganov, M. I., and Tanatarov, L. V., “On the Theory of Radiation-Induced Changes in Metals,” *Journal of Nuclear Energy, Part A: Reactor Science*, vol. 12, no. 1-2, pp. 69–78, 1960.

[52] Anisimov, S. I., Kapeliovich, B. L., and Perel’man, T. L., “Electron emission from metal surfaces exposed to ultrashort laser pulses,” *Soviet Physics JETP*, vol. 39, no. 2, pp. 375–377, 1974.

[53] Tomko, J., *Thermal transport and energy transfer mechanisms across interfaces composed of varying phases of matter*. PhD thesis, University of Virginia, 2020.

[54] Swartz, E. T. and Pohl, R. O., "Thermal boundary resistance," *Reviews of Modern Physics*, vol. 61, no. 3, pp. 605–668, 1989.

[55] John William Strutt, B. R., *The Theory of Sound: Volume I.* London: Macmillan and Co., 2 ed., 1984.

[56] Gundrum, B. C., Cahill, D. G., and Averback, R. S., "Thermal conductance of metal-metal interfaces," *Physical Review B - Condensed Matter and Materials Physics*, vol. 72, no. 24, 2005.

[57] Cahill, D. G., "Analysis of heat flow in layered structures for time-domain thermoreflectance," *Review of Scientific Instruments*, vol. 75, no. 12, pp. 5119–5122, 2004.

[58] Schmidt, A. J., Cheaito, R., and Chiesa, M., "A frequency-domain thermoreflectance method for the characterization of thermal properties," *Review of Scientific Instruments*, vol. 80, p. 094901, sep 2009.

[59] Yang, J., Maragliano, C., and Schmidt, A. J., "Thermal property microscopy with frequency domain thermoreflectance," *Review of Scientific Instruments*, vol. 84, no. 104904, 2013.

[60] Braun, J. L., **Olson, D. H.**, Gaskins, J. T., and Hopkins, P. E., "A steady-state thermoreflectance method to measure thermal conductivity," *Review of Scientific Instruments*, vol. 90, no. 2, 2019.

[61] Wang, Y., Park, J. Y., Koh, Y. K., and Cahill, D. G., "Thermoreflectance of metal transducers for time-domain thermoreflectance," *Journal of Applied Physics*, vol. 108, no. 4, p. 43507, 2010.

[62] Wilson, R. B., Apgar, B. A., Martin, L. W., and Cahill, D. G., "Thermoreflectance of metal transducers for optical pump-probe studies of thermal properties," *Optics Express*, vol. 20, no. 27, pp. 2267–2269, 2012.

[63] O'hara, K. E., Hu, X., and Cahill, D. G., "Characterization of nanostructured metal films by picosecond acoustics and interferometry," *Nanoscale thermal transport Journal of Applied Physics*, vol. 90, no. 4852, p. 793, 2001.

[64] Tas, G., Loomis, J. J., Maris, H. J., Bailes, A. A., and Seiberling, L. E., "Picosecond ultrasonics study of the modification of interfacial bonding by ion implantation," *Applied Physics Letters*, vol. 72, no. 18, pp. 2235–2237, 1998.

[65] Duda, J. C., Yang, C.-Y. P., Foley, B. M., Cheaito, R., Medlin, D. L., Jones, R. E., and Hopkins, P. E., "Influence of interfacial properties on thermal transport at gold:silicon contacts," *Applied Physics Letters*, vol. 102, no. 8, p. 81902, 2013.

[66] Lide, D. R., *CRC Handbook of Chemistry and Physics.* Boca Raton: CRC Press LLC, 2005.

[67] Capinski, W. S. and Maris, H. J., "Improved apparatus for picosecond pump-and-probe optical measurements," *Review of Scientific Instruments*, vol. 67, no. 8, pp. 2720–2726, 1996.

[68] Feser, J. P., Liu, J., and Cahill, D. G., "Pump-probe measurements of the thermal conductivity tensor for materials lacking in-plane symmetry," *Review of Scientific Instruments*, vol. 85, no. 10, p. 104903, 2014.

[69] Qian, X., Ding, Z., Shin, J., Schmidt, A. J., and Chen, G., "Accurate measurement of in-plane thermal conductivity of layered materials without metal film transducer using frequency domain thermoreflectance," *Review of Scientific Instruments*, vol. 91, no. 6, 2020.

[70] Liu, J., Zhu, J., Tian, M., Gu, X., Schmidt, A., and Yang, R., "Simultaneous measurement of thermal conductivity and heat capacity of bulk and thin film materials using frequency-dependent transient thermoreflectance method," *Review of Scientific Instruments*, vol. 84, no. 034902, 2013.

[71] **Olson, D. H.**, Rost, C. M., Gaskins, J. T., Szwejkowski, C. J., Braun, J. L., and Hopkins, P. E., "Size effects on the cross-plane thermal conductivity of transparent conducting indium tin oxide and fluorine tin oxide thin films," *IEEE Transactions on Components, Packaging and Manufacturing Technology*, vol. 9, no. 1, pp. 51–57, 2019.

[72] Wei, C., Zheng, X., Cahill, D. G., and Zhao, J.-C., "Invited Article: Micron resolution spatially resolved measurement of heat capacity using dual-frequency time-domain thermoreflectance," *Review of Scientific Instruments*, vol. 84, p. 71301, 2013.

[73] Carslaw, H. and Jaeger, J. C., *Conduction of Heat in Solids*. Oxford University Press, second ed., 1959.

[74] Koh, Y. K. and Cahill, D. G., "Frequency dependence of the thermal conductivity of semiconductor alloys," *Physical Review B - Condensed Matter and Materials Physics*, vol. 76, no. 7, pp. 1–5, 2007.

[75] Regner, K. T., Sellan, D. P., Su, Z., Amon, C. H., McGaughey, A. J., and Malen, J. A., "Broadband phonon mean free path contributions to thermal conductivity measured using frequency domain thermoreflectance," *Nature Communications*, vol. 4, pp. 1640–1647, 2013.

[76] Sood, A., Xiong, F., Chen, S., Cheaito, R., Lian, F., Asheghi, M., Cui, Y., Donadio, D., Goodson, K. E., and Pop, E., "Quasi-Ballistic Thermal Transport Across MoS_2 Thin Films," *Nano Letters*, vol. 19, no. 4, pp. 2434–2442, 2019.

[77] Braun, J. L. and Hopkins, P. E., "Upper limit to the thermal penetration depth during modulated heating of multilayer thin films with pulsed and continuous wave lasers: A numerical study," *Journal of Applied Physics*, vol. 121, no. 175107, 2017.

[78] Smith, A. N. and Norris, P. M., "Numerical Solution for the Diffusion of High Intensity , Ultrashort Laser Pulses within Metal Films," in *International Heat Transfer Conference 11*, vol. 246, pp. 241–246, 2016.

[79] Ozisik, M. N., Orlande, H. R., Colaco, M. J., and Cotta, R. M., *Finite Difference Methods in Heat Transfer*. Florida: Taylor & Francis, 2 ed., 2017.

[80] Pettersson, L. A. A., Roman, L. S., and Inganäs, O., "Modeling photocurrent action spectra of photovoltaic devices based on organic thin films," *Journal of Applied Physics*, vol. 86, no. 1, p. 487, 1999.

[81] Brorson, S. D., Kazeroonian, A., Moodera, J. S., Face, D. W., Cheng, T. K., Ippen, E. P., Dresselhaus, M. S., and Dresselhaus, G., "Femtosecond room-temperature measurement of the electron-phonon coupling constant γ in metallic superconductors," *Physical Review Letters*, vol. 64, pp. 2172–2175, apr 1990.

[82] Choi, G.-M., Wilson, R. B., and Cahill, D. G., "Indirect heating of Pt by short-pulse laser irradiation of Au in a nanoscale Pt/Au bilayer," *Physical Review B*, vol. 89, no. 6, p. 64307, 2014.

[83] Jang, H., Kimling, J., and Cahill, D. G., "Nonequilibrium heat transport in Pt and Ru probed by an ultrathin Co thermometer," *Physical Review B*, vol. 101, no. 6, 2020.

[84] Chen, G. and Tien, C. L., "Internal reflection effects on transient photothermal reflectance," *Journal of Applied Physics*, vol. 73, no. 7, pp. 3461–3466, 1993.

[85] Hecht, E., *Optics*. Pearson education, Addison-Wesley, 4 ed., 2002.

[86] **Olson, D. H.**, Avincola, V. A., Parker, C. G., Braun, J. L., Gaskins, J. T., Tomko, J. A., Opila, E. J., and Hopkins, P. E., "Anisotropic thermal conductivity tensor of β-$Y_2Si_2O_7$ for orientational control of heat flow on micrometer scales," *Acta Materialia*, vol. 189, pp. 299–305, 2020.

[87] Liebert, C. H. and Stepka, F. S., "Industry Tests of NASA Ceramic Thermal Barrier Coating," tech. rep., Lewis Research Center, 1979.

[88] Rossette, A. H., C, Z. M., Demeulenaere, A., and Roque López Hernández, J. A., "The effect of start-up cycle in ceramic coating used as thermal barrier for a gas turbine bucket," *Applied Thermal Engineering*, vol. 29, no. 14-15, pp. 3056–3065, 2009.

[89] LeMieux, D. H., "On-Line Thermal Barrier Coating (TBC) Monitor for Real-Time Failure Protection and Life Maximization," tech. rep., Siemens Power Generation, Inc, 2005.

[90] Beals, M. D. and Zerfoss, S., "Volume change attending low-to-high inversion of cristobalite," *Journal of the American Ceramic Society*, vol. 27, pp. 285–292, nov 1944.

[91] Peacor, D. R., "High-temperature single-study of the Cristobalite Inversion," *Zeitschrift für Kristallographie*, vol. 138, pp. 274–298, 1973.

[92] Heaney, P. J. and Prewitt, C. T., *Silica: Physical Behavior, Geochemistry and Materials Applications*. Mineralogical Scoeity of America, 1994.

[93] Opila, E. J. and Hann, R. E., "Paralinear oxidation of CVD SiC in water vapor," *Journal of the American Ceramic Society*, vol. 80, no. 1, pp. 197–205, 1997.

[94] Opila, E. J., Smialek, J. L., Robinson, R. C., Fox, D. S., and Jacobson, N. J., "SiC recession caused by SiO_2 scale volatility under combustion conditions: I, Thermodynamics and Gaseous-Diffusion Model," *Journal of the American Ceramic Society*, vol. 82, no. 7, pp. 1826–34, 1999.

[95] Richards, B. T., Young, K. A., de Francqueville, F., Sehr, S., Begley, M. R., and Wadley, H. N., "Response of ytterbium disilicatesilicon environmental barrier coatings to thermal cycling in water vapor," *Acta Materialia*, vol. 106, pp. 1–14, mar 2016.

[96] Arai, Y., Aoki, Y., and Kagawa, Y., "Effect of cristobalite formation on the delamination resistance of an oxide/Si/(SiC/SiC) environmental barrier coating system after cyclic high temperature thermal exposure," *Scripta Materialia*, vol. 139, pp. 58–62, 2017.

[97] Richards, B. T., Begley, M. R., and Wadley, H. N., "Mechanisms of Ytterbium Monosilicate/Mullite/Silicon Coating Failure during Thermal Cycling in Water Vapor," *Journal of the American Ceramic Society*, vol. 98, no. 12, pp. 4066–4075, 2015.

[98] Zok, F. W., "Ceramic-matrix composites enable revolutionary gains in turbine engine efficiency," *American Ceramic Society Bulletin*, vol. 95, no. 5, pp. 22–28, 2016.

[99] Eaton, H. E., Linsey, G. D., More, K. L., Kimmel, J. B., Price, J. R., and Miriyala, N., "EBC Protection of SiC/SiC Composites in the Gas Turbine Combustion Environment," in *ASME Turbo Expo 2000: Power for Land, Sea, and Air*, p. V004T02A018, ASME, may 2000.

[100] Aparicio, M. and Durán, A., "Yttrium Silicate Coatings for Oxidation Protection of Carbon-Silicon Carbide Composites," *Journal of the American Ceramic Society*, vol. 83, pp. 1351–1355, dec 2004.

[101] Sun, Z., Zhou, Y., Wang, J., and Li, M., "Thermal Properties and Thermal Shock Resistance of γ-$Y_2Si_2O_7$," *Journal of the American Ceramic Society*, vol. 91, pp. 2623–2629, aug 2008.

[102] Klemm, H., "Silicon Nitride for High-Temperature Applications," *Journal of the American Ceramic Society*, vol. 93, pp. 1501–1522, jun 2010.

[103] Fukuda, K. and Matsubara, H., "Thermal Expansion of δ-Yttrium Disilicate," *Journal of the American Ceramic Society*, vol. 87, no. 1, pp. 89–92, 2004.

[104] Dolan, M. D., Harlan, B., White, J. S., Hall, M., Misture, S. T., Bancheri, S. C., and Bewlay, B., “Structures and anisotropic thermal expansion of the α, β, γ, and δ polymorphs of $Y_2Si_2O_7$,” *Powder Diffraction*, vol. 23, no. 1, pp. 20–25, 2008.

[105] Al Nasiri, N., Patra, N., Horlait, D., Jayaseelan, D. D., and Lee, W. E., “Thermal Properties of Rare-Earth Monosilicates for EBC on Si-Based Ceramic Composites,” *Journal of the American Ceramic Society*, vol. 99, no. 2, pp. 589–596, 2015.

[106] Clarke, D. R., “Materials selection guidelines for low thermal conductivity thermal barrier coatings,” *Surface and Coatings Technology*, vol. 163, pp. 67–74, 2003.

[107] Wu, Z., Sun, L., Wan, P., Li, J., Hu, Z., and Wang, J., “In situ foam-gelcasting fabrication and properties of highly porous γ-$Y_2Si_2O_7$ ceramic with multiple pore structures,” *Scripta Materialia*, vol. 103, pp. 6–9, 2015.

[108] Wu, Z., Sun, L., Wan, P., and Wang, J., “Preparation, microstructure and high temperature performances of porous γ-$Y_2Si_2O_7$ by in situ foam-gelcasting using gelatin,” *Ceramics International*, vol. 41, pp. 14230–14238, 2015.

[109] Cahill, D. G., Watson, S. K., and Pohl, R. O., “Lower limit to the thermal conductivity of disordered crystals,” *Physical Review B*, vol. 46, pp. 6131–6140, sep 1992.

[110] Redhammer, G. J. and Roth, G., “β-$Y_2Si_2O_7$, a new thortveitite-type compound, determined at 100 and 280 K,” *Acta Crystallographica Section C: Crystal Structure Communications*, vol. 59, no. 10, 2003.

[111] Hopkins, P. E., Serrano, J. R., Phinney, L. M., Kearney, S. P., Grasser, T. W., and Harris, C. T., “Criteria for cross-plane dominated thermal transport in multilayer thin film systems during modulated laser heating,” *Journal of Heat Transfer*, vol. 132, no. 8, p. 81302, 2010.

[112] Schmidt, A. J., Chen, X., and Chen, G., “Pulse accumulation, radial heat conduction, and anisotropic thermal conductivity in pump-probe transient thermoreflectance,” *Review of Scientific Instruments*, vol. 79, p. 114902, nov 2008.

[113] Feser, J. P. and Cahill, D. G., “Probing anisotropic heat transport using time-domain thermoreflectance with offset laser spots,” *Review of Scientific Instruments*, vol. 83, p. 104901, 2012.

[114] Rodin, D., Yee, S. K., and Woodruff, G. W., “Simultaneous measurement of in-plane and through-plane thermal conductivity using beam-offset frequency domain thermoreflectance,” *Journal of Applied Physics*, vol. 88, p. 14902, 2017.

[115] Jiang, P., Qian, X., and Yang, R., “A new elliptical-beam method based on time-domain thermoreflectance (TDTR) to measure the in-plane anisotropic thermal conductivity and its comparison with the beam-offset method,” *Review of Scientific Instruments*, vol. 89, no. 9, 2018.

[116] Li, M., Kang, J. S., and Hu, Y., “Anisotropic thermal conductivity measurement using a new Asymmetric-Beam Time-Domain Thermoreflectance (AB-TDTR) method,” *Review of Scientific Instruments*, vol. 89, p. 84901, 2018.

[117] Jiang, P., Qian, X., and Yang, R., “Tutorial: Time-domain thermoreflectance (TDTR) for thermal property characterization of bulk and thin film materials,” *Journal of Applied Physics*, vol. 124, p. 161103, oct 2018.

[118] Sood, A., Cheaito, R., Bai, T., Kwon, H., Wang, Y., Li, C., Yates, L., Bougher, T., Graham, S., Asheghi, M., Goorsky, M., and Goodson, K. E., “Direct Visualization of Thermal Conductivity Suppression Due to Enhanced Phonon Scattering Near Individual Grain Boundaries,” *Nano Letters*, vol. 18, no. 6, pp. 3466–3472, 2018.

[119] Newnham, R. E., *Properties of Materials: Anisotropy, Symmetry, Structure*. Oxford, United Kingdom: Oxford University Press USA - OSO, 2004.

[120] Einstein, A., "Über die von der molekularkinetischen Theorie der Wärme geforderte Bewegung von in ruhenden Flüssigkeiten suspendierten Teilchen," *Annalen der Physik*, vol. 322, pp. 549–560, jan 1905.

[121] Tian, Z., Zheng, L., Li, Z., Li, J., and Wang, J., "Exploration of the low thermal conductivities of γ-$Y_2Si_2O_7$, β-$Y_2Si_2O_7$, β-$Yb_2Si_2O_7$, and β-$Lu_2Si_2O_7$ as novel environmental barrier coating candidates," *Journal of the European Ceramic Society*, vol. 36, pp. 2813–2823, sep 2016.

[122] Jaeken, J. W. and Cottenier, S., "Solving the Christoffel equation: Phase and group velocities," *Computer Physics Communications*, vol. 207, pp. 445–451, oct 2016.

[123] Zhou, L., Huang, J., Cao, L., Ouyang, H., Wu, J., Liu, J., Wang, X., and Hao, W., "Synthesis of β-$Y_2Si_2O_7$ nanowires via a facile molten salt method and their thermal properties," *Journal of Alloys and Compounds*, vol. 699, pp. 210–215, mar 2017.

[124] **Olson, D. H.**, Deijkers, J. A., Quiambao-Tomko, K., Gaskins, J. T., Richards, B. T., Opila, E. J., Hopkins, P. E., and Wadley, H. N. G., "Evolution of microstructure and thermal conductivity of multifunctional environmental barrier coating systems," *Materials Today Physics*, vol. 17, 2021.

[125] Robinson, R. C. and Smialek, J. L., "SiC recession caused by SiO_2 scale volatility under combustion conditions: I. Experimental results and empirical model," *Journal of the American Ceramic Society*, vol. 82, no. 7, pp. 1817–1825, 1999.

[126] Zhou, Y. C., Zhao, C., Wang, F., Sun, Y. J., Zheng, L. Y., and Wang, X. H., "Theoretical prediction and experimental investigation on the thermal and mechanical properties of bulk β-$Yb_2Si_2O_7$," *Journal of the American Ceramic Society*, vol. 96, no. 12, pp. 3891–3900, 2013.

[127] Fritsch, M., *Heibgaskorrosion keramischer Werkstoffe in H_2O-Haltigen Rauchgasatmospharen*. PhD thesis, Fraunhofer-Institut fur Keramische Technologien und Systeme IKTS, 2007.

[128] Fernández-Carrión, A. J., Allix, M., and Becerro, A. I., "Thermal expansion of rare-earth pyrosilicates," *Journal of the American Ceramic Society*, vol. 96, pp. 2298–2305, jul 2013.

[129] Ueno, S., Jayaseelan, D. D., Kita, H., Ohji, T., and Lin, H. T., "Comparison of Water Vapor Corrosion Behaviors of $Ln_2Si_2O_2$ (Ln=Yb and Lu) and $ASiO_4$ (A=Ti, Zr and Hf) EBC's," *Key Engineering Materials*, vol. 317-318, pp. 557–560, 2006.

[130] Richards, B. T. and Wadley, H. N., "Plasma spray deposition of tri-layer environmental barrier coatings," *Journal of the European Ceramic Society*, vol. 34, no. 12, pp. 3069–3083, 2014.

[131] Khan, Z. S., Zou, B., Huang, W., Fan, X., Gu, L., Chen, X., Zeng, S., Wang, C., and Cao, X., "Synthesis and characterization of Yb and Er based monosilicate powders and durability of plasma sprayed Yb_2SiO_5 coatings on C/C-SiC composites," *Materials Science and Engineering B: Solid-State Materials for Advanced Technology*, vol. 177, no. 2, pp. 184–189, 2012.

[132] Ridley, M., Gaskins, J. T., Hopkins, P. E., and Opila, E. J., "Tailoring Thermal Properties of EBCs in High Entropy Rare Earth Monosilicates," *Acta Materialia*, 2020.

[133] Oerlikon,, "Material Product Data Sheet. High purity silicon powder for thermal spray," tech. rep., Oerlikon Metco, 2017.

[134] Okada, Y. and Tokumaru, Y., "Precise determination of lattice parameter and thermal expansion coefficient of silicon between 300 and 1500 K," *Journal of Applied Physics*, vol. 56, no. 2, pp. 314–320, 1984.

[135] Gulbransen, E. A. and Jansson, S. A., “The high-temperature oxidation, reduction, and volatilization reactions of silicon and silicon carbide,” *Oxidation of Metals*, vol. 4, no. 3, pp. 181–201, 1972.

[136] Sharafat, S., Jones, R. H., Kohyama, A., and Fenici, P., “Status and prospects for SiC–SiC composite materials development for fusion applications,” *Fusion Engineering and Design*, vol. 29, no. C, pp. 411–420, 1995.

[137] Hurley, D., Fazbod, F., Hua, Z., Reese, S., and Khafizov, M., “Advanced Measurements of Silicon Carbide Ceramic Matrix Composites,” Tech. Rep. August, Idaho National Laboratory Materials, Idaho Falls, 2012.

[138] Jones, R. E., Petrak, D., Rabe, J., and Szweda, A., “SYLRAMIC^{TM} SiC fibers for CMC reinforcement,” *Journal of Nuclear Materials*, vol. 283-287, no. PART I, pp. 556–559, 2000.

[139] Stockmeier, M., Müller, R., Sakwe, S. A., Wellmann, P. J., and Magerl, A., “On the lattice parameters of silicon carbide,” *Journal of Applied Physics*, vol. 105, no. 3, 2009.

[140] Robinson, R. C., “SiC Recession Due to SiO_2 Scale Volatility Under Combustor Conditions,” Tech. Rep. July 1999, NASA Glenn Research Center, Cleveland, 1997.

[141] Lee, K. N., “$Yb_2Si_2O_7$ Environmental barrier coatings with reduced bond coat oxidation rates via chemical modifications for long life,” *Journal of the American Ceramic Society*, vol. 102, no. 3, pp. 1507–1521, 2019.

[142] Leadbetter, A. J. and Wright, A. F., “The α–β transition in the cristobalite phases of SiO_2 and $AIPO_4$ I. X-ray studies,” *The Philosophical Magazine: A Journal of Theoretical Experimental and Applied Physics*, vol. 33, pp. 105–112, jan 1976.

[143] Lee, K. N., “Current status of environmental barrier coatings for Si-based ceramics,” *Surface and Coatings Technology*, vol. 133-134, pp. 1–7, 2000.

[144] Federer, J. I., “Alumina base coatings for protection of SiC ceramics,” *Journal of Materials Engineering*, vol. 12, pp. 141–149, jun 1990.

[145] Price, J., van Roode, M., and Stala, C., “Ceramic Oxide-Coated Silicon Carbide for High Temperature Corrosive Environments,” *Key Engineering Materials*, vol. 72-74, pp. 71–84, 1992.

[146] Garcia, E., Lee, H., and Sampath, S., “Phase and microstructure evolution in plasma sprayed $Yb_2Si_2O_7$ coatings,” *Journal of the European Ceramic Society*, vol. 39, no. 4, pp. 1477–1486, 2019.

[147] Costa, G. C. and Jacobson, N. S., “Mass spectrometric measurements of the silica activity in the Yb_2O_3-SiO_2 system and implications to assess the degradation of silicate-based coatings in combustion environments,” *Journal of the European Ceramic Society*, vol. 35, no. 15, pp. 4259–4267, 2015.

[148] Jacobson, N. S., Fox, D. S., Smialek, J. L., Opila, E. J., Dellacorte, C., Glenn, N., Lee, K. N., and State, C., *Performance of Ceramics in Severe Environments*, vol. 13. corrosion: ed., 2005.

[149] Xiang, H., Feng, Z., and Zhou, Y., “Mechanical and thermal properties of Yb_2SiO_5: First-principles calculations and chemical bond theory investigations,” *Journal of Materials Research*, vol. 29, no. 15, pp. 1609–1619, 2014.

[150] Foley, B. M., Brown-Shaklee, H. J., Duda, J. C., Cheaito, R., Gibbons, B. J., Medlin, D., Ihlefeld, J. F., and Hopkins, P. E., “Thermal conductivity of nano-grained $SrTiO_3$ thin films,” *Applied Physics Letters*, vol. 101, no. 23, p. 231908, 2012.

[151] Donovan, B. F., Foley, B. M., Ihlefeld, J. F., Maria, J.-P., and Hopkins, P. E., “Spectral phonon scattering effects on the thermal conductivity of nano-grained barium titanate,” *Applied Physics Letters*, vol. 105, no. 8, p. 82907, 2014.

[152] Wada, M., Matsudaira, T., Kawashima, N., Kitaoka, S., and Takata, M., "Mass transfer in polycrystalline ytterbium disilicate under oxygen potential gradients at high temperatures," *Acta Materialia*, vol. 135, pp. 372–381, 2017.

[153] Richards, B. T., Zhao, H., and Wadley, H. N., "Structure, composition, and defect control during plasma spray deposition of ytterbium silicate coatings," *Journal of Materials Science*, vol. 50, no. 24, pp. 7939–7957, 2015.

[154] Huxtable, S., Cahill, D. G., Fauconnier, V., White, J. O., and Zhao, J.-C., "Thermal conductivity imaging at micrometre-scale resolution for combinatorial studies of materials," *Nature Materials*, vol. 3, pp. 298–301, may 2004.

[155] Zheng, X., Cahill, D. G., and Zhao, J. C., "Thermal conductivity imaging of thermal barrier coatings," *Advanced Engineering Materials*, vol. 7, no. 7, pp. 622–626, 2005.

[156] López-Honorato, E., Chiritescu, C., Xiao, P., Cahill, D. G., Marsh, G., and Abram, T., "Thermal conductivity mapping of pyrolytic carbon and silicon carbide coatings on simulated fuel particles by time-domain thermoreflectance," *Journal of Nuclear Materials*, vol. 378, pp. 35–39, aug 2008.

[157] **Olson, D. H.**, Braun, J. L., and Hopkins, P. E., "Spatially resolved thermoreflectance techniques for thermal conductivity measurements from the nanoscale to the mesoscale," *Journal of Applied Physics*, vol. 126, no. 150901, pp. 47–55, 2019.

[158] Fan, D. and Chen, L. Q., "Diffusion-controlled grain growth in two-phase solids," *Acta Materialia*, vol. 45, no. 8, pp. 3297–3310, 1997.

[159] Kirchheim, R., "Grain coarsening inhibited by solute segregation," *Acta Materialia*, vol. 50, no. 2, pp. 413–419, 2002.

[160] Szwejkowski, C. J., Creange, N. C., Sun, K., Giri, A., Donovan, B. F., Constantin, C., and Hopkins, P. E., "Size effects in the thermal conductivity of gallium oxide (β-Ga_2O_3) films grown via open-atmosphere annealing of gallium nitride," *Journal of Applied Physics*, vol. 117, no. 8, p. 84308, 2015.

[161] Łatka, L., Pawłowski, L., Valette, S., Pateyron, B., Lecompte, J. P., Denoirjean, A., Cattini, A., and Kumar, R., "Thermal diffusivity and conductivity of yttria stabilized zirconia coatings obtained by suspension plasma spraying," *Proceedings of the International Thermal Spray Conference*, vol. 208, pp. 800–804, 2012.

[162] Schlichting, K. W., Padture, N. P., and Klemens, P. G., "Thermal conductivity of dense and porous yttria-stabilized zirconia," *Journal of Materials Science*, vol. 36, no. 12, pp. 3003–3010, 2001.

[163] Chi, W., Sampath, S., and Wang, H., "Microstructure-thermal conductivity relationships for plasma-sprayed yttria-stabilized zirconia coatings," *Journal of the American Ceramic Society*, vol. 91, no. 8, pp. 2636–2645, 2008.

[164] Bondar, I. A., "Rare-Earth Silicates," *Ceramics International*, vol. 8, no. 3, pp. 83–89, 1982.

[165] Webster, J., Westwood, M., Hayes, F., Day, R. J., Taylor, R., Duran, A., Aparicio, M., Rebstock, K., and Vogel, W., "Oxidation Protection Coatings for C/SiC Based on Y_2SiO_5," *Key Engineering Materials*, vol. 132, pp. 1641–1644, apr 1997.

[166] Poerschke, D. L., Hass, D. D., Eustis, S., Seward, G. G., Van Sluytman, J. S., and Levi, C. G., "Stability and CMAS resistance of ytterbium-silicate/hafnate EBCs/TBC for SiC composites," *Journal of the American Ceramic Society*, vol. 98, no. 1, pp. 278–286, 2015.

[167] Poerschke, D. L., Van Sluytman, J. S., Wong, K. B., and Levi, C. G., "Thermochemical compatibility of ytterbia-(hafnia/silica) multilayers for environmental barrier coatings," *Acta Materialia*, vol. 61, no. 18, pp. 6743–6755, 2013.

[168] **Olson, D. H.**, Gaskins, J. T., Tomko, J. A., Opila, E. J., Golden, R. A., Harrington, G. J., Chamberlain, A. L., and Hopkins, P. E., "Local thermal conductivity measurements to determine the fraction of α-cristobalite in thermally grown oxides for aerospace applications," *Scripta Materialia*, vol. 177, pp. 214–217, 2020.

[169] Wisniewski, W., Berndt, S., Müller, M., and Rüssel, C., "Stress induced texture formation in surface crystallized SiO_2 glass," *CrystEngComm*, vol. 15, no. 13, pp. 2392–2400, 2013.

[170] Birch, A. F. and Clark, H., "The thermal conductivity of rocks and its dependence upon temperature and composition," *American Journal of Science*, vol. 238, pp. 529–558, aug 1940.

[171] Kingery, W. D., "Thermal Conductivity: XII, Temperature Dependence of Conductivity for Single-Phase Ceramics," *Journal of the American Ceramic Society*, vol. 38, pp. 251–255, jul 1955.

[172] Ratcliffe, E. H., "Thermal conductivities of fused and crystalline quartz," *British Journal of Applied Physics*, vol. 10, pp. 22–25, jan 1959.

[173] Cahill, D. G., "Thermal conductivity measurement from 30 to 750 K: the 3ω method," *Review of Scientific Instruments*, vol. 61, p. 802, 1990.

[174] Kunugi, M., Soga, N., Sawa, H., and Konishi, A., "Thermal Conductivity of Cristobalite," *Journal of the American Ceramic Society*, vol. 55, pp. 580–580, nov 1972.

[175] Richet, P., Bottinga, Y., Denielou, L., Petitet, J., and Tequi, C., "Thermodynamic properties of quartz, cristobalite and amorphous SiO_2: drop calorimetry measurements between 1000 and 1800 K and a review from 0 to 2000 K," *Geochimica et Cosmochimica Acta*, vol. 46, pp. 2639–2658, dec 1982.

[176] Hofmeister, A. M., "Heat Transport Properties of Cristobalite and Discussion of Snowflake Formation," *The Canadian Mineralogist*, vol. 51, pp. 705–714, oct 2013.

[177] Allen, P. B., Feldman, J. L., Fabian, J., and Wooten, F., "Diffusons, Locons, Propagons: Character of Atomic Vibrations in Amorphous Si," *Philosophical Magazine Part B*, vol. 79, pp. 1715–1731, 1999.

[178] Touloukian, Y. S. and Buyco, E. H., eds., *Thermophysical Properties of Matter - the TPRC Data Series. Volume 5. Specific Heat - Nonmetallic Solids*. New York: Plenum, 1970.

[179] Li, C., Zheng, W., Zhu, Q., Chen, J., Wang, B. Y., and Ju, X., "Microstructure variation in fused silica irradiated by different fluence of UV laser pulses with positron annihilation lifetime and Raman scattering spectroscopy," *Nuclear Instruments and Methods in Physics Research, Section B: Beam Interactions with Materials and Atoms*, vol. 384, pp. 23–29, 2016.

[180] Kingma, K. J. and Hemley, R. J., "Raman spectroscopic study of microcrystalline silica," *American Mineralogist*, vol. 79, no. 3-4, pp. 269–273, 1994.

[181] Bates, J. B., "Raman Spectra of α and β Cristobalite," *The Journal of Chemical Physics*, vol. 57, no. 9, pp. 4042–4047, 2004.

[182] Scott, J. F. and Porto, S. P. S., "Longitudinal and transverse optical lattice vibrations in quartz," *Physical Review*, vol. 161, no. 3, pp. 903–910, 1967.

[183] Kang, K., Koh, Y. K., Chiritescu, C., Zheng, X., and Cahill, D. G., "Two-tint pump-probe measurements using a femtosecond laser oscillator and sharp-edged optical filters," *Review of Scientific Instruments*, vol. 79, no. 114901, 2008.

[184] Thomsen, C., Maris, H. J., and Tauc, J., “Picosecond acoustics as a non-destructive tool for the characterization of very thin films,” *Thin Solid Films*, vol. 154, no. 1, pp. 217–223, 1987.

[185] Tessier, G., Bardoux, M., Boú, C., Filloy, C., and Fournier, D., “Back side thermal imaging of integrated circuits at high spatial resolution,” *Applied Physics Letters*, vol. 90, no. 17, pp. 1–4, 2007.

[186] Gomes, S., Assy, A., and Chapuis, P.-O., “Scanning thermal microscopy: A review,” *Physica status solidis (a)*, vol. 212, no. 3, pp. 477–494, 2015.

[187] Majumdar, A., “Scanning Thermal Microscopy,” *Annual Review of Materials Science*, vol. 29, pp. 505–585, 1999.

[188] Roh, H. H., Lee, J. S., Kim, D. L., Park, J., Kim, K., Kwon, O., Park, S. H., Choi, Y. K., and Majumdar, A., “Novel nanoscale thermal property imaging technique: The 2ω method. II. Demonstration and comparison,” *Journal of Vacuum Science and Technology B: Microelectronics and Nanometer Structures*, vol. 24, no. 5, pp. 2405–2411, 2006.

[189] Roh, H. H., Lee, J. S., Kim, D. L., Park, J., Kim, K., Kwon, O., Park, S. H., Choi, Y. K., and Majumdar, A., “Novel nanoscale thermal property imaging technique: The 2ω method. I. Principle and the 2ω signal measurement,” *Journal of Vacuum Science and Technology B: Microelectronics and Nanometer Structures*, vol. 24, no. 5, pp. 2398–2404, 2006.

[190] Kim, K., Chung, J., Hwang, G., Kwon, O., and Lee, J. S., “Quantitative measurement with scanning thermal microscope by preventing the distortion due to the heat transfer through the air,” *ACS Nano*, vol. 5, no. 11, pp. 8700–8709, 2011.

[191] Lefèvre, S., Volz, S., and Chapuis, P. O., “Nanoscale heat transfer at contact between a hot tip and a substrate,” *International Journal of Heat and Mass Transfer*, vol. 49, no. 1-2, pp. 251–258, 2006.

[192] Rivoaland, L., Maurice, V., Josso, P., Bacos, M. P., and Marcus, P., “The effect of sulfur segregation on the adherence of the thermally-grown oxide on NiAl-II: The oxidation behavior at 900°C of standard, desulfurized or sulfur-doped NiAl(001) single-crystals,” *Oxidation of Metals*, vol. 60, no. 1-2, pp. 159–178, 2003.

[193] Rivoaland, L., Maurice, V., Josso, P., Bacos, M. P., and Marcus, P., “The effect of sulfur segregation on the adherence of the thermally-grown oxide on NiAl-I: Sulfur segregation on the metallic surface of NiAl(001) single-crystals and at NiAl(001)/Al_2O_3 interfaces,” *Oxidation of Metals*, vol. 60, no. 1-2, pp. 137–157, 2003.

[194] Liu, Y. Z., Zheng, S. J., Zhu, Y. L., Wei, H., and Ma, X. L., “Microstructural evolution at interfaces of thermal barrier coatings during isothermal oxidation,” *Journal of the European Ceramic Society*, vol. 36, no. 7, pp. 1765–1774, 2016.

[195] Liu, X., Wang, T., Li, C., Zheng, Z., and Li, Q., “Microstructural evolution and growth kinetics of thermally grown oxides in plasma sprayed thermal barrier coatings,” *Progress in Natural Science: Materials International*, vol. 26, no. 1, pp. 103–111, 2016.

[196] Chen, H., Zhang, C., Xuan, J., Liu, B., Yang, G., Gao, Y., and Luo, H., “Effect of TGO evolution and element diffusion on the life span of YSZ/PtAl and YSZ/NiCrAlY coatings at high temperature,” *Ceramics International*, vol. 46, no. 1, pp. 813–823, 2020.

[197] **Olson, D. H.**, Freedy, K. M., McDonnell, S. J., and Hopkins, P. E., “The influence of titanium adhesion layer oxygen stoichiometry on thermal boundary conductance at gold contacts,” *Applied Physics Letters*, vol. 112, no. 171602, 2018.

[198] Cahill, D. G., Ford, W. K., Goodson, K. E., Mahan, G. D., Majumdar, A., Maris, H. J., Merlin, R., and Phillpot, S. R., “Nanoscale thermal transport,” *Journal of Applied Physics*, vol. 93, no. 2, pp. 793–818, 2003.

[199] Hopkins, P. E., “Thermal transport across solid interfaces with nanoscale imperfections: Effects of roughness, disorder, dislocations, and bonding on thermal boundary conductance,” *ISRN Mechanical Engineering*, vol. 2013, p. 682586, 2013.

[200] Cahill, D. G., Braun, P. V., Chen, G., Clarke, D. R., Fan, S., Goodson, K. E., Keblinski, P., King, W. P., Mahan, G. D., Majumdar, A., Maris, H. J., Phillpot, S. R., Pop, E., Shi, L., and Others,, “Nanoscale thermal transport. II. 2003–2012,” *Applied Physics Reviews*, vol. 1, no. 1, p. 11305, 2014.

[201] Monachon, C., Weber, L., and Dames, C., “Thermal boundary conductance: A materials science perspective,” *Annual Review of Materials Research*, vol. 46, pp. 433–463, 2016.

[202] Little, W. A., “The transport of heat between dissimilar solids at low temperatures,” *Canadian Journal of Physics*, vol. 37, no. 3, pp. 334–349, 1959.

[203] Cheeke, J. D. N., Ettinger, H., and Hebral, B., “Analysis of heat transfer between solids at low temperatures,” *Canadian Journal of Physics*, vol. 54, pp. 1749–1771, 1976.

[204] Hopkins, P. E., Phinney, L. M., Serrano, J. R., and Beechem, T. E., “Effects of surface roughness and oxide layer on the thermal boundary conductance at aluminum/silicon interfaces,” *Physical Review B*, vol. 82, p. 85307, 2010.

[205] Duda, J. C. and Hopkins, P. E., “Systematically controlling Kapitza conductance via chemical etching,” *Applied Physics Letters*, vol. 100, no. 11, p. 111602, 2012.

[206] Hopkins, P. E., Duda, J. C., Clark, S. P., Hains, C. P., Rotter, T. J., Phinney, L. M., and Balakrishnan, G., “Effect of dislocation density on thermal boundary conductance across GaSb/GaAs interfaces,” *Applied Physics Letters*, vol. 98, p. 161913, 2011.

[207] Hopkins, P. E., Norris, P. M., Stevens, R. J., Beechem, T., and Graham, S., “Influence of interfacial mixing on thermal boundary conductance across a chromium/silicon interface,” *Journal of Heat Transfer*, vol. 130, p. 62402, 2008.

[208] Gaskins, J. T., Bulusu, A., Giordano, A. J., Duda, J. C., Graham, S., and Hopkins, P. E., “Thermal Conductance across Phosphonic Acid Molecules and Interfaces: Ballistic versus Diffusive Vibrational Transport in Molecular Monolayers,” *Journal of Physical Chemistry C*, vol. 119, no. 36, pp. 20931–20939, 2015.

[209] Hopkins, P. E., Duda, J. C., Petz, C. W., and Floro, J. A., “Controlling thermal conductance through quantum dot roughening at interfaces,” *Physical Review B*, vol. 84, p. 35438, 2011.

[210] Gorham, C. S., Hattar, K., Cheaito, R., Duda, J. C., Gaskins, J. T., Beechem, T. E., Ihlefeld, J. F., Biedermann, L. B., Piekos, E. S., Medlin, D. L., and Hopkins, P. E., “Ion irradiation of the native oxide/silicon surface increases the thermal boundary conductance across aluminum/silicon interfaces,” *Physical Review B*, vol. 90, p. 24301, 2014.

[211] Hopkins, P. E., Hattar, K., Beechem, T., Ihlefeld, J. F., Medlin, D. L., and Piekos, E. S., “Reduction in thermal boundary conductance due to proton implantation in silicon and sapphire,” *Applied Physics Letters*, vol. 98, p. 231901, 2011.

[212] Hopkins, P. E., Beechem, T. E., Duda, J. C., Hattar, K., Ihlefeld, J. F., Rodriguez, M. A., and Piekos, E. S., “Influence of anisotropy on thermal boundary conductance at solid interfaces,” *Physical Review B*, vol. 84, p. 125408, 2011.

[213] Hopkins, P. E., Hattar, K., Beechem, T., Ihlefeld, J. F., Medlin, D. L., and Piekos, E. S., "Addendum: "Reduction in thermal boundary conductance due to proton implantation in silicon and sapphire" [Appl. Phys. Lett. 98, 231901 (2011)]," *Applied Physics Letters*, vol. 101, no. 9, p. 99903, 2012.

[214] Duda, J. C., English, T. S., Piekos, E. S., Beechem, T. E., Kenny, T. W., and Hopkins, P. E., "Bidirectionally tuning Kapitza conductance through the inclusion of substitutional impurities," *Journal of Applied Physics*, vol. 112, no. 7, p. 73519, 2012.

[215] English, T. S., Duda, J. C., Smoyer, J. L., Jordan, D. A., Norris, P. M., and Zhigilei, L. V., "Enhancing and tuning phonon transport at vibrationally mismatched solid-solid interfaces," *Physical Review B*, vol. 85, no. 3, p. 35438, 2012.

[216] Hopkins, P. E., Baraket, M., Barnat, E. V., Beechem, T. E., Kearney, S. P., Duda, J. C., Robinson, J. T., and Walton, S. G., "Manipulating thermal conductance at metal-graphene contacts via chemical functionalization," *Nano Letters*, vol. 12, pp. 590–595, 2012.

[217] Foley, B. M., Hernández, S. C., Duda, J. C., Robinson, J. T., Walton, S. G., and Hopkins, P. E., "Modifying Surface Energy of Graphene via Plasma-Based Chemical Functionalization to Tune Thermal and Electrical Transport at Metal Interfaces," *Nano Letters*, vol. 15, pp. 4876–4882, aug 2015.

[218] Walton, S. G., Foley, B. M., Hernández, S. C., Boris, D. R., Baraket, M., Duda, J. C., Robinson, J. T., and Hopkins, P. E., "Plasma-based chemical functionalization of graphene to control the thermal transport at graphene-metal interfaces," *Surface and Coatings Technology*, vol. 314, pp. 148–154, mar 2017.

[219] Losego, M. D., Grady, M. E., Sottos, N. R., Cahill, D. G., and Braun, P. V., "Effects of chemical bonding on heat transport across interfaces," *Nature Materials*, vol. 11, no. 6, pp. 502–506, 2012.

[220] O'Brien, P. J., Shenogin, S., Liu, J., Chow, P. K., Laurencin, D., Mutin, P. H., Yamaguchi, M., Keblinski, P., and Ramanath, G., "Bonding-induced thermal conductance enhancement at inorganic heterointerfaces using nanomolecular monolayers," *Nature Materials*, vol. 12, pp. 118–122, 2013.

[221] Duda, J. C., English, T. S., Piekos, E. S., Soffa, W. A., Zhigilei, L. V., and Hopkins, P. E., "Implications of cross-species interactions on the temperature dependence of Kapitza conductance," *Physical Review B*, vol. 84, no. 19, p. 193301, 2011.

[222] Giri, A., Braun, J. L., and Hopkins, P. E., "Implications of Interfacial Bond Strength on the Spectral Contributions to Thermal Boundary Conductance across Solid, Liquid, and Gas Interfaces: A Molecular Dynamics Study," *Journal of Physical Chemistry C*, vol. 120, pp. 24847–24856, 2016.

[223] Wang, Z., Carter, J. A., Lagutchev, A., Koh, Y. K., Seong, N. H., Cahill, D. G., and Dlott, D. D., "Ultrafast flash thermal conductance of molecular chains," *Science*, vol. 317, pp. 787–789, 2007.

[224] Wang, Z., Cahill, D. G., Carter, J. A., Koh, Y. K., Lagutchev, A., Seong, N. H., and Dlott, D. D., "Ultrafast dynamics of heat flow across molecules," *Chemical Physics*, vol. 350, pp. 31–44, 2008.

[225] Giri, A., Niemelä, J.-P., Tynell, T., Gaskins, J. T., Donovan, B. F., Karppinen, M., and Hopkins, P. E., "Heat-transport mechanisms in molecular building blocks of inorganic/organic hybrid superlattices," *Physical Review B*, vol. 93, p. 115310, 2016.

[226] Vieira, E. M. F., Ribeiro, J. F., Sousa, R., Silva, M. M., Dupont, L., and Goncalves, L. M., "Titanium Oxide Adhesion Layer for High Temperature Annealed $Si/Si_3N_4/TiO_x/Pt/LiCoO_2$ Battery Structures," *Journal of Electronic Materials*, vol. 45, pp. 910–916, feb 2016.

[227] Hsieh, S., Beck, D., Matsumoto, T., and Koel, B. E., "Thermal stability of ultrathin titanium films on a Pt (111) substrate," *Thin Solid Films*, vol. 466, no. 1, pp. 123–127, 2004.

[228] Lahiri, B., Dylewicz, R., Rue, R. M. D. L., and Johnson, N. P., “Impact of titanium adhesion layers on the response of arrays of metallic split-ring resonators (SRRs),” *Opt. Express*, vol. 18, pp. 11202–11208, may 2010.

[229] Jeppesen, C., Mortensen, N. A., and Kristensen, A., “The effect of Ti and ITO adhesion layers on gold split-ring resonators,” *Applied Physics Letters*, vol. 97, no. 26, p. 263103, 2010.

[230] Ekmekci, E., Strikwerda, A. C., Fan, K., Keiser, G., Zhang, X., Turhan-Sayan, G., and Averitt, R. D., “Frequency tunable terahertz metamaterials using broadside coupled split-ring resonators,” *Phys. Rev. B*, vol. 83, p. 193103, may 2011.

[231] Aouani, H., Wenger, J., Gérard, D., Rigneault, H., Devaux, E., Ebbesen, T. W., Mahdavi, F., Xu, T., and Blair, S., “Crucial Role of the Adhesion Layer on the Plasmonic Fluorescence Enhancement,” *ACS Nano*, vol. 3, no. 7, pp. 2043–2048, 2009.

[232] Habteyes, T. G., Dhuey, S., Wood, E., Gargas, D., Cabrini, S., Schuck, P. J., Alivisatos, A. P., and Leone, S. R., “Metallic Adhesion Layer Induced Plasmon Damping and Molecular Linker as a Nondamping Alternative,” *ACS Nano*, vol. 6, no. 6, pp. 5702–5709, 2012.

[233] Giri, A., Gaskins, J. T., Donovan, B. F., Szwejkowski, C., Warzoha, R. J., Rodriguez, M. A., Ihlefeld, J., and Hopkins, P. E., “Mechanisms of nonequilibrium electron-phonon coupling and thermal conductance at interfaces,” *Journal of Applied Physics*, vol. 117, p. 105105, mar 2015.

[234] Freedy, K. M., Giri, A., Foley, B. M., Barone, M. R., Hopkins, P. E., and McDonnell, S., “Titanium Contacts to Graphene: Process-Induced Variability in Electronic and Thermal Transport,” *Nanotechnology*, vol. 29, no. 145201, 2018.

[235] Freedy, K. M., Litwin, P. M., and McDonnell, S. J., “In-Vacuo Studies of Transition Metal Dichalcogenide Synthesis and Layered Material Integration,” *ECS Transactions*, vol. 77, no. 8, pp. 11–25, 2017.

[236] Sham, T. K. and Lazarus, M. S., “X-ray photoelectron spectroscopy (XPS) studies of clean and hydrated TiO_2 (rutile) surfaces,” *Chemical Physics Letters*, vol. 68, no. 2, pp. 426–432, 1979.

[237] McDonnell, S., Smyth, C., Hinkle, C. L., and Wallace, R. M., “MoS_2–Titanium Contact Interface Reactions,” *ACS Applied Materials and Interfaces*, vol. 8, no. 12, pp. 8289–8294, 2016.

[238] Atkins, P. and De Paula, J., *Thermodynamics and Kinetics*. W.H. Freeman and Co., 2005.

[239] **Olson, D. H.**, Sales, M. G., Tomko, J. A., Lu, T. F., Prezhdo, O. V., McDonnell, S. J., and Hopkins, P. E., “Band alignment and defects influence the electron-phonon heat transport mechanisms across metal interfaces,” *Applied Physics Letters*, vol. 118, no. 16, pp. 1–7, 2021.

[240] Johnston, M. B. and Herz, L. M., “Hybrid Perovskites for Photovoltaics: Charge-Carrier Recombination, Diffusion, and Radiative Efficiencies,” *Accounts of Chemical Research*, vol. 49, no. 1, pp. 146–154, 2016.

[241] Krüger, J., Plass, R., Cevey, L., Piccirelli, M., Grätzel, M., and Bach, U., “High efficiency solid-state photovoltaic device due to inhibition of interface charge recombination,” *Applied Physics Letters*, vol. 79, no. 13, pp. 2085–2087, 2001.

[242] Pivrikas, A., Sariciftci, N. S., Juska, G., and Osterbacka, R., “A Review of Charge Transport and Recombination in Polymer/Fullerine Organic Solar Cells,” *Progress in Photovoltaics: Research and Applications*, vol. 15, pp. 677–696, 2007.

[243] Nie, Z., Gao, X., Ren, Y., Xia, S., Wang, Y., Shi, Y., Zhao, J., and Wang, Y., "Harnessing Hot Phonon Bottleneck in Metal Halide Perovskite Nanocrystals via Interfacial Electron-Phonon Coupling," *Nano Letters*, vol. 20, no. 6, pp. 4610–4617, 2020.

[244] Qian, R., Zong, H., Schneider, J., Zhou, G., Zhao, T., Li, Y., Yang, J., Bahnemann, D. W., and Pan, J. H., "Charge carrier trapping, recombination and transfer during TiO_2 photocatalysis: An overview," *Catalysis Today*, vol. 335, no. October 2018, pp. 78–90, 2019.

[245] Hammarström, L., "Accumulative Charge Separation for Solar Fuels Production: Coupling Light-Induced Single Electron Transfer to Multielectron Catalysis," *Accounts of Chemical Research*, vol. 48, no. 3, pp. 840–850, 2015.

[246] Albrecht, U. and Bässler, H., "Efficiency of charge recombination in organic light emitting diodes," *Chemical Physics*, vol. 199, no. 2-3, pp. 207–214, 1995.

[247] Kalinowski, J., Cocchi, M., Di Marco, P., Stampor, W., Giro, G., and Fattori, V., "Impact of high electric fields on the charge recombination process in organic light-emitting diodes," *Journal of Physics D: Applied Physics*, vol. 33, no. 19, pp. 2379–2387, 2000.

[248] Scheibenzuber, W. G., Schwarz, U. T., Sulmoni, L., Dorsaz, J., Carlin, J. F., and Grandjean, N., "Recombination coefficients of GaN-based laser diodes," *Journal of Applied Physics*, vol. 109, no. 9, 2011.

[249] Coldren, L. A., Corzine, S. W., and Masanovic, M. L., *Diode Lasers and Photonic Integrated Circuits*. John Wiley & Sons, Ltd, 2 ed., 2011.

[250] Na-Phattalung, S., Smith, M. F., Kim, K., Du, M. H., Wei, S. H., Zhang, S. B., and Limpijumnong, S., "First-principles study of native defects in anatase TiO_2," *Physical Review B - Condensed Matter and Materials Physics*, vol. 73, no. 12, pp. 1–6, 2006.

[251] Bai, Y., Mora-Seró, I., De Angelis, F., Bisquert, J., and Wang, P., "Titanium dioxide nanomaterials for photovoltaic applications," *Chemical Reviews*, vol. 114, no. 19, pp. 10095–10130, 2014.

[252] Kentsch, R., Scholz, M., Horn, J., Schlettwein, D., Oum, K., and Lenzer, T., "Exciton Dynamics and Electron-Phonon Coupling Affect the Photovoltaic Performance of the $Cs_2AgBiBr_6$ Double Perovskite," *Journal of Physical Chemistry C*, vol. 122, no. 45, pp. 25940–25947, 2018.

[253] Das, T. K., Ilaiyaraja, P., and Sudakar, C., "Template assisted nanoporous TiO_2 nanoparticles: The effect of oxygen vacancy defects on photovoltaic performance of DSSC and QDSSC," *Solar Energy*, vol. 159, no. November 2017, pp. 920–929, 2018.

[254] Das, T. K., Ilaiyaraja, P., Mocherla, P. S., Bhalerao, G. M., and Sudakar, C., "Influence of surface disorder, oxygen defects and bandgap in TiO_2 nanostructures on the photovoltaic properties of dye sensitized solar cells," *Solar Energy Materials and Solar Cells*, vol. 144, pp. 194–209, 2016.

[255] Ma, X., Cheng, Z., Tian, M., Liu, X., Cui, X., Huang, Y., Tan, S., Yang, J., and Wang, B., "Formation of Plasmonic Polarons in Highly Electron-Doped Anatase TiO_2," *Nano Letters*, pp. 0–6, 2020.

[256] Radecka, M., Brudnik, A., Kulinowski, K., Kot, A., Leszczyński, J., Kanak, J., and Zakrzewska, K., "Titanium Dioxide Thin Films with Controlled Stoichiometry for Photoelectrochemical Systems," *Journal of Electronic Materials*, vol. 48, no. 9, pp. 5481–5490, 2019.

[257] Sharma, V., Das, T. K., Ilaiyaraja, P., and Sudakar, C., "Oxygen non-stoichiometry in TiO_2 and ZnO nano rods: Effect on the photovoltaic properties of dye and Sb_2S_3 sensitized solar cells," *Solar Energy*, vol. 191, no. July, pp. 400–409, 2019.

[258] Cheaito, R., *The Role of Size Effects on the Thermal Conductivity of Thin Film Alloys and Superlattices*. PhD thesis, University of Virginia, 2015.

[259] Wilson, R. B. and Cahill, D. G., "Experimental validation of the interfacial form of the Wiedemann-Franz law," *Physical Review Letters*, vol. 108, no. 25, pp. 1–5, 2012.

[260] Paddock, C. A. and Eesley, G. L., "Transient thermoreflectance from thin metal films," *Journal of Applied Physics*, vol. 60, pp. 285–290, jul 1986.

[261] Tas, G. and Maris, H. J., "Electron diffusion in metals studied by picosecond ultrasonics," *Physical Review B*, vol. 49, pp. 15046–15054, jun 1994.

[262] Kittel, C., *Introduction to solid state*, vol. 162. John Wiley & Sons, 1966.

[263] Scott, E. A., Gaskins, J. T., King, S. W., and Hopkins, P. E., "Thermal conductivity and thermal boundary resistance of atomic layer deposited high-k dielectric aluminum oxide, hafnium oxide, and titanium oxide thin films on silicon," *APL Materials*, vol. 6, no. 5, 2018.

[264] Johnson, P. B. and Christy, R. W., "Optical Constant of the Nobel Metals," *Physical Review B*, vol. 6, no. 12, pp. 4370–4379, 1972.

[265] Sarkar, S., Gupta, V., Kumar, M., Schubert, J., Probst, P. T., Joseph, J., and König, T. A., "Hybridized Guided-Mode Resonances via Colloidal Plasmonic Self-Assembled Grating," *ACS Applied Materials and Interfaces*, vol. 11, no. 14, pp. 13752–13760, 2019.

[266] Malitson, I. H. and Dodge, M. J., "Refractive Index and Birefringence of Synthetic Sapphire," *J. Opt. Soc. Am.*, vol. 62, p. 1405, nov 1972.

[267] Tomko, J. A., Runnerstrom, E. L., Wang, Y. S., Chu, W., Nolen, J. R., **Olson, D. H.**, Kelley, K. P., Cleri, A., Nordlander, J., Caldwell, J. D., Prezhdo, O. V., Maria, J. P., and Hopkins, P. E., "Long-lived modulation of plasmonic absorption by ballistic thermal injection," *Nature Nanotechnology*, vol. 16, pp. 47–51, 2021.

[268] Hostetler, J. L., Smith, A. N., Czajkowsky, D. M., and Norris, P. M., "Measurement of the electron-phonon coupling factor dependence on film thickness and grain size in Au, Cr, and Al," *Applied Optics*, vol. 38, no. 16, p. 3614, 1999.

[269] Elsayed-Ali, H. E., Juhasz, T., Smith, G. O., and Bron, W. E., "Femtosecond thermoreflectivity and thermotransmissivity of polycrystalline and single-crystalline gold films," *Physical Review B*, vol. 43, pp. 4488–4491, feb 1991.

[270] Groeneveld, R. H. M., Sprik, R., and Lagendijk, A., "Femtosecond spectroscopy of electron-electron and electron-phonon energy relaxation in Ag and Au," *Physical Review. B, Condensed Matter*, vol. 51, pp. 11433–11445, 1995.

[271] Hohlfeld, J., Wellershoff, S.-S., Gudde, J., Conrad, U., Jahnke, V., and Matthias, E., "Electron and lattice dynamics following optical excitation of metals," *Chemical Physics*, vol. 251, pp. 237–258, 2000.

[272] Lu, T. F., Wang, Y. S., Tomko, J. A., Hopkins, P. E., Zhang, H. X., and Prezhdo, O. V., "Control of Charge Carrier Dynamics in Plasmonic Au Films by TiO_x Substrate Stoichiometry," *Journal of Physical Chemistry Letters*, vol. 11, no. 4, pp. 1419–1427, 2020.

[273] Giustino, F., "Electron-phonon interactions from first principles," *Reviews of Modern Physics*, vol. 89, no. 1, pp. 1–68, 2017.

[274] Freedy, K. M., **Olson, D. H.**, Hopkins, P. E., and McDonnell, S. J., “Titanium contacts to MoS_2 with interfacial oxide: Interface chemistry and thermal transport,” *Physical Review Materials*, vol. 3, no. 10, pp. 1–7, 2019.

[275] Donovan, B. F., Tomko, J. A., Giri, A., **Olson, D. H.**, Braun, J. L., Gaskins, J. T., and Hopkins, P. E., “Localized thin film damage sourced and monitored via pump-probe modulated thermoreflectance,” *Review of Scientific Instruments*, vol. 88, no. 5, 2017.

[276] Tomko, J. A., **Olson, D. H.**, Braun, J. L., Kelliher, A. P., Kaehr, B., and Hopkins, P. E., “Substrate thermal conductivity controls the ability to manufacture microstructures via laser-induced direct write,” *Applied Physics Letters*, vol. 112, no. 5, 2018.

[277] Giri, A., King, S. W., Lanford, W. A., Mei, A. B., Merrill, D., Li, L., Oviedo, R., Richards, J., **Olson, D. H.**, Braun, J. L., Gaskins, J., Deangelis, F., Henry, A., and Hopkins, P. E., “Interfacial Defect Vibrations Enhance Thermal Transport in Amorphous Multilayers with Ultrahigh Thermal Boundary Conductance,” *Advanced Materials*, vol. 30, no. 44, pp. 1–6, 2018.

[278] Braun, J. L., Rost, C. M., Lim, M., Giri, A., **Olson, D. H.**, Kotsonis, G. N., Stan, G., Brenner, D. W., Maria, J. P., and Hopkins, P. E., “Charge-induced disorder controls the thermal conductivity of entropy-stabilized oxides,” *Advanced Materials*, vol. 30, no. 51, pp. 1–8, 2018.

[279] Tomko, J. A., **Olson, D. H.**, Giri, A., Gaskins, J. T., Donovan, B. F., O’Malley, S. M., and Hopkins, P. E., “Nanoscale Wetting and Energy Transmission at Solid/Liquid Interfaces,” *Langmuir*, vol. 35, pp. 2106–2114, 2019.

[280] Rosul, M. G., Lee, D., **Olson, D. H.**, Liu, N., Wang, X., Hopkins, P. E., Lee, K., and Zebarjadi, M., “Thermionic transport across gold-graphene-WSe_2 van der Waals heterostructures,” *Science Advances*, vol. 5, no. 11, 2019.

[281] Aryana, K., Gaskins, J. T., Nag, J., Read, J. C., **Olson, D. H.**, Grobis, M. K., and Hopkins, P. E., “Thermal properties of carbon nitride toward use as an electrode in phase change memory devices,” *Applied Physics Letters*, vol. 116, no. 4, 2020.

[282] Freedy, K. M., Zhu, T., **Olson, D. H.**, Litwin, P. M., Hopkins, P. E., Zebarjadi, M., and McDonnell, S. J., “Interface chemistry and thermoelectric characterization of Ti and TiO_x contacts to MBE-grown WSe_2,” *2D Materials*, vol. 7, no. 4, 2020.

[283] Giri, A., Chou, S. S., Drury, D. E., Tomko, K. Q., **Olson, D. H.**, Gaskins, J. T., Kaehr, B., and Hopkins, P. E., “Molecular tail chemistry controls thermal transport in fullerene films,” *Physical Review Materials*, vol. 4, no. 6, pp. 1–8, 2020.

[284] Zhu, T., **Olson, D. H.**, Hopkins, P. E., and Zebarjadi, M., “Heat diffusion imaging: In-plane thermal conductivity measurement of thin films in a broad temperature range,” *Review of Scientific Instruments*, vol. 91, no. 11, 2020.

[285] Rasel, M. A. J., Giri, A., **Olson, D. H.**, Ni, C., Hopkins, P. E., and Feser, J. P., “Chain-Length Dependence of Thermal Conductivity in 2D Alkylammonium Lead Iodide Single Crystals,” *ACS Applied Materials and Interfaces*, vol. 12, no. 48, pp. 53705–53711, 2020.

[286] Zhang, F., Zheng, B., Sebastian, A., **Olson, D. H.**, Liu, M., Fujisawa, K., Pham, Y. T. H., Jimenez, V. O., Kalappattil, V., Miao, L., Zhang, T., Pendurthi, R., Lei, Y., Elías, A. L., Wang, Y., Alem, N., Hopkins, P. E., Das, S., Crespi, V. H., Phan, M. H., and Terrones, M., “Monolayer Vanadium-Doped Tungsten Disulfide: A Room-Temperature Dilute Magnetic Semiconductor,” *Advanced Science*, vol. 7, no. 24, pp. 1–9, 2020.

[287] Liu, H., Grasseschi, D., Dodda, A., Fujisawa, K., **Olson, D. H.**, Kahn, E., Zhang, F., Zhang, T., Lei, Y., Branco, R. B. N., El'ias, A. L., Silva, R. C., Yeh, Y.-T., Maroneze, C. M., Seixas, L., Hopkins, P., Das, S., de Matos, C. J. S., and Terrones, M., "Spontaneous chemical functionalization via coordination of Au single atoms on monolayer MoS_2," *Science Advances*, vol. 6, no. 49, 2020.

[288] Aryana, K., Gaskins, J. T., Nag, J., Stewart, D. A., Bai, Z., Mukhopadhyay, S., Read, J. C., **Olson, D. H.**, Hoglund, E. R., Howe, J. M., Giri, A., Grobis, M. K., and Hopkins, P. E., "Interface controlled thermal properties of ultra-thin chalcogenide-based phase change memory devices," *Nature Communications*, vol. 12, 2021.

[289] Fields, S. S., **Olson, D. H.**, Jaszewski, S. T., Fancher, C. M., Smith, S. W., Dickie, D. A., Esteves, G., Henry, M. D., Davids, P. S., Hopkins, P. E., and Ihlefeld, J. F., "Compositional and phase dependence of elastic modulus of crystalline and amorphous $Hf_{1-x}Zr_xO_2$ thin films," *Applied Physics Letters*, vol. 118, no. 10, 2021.

[290] Hohensee, G. T., Hsieh, W. P., Losego, M. D., and Cahill, D. G., "Interpreting picosecond acoustics in the case of low interface stiffness," *Review of Scientific Instruments*, vol. 83, no. 11, 2012.

[291] Cordfunke, E. H. P., Booij, A. S., and Van Der Laan, R. R., "The thermochemical properties of $Y_2Si_2O_7$ and $Dy_2Si_2O_7$," tech. rep., Netherlands Energy Research Foundation ECN, 1998.

[292] Jiang, P., Qian, X., Li, X., and Yang, R., "Three-dimensional anisotropic thermal conductivity tensor of single crystalline β-Ga_2O_3," *Applied Physics Letters*, vol. 113, p. 232105, dec 2018.

[293] Nye, J. F., *Physical Properties of Crystals*. London: Oxford University Press, 1967.

[294] Luo, Y., Wang, J., Li, J., Hu, Z., and Wang, J., "Theoretical study on crystal structures, elastic stiffness, and intrinsic thermal conductivities of β-, γ-, and δ-$Y_2Si_2O_7$," *Journal of Materials Research*, vol. 30, no. 4, pp. 493–502, 2015.

[295] Tian, Z., Zheng, L., Wang, J., Wan, P., Li, J., and Wang, J., "Theoretical and experimental determination of the major thermo-mechanical properties of RE_2SiO_5 (RE=Tb, Dy, Ho, Er, Tm, Yb, Lu, and Y) for environmental and thermal barrier coating applications," *Journal of the European Ceramic Society*, 2016.

[296] Ogawa, T., Otani, N., Yokoi, T., Fisher, C. A., Kuwabara, A., Moriwake, H., Yoshiya, M., Kitaoka, S., and Takata, M., "Density functional study of the phase stability and Raman spectra of Yb_2O_3, Yb_2SiO_5 and $Yb_2Si_2O_7$ under pressure," *Physical Chemistry Chemical Physics*, vol. 20, no. 24, pp. 16518–16527, 2018.

[297] Bretheau-Raynal, F., P, D. J., Driffor, M., and Blanzat, B., "Raman Spectroscopic Study of Thortveitite Structure Silicates," *Journal of Raman Spectroscopy*, vol. B, no. 1, pp. 39–42, 1979.

[298] Einollahzadeh-Samadi, M., Dariani, R. S., and Abdi, M., "Characterization of nanocrystalline Ti films deposited by DC magnetron sputtering onto FTO glass substrate," *Journal of Materials Research*, vol. 30, no. 20, pp. 3093–3103, 2015.

[299] Yang, T.-S., Shiu, C.-B., and Wong, M.-S., "Structure and hydrophilicity of titanium oxide films prepared by electron beam evaporation," *Surface Science*, vol. 548, no. 1, pp. 75–82, 2004.

[300] Scofield, J. H., "Hartree-Slater subshell photoionization cross-sections at 1254 and 1487 eV," *Journal of Electron Spectroscopy and Related Phenomena*, vol. 8, no. 2, pp. 129–137, 1976.

[301] Himpsel, F. J., McFeely, F. R., Taleb-Ibrahimi, A., Yarmoff, J. A., and Hollinger, G., "Microscopic structure of the SiO_2/Si interface," *Phys. Rev. B*, vol. 38, pp. 6084–6096, sep 1988.

[302] Briggs, D., “Handbook of X-ray Photoelectron Spectroscopy,” *Surface and Interface Analysis*, vol. 3, pp. 72–73, 1981.

[303] Radue, E. L., Tomko, J. A., Giri, A., Braun, J. L., Zhou, X., Prezhdo, O. V., Runnerstrom, E. L., Maria, J. P., and Hopkins, P. E., “Hot Electron Thermoreflectance Coefficient of Gold during Electron-Phonon Nonequilibrium,” *ACS Photonics*, vol. 5, no. 12, pp. 4880–4887, 2018.

[304] Powell, R. W. and Tye, R. P., “The thermal and electrical conductivity of titanium and its alloys,” *Journal of the Less Common Metals*, vol. 3, no. 3, pp. 226–233, 1961.

[305] Stoner, R. J. and Maris, H. J., “Kapitza conductance and heat flow between solids at temperatures from 50 to 300 K,” *Physical Review B*, vol. 48, no. 22, pp. 16373–16387, 1993.

[306] Akimov, A. V. and Prezhdo, O. V., “The PYXAID program for non-adiabatic molecular dynamics in condensed matter systems,” *Journal of Chemical Theory and Computation*, vol. 9, no. 11, pp. 4959–4972, 2013.

[307] Akimov, A. V. and Prezhdo, O. V., “Advanced capabilities of the PYXAID program: Integration schemes, decoherence effects, multiexcitonic states, and field-matter interaction,” *Journal of Chemical Theory and Computation*, vol. 10, no. 2, pp. 789–804, 2014.

[308] Giannozzi, P., Baroni, S., Bonini, N., Calandra, M., Car, R., Cavazzoni, C., Ceresoli, D., Chiarotti, G. L., Cococcioni, M., Dabo, I., Dal Corso, A., De Gironcoli, S., Fabris, S., Fratesi, G., Gebauer, R., Gerstmann, U., Gougoussis, C., Kokalj, A., Lazzeri, M., Martin-Samos, L., Marzari, N., Mauri, F., Mazzarello, R., Paolini, S., Pasquarello, A., Paulatto, L., Sbraccia, C., Scandolo, S., Sclauzero, G., Seitsonen, A. P., Smogunov, A., Umari, P., and Wentzcovitch, R. M., “QUANTUM ESPRESSO: A modular and open-source software project for quantum simulations of materials,” *Journal of Physics Condensed Matter*, vol. 21, no. 39, 2009.

[309] Tully, J. C., “Molecular dynamics with electronic transitions,” *The Journal of Chemical Physics*, vol. 93, no. 2, pp. 1061–1071, 1990.

[310] Perdew, J. P., Burke, K., and Ernzerhof, M., “Generalized gradient approximation made simple,” *Physical Review Letters*, vol. 77, no. 18, pp. 3865–3868, 1996.

[311] Kresse, G. and Joubert, D., “From ultrasoft pseudopotentials to the projector augmented-wave method,” *Physical Review B - Condensed Matter and Materials Physics*, vol. 59, no. 3, pp. 1758–1775, 1999.

[312] Nehaoua, N., Belkada, R., Tala-Ighil, R. Z., Thomas, L., Chemam, R., and Mekki, D. E., “Adsorption and dissociation of H_2S on the anatase TiO_2 (100) surface: DFT + U study,” *Materials Research Express*, vol. 6, no. 2, 2019.

[313] Private communication with Pepe Silvia and Carol from H.R.